

# **Single Molecules and Nanocrystals: Molecular Recognition Forces and Optomechanical Switching**

**DISSERTATION**

**submitted in partial fulfillment  
of the requirements for the degree of  
Doktor der Naturwissenschaften  
(Dr. rer. nat.)**

**RAINER ECKEL**

**Faculty of Physics  
University of Bielefeld  
December 2005**



## **Erklärung**

Hiermit erkläre ich an Eides statt, daß ich die vorliegende Arbeit selbständig verfaßt und dabei keine weiteren als die angegebenen Hilfsmittel verwendet habe.  
Mit einer Auslegung in der Universitätsbibliothek bin ich einverstanden.

Bielefeld, den 09. Januar 2006

(Rainer Eckel)

Diese Arbeit entstand unter der Leitung von Herrn **PD Dr. Robert Ros** sowie Herrn **Prof. Dr. Dario Anselmetti** in der Arbeitsgruppe Experimentelle Biophysik und Angewandte Nanowissenschaften der Fakultät für Physik der Universität Bielefeld im Rahmen des Sonderforschungsbereichs 613: Physik von Einzelmolekülprozessen und molekularer Erkennung in organischen Systemen.

**2. Gutachter:** Prof. Dr. Armin Gölzhäuser

Actioni contrariam semper et aequalem esse reactionem: sive corporum duorum actiones in se mutuo semper esse aequales et in partes contrarias dirigi.

To every action there is always opposed an equal reaction; or, the mutual actions of two bodies upon each other are always equal, and directed to contrary parts.

Isaac Newton, *Philosophiae Naturalis Principia Mathematica* (London, 1687)

# Contents

<b>1 General Introduction</b>	<b>1</b>
<b>2 Discrimination of Binding Mechanisms in Individual DNA-Ligand Complexes</b>	<b>6</b>
2.1 Introduction . . . . .	6
2.1.1 Single Molecule Force Spectroscopy (SMFS) with the AFM . . . . .	7
2.1.2 SMFS with Optical Tweezers . . . . .	10
2.1.3 Immobilization Methods for SMFS . . . . .	13
2.1.4 Overstretching Double-Stranded DNA . . . . .	14
2.1.5 Binding of Small Ligands to DNA . . . . .	16
2.1.6 Simple Models for the Molecular Elasticity of DNA . . . . .	19
2.2 Publication I . . . . .	21
2.2.1 Contribution . . . . .	21
2.3 Publications II and III . . . . .	28
2.3.1 Contributions . . . . .	28
<b>3 SMFS Affinity Ranking of Native and Synthetic Point-Mutated Transcription Factors</b>	<b>42</b>
3.1 Introduction . . . . .	42
3.1.1 Molecular Recognition in Transcription Regulation . . . . .	43
3.1.2 The Transcription Factor PhoB . . . . .	45
3.1.3 Forces and Kinetics in SMFS: The Standard Theory . . . . .	48
3.2 Publication IV . . . . .	53
3.2.1 Contribution . . . . .	53
3.3 SMFS Studies with the Native Protein PhoB: The Role of the Protein Environment . . . . .	58
3.3.1 Materials and Methods . . . . .	61
<b>4 SMFS of Molecular Recognition in Supramolecular Guest-Host Systems</b>	<b>63</b>

## Contents

---

4.1	Introduction . . . . .	63
4.1.1	Supramolecular Chemistry . . . . .	64
4.1.2	Calixarenes and Resorc[4]arenes . . . . .	64
4.1.3	Molecular Optical Switches . . . . .	66
4.2	Publication V . . . . .	68
4.2.1	Contribution . . . . .	68
4.3	SMFS Experiments with a Photoswitchable Resorc[4]arene . . . . .	74
4.3.1	Materials and Methods . . . . .	77
<b>5</b>	<b>An Improved Theory for SMFS Analysis: Heterogeneity of Chemical Bonds</b>	<b>78</b>
5.1	Introduction . . . . .	78
5.2	Publication VI . . . . .	81
5.2.1	Contribution . . . . .	81
<b>6</b>	<b>Mechanical Emission Control of Individually Addressed Nanocrystals</b>	<b>97</b>
6.1	Introduction . . . . .	97
6.1.1	Mechanical Switching of Single Nanoobjects . . . . .	97
6.1.2	Semiconductor Nanocrystals . . . . .	98
6.1.3	Fluorescence Quenching . . . . .	102
6.1.4	Single Molecule Fluorescence Microscopy . . . . .	104
6.1.5	Total Internal Reflection Fluorescence Microscopy (TIRFM) . . . . .	106
6.2	Publication VII . . . . .	109
6.2.1	Contribution . . . . .	109
6.3	Publication VIII . . . . .	121
6.3.1	Contribution . . . . .	121
<b>7</b>	<b>Conclusions and Outlook</b>	<b>130</b>
<b>Bibliography</b>		<b>135</b>
<b>Acknowledgements</b>		<b>146</b>
<b>Appendix</b>		<b>148</b>
List of Publications . . . . .	148	
Contributions to Conferences . . . . .	149	
Curriculum Vitae . . . . .	152	

# 1 General Introduction

In the future, the emerging field of nanoscale science will stimulate the implementation of novel materials and techniques into everyday life, with applications ranging from communication to health care. This revolution is accompanied and supported by the ongoing and accelerating development of the life sciences in the post-genome era. Especially molecular biophysics has opened new perspectives and contributes substantially to progress in the field.

The definition that delimits the vast variety of nanoscience to other scientific subjects is given by the word itself, which is derived from the prefix “nano” ( $\cdot 10^{-9}$ ; from the greek *νάνος* for “dwarf”): It deals with objects whose physical dimensions are of the order of nanometers (nm). This is the typical length scale of entities constituted of only a small number of atoms, giving rise to molecules (if the atoms are linked covalently) and nanocrystals (if the valence electrons of the constituting atoms are quasi-free, much like in an extensive solid). The properties of nanoobjects result from their dimensionality and are in many respects intermediate between the corresponding features of single atoms on the one and bulk matter on the other hand. The study of these interesting properties is a highly interdisciplinary venture where the classical frontiers of scientific disciplines become blurred. The nanosciences have the potential to fulfill great expectations from all fields of science. Physicists are investigating quantum mechanical concepts at work which have long since been only theoretical postulates. Chemists aspire the design of “intelligent” molecules and materials atom by atom. Molecular biologists can study and manipulate the interplay of the complex machinery involved in metabolic processes at the single molecule level. Moreover, the fundamental research done on nanoscale objects will also foster a manifold of applications. Nanoscaled electronic, optical and mechanical devices for the storage, processing and transmission of information are conceived which might someday bring about a new technological revolution in computer science. Novel, designed molecular machines facilitating the control and manipulation of specific biochemical processes may have a great impact on medicinal progress.

A crucial task in this context is the study of individual (macro)molecules. The data obtained on molecular properties by means of classical ensemble experiments always represent mean values, averaged over a vast number of molecules (typically of the order of a mole, i.e.  $\approx 10^{23}$  molecules). The statistical treatment of these ensembles is the basis for the definition of thermodynamic state functions. This approach limits the available information to the respective mean of a distribution of molecular properties. Often, these average values are sufficient and all we need to know about a certain system. In some cases, however, the interesting issue is the very distribution of a molecular property itself. For example, consider a chemical reaction. The temperature of the reaction mixture is a bulk property (and a thermodynamic state function). It is an average over the distribution of the respective kinetic energies of all the molecules forming the ensemble. In this distribution, only a small number of molecules will have enough energy to overcome the activational barrier for reaction in a collision. It is only these few molecules which will react, releasing products which will drive the reaction further. We need a single molecule experiment to monitor their behavior. Experiments on individual molecules or nanocrystals facilitate the observation of transient intermediates, reaction pathways, and molecular dynamics without the need to synchronize an ensemble, and the variety of single molecule techniques available has developed rapidly during the last two decades.

A very important physical quantity which allows statements about population heterogeneities and intramolecular transitions is force. A whole group of experimental methods which are capable to measure forces acting on single molecules and molecular complexes has evolved. Among these, a widely applied is the atomic force microscope (AFM) [1], where forces are measured by monitoring the mechanical deflection of a microfabricated cantilever, mostly by detecting the position of a reflected laser beam (light pointer) [2]. Cantilever spring constants ranging from  $10 \text{ pN nm}^{-1}$  up to  $100 \text{ nN nm}^{-1}$  and the sensor sensitivity which is capable to indicate deflections of less than a nanometer enable the measurement of forces ranging from  $10 \text{ nN}$  down to the aN regime. Related techniques also featuring a mechanical force transducer are based upon microneedle [3] or biomembrane [4] force probes. A different approach to force detection is based on the manipulation of microscale beads in external fields, among which are laminar hydrodynamic flux [5], magnetic [6] and electromagnetic [7] fields, the latter giving rise to the technique of optical traps and tweezers. In an optical tweezers (OT) experiment, a dielectric bead is trapped in the electric field gradient of a laser focus. Out-of-focus movements effect restoring forces which can be detected from  $200 \text{ pN}$  down to sub-pN values.

---

Single molecule force spectroscopy (SMFS) experiments can be performed on single, chain-like macromolecules and on single ligand-receptor complexes. Intramolecular forces directly mirror the mechanics and elasticity of a single molecule. Pathbreaking experiments which demonstrated the force response of a single molecule to an external force were performed on polysaccharides [8] and the muscle protein titin [9], where even the unfolding of single protein domains could be observed and compared to molecular dynamics simulations. The first intramolecular SMFS experiments on single DNA molecules [10] exhibited several structural transitions induced by the externally applied force (cf. chapter 2.1.3). It could be shown that the forces involved in these intramolecular transitions were sequence-dependent [11]. The first part of the work presented here is concerned with the question how the binding of small molecules to DNA influences the mechanical response and the intramolecular transitions observed for free DNA in SMFS experiments, and how this influence can be quantified in terms of molecular elasticity models. It will turn out that the force response of individual DNA-ligand complexes can be used to distinguish between different binding modes of the ligands (chapter 2). SMFS with the AFM can also give important information on intermolecular forces acting between individual ligand and receptor molecules. In these experiments, one of the binding partners is attached to the force sensor (cantilever), while the other molecule is immobilized on the sample surface (which is connected to the AFM piezo element). In thermally activated systems, the force distribution is a function of the “loading rate”, i.e. the development of the acting force with time [12]. A slowly increasing load leaves enough time for thermal fluctuations to drive the system across the activational barrier of the binding potential, giving rise to small unbinding forces (and vice versa). Dynamic force spectroscopy, i.e. SMFS experiment series at different loading rates, yield data which characterize the energy landscape and yield the thermal off-rate for the dissociation process as kinetic information [13]. In 1997, Evans and Ritchie proposed a theory for the analysis of intermolecular SMFS data [12] which has since, though there have been several improvements, equaled the status of a standard theory. This theory draws upon several assumptions whose justification is still a matter of discussion. In this work, a novel approach for theoretical analysis is presented which drops a major constraint of the standard theory. This extended theory takes a heterogeneity of chemical bonds into account which effects a random variation of the force-dependent off-rates. This analysis is tested upon several sets of experimental data (chapter 5).

The most interesting issue tackled by intermolecular SMFS is molecular recognition. The term signifies the specific interaction of macromolecules or macromolecular assemblies with defined kinetics, based upon weak intermolecular forces which give rise to

ionic, hydrogen and van der Waals bonds. The high selectivity of molecular recognition reactions is due to the specific combination and complementarity of usually many interactions at a time. The importance of recognition reactions in biological systems cannot be overestimated: All processes in a living cell dealing with the storage and expression of genetic information, every single enzymatic reaction playing a role in the building of complex molecules from simpler building blocks or in their degradation to simpler ones accompanied by the gain of metabolic energy, the vast majority of signalling events in a cell - all rely on the specific recognition between individual ligands and receptors. A large variety of systems have been the subject of SMFS investigations in the past decade, including (strept)avidin-biotin complexes [14, 15], complementary DNA strands [16, 17], selectins [18], aggregation factors [19], and antibody-antigen complexes [20, 21, 22]. Another important problem in this context is the recognition of specific DNA sequences by transcription factors which has also been studied by SMFS [23, 24, 25]. A part of this work deals with the interaction of the transcription factor PhoB (from the bacterium *E. coli*) with a specific regulatory sequence on the DNA. Peptide fragments mimicking the recognition helix of the protein and peptides bearing point mutations have been synthesized and put to the test in SMFS experiments in order to elucidate the contribution of single amino acids to binding strength and specificity. Subsequently, also experiments with the PhoB protein were performed and the results of the peptide and protein compared. It will be demonstrated that AFM SMFS is capable to distinguish between single point mutants of a molecule (chapter 3).

The sensitivity and beauty of molecular recognition in nature has been an inspiration for the design of many synthetic systems which sometimes try to mimic biological function, sometimes are designed to build up novel intermolecular architectures. The forces observed in these supramolecular compounds are the same as in the biological systems, though supramolecular aggregates, due to the requirements of chemical bottom-up synthesis, usually are simpler and have a higher symmetry than large biomolecules. This simplicity is an advantage for the study of the interaction process, since the forces acting between the ligand and receptor molecules are more defined. A part of this work deals with SMFS experiments performed on a supramolecular host-guest system consisting of a resorc[4]arene cavitand and different tetra(organyl)ammonium guests. It will be demonstrated that SMFS can yield kinetic and structural data on a supramolecular recognition process mediated by very weak forces, and that it is possible to affinity-rank different ligands (chapter 4).

The switching of the physical properties of single nanoobjects by external stimuli is an issue of nanoscale science which constantly gains importance, leading the way to intelli-

---

gent materials and nanoelectronic or nanooptical devices. A simple means to externally control the conformation of a molecule is the introduction of a photoisomerizable group which suffers a conformational change if subjected to irradiation. A part of this work will present the first SMFS experiments on a supramolecular host system which can be switched between a high affinity and a low affinity isomer by ultraviolet light. The experiments should prove if the host molecule is able to catch and release guest molecules on photochemical induction (chapter 4).

The previous paragraph dealt with the switching of a mechanical property (the conformation of a molecule) by an optical stimulus. The question arises whether the opposite effect, i.e. the mechanical switching of the light emission of a single nanoobject, can also be achieved.

If we are interested in the optical properties of single molecules or nanocrystals, we have to find a means to detect the emission of these objects. Many single molecule optical methods detecting fluorescent light have developed, the most important being confocal microscopy [26], scanning near-field optical microscopy (SNOM) [27], conventional wide-field epifluorescence (using high resolution detectors) and total internal reflection fluorescence microscopy [28, 29] (TIRFM; for details please cf. chapters 6.1.3 and 6.1.4). These, due to their ability to detect light and hence provide an insight into the energy changes in and transfer between single molecules rather than forces, are in many respects complementary to the force-sensitive methods described above.

Nanoscale fluorescence applications demand very photostable, biocompatible fluorophores. Semiconductor nanocrystals (“quantum dots”) fulfill these requirements and show properties which are in many respects superior to those of organic dye molecules (for a detailed discussion of their properties, cf. chapter 6.1.2). They can serve as active reporters which carry information about their local environment.

The last part of this work presents a very fundamental experiment in a novel, combined AFM-TIRFM setup which enables simultaneous SMFS and fluorescence imaging with single nanoobject sensitivity. This experiment deals with the mechanical fluorescence emission control of a single semiconductor nanocrystal. It will be demonstrated that the mechanical movement of an AFM tip functionalized with gold nanoparticles can effectively switch the nanocrystal between emitting (blinking) and dark (quenched) state (nanophotonic switch; chapter 6).

# **2 Discrimination of Binding Mechanisms in Individual DNA-Ligand Complexes**

## **2.1 Introduction**

The helical structure of double-stranded DNA provides different topological features which are accessible to the attack of small molecules. The interaction of these ligands with DNA is based on weak, non-covalent forces (electrostatic, van der Waals, and hydrogen bonds as well as hydrophobic effects) and can or cannot show a specificity for a certain sequence. One can distinguish several binding modes, the most important being intercalation and binding to the DNA minor or major groove. Many DNA-recognizing molecules have a considerable influence on important biochemical processes such as replication, recombination and gene expression (cf. chapter 3.1.1) and act as mutagenics; some find applications as drugs in cancer therapy. Other compounds are fluorophores and serve as dyes to label DNA, e.g. in gel electrophoresis.

In this work, the binding of small ligands to single DNA strands was investigated by single molecule force spectroscopy (SMFS) experiments using the AFM and optical tweezers. Two main topics should be addressed:

- In how far does the binding of small ligands perturb and influence the tension-induced structural transitions observed in free single DNA molecules?
- Do the force-distance traces obtained for the DNA-ligand complexes allow for the distinction between the different binding modes?

This section is meant to give an introduction into the works reported in chapters 2.2 and 2.3. Firstly, in chapters 2.1.1 and 2.1.2, the experimental basics of single molecule

force spectroscopy using an atomic force microscope (AFM) or an optical tweezers (OT) setup, respectively, will be presented. Chapter 2.1.3 gives a short survey of the methods used to immobilize single molecules and nanocrystals which are used throughout this work. Chapter 2.1.4 deals with the force-induced transitions which can be observed in overstretched single DNA molecules, whereas chapter 2.1.5 introduces the DNA binding systems (intercalants, minor and major groove binding peptides) which were to be investigated. Finally, chapter 2.1.6 presents some molecular elasticity models which are appropriate to describe the behaviour of double-stranded DNA under external stress.

### 2.1.1 Single Molecule Force Spectroscopy (SMFS) with the AFM

The atomic force microscope, invented in 1986 [1], belongs to the category of scanning probe microscopes (SPM). The common feature among these techniques is a tiny sensor tip, ideally of atomic dimensions, which is scanned in contact or in the near field (i.e. at a distance typically below 50 nm) of the sample to be investigated. The specific interaction between the probe and sample is monitored, and subsequent analysis yields information about the surface. Scanning probe techniques combine precise control of the sensor movement with a highly sensitive detection of the respective interactions. In this way, topographic, electronic or optical maps as well as local spectroscopic data can be obtained. Depending on the specific interaction, one can distinguish several methods. The scanning tunneling microscope [30, 31] is capable of measuring tunneling currents between a conducting sample surface and a metallic (e.g. tungsten) tip in the range from nA to pA. The basic principle of the scanning near-field optical microscope (SNOM) [27] is the interaction of light waves emitted by a nanometer-sized aperture (typically diameter: 50 nm) with the sample in the near-field, enabling optical resolution beyond the diffraction limit (cf. chapter 6.1.3). There are also scanning probe methods which make use of magnetic or electrostatic interactions.

The atomic force microscope (Fig. 2.1), which is our major concern here, is based on the physical interaction between the sensor and sample. The forces acting on the tip, which features an apex radius of a few nm, effect a mechanical deflection of the micro-fabricated cantilever onto which the tip is mounted. To detect the cantilever deflection with sub-Å sensitivity, one makes use of the light pointer principle: A collimated laser beam is reflected from the back of the cantilever (which is often metal-coated to ensure high reflectivity) and projected to a quadrant photodiode detector. The position of the laser spot on the detector varies with the force experienced by the sensor. The detector signal is used in a feedback loop to control the vertical movement of the sensor (or the

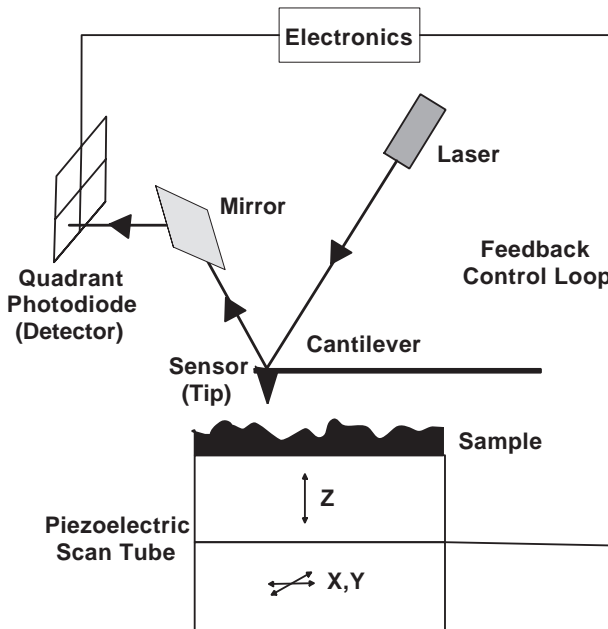


Figure 2.1: Atomic force microscope (schematic representation)

sample) which is performed by piezoelectric actuators (as well as the scanning in the x,y directions). A major advantage of the AFM over the STM is the possibility to measure non-conducting samples in aqueous solution, which is a *conditio sine qua non* for the investigation of functional biological systems.

Apart from being an imaging tool, the AFM is also capable of measuring interaction

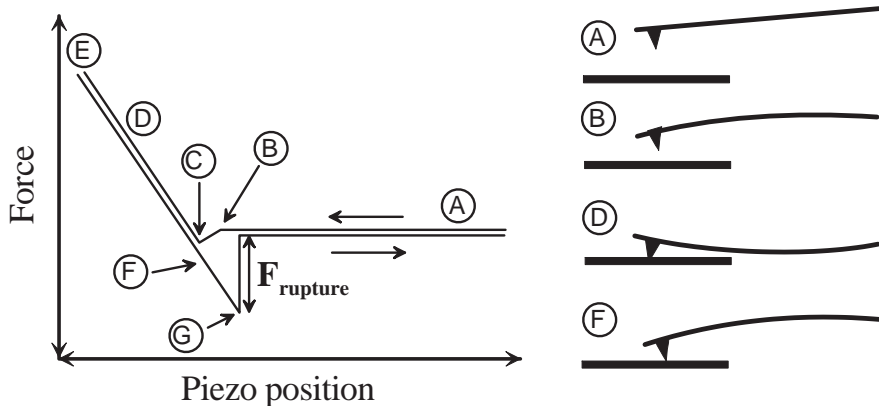


Figure 2.2: Force-distance curve (schematic representation)

forces locally, for example in single molecule force spectroscopy (SMFS) experiments. In this mode, the sensor is cycled between approach and retraction at a fixed x,y position above the sample, and the force as a function of distance is monitored. The force-distance curve resulting from a single approach-retraction cycle exhibits several regimes

(Fig. 2.2). At (A), the tip is still far from the sample surface and in its equilibrium position (no force is acting). If the sensor approaches the surface, the cantilever will be deflected: If the forces are mainly attractive (e.g. electrostatic forces resulting from unlike net charges; van der Waals forces), he will bend to the sample, if they are repulsive (e.g. electrostatic forces resulting from like net charges), he will bend away from it. (B) shows the situation if the long-range interaction is predominantly attractive: The cantilever is deflected until its elastic restoring force compensates the attractive force experienced. At (C), the sensor “snaps” into contact with the surface. Further movement presses the sensor into the sample (D); the deflection is proportional to the cantilever travel (Hooke’s Law!). The slope of the force-distance curve in this regime yields the conversion factor for turning the voltage signal from the detector into a force if the spring constant of the cantilever (see below) is known. At (E), the movement of the sensor is reversed. During the retraction, attractive interactions (adhesion) give rise to a deflection hysteresis (F). The cantilever is bent into the direction of the sample until the elastic restoring force exceeds the attractive force (G); now the bond between tip and sample breaks and the cantilever can relax into the initial position. The difference between the maximum deflection before bond rupture and the relaxed position is the rupture force  $F_{\text{rupture}}$ , which is the primary quantity obtained in a single molecule force spectroscopy experiment.

An important requirement for SMFS is a reliable method to evaluate the spring constant (the intrinsic stiffness) of the cantilever (the nominal values are only give the order of magnitude). There are several different techniques to do so: The spring constant can be computed from the geometric and physical properties (length, thickness, density, elastic modulus) of the cantilever [32]; it can be determined by coupling the cantilever with an additional load [33] or another spring [34]. An alternative (which in this work was the method of choice) is to derive the spring constant from the analysis of its thermal noise spectrum [35, 36, 37]. For performances  $Q \gg 1$  and oscillations with a small amplitude, a cantilever can be modeled as a harmonic oscillator with the Hamiltonian

$$\hat{H} = \frac{p^2}{2m_{\text{eff}}} + \frac{1}{2}m_{\text{eff}}\omega_0^2 q^2 \quad (2.1)$$

where  $m_{\text{eff}}$  designates the effective mass,  $q$  the displacement,  $p$  the linear momentum, and  $\omega_0$  the resonance frequency of the cantilever. The equipartition theorem establishes a relation between the thermal energy  $k_B T$  and the mean square displacement  $\langle q^2 \rangle$ :

$$\frac{1}{2}m_{\text{eff}}\omega_0^2 \langle q^2 \rangle = \frac{1}{2}k_B T \quad (2.2)$$

Using  $\omega_0^2 = k/m_{eff}$ , we obtain a relation for the spring constant

$$k = \frac{k_B T}{\langle q^2 \rangle}. \quad (2.3)$$

The Langevin equation for the motion of an externally driven harmonic oscillator in the presence of friction is

$$\frac{d^2q}{dt^2} + 2\lambda \frac{dq}{dt} + \nu_r^2 q = \frac{F}{m_{eff}} e^{i\nu t} \quad (2.4)$$

where  $\nu$  is frequency,  $\nu_r$  the resonance frequency,  $\lambda$  the damping constant, and  $F$  the external driving force. The solution for stationary oscillation in thermal equilibrium with the surroundings in the case of small damping ( $2\lambda \ll \nu_r$ ) and for  $\nu \approx \nu_r$  is approximately:

$$q(t) = \frac{F}{2m_{eff}\nu_r \sqrt{(\nu_r - \nu)^2 + \lambda^2}} \cos(\nu t + \delta) \quad (2.5)$$

This is a Lorentzian profile. Measurement of the time-dependent square displacement, i.e. the Fourier transform of  $q^2(t)$ , yields another Lorentzian for  $\hat{q}^2(\nu)$ , which can be obtained by a fit to the experimental data of the kind

$$\hat{q}^2(\nu) = q_0 + \frac{A}{(\nu_r - \nu)^2 + B} \quad (2.6)$$

where  $q_0$ ,  $A$  and  $B$  are fitting constants. The mean square displacement of the cantilever can now be obtained from the integral

$$\langle q^2 \rangle = \int_0^\infty (\hat{q}^2(\nu) - q_0) d\nu \quad (2.7)$$

and the spring constant from equation 2.3.

### 2.1.2 SMFS with Optical Tweezers

Optical tweezers (OT), first invented at the Bell laboratories [7], use the radiation pressure of a strongly focussed laser beam to trap and manipulate small objects ranging in size from single atoms up to whole cells (optical trap). The technique can be used to apply forces in the range from  $\approx 200$  pN down to 0.2 pN and to measure displacements of objects ranging in size from 1  $\mu\text{m}$  up to over 100 mm with nm sensitivity. It has been applied to detect forces in a wide range of systems, from dielectric micron-sized beads to living pro- and eucaryotic cells, virus particles, and even single DNA strands. The main applications in SMFS have been the study of molecular motors and the elastic properties of DNA. Experiments of the latter kind are performed by biochemically immobilizing a

DNA strand at one end to a glass or polystyrene microbead and to fix it by suction of a micropipette or immobilization to another bead at the other end (for immobilization techniques cf. next chapter). These experiments on single DNA strands basically yield the same data as AFM SMFS experiments, but within a different force regime and with a significantly higher sensitivity (typical force noise in an OT: 0.2 pN as compared to 10 pN in an AFM SMFS experiment). The disadvantage with OT measurements is the limitation to long macromolecules.

Here, the principle of optical trapping will be explained considering a dielectric bead as an example. Firstly, let us consider the situation if the bead is small enough for its optical properties to be adequately described within the Rayleigh regime, i.e. if its radius is well below the wavelength of the trapping radiation ( $r < 0.1\lambda$ ). The particle, located in the focus of a laser beam of an intensity  $I_0$ , experiences a scattering force

$$\mathbf{F}_{\text{scat}} = \frac{128\pi^5 r^6 I_0}{3\lambda^4 c} \left( \frac{m^2 - 1}{m^2 + 1} \right)^2 n_M \quad (2.8)$$

where  $c$  is the vacuum speed of light,  $n_M$  the refractive index of the surrounding medium and  $m = n_P/n_M$  the effective refraction index (with  $n_P$ , the particle's refractive index).  $\mathbf{F}_{\text{scat}}$  has the same direction as the  $\mathbf{k}$  vector of the incident light. A second force, termed gradient force, results from the interaction between the dipole induced by the laser's electric field and the laser field itself:

$$\mathbf{F}_{\text{grad}} = -\frac{n_M}{2}\alpha \nabla \mathbf{E}^2 = -\frac{n_M^3 r^3}{2} \left( \frac{m^2 - 1}{m^2 + 1} \right) \nabla \mathbf{E}^2 \quad (2.9)$$

Here,  $\alpha$  denotes the polarizability of the dielectric particle and  $\mathbf{E}$  the electric field strength of the incident radiation. For a particle to be trapped stably in the focus of the optical trap,  $\mathbf{F}_{\text{grad}}$  must be opposed to and greater than  $\mathbf{F}_{\text{scat}}$  in amount ( $F_{\text{grad}}/F_{\text{scat}} \geq 1$ ).

If we regard trapped particles with a radius well above the wavelength of the incident light ( $2r \gg \lambda$ , i.e. Mie scattering regime), which is usually the case for microbeads used in biological applications, it is feasible to describe the situation within the framework of geometrical optics (Fig. 2.3). The strongly convergent rays  $a$  and  $b$  are refracted twice at the interfaces between bead and medium; the emanating rays  $a'$  and  $b'$  have changed their direction with respect to the incident rays  $a$  and  $b$ , and the momentum difference is transferred to the bead, giving rise to the gradient forces  $F_{G,a}$  and  $F_{G,b}$ . The resultant  $F_{G,ab}$  tends to draw the bead towards the geometrical focus  $f$  of the objective. The scattering forces due to reflections at the bead-medium interfaces (represented as the rays  $R_{a1}$ ,  $R_{b1}$ ,  $R_{a2}$  and  $R_{b2}$ ) generate a net scattering force  $F_{S,ab}$  tending to drive

the bead off the focus. Equilibrium is reached if  $F_{S,ab}$  equals  $F_{G,ab}$ . In the case that additional forces act on the bead (gravity, Stokes friction, external pulling forces in an SMFS experiment), the condition of equilibrium is that all forces acting on the bead sum up to yield the zero vector.

A typical OT setup for SMFS experiments uses a glass or polystyrene microbead

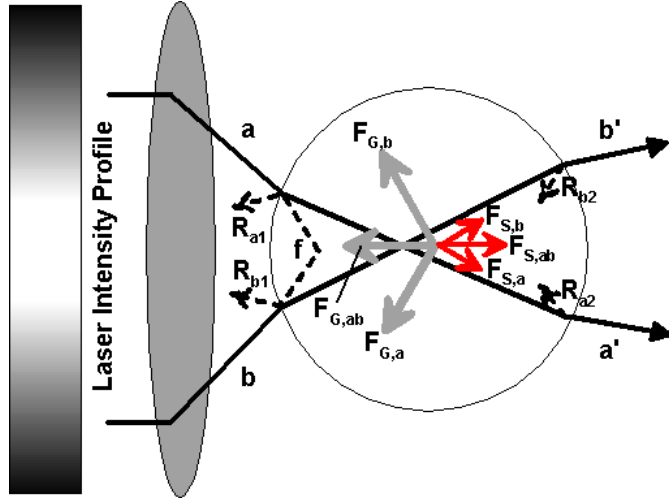


Figure 2.3: Scattering and gradient forces acting on an optically trapped dielectric bead

trapped by an infrared laser (e.g. Nd:YAG at  $\lambda = 1064$  nm) which is projected and focussed through the high-NA objective of an optical microscope. The infrared wavelength ensures that irreversible damage of biological samples and absorption by water molecules is avoided. A quadrant photodiode detector monitors the position of the trapped particle.

The OT can be calibrated by analyzing the Brownian motion of the trapped object. Assuming a harmonic trapping potential  $V(q) = 1/2kq^2$  ( $q$ : displacement,  $k$ : spring constant), the equation of motion for the particle is given by the Langevin term (inertial terms can be neglected due to heavy damping):

$$F(t) = kq + \gamma \frac{dq}{dt} \quad (2.10)$$

with  $F(t)$  signifying the stochastic force acting on the particle due to thermal motion of molecules in the medium and  $\gamma$  the drag coefficient. Using  $|F(\nu)|^2 = 4\gamma k_B T$ , the Fourier transform of  $q^2(t)$  yields the power spectrum

$$S(\nu) = \frac{k_B T}{\gamma \pi^2 (\nu^2 + \nu_c^2)} \quad (2.11)$$

where  $\nu_c = k/2\pi\gamma$  is the corner frequency. The drag coefficient  $\gamma$  for a spherical particle is known from Stokes' law ( $\gamma = 6\pi\eta r$ ,  $\eta$ : medium viscosity). In this way, the corner frequency the spring constant can be obtained by determination of the corner frequency. The calibration of the trap can then be performed using equation 2.3.

A simpler possibility to calibrate the optical trap is to measure the maximum trapping force at different laser powers. The trapping force can be calculated from Stokes' friction according to  $F = -\gamma v$ , and the calibration is performed by comparison of the actual Stokes' frictional force with the voltage signal at the quadrant detector.

### 2.1.3 Immobilization Methods for SMFS

A *conditio sine qua non* for SMFS experiments is an immobilization method which ensures that the forces attaching the molecules to their respective surfaces (tip and sample) are stronger than the rupture forces which shall be observed.

In some cases, it is sufficient to fix the objects of interest to a surface by physisorption, i.e. the molecules adhere to the surface via electrostatic or hydrophobic interactions.

An example for this method is the immobilization of the DNA-ligand complexes studied in this chapter: DNA shows strong adhesion to freshly prepared gold surfaces due to electrostatic interactions between the negatively charged backbone of the DNA and mirror charges in the metal. This adhesion bond is stronger than the forces inducing the intramolecular transitions discussed in the following chapter. The flatness of the gold surface is not as critical a requirement for SMFS experiments as it is for imaging DNA. A gold-coated AFM tip is used to pick the DNA from the surface by adhesion.

Another example for physisorption is the immobilization of the hydrophobic semiconductor nanocrystals discussed in chapter 6. For immobilization, they are dissolved in chloroform and deposited on a flat glass surface. Fig. 2.4 (b) shows an AFM micrograph of immobilized nanocrystals.

Another immobilization protocol which has found many applications in single molecule experiments draws upon the strong affinity ( $K_{Diss} = 10^{-15}$  M) between the small molecule biotin (also known as vitamin H) and the proteins avidin (from chicken albumen) or streptavidin (from the bacteria *Streptomyces avidinii*) which both provide four binding sites for biotin. Both biotin and avidin/streptavidin can be readily linked to other biomolecules. This immobilization procedure was applied for the OT SMFS experiments presented in this thesis (chapter 2.3). However, in most cases a covalent immobilization is required. In this work, two substrates were chosen for covalent modification. Flat flame-annealed gold surfaces can be used for the attachment of objects

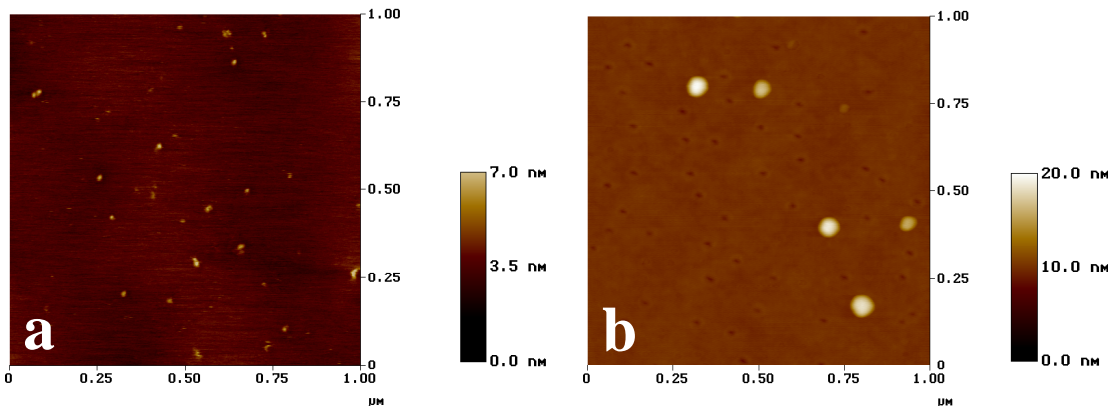


Figure 2.4: (a) AFM image of single protein molecules covalently immobilized on a mica surface. (b) AFM image of semiconductor nanocrystals deposited on a cover glass.

carrying thiol moieties, like the thiol-modified proteins discussed in chapter 3.3 (Fig. 2.4 (a)); a (quasi-)covalent bond is formed between the thiol sulfur and the gold surface. These substrates are also suited for the deposition of mixed self-assembled monolayers (SAMs) consisting of sulfides and sulfide-carrying supramolecular compounds like the resorc[4]arenes of chapter 4.

A second method for covalent immobilization uses mica substrates. Mica is a flat, stratified silicate which carries negatively charged silanol groups at medium pH. It can be modified by reaction with triethoxysilane derivatives carrying amino or thiol groups. The same method can be successfully applied to functionalize  $\text{Si}_3\text{N}_4$  AFM tips which have a surface chemistry similar to mica, or even glass surfaces which also provide free silanol groups. In order to spatially separate the immobilized molecules from the respective surface, bifunctional crosslinkers can be used carrying succinimidyl (reacts covalently with amino groups) or maleimidyl (binds to thiol groups) moieties.

#### 2.1.4 Overstretching Double-Stranded DNA

In force spectroscopy experiments with double-stranded DNA (dsDNA), several intramolecular transitions are observable (Fig. 2.5). The first transition manifests itself as a distinct plateau in the force-extension trace. After stretching of the B-DNA, the molecule can be extended (“overstretched”) over distances up to 170% of the B-DNA contour length without a marked increase in force [10, 38, 39, 40]. This transition occurs at forces between 45 and 75 pN, dependent on the DNA sequence. The transition is

reversible (on the time scale of the force spectroscopy experiment) and highly cooperative.

There are mainly two different interpretations of the phenomenon. The first assumes

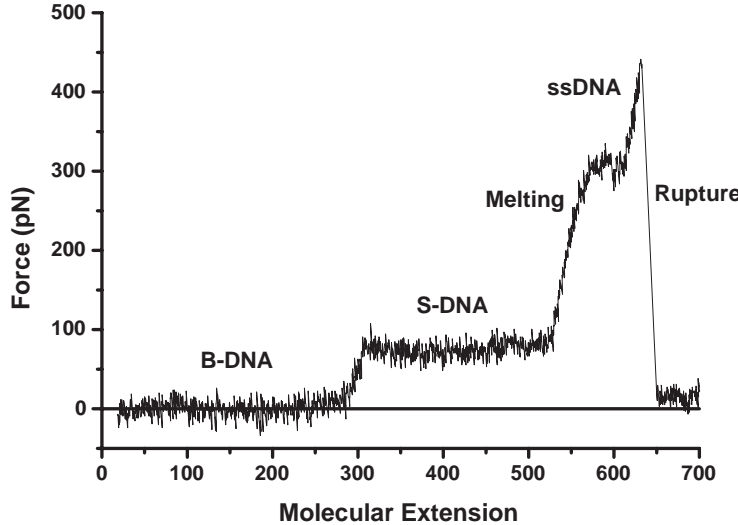


Figure 2.5: Typical force-extension trace for Poly(dG-dC) dsDNA

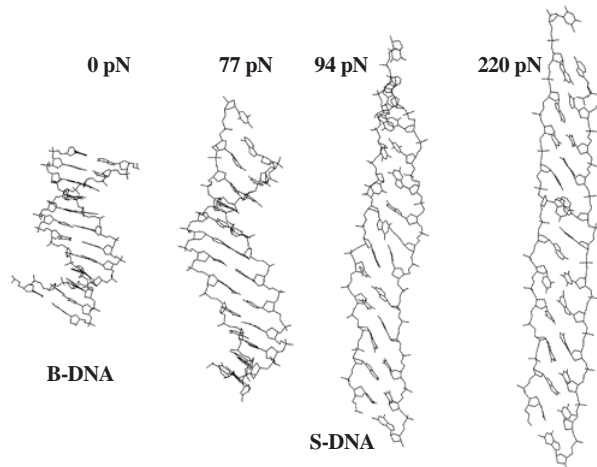


Figure 2.6: Dependence of dsDNA structure from external force (molecular dynamics simulation) [41])

that the plateau corresponds to a transition of the B-DNA to a novel, overstretched conformation termed S-DNA (S for “stretched”) [42]. This view is supported by molecular dynamics simulations like the one shown in Fig. 2.6 which represents stretching of

dsDNA in the 3'-3'-direction [43, 41]. Clearly visible is the transition to a ladder-like S-DNA conformation at higher forces. Related studies [44] indicate a (right-hand) helicity of the S-DNA with 38 base pairs per turn such that the structure rather resembles a slightly twisted ladder. The second, alternative interpretation explains the overstretching transition as an equilibrium force-induced melting process [45, 46].

At higher pulling forces, a second structural transition can be observed (Fig. 2.5). This process is viewed as a rate-dependent (nonequilibrium) melting of the double helix induced by the action of the external pulling force [47, 45, 46]. The form of the melting curve is strongly sequence-dependent.

### 2.1.5 Binding of Small Ligands to DNA

Double-stranded DNA (dsDNA) can serve as a “host” for numerous “guests”, i.e. DNA-binding ligands. The interaction of these ligands with DNA is due to many different non-covalent bonds which sum up to give a substantial bond strength. There is a seamless transition between sequence-unspecific DNA binding and the recognition of specific target sequences by small effector molecules; some ligands only show preferences for G-C- or A-T-rich sequences. Essentially, there are two different binding modes of small ligands to DNA: Binding in the DNA minor or major groove and intercalation.

The binding of small, often positively charged molecules to the dsDNA minor or ma-

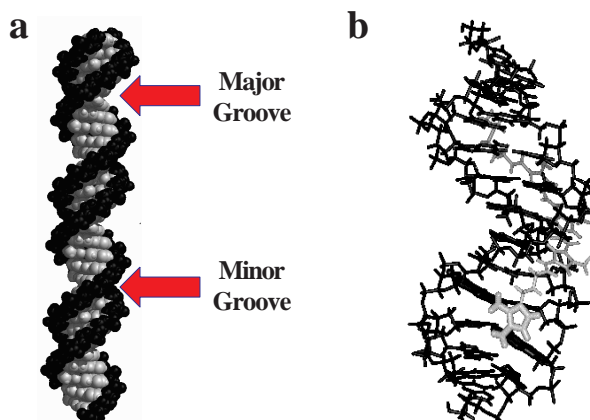


Figure 2.7: (a) Model of B-DNA. The position of the minor and major grooves is indicated. (b) Binding of Distamycin A to the DNA minor groove.

jor groove is mediated via electrostatic interactions with the negatively charged DNA backbone. It is accompanied by drastic changes in hydration. The helix geometry is

only slightly influenced; groove binders induce a small bending of the DNA molecule. Fig. 2.7 (a) indicates the position of the minor and major grooves along the dsDNA helix.

The synthetic peptide distamycin A is a prominent example of a minor groove binding

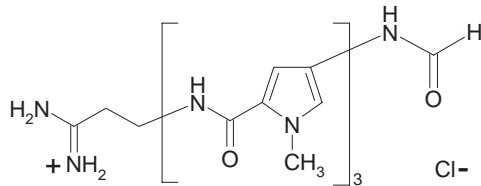


Figure 2.8: Structure of the minor groove binder distamycin A

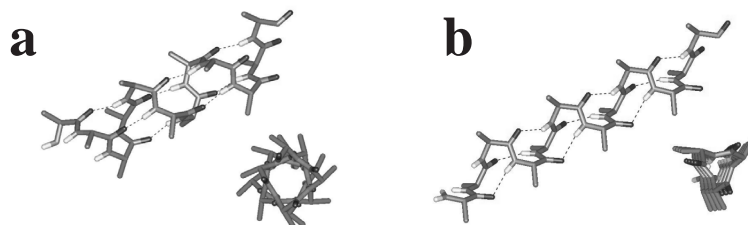


Figure 2.9: (a) Structure of the  $\alpha$ -helical peptide Ac-(Leu-Ala-Arg-Leu)<sub>3</sub>-NH<sub>2</sub>.  
(b) Structure of the  $3_{10}$ -helical peptide Ac-(Aib-Leu-Arg)<sub>4</sub>-NH<sub>2</sub>.

agent (Fig. 2.7 (b)). Fig. 2.8 shows the structure which features three N-methylpyrrole units in a row; this design serves as a leitmotif for a whole class of non-intercalating mutagenic compounds with applications in cancer therapy [48, 49]. The cytostatic effect is mainly due to induced chromosome decondensation [50].

Structurally related to distamycin are the amphipathic helical peptides Ac-(Leu-Ala-Arg-Leu)<sub>3</sub>-NH<sub>2</sub> and Ac-(Aib-Leu-Arg)<sub>4</sub>-NH<sub>2</sub> (Aib:  $\alpha$ -aminoisobutyric acid) which were synthesized as model systems for DNA-binding protein domains [51]. Ac-(Leu-Ala-Arg-Leu)<sub>3</sub>-NH<sub>2</sub> forms an  $\alpha$ -helical structure (Fig. 2.9 (a)) where the part of the helix which is exposed to the DNA backbone carries charged arginine residues which are separated by three nonpolar amino acids. This amphipathic structural motif can also be found in apolipoproteins and peptide hormones. The second peptide, Ac-(Aib-Leu-Arg)<sub>4</sub>-NH<sub>2</sub>, contains the non-standard amino acid  $\alpha$ -aminoisobutyric acid which induces a  $\beta$  turn in the secondary structure, giving rise to a so-called  $3_{10}$ -helix.

Intercalation is characterized by the insertion of small, flat or wedge-like molecules into the base sequence of dsDNA. Intercalants often have planar aromatic rings which can interact with the surrounding base pairs via van der Waals forces. In some cases, ionic

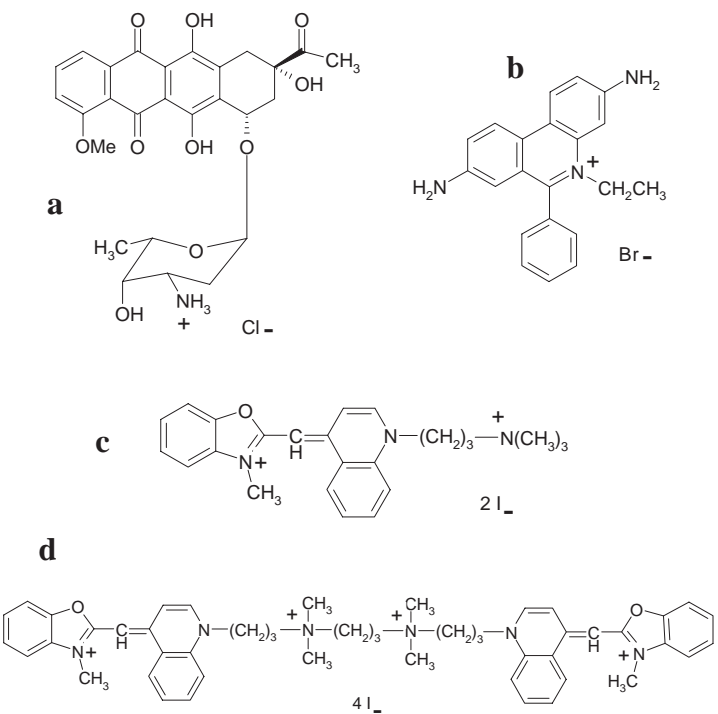


Figure 2.10: Intercalant structures. (a) Daunomycin, (b) ethidium bromide, (c) YO, (d) YOYO.

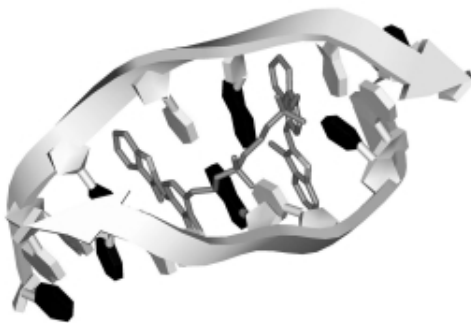


Figure 2.11: Binding of the intercalant YOYO to DNA.

interactions between positively charged groups at the intercalant and the negatively charged backbone add to the stability of the complex. A positive charge also promotes the kinetics of bond formation: The intercalation is the second, rate determining step which follows upon the (fast) association of the intercalant with the backbone. Intercalation always goes with a considerable widening and de-wreathing of the DNA molecule. Many intercalants are used as anti-tumor drugs in chemotherapy, their cytostatic effect being due to a stabilization of the complex between DNA and topoisomerase II.

An example is the cytostatic drug daunomycin (daunorubicin), an anthracycline antibiotic (Fig. 2.10 (a)). It interacts with DNA via its tetracyclin ring system [52, 53, 54]. A smaller and simpler intercalant is the well-known fluorescent dye ethidium bromide featuring a phenanthridin ring system (Fig. 2.10 (b)). Intercalation of the dye increases its quantum efficiency [55, 56]. Other intercalating fluorescence markers for dsDNA are the compounds “YO-1” and “YOYO-1” (Fig. 2.10 (c) and (d)), which is basically a linked YO-1 dimer. Both can intercalate via their extended heterocyclic ring systems [57]. YOYO-1 as a bis-intercalant encloses two basepairs when binding to dsDNA (Fig. 2.11).

### 2.1.6 Simple Models for the Molecular Elasticity of DNA

Free DNA in aqueous solution adopts the form of a random coil. This conformation ensures that a maximum of configurations is available for the total system consisting of the biopolymer and the surrounding water molecules: Its entropy is at a maximum. An external force pulling at the ends of the polymer strand reduces the number of possible configurations, and work must be done to reduce the entropy of the system if a certain end-to-end distance shall be obtained. At full elongation of the molecule, there is only one possible configuration left for the polymer chain, and the end-to-end distance of the strand equals its contour length. However, the assumption that the forces observed in dsDNA stretching experiments are mainly entropic only holds in the regime below 10 pN; above this value, enthalpic corrections become necessary. A simple model describing the entropic elasticity of stiff polymer chains (a criterion met by dsDNA) is the so-called Worm-Like Chain (WLC). The total energy for an entropic chain of contour length  $L_0$  experiencing a stretching force  $F$  at its ends is given by [58, 59, 60]:

$$\frac{E_{WLC}}{k_B T} = \frac{\xi}{2} \int_0^{L_0} \left( \frac{\partial \mathbf{t}}{\partial s} \right)^2 ds - F \int_0^{L_0} \cos \Theta(s) ds \quad (2.12)$$

Here,  $\mathbf{t}$  denotes the tangent vector at a position  $s$  along the chain,  $k_B T$  is the thermal energy,  $\Theta$  the angle between two infinitesimally distant tangent vectors and  $\xi$  the so-called persistence length, a measure for the decay of angular correlation of the tangent vectors along the chain; it is given by the flexural stiffness of the chain, divided by the thermal energy. In the low force regime, the exact force-extension relation for the WLC can be approximated by an asymptotically correct interpolation formula [58, 61]:

$$\frac{F\xi}{k_B T} = \frac{1}{4} \frac{1}{(1 - x/L_0)^2} - \frac{1}{4} + \frac{x}{L_0} \quad (2.13)$$

An elasticity model describing the conformative behavior of dsDNA in the regime of the B-S transition was proposed by Ahsan, Rudnick and Bruinsma [62]. It combines the assumptions of the WLC with a one-dimensional Ising model [63, 10, 64]. The DNA chain is divided into a sequence of short segments of length  $a_0$  which can adopt either the B or the S state. The energy required to transform a segment from state B to state S is assumed to only depend on the states of the directly neighbouring segments. If we denote the state of a B segment by  $\uparrow$  and the state of an S segment by  $\downarrow$ , a simple assumption for the energy spectrum is

$$\Delta E(\uparrow\uparrow) = 2H + 4J \quad (2.14)$$

$$\Delta E(\uparrow\downarrow) = \Delta E(\downarrow\uparrow) = 2H \quad (2.15)$$

$$\Delta E(\downarrow\downarrow) = 2H - 4J \quad (2.16)$$

The two parameters,  $H$  and  $J$ , can be determined by molecular modeling or by fitting to experimental data.  $2H$  corresponds to the (zero-tension) free-energy difference per segment between the B and S states.  $J$  is the correlation energy between adjacent segments; the exponential  $\sigma = \exp(-4J\beta)$  (with  $\beta = 1/k_B T$ ) is a measure for the cooperativity of the transition ( $\sigma \ll 1$  corresponds to high cooperativity). The relation between chain conformation and internal structure is given by the expression

$$L(\{S_i\}) = L_0 \left( 1 - \frac{\epsilon}{2N} \sum_{i=1}^N (S_i - 1) \right) \quad (2.17)$$

where  $L_0$  denotes the B-DNA contour length,  $N$  the number of segments,  $i$  the segment index, and  $\epsilon$  the fractional elongation of the S over the B state. For the B and S states,  $S_i$  adopts the values  $S_i = 1$  and  $S_i = -1$ , respectively. The chain length  $L$  has become a statistical variable whose ensemble average  $\langle L \rangle$  must be determined by minimizing a suited derivative of the free energy. The conformative part of the internal energy  $H_{int}$  is given by

$$H_{int} = -J \sum_{i=1}^N S_i S_{i+1} - H \sum_{i=1}^N S_i \quad (2.18)$$

To the Ising Hamiltonian the WLC bending energy must be added.

The resulting Two-State WLC model for the tension-induced B-S-transition yields an analytical expression for the relation between extension and stretching force (which appears in the equation as a dimensionless tension  $t$ ):

$$\frac{x}{L_0} = y(t) \left( 1 + \frac{\epsilon}{2} (1 - \langle S \rangle) \right) \quad (2.19)$$

with

$$y(t) = 1 - \frac{1}{(2 + \sqrt{4 - (4/3t - 1)^3})^{1/3} + \frac{4/3 t - 1}{(2 + \sqrt{4 - (4/3 t - 1)^3})^{1/3}}} \quad (2.20)$$

and

$$\langle S \rangle = \frac{e^{J\beta} \sinh(\tilde{H}\beta) + 1/2 e^{2J\beta} \sinh(2\tilde{H}\beta)(e^{2J\beta} \cosh^2(2\tilde{H}\beta) - 2 \sinh(2J\beta))^{-1/2}}{Q(J, \tilde{H})} \quad (2.21)$$

and  $\tilde{H}$  as a renormalized  $H$  parameter.

The advantages of this model over more elaborate ones (like, e.g., the one by Zhou et al. [65]) are its clear, even if somewhat coarse, assumptions and the fact that an analytical expression is obtained which yields parameters that characterize the elastic properties of the system.

## 2.2 Publication I

**Rainer Eckel**, Robert Ros, Alexandra Ros, Sven David Wilking, Norbert Sewald, and Dario Anselmetti. Identification of binding mechanisms in single molecule - DNA complexes. *Biophys. J.* 85 (2003), 1968-1973.

### 2.2.1 Contribution

All experimental work and data analysis performed by the author.

# Identification of Binding Mechanisms in Single Molecule–DNA Complexes

Rainer Eckel,\* Robert Ros,\* Alexandra Ros,\* Sven David Wilking,<sup>†</sup> Norbert Sewald,<sup>†</sup> and Dario Anselmetti\*

\*Experimental Biophysics and Applied Nanosciences, Faculty of Physics, Bielefeld University, 33615 Bielefeld, Germany; and

<sup>†</sup>Organic and Bioorganic Chemistry, Faculty of Chemistry, Bielefeld University, 33615 Bielefeld, Germany

**ABSTRACT** Changes in the elastic properties of single deoxyribonucleic acid (DNA) molecules in the presence of different DNA-binding agents are identified using atomic force microscope single molecule force spectroscopy. We investigated the binding of poly(dG-dC) dsDNA with the minor groove binder distamycin A, two supposed major groove binders, an  $\alpha$ -helical and a  $3_{10}$ -helical peptide, the intercalants daunomycin, ethidium bromide and YO, and the bis-intercalant YOYO. Characteristic mechanical fingerprints in the overstretching behavior of the studied single DNA-ligand complexes were observed allowing the distinction between different binding modes. Docking of ligands to the minor or major groove of DNA has the effect that the intramolecular B-S transition remains visible as a distinct plateau in the force-extension trace. By contrast, intercalation of small molecules into the double helix is characterized by the vanishing of the B-S plateau. These findings lead to the conclusion that atomic force microscope force spectroscopy can be regarded as a single molecule biosensor and is a potent tool for the characterization of binding motives of small ligands to DNA.

## INTRODUCTION

The investigation of interactions between double-stranded deoxyribonucleic acid (DNA) and DNA-binding agents is crucial to a deeper understanding of such important biochemical processes as replication, repair, recombination, and expression of genes. In principle, the possible binding mechanisms of ligands to double-stranded (ds) DNA can be divided into sequence-specific binding, and, on the other hand, binding modes that lack sequence specificity. Specific binding between ligand (protein) and receptor (dsDNA), often also termed “molecular recognition,” is the basis for the interaction of many transcription factors with DNA. Small agents that bind unspecifically or with lower sequence specificity to dsDNA are often capable of influencing or inhibiting these processes and intrinsically exhibit mutagenic properties. By consequence, these molecules find applications as pharmaceuticals, mainly in the treatment of cancer. Others are employed as DNA staining agents, for example in fluorescence assays.

We compared the effects exerted on the mechanical properties of dsDNA by unspecific binding of seven different ligands. When considering unspecific, noncovalent binding of molecules to dsDNA, at least three different modes are known. Binding of small, positively charged peptides may occur in the minor groove of DNA. This binding mode requires only slight conformational adaptions of the double helix. An example for this binding mechanism is the interaction of the peptide distamycin A with the minor groove. Distamycin A induces chromosome decondensation

and is used as a lead structure for a whole class of nonintercalating mutagenic drugs (Baguley, 1982; Turner and Denny, 1996; Bailly and Chaires, 1998). As for minor groove binding, major groove binding is dominated by electrostatic interactions of helical ligands with the backbone assisted by hydrogen bonds. We investigated the synthetic amphipathic peptides Ac-(Leu-Ala-Arg-Leu)<sub>3</sub>-NH-linker (linker: 1,8-diamino-3,6-dioxaoctane), forming a  $3.6_{16}$ - $(\alpha)$ -helix, and the  $3_{10}$ -helix Ac-(Aib-Leu-Arg)<sub>4</sub>-NH-linker containing the  $\beta$ -loop-builder  $\alpha$ -aminoisobutyric acid (Aib). Both peptides are supposed to be major groove binding agents (Niidome et al., 1996).

Intercalation is a different mode of interaction of small molecules (not necessarily peptides) with DNA. It is characterized by the sliding-in of flat, planar molecules into the base pair stack of dsDNA via interaction of their aromatic ring systems with the  $\pi$ -systems of the adjacent base pairs. The anthracycline-antibiotic daunomycin (also known as daunorubicin), which is a potent anticancer drug primarily used in the treatment of leukemia (Aubel-Sadron and Londos-Gagliardi, 1984; Hortobagyi, 1997), serves as an important example of an intercalant. The fluorescence dye ethidium bromide for DNA staining (Morgan et al., 1979) has a central phenanthridine ring system that intercalates into DNA. Other very stable fluorescent dyes are the rather complicated molecules YO and YOYO (Glazer and Rye, 1992). YO also has an extended aromatic system which enables the compound to intercalate into the double helix. YOYO is a bridged YO-dimer and a bis-intercalant: when sliding into the base sequence, the two ring systems enclose two base pairs. It has been proposed that at higher concentrations, both YO and YOYO are also able to interact with DNA by a major groove binding mode (Larsson et al., 1994).

The development and maturation of ultrasensitive force sensors during the past fifteen years has rendered experiments with single molecules or molecule complexes

Submitted October 11, 2002, and accepted for publication May 19, 2003.

Address reprint requests to Robert Ros, Universitätsstrasse 25, 33615 Bielefeld, Germany. Tel: +49-521-1065388; Fax: +49-521-1062959. E-mail: robert.ros@physik.uni-bielefeld.de.

© 2003 by the Biophysical Society

0006-3495/03/09/1968/06 \$2.00

possible. In contrast to classical ensemble measurements, single molecule techniques focus on molecular individuals. In atomic force microscope (AFM) force spectroscopy, forces on the single molecule level are detected by measuring the deflection of an AFM cantilever, yielding a force versus distance plot. This technique has been applied to the investigation of intermolecular forces in receptor-ligand interactions like biotin-streptavidin/avidin (Florin et al., 1994; Moy et al., 1994; Lee et al., 1994b), antibody-antigen (Hinterdorfer et al., 1996; Dammer et al., 1996; Ros et al., 1998), or selectin-ligand (Fritz et al., 1998), interactions between complementary strands of DNA (Lee et al., 1994a; Florin et al., 1995; Strunz et al., 1999), and cell adhesion proteoglycans (Dammer et al., 1995). AFM force spectroscopy also proves a potent tool to examine intramolecular forces. In this setup, a single molecule is mechanically stretched between the tip and the surface. The plot of pulling force against molecular extension contains information about intramolecular structural transitions, which were observed in single dextran (Rief et al., 1997b), titin (Rief et al., 1997a), and DNA (Rief et al., 1999; Clausen-Schaumann et al., 2000) molecules. In addition, force spectroscopy experiments on DNA have also been performed using related techniques such as optical tweezers (Smith et al., 1996) and magnetic tweezers (Smith et al., 1992; Strick et al., 1998). Therein a highly cooperative transition to an overstretched conformation 1.7 times as long as the B-DNA contour length, which was termed S-DNA, was reported (Cluzel et al., 1996). An alternative explanation for this overstretching transition was given by Rouzina and Bloomfield (Rouzina and Bloomfield, 2001a,b), interpreting the phenomenon as an equilibrium force-induced melting process. (For simplicity, the overstretching transition, however interpreted, will be called "B-S transition" in the following text.)

This transition was reported by Clausen-Schaumann et al. (2000) to appear in the force-extension curve as a plateau at  $\sim 65$  pN for poly(dG-dC) dsDNA. Recent investigations (Wenner et al., 2002) examined the salt-dependence of this overstretching plateau, exhibiting an increase in the overstretching force with decreasing  $\text{Na}^+$  concentration. At higher pulling forces, a second structural transition is observed. This transition, as opposed to the B-S transition, is a nonequilibrium process on the time scale of the AFM experiment and interpreted as a rate-dependent melting of the double helix induced by the action of the external force (Clausen-Schaumann et al., 2000; Rouzina and Bloomfield, 2001a,b). Melting proceeds until the strands are fully separated, leaving only a single strand attached to the tip.

It has recently been shown that binding to DNA significantly affects the force response and allows for the differentiation between binding mechanisms of small molecules to DNA via their force-extension profiles (Anselmetti et al., 2000; Krautbauer et al., 2002a,b). These studies centered on the interaction of DNA with the mutagenic agents ethidium

bromide, berenil, and *cis*-platin. Our study further corroborates these results by extending the measurements to a wider range of systems such as supposed major-groove binding helical peptides and bis-intercalants.

## MATERIALS AND METHODS

### Sample preparation

For all experiments poly(dG-dC) dsDNA (Amersham Bioscience, Piscataway, NJ) with an average length of 724 bp was used. For preparation, the DNA was diluted in 10 mM Tris buffer (Sigma, Steinheim, Germany) at pH 8.3 containing 150 mM NaCl and 1 mM EDTA (Sigma) to a concentration of 1 mg ml<sup>-1</sup>.

The peptides were prepared by solid phase synthesis on aliphatic safety-catch resin (Advanced ChemTech, Louisville, KY) using Fmoc-protected amino acids. Ac-(Leu-Ala-Arg-Leu)<sub>3</sub>-NH-linker and Ac-(Aib-Leu-Arg)<sub>4</sub>-NH-linker, respectively, were obtained upon activation of the safety-catch resin with iodoacetonitrile followed by reaction of Ac-(Leu-Ala-Arg-Leu)<sub>3</sub>-resin and Ac-(Aib-Leu-Arg)<sub>4</sub>-resin with the linker 1,8-diamino-3,6-dioxaocetane. The synthesized peptide derivatives were purified by high-pressure liquid chromatography on a reverse phase column (218 TP 1022 Efficiency, protein & peptide C18, 250 × 22 mm, Vydac, Columbia, MD), using acetonitrile/water/TFA gradients. The final products were identified by elemental analysis and matrix-assisted laser desorption ionization mass spectroscopy using a Voyager DE MALDI (PerSeptive Biosystems, Framingham, MA) apparatus.

The DNA-binding agents daunomycin (Sigma), ethidium bromide (Merck, Darmstadt, Germany), distamycin A (Sigma), YO (Molecular Probes, Eugene, OR), YOYO (Molecular Probes), Ac-(Leu-Ala-Arg-Leu)<sub>3</sub>-NH-linker and Ac-(Aib-Leu-Arg)<sub>4</sub>-NH-linker were added to 10  $\mu\text{l}$  of the DNA solution in a concentration of 150  $\mu\text{M}$ , corresponding to a 1:10 ratio of agent molecules per base pair. Constant molar ratios were applied because reliable binding constants are not available yet for the binding of the peptides to DNA. The solution was incubated for 24 h at 4°C. For immobilization, the solution was incubated for 24 h on a freshly evaporated gold surface (30 nm on glass slides) at ambient temperature. Before use, the samples were rinsed with buffer solution to remove excess DNA-ligand complexes from the surface.

### Force spectroscopy

Force spectroscopy measurements were performed on a commercial AFM (Multimode, Veeco Instruments, Santa Barbara, CA). The acquisition of the cantilever deflection force signal and the vertical movement of the piezo electric elements was controlled by a 16 bit AD/DA card (PCI-6052E, National Instruments, Austin, TX) and a high-voltage amplifier (600H, NanoTechTools, Echandens, Switzerland) via a home-built software based on Labview (National Instruments). The deflection signal was low pass filtered (<10 kHz) and averaged by a factor of 5.

The spring constants of all AFM cantilevers ( $\text{Si}_3\text{Ni}_4$ -Microlever, Thermomicroscopes, Sunnyvale, CA) were calibrated by the thermal fluctuation method (Hutter and Bechhoefer, 1993) with an absolute uncertainty of 15%. All given measurements were performed with different cantilevers with spring constants ranging from 12 pN nm<sup>-1</sup> to 14 pN nm<sup>-1</sup>.

The dsDNA strands were mechanically contacted with the tip from the gold surface by applying a contact force of 1–2 nN (Rief et al., 1999; Clausen-Schaumann et al., 2000) and extended with a piezo velocity of 1000 nm s<sup>-1</sup>. All measurements were performed under identical Tris buffer solution (see above) at 20°C. The experimental setup is sketched schematically in Fig. 1 A.

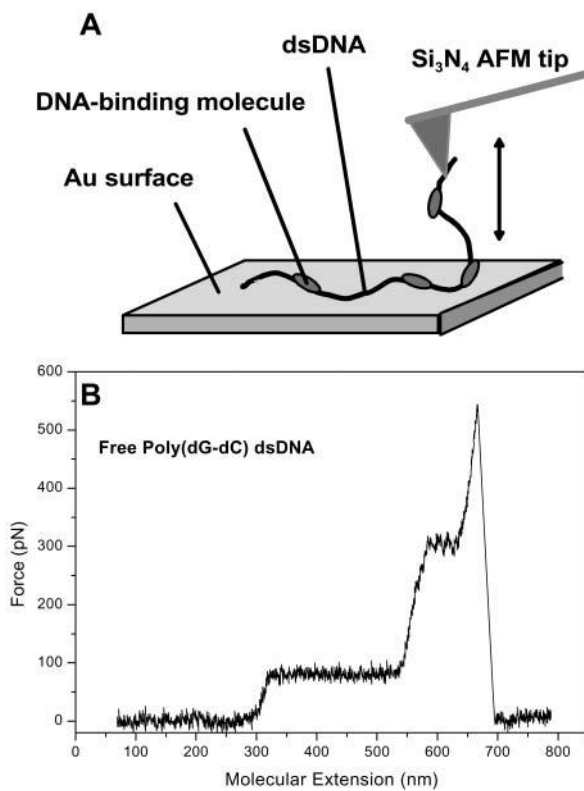


FIGURE 1 (A) Experimental setup; (B) Force-extension trace for free poly(dG-dC) dsDNA.

## RESULTS AND DISCUSSION

### Free dsDNA

The quantitative results of the force spectroscopy measurements on the reference molecule free poly(dG-dC) dsDNA basically confirm the findings previously reported by Rief et al. (1999; Clausen-Schaumann et al., 2000). Fig. 1 B shows the respective force-extension curve. Clearly discernible is the plateau at 75 pN due to overstretching of the double helix to >170% its B-DNA contour length, which corresponds to the reported 65 pN (Rief et al., 1999; Clausen-Schaumann et al., 2000) within the error of measurement dominated by the uncertainty in the cantilever spring constant calibration. The value for the fractional elongation of the fully extended S-DNA over the B-DNA contour length, 70%, has also been reported by other groups performing DNA stretching by means of optical or magnetic tweezers (Smith et al., 1992, 1996; Cluzel et al., 1996).

Force-induced melting of the double helix begins at an extension of 550 nm up to a force of 300 pN. The melting transition is followed by single-strand stretching. At a force of 540 pN and an extension of 660 nm, the single strand is detached from the tip and the cantilever relaxes. In our experiments, the contour length strongly depends on where the DNA molecule was picked up by the tip and thus varied

from molecule to molecule. However, the forces at which the force-induced structural transitions occurred were independent of the specific value of the contour length.

### Minor groove binding

Binding of the peptide distamycin A in the minor groove obviously does not have a large impact on the conformation

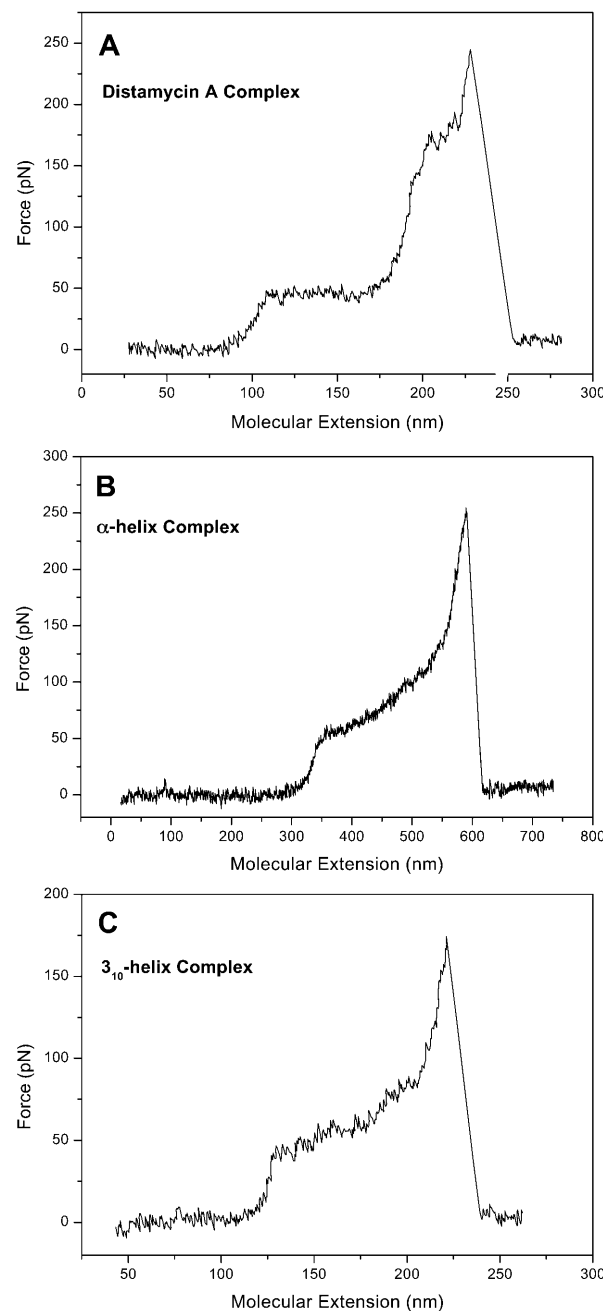


FIGURE 2 Force-extension traces for (A) the DNA-distamycin A complex; (B) the DNA complex with the  $\alpha$ -helical peptide Ac-(Leu-Ala-Arg-Leu)<sub>3</sub>-NH-linker; (C) the complex of DNA with the 3<sub>10</sub>-helical peptide Ac-(Aib-Leu-Arg)<sub>4</sub>-NH-linker.

of the DNA, as can be inferred from the qualitative agreement between the force-extension curves of free DNA and the complex (Fig. 2 A). The complex of DNA with the minor groove binding agent still exhibits the internal transitions due to overstretching and melting of the double helix characteristic for free DNA. The B-S transition plateau remains distinct from the melting transition. In contrast to the results for free DNA, we observed a considerable lowering of the B-S plateau to 50 pN. To avoid the uncertainty in the cantilever calibration, we performed comparative experiments on free DNA and the DNA-distamycin complex using the same AFM tip. This direct comparison showed that the decrease in force was highly reproducible. As reported by Krautbauer et al. (2002a,b), binding of the minor groove binder netropsin to  $\lambda$ -DNA led to an increase of the plateau force, a finding which we could reproduce also for distamycin in our group by means of optical tweezers measurements (Sischka et al., unpublished results). Thus, the decrease in the B-S transition force found for the complex of distamycin A to poly(dG-dC) dsDNA must be due to the sequence differences between  $\lambda$ -DNA and poly(dG-dC) dsDNA, distamycin showing a preferred binding to A-T-rich regions in a mixed sequence.

### Major groove binding

In the force-extension trace for the complex of poly(dG-dC) dsDNA with the  $\alpha$ -helical peptide (Fig. 2 B), no B-S transition separate from the melting transition is observed. Thus, the B-S transition does not appear as a plateau. Nevertheless, the point of maximum B-DNA elongation can still be discriminated. This finding suggests that the peptide, showing a force-extension characteristic that differs from both the one for the minor groove binder distamycin and the curves of the intercalants (Fig. 3), adopts a binding mechanism different from the one of the minor groove binding peptide distamycin A. Regarding the chemistry of the system, it was supposed that a possible binding of the  $\alpha$ -helix to DNA should be based upon unspecific electrostatic interactions between the guanidino groups of the peptide and the negatively charged DNA backbone and should occur in the major groove of the double helix (Niidome et al., 1996). Force spectroscopy measurements now indicate a mechanism that differs from both intercalation and minor groove binding, supporting the interpretation that the peptide binds to the major groove. The internal transition onset of the complex starts at a pulling force of  $\sim 60$  pN.

Binding of the  $3_{10}$ -helical peptide to poly(dG-dC) dsDNA

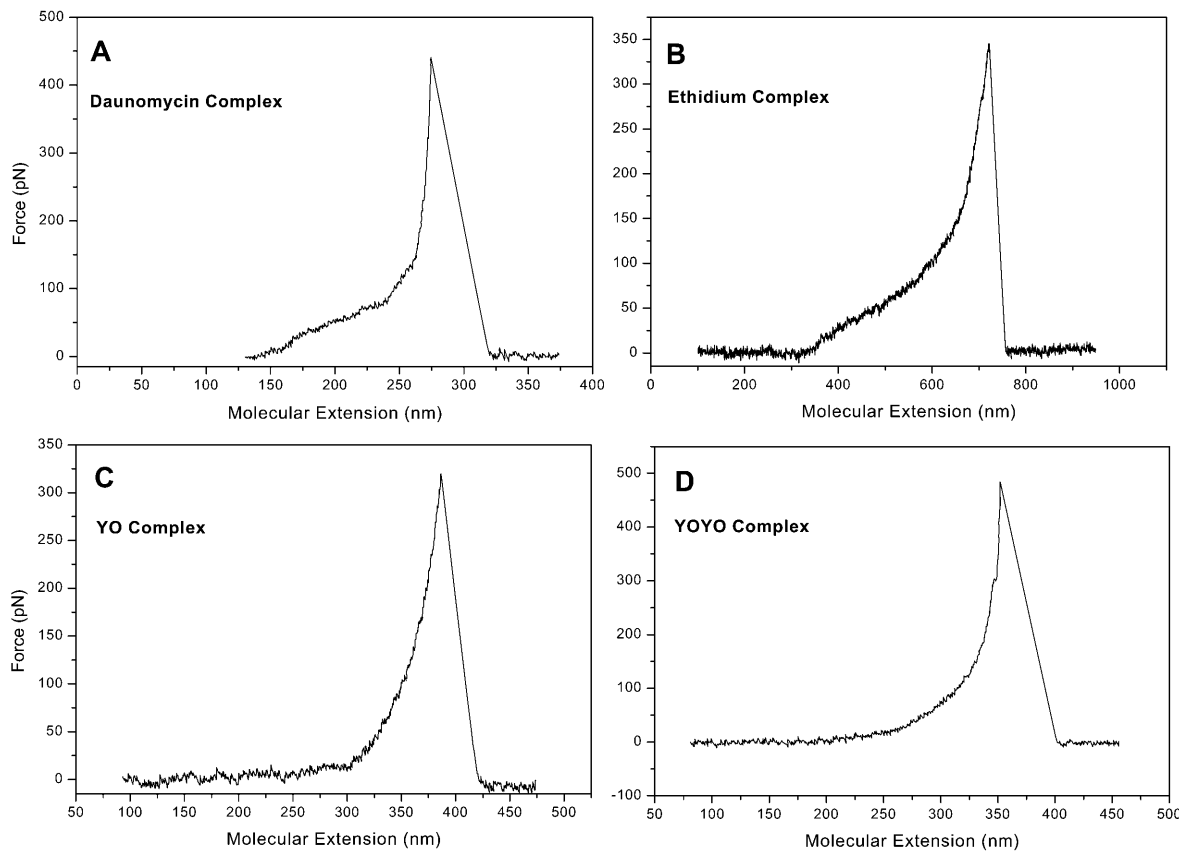


FIGURE 3 Force-extension traces for the complexes of poly(dG-dC) dsDNA with the intercalants (A) daunomycin; (B) ethidium bromide; (C) YO; (D) YOYO.

has almost the same effects as the binding of the  $\alpha$ -helix: The force-extension curve in Fig. 2 C is very similar to the one in Fig. 2 B, with the exception that the onset of the structural transition starts at a pulling force of  $\sim 50$  pN.

### Intercalation

Daunomycin as an intercalant inserts into DNA via a stacking interaction of its aromatic ring system with the base pairs. Intercalated DNA should display a considerable resistance against pulling with an external force. The force-extension curve in Fig. 3 A confirms this assumption: The force-extension trace for the complex of poly(dG-dC) dsDNA with the intercalant shows that, upon intercalation, the overstretching plateau vanishes. An intramolecular transition can only be distinguished from the double helix melting as a region of minor slope compared to the actual melting and only gives rise to a slight flattening of the curve up to forces of 75 pN.

Fig. 3 B shows the corresponding force-extension curve for the complex consisting of poly(dG-dC) dsDNA and the intercalant ethidium bromide. As for daunomycin, the elastic properties of DNA are significantly changed upon intercalation, so there is no distinct B-S transition observable. The slope of the force-extension curve is steeper than for the daunomycin complex. Up to 100 pN, there is still a flatter region discernible. These findings correlate well with previously reported results (Anselmetti et al., 2000; Krautbauer et al., 2002a,b).

Intercalation and major groove binding of DNA by the intercalants YO and YOYO leads to a uniform force-distance curve with an increasing gradient. The force-extension curve for the YO-DNA complex can be seen in Fig. 3 C. There is no indication for an intramolecular change in conformation. Binding of excess YO results in a force-extension trace with a steadily rising slope. Finally, as can be inferred from the force-extension curve (Fig. 3 D), the bis-intercalative binding mode of YOYO does not cause significant deviations in the overstretching behavior of the DNA complex in comparison to the corresponding YO-DNA complex.

### CONCLUSIONS

We have shown that AFM-based force spectroscopy measurements on single molecules provide a powerful tool to distinguish between different binding modes of small sequence-unspecific ligands to dsDNA such as intercalation, minor and major groove binding. Distinct characteristics could be detected in the force-extension traces of free poly(dG-dC) dsDNA and the DNA complexes with the minor groove binder distamycin A, supposed major groove binding  $\alpha$ -helical and  $3_{10}$ -helical peptides, the intercalants daunomycin and ethidium bromide, the intercalant and major groove binder YO and the bis-intercalant and major groove

binder YOYO. It could be demonstrated that the intramolecular B-S transition visible in the force-extension curves of free DNA also occurs in complexes of DNA with groove binders, whereas it vanishes as a distinct plateau in the corresponding DNA-intercalant curves. B-S transition of poly(dG-dC) dsDNA complexes with groove binding molecules like distamycin A and the synthetic helical peptides studied here showed a tendency to occur at forces slightly lowered by 10 pN compared to free poly(dG-dC) dsDNA. Intercalation of dsDNA by the agents daunomycin and ethidium bromide has the effect that an intramolecular transition besides the melting can only be discerned as a slight flattening of the force-extension curve slope. The intercalants act to withstand the partial unwinding of the DNA that accompanies the B-S transition. This effect was even more pronounced for the intercalant YO and the bis-intercalant YOYO.

Advanced theoretical models explaining our results should lead to a quantitative analysis of the binding behavior. An improved understanding of binding process and mechanisms will provide interesting perspectives for fundamental research in the fields of biochemistry, pharmacology, and genetics. In this context, AFM force spectroscopy will gain importance as a molecular biosensor that allows for the identification of distinct binding motives in the interaction of biological systems at the single molecule level.

This work was supported by the Deutsche Forschungsgemeinschaft (Sonderforschungsbereich 613).

### REFERENCES

- Anselmetti, D., J. Fritz, B. Smith, and X. Fernandez-Busquets. 2000. Single molecule DNA biophysics with atomic force microscopy. *Single Molecules*. 1:17–23.
- Aubel-Sadron, G., and D. Londos-Gagliardi. 1984. Daunorubicin and doxorubicin, anthracycline antibiotics, a physicochemical and biological review. *Biochimie*. 66:333–352.
- Baguley, B. C. 1982. Nonintercalative DNA-binding antitumour compounds. *Mol. Cell. Biochem.* 43:167–181.
- Bailly, C., and J. B. Chaires. 1998. Sequence-specific DNA minor groove binders. Design and synthesis of netropsin and distamycin analogues. *Bioconjug. Chem.* 9:513–538.
- Clausen-Schaumann, H., M. Rief, C. Tolkendorf, and H. E. Gaub. 2000. Mechanical stability of single DNA molecules. *Biophys. J.* 78:1997–2007.
- Cluzel, P., A. Lebrun, C. Heller, R. Lavery, J.-L. Viovy, D. Chatenay, and F. Caron. 1996. DNA: An extensible molecule. *Science*. 271:792–794.
- Dammer, U., M. Hegner, D. Anselmetti, P. Wagner, M. Dreier, W. Huber, and H.-J. Güntherodt. 1996. Specific antigen/antibody interactions measured by force microscopy. *Biophys. J.* 70:2437–2441.
- Dammer, U., O. Popescu, P. Wagner, D. Anselmetti, H.-J. Güntherodt, and G. N. Misevic. 1995. Binding strength between cell adhesion proteoglycans measured by atomic force microscopy. *Science*. 267:1173–1175.
- Florin, E.-L., V. T. Moy, and H. E. Gaub. 1994. Adhesion forces between individual ligand-receptor pairs. *Science*. 264:415–417.

- Florin, E.-L., M. Rief, H. Lehmann, M. Ludwig, C. Dormair, V. T. Moy, and H. E. Gaub. 1995. Sensing specific molecular interactions with the atomic force microscope. *Biosens. Bioelectron.* 10:895–901.
- Fritz, J., A. G. Katopodis, F. Kolbinger, and D. Anselmetti. 1998. Force-mediated kinetics of single P-selectin/ligand complexes observed by atomic force microscopy. *Proc. Natl. Acad. Sci. USA.* 95:12283–12288.
- Glazer, A. N., and H. S. Rye. 1992. Stable dye-DNA intercalation complexes as reagents for high-sensitivity fluorescence detection. *Nature.* 359:859–861.
- Hinterdorfer, P., W. Baumgartner, H. Gruber, K. Schilcher, and H. Schindler. 1996. Detection and localization of individual antibody-antigen recognition events by atomic force microscopy. *Proc. Natl. Acad. Sci. USA.* 93:3477–3481.
- Hortobagyi, G. N. 1997. Anthracyclines in the treatment of cancer. *Drugs.* 54:1–7.
- Hutter, J. L., and J. Bechhoefer. 1993. Calibration of atomic-force microscope tips. *Rev. Sci. Instrum.* 7:1868–1873.
- Krautbauer, R., S. Fischerländer, S. Allen, and H. E. Gaub. 2002a. Mechanical fingerprints of DNA drug complexes. *Single Molecules.* 3:97–103.
- Krautbauer, R., L. H. Pope, T. E. Schrader, S. Allen, and H. E. Gaub. 2002b. Discriminating small molecule DNA binding modes by single molecule force spectroscopy. *FEBS Lett.* 510:154–158.
- Larsson, A., C. Carlsson, M. Jonsson, and B. Albinsson. 1994. Characterization of the binding of the fluorescent dyes YO and YOYO to DNA by polarized light spectroscopy. *J. Am. Chem. Soc.* 116:8459–8465.
- Lee, G. U., L. A. Chrisey, and R. J. Colton. 1994a. Direct measurement of the forces between complementary strands of DNA. *Science.* 266:771–773.
- Lee, G. U., D. A. Kidwell, and R. J. Colton. 1994b. Sensing discrete streptavidin-biotin interactions with atomic force microscopy. *Langmuir.* 10:354–357.
- Morgan, A. R., D. H. Evans, G. U. Lee, and D. E. Pulleyblank. 1979. Review: Ethidium fluorescence assays, part 2: Enzymatic studies and DNA-protein interactions. *Nucleic Acids Res.* 10:571–594.
- Moy, V. T., E.-L. Florin, and H. E. Gaub. 1994. Intermolecular forces and energies in between ligands and receptors. *Science.* 266:257–259.
- Niidome, T., N. Ohmori, A. Ichinose, A. Wada, H. Mihara, T. Hirayama, and H. Aoyagi. 1996. Binding of cationic alpha-helical peptides to plasmid DNA and their gene-transfer abilities into cells. *J. Biol. Chem.* 272:15307–15312.
- Rief, M., H. Clausen-Schaumann, and H. E. Gaub. 1999. Sequence-dependent mechanics of single DNA molecules. *Nat. Struct. Biol.* 6:346–349.
- Rief, M., M. Gautel, F. Oesterhelt, J. M. Fernandez, and H. E. Gaub. 1997a. Reversible unfolding of individual titin immunoglobulin domains by AFM. *Science.* 276:1109–1112.
- Rief, M., F. Oesterhelt, B. Heymann, and H. E. Gaub. 1997b. Single molecule force spectroscopy on polysaccharides by atomic force microscopy. *Science.* 275:1295–1297.
- Ros, R., F. Schwesinger, D. Anselmetti, M. Kubon, R. Schäfer, A. Plückthun, and L. Tiefenauer. 1998. Antigen binding forces of individually addressed single-chain Fv antibody molecules. *Proc. Natl. Acad. Sci. USA.* 95:7402–7405.
- Rouzina, J., and V. A. Bloomfield. 2001a. Force-induced melting of the DNA double helix. 1. Thermodynamic analysis. *Biophys. J.* 80:882–893.
- Rouzina, J., and V. A. Bloomfield. 2001b. Force-induced melting of the DNA double helix. 2. Effect of solution conditions. *Biophys. J.* 80:894–900.
- Smith, S. B., Y. Cui, and C. Bustamante. 1996. Overstretching B-DNA: The elastic response of individual double-stranded and single-stranded DNA molecules. *Science.* 271:795–799.
- Smith, S. B., L. Finzi, and C. Bustamante. 1992. Direct mechanical measurements of the elasticity of single DNA molecules by using magnetic beads. *Science.* 258:1122–1126.
- Strick, T. R., J.-F. Allemand, D. Bensimon, and V. Croquette. 1998. Behaviour of supercoiled DNA. *Biophys. J.* 74:2016–2028.
- Strunz, T., K. Oroszlan, R. Schäfer, and H.-J. Güntherodt. 1999. Dynamic force spectroscopy of single DNA molecules. *Proc. Natl. Acad. Sci. USA.* 96:11277–11282.
- Turner, P. R., and W. A. Denny. 1996. The mutagenic properties of DNA minor groove binding ligands. *Mutat. Res.* 355:141–169.
- Wenner, J. R., M. C. Williams, J. Rouzina, and V. A. Bloomfield. 2002. Salt dependence of the elasticity and overstretching transition of single DNA molecules. *Biophys. J.* 82:3160–3169.

## 2.3 Publications II and III

Andy Sischka, **Rainer Eckel**, Katja Toensing, Robert Ros, and Dario Anselmetti. Compact microscope-based optical tweezers system for molecular manipulation. *Rev. Sci. Instr.* 74, 11 (2003), 4827-4831.

Andy Sischka, Katja Toensing, **Rainer Eckel**, Sven David Wilking, Norbert Sewald, Robert Ros, and Dario Anselmetti. Molecular mechanisms and kinetics between DNA and DNA binding ligands. *Biophys. J.* 88 (2005), 404-411.

### 2.3.1 Contributions

The author participated substantially in the analysis of the OT force spectroscopy data. For publication II, he calculated the Two-State WLC fit yielding structural and energy parameters characterizing the B-S transition observed for free DNA (Fig. 4). He also determined the WLC contour and persistence lengths reported in publication III (Table 1). Moreover, part of the chemical compounds which were investigated in both works were prepared by the author.

# Compact microscope-based optical tweezers system for molecular manipulation

Andy Sischka,<sup>a)</sup> Rainer Eckel, Katja Toensing, Robert Ros, and Dario Anselmetti  
*Experimental Biophysics and Applied Nanosciences, Faculty of Physics, Bielefeld University,  
 33615 Bielefeld, Germany*

(Received 18 February 2003; accepted 14 August 2003)

A compact single beam optical tweezers system for force measurements and manipulation of individual double-stranded deoxyribonucleic acid (DNA) molecules was integrated into a commercial inverted optical microscope. A maximal force of 150 pN combined with a force sensitivity of less than 0.5 pN allows measurements of elastic properties of single molecules which complements and overlaps the force regime accessible with atomic force microscopy (AFM). The manipulation and measurement performance of this system was tested with individual  $\lambda$ -DNA molecules and renders new aspects of dynamic forces phenomena with higher precision in contrast to AFM studies. An integrated liquid handling system with a fluid cell allows investigation of the force response of individual DNA molecules in the presence of DNA binding agents. Comparison of YOYO-1-, ethidium bromide intercalated DNA, and distamycin-A complexed DNA revealed accurate and reproducible differences in the force response to an external load. This opens the possibility to use it as a single molecule biosensor to investigate DNA binding agents and even to identify molecular binding mechanisms. © 2003 American Institute of Physics.

[DOI: 10.1063/1.1619545]

## I. INTRODUCTION

The invention of optical tweezers by Ashkin<sup>1,2</sup> pioneered the application of noninvasive micromanipulation of dielectric particles in the Rayleigh and Mie size regimes.<sup>3–5</sup> Static and dynamic forces can be detected by using a trapped particle deflected by an external force.<sup>6</sup> These trapping techniques have been used for manipulation of living cells, organelles, bacteria, and viruses in biology.<sup>7–9</sup>

The manipulation and control of individual molecules with optical tweezers was introduced by Block and co-workers<sup>10</sup> with kinesin molecules, whereas Bustamante and co-workers<sup>11</sup> investigated single- and double-stranded deoxyribonucleic acid DNA (dsDNA) molecules via attaching biotin-streptavidin functionalized microspheres to these molecules. They were able to measure the elastic response and mechanical properties of individual DNA molecules. Thus, DNA intercalating- and minor groove binding molecules and structural transitions in those molecules have also been investigated in experiments with atomic force microscopy (AFM),<sup>12–14</sup> dual beam optical tweezers<sup>15</sup> and micropipettes.<sup>16</sup> Recently, it has been shown that different binding modes of DNA binders could be identified which allowed deeper insights into the molecular interplay between DNA and small ligands.<sup>15,17</sup>

In this article, we introduce a compact and versatile single-beam optical tweezers setup (see Fig. 1) which is based on a commercial inverted optical microscope. This allows high precision force measurements in single-molecule

force experiments up to 150 pN and ideally overlaps the force range but outclass the force sensitivity of AFM systems.<sup>18</sup> After calibration, the setup was tested in experiments with DNA and different DNA binding ligands, showing distinct differences in the force response which allow discrimination between different binding modes.

## II. EXPERIMENTAL SETUP

The optical tweezers system is installed on an optical tabletop (VH-3660W-OPT, Newport, CA) for vibration isolation. A diode-pumped Nd:YAG-laser (LCS-DTL-322, Laser 2000, Germany) emits at  $\lambda = 1064$  nm linear polarized and collimated light ( $\text{TEM}_{00}$ ) with a maximum power of 1000 mW and a beam width of 1.5 mm. In order to reduce vibrational noise from the force signal, the original cooling fan was replaced by a solid copper heat sink and special emphasis was put to a compact and stable setup. A long pass filter (RG-850, Linos, Germany; 0.2% transmission at 810 nm, 98% transmission at 1064 nm) blocks the excitation radiation (810 nm) of the laser pumping unit. The laser beam is redirected by two flat mirrors (10D20-ER.2, Newport, CA) into a 10× beam expander (S6A SS 0107, Sill Optics, Germany) mounted on the epifluorescence port of a commercial optical inverted microscope (Axiovert 100, Carl Zeiss, Germany). An enclosure around the lightpath prevents distortions from airflow. The laser beam passes a dichroic mirror (TFP1064nm56°, Laseroptik, Germany; approximately 80% transmission at 400–700 nm, >96% reflection at 1064 nm) and is fed into a 60× water immersion objective (UPLAPO60W/IR, Olympus, Japan). The objective has a back side aperture diameter of 8.5 mm with a numerical aperture of 1.20 and a working distance of 300  $\mu\text{m}$ . Whenever a

<sup>a)</sup>Author to whom correspondence should be addressed at: Universitaet Bielefeld, Fakultaet Physik, Universitaetsstrasse 25, 33615 Bielefeld, Germany; electronic mail: andy.sischka@physik.uni-bielefeld.de

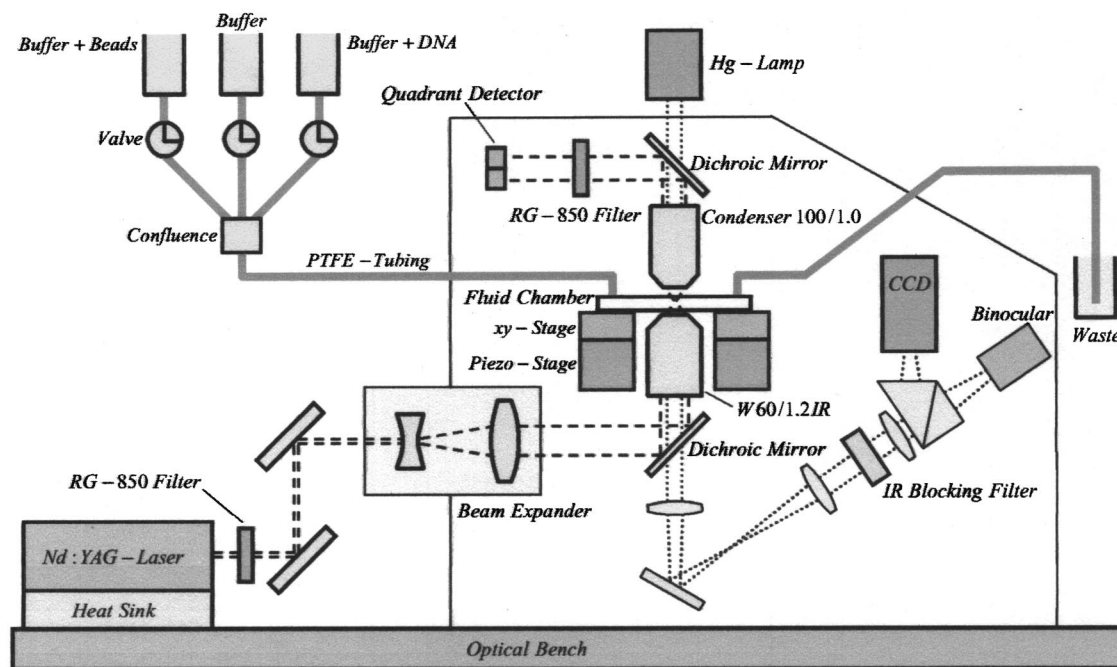


FIG. 1. Optical tweezers setup with integrated flow system.

transparent particle is trapped within the focus, the forward scattered light can be used for displacement detection.<sup>19</sup> In our setup, the forward scattered light is collected by a water immersion condenser objective (Achroplan 100/1.0 W, Carl Zeiss, Germany). This high numerical aperture is needed (a) to collect as much forward scattered light as possible to obtain a high signal-to-noise ratio for further signal processing and (b) to observe all intensity distributions and variations inside the forward scattered beam profile. The light collected by the condenser is reflected by a dichroic mirror (TFP1064nm56°, Laseroptik, Germany), passes a long pass filter (RG-850, Linos, Germany) and is position analyzed by a quadrant photodiode (SD 380-23-21-051, Silicon Detector Corp., USA) adjustable in the *x* and *y* directions. The quadrant detector readout (four current–voltage amplifiers, OPA-111, Burn-Brown, USA) and an analog processing unit (University of Basel, Switzerland) transform the light intensity variations into a direct or normalized voltage signal proportional to the bead position in the optical trap. This voltage signal is digitized with a transfer rate of 388 000 samples/s and further processed by a custom-made software based on a commercial software library (LABVIEW 6.0, National Instruments, TX). This high acquisition rate allows statistical noise averaging up to a factor of 300 per data point.

Real-time observation of the trapped particle is possible by a charge coupled device camera on the binocular side port and a mechanically detached halogen lamp. For eye and camera protection, two IR blocking filter (KG-5, Schott, Germany; 10<sup>-5</sup>% transmission at 1064 nm for each filter) are placed into the optical path.

The position control of the trap is realized by moving a fluid cell with respect to the trap via a three-dimensional piezostage (P-517.3CD, Physik Instrumente, Germany; *x,y*: 100  $\mu\text{m}$  and *z*: 20  $\mu\text{m}$ ) controlled by digital stage electronics.

An additional manual coarse positioning stage allows further coarse adjustments of the fluid cell.

The fluid cell is a homebuilt sandwich construction of two glass coverslips (see Fig. 2) (60 mm  $\times$  24 mm  $\times$  0.15 mm) separated by two parafilms (American National Can, CT) where the flow channel (42 mm  $\times$  1 mm) is embossed into. Two holes (1 mm diameter) within the upper coverslip allow liquid in and outlet. An integrated micropipette (KG-33, Garner Glass, CA) older diameter (o.d.) = 150  $\mu\text{m}$ , inner diameter (i.d.) = 80  $\mu\text{m}$ , *L* = 100 mm) pointing directly along the flow channel was pulled (Pipette Puller P-2000, Sutter Instrument Co., CA) to form a tip with a diameter of 1.5  $\mu\text{m}$  with a wall thickness of less than 0.5  $\mu\text{m}$ . This micropipette allows mechanical trapping of individual micron-sized beads by applying low pressure.

A compact, unsusceptible, and simple liquid handling system established with teflon tubings (Bohlender, Germany; o.d. = 1.6 mm i.d. = 0.3 mm) and driven by hydrostatic pres-

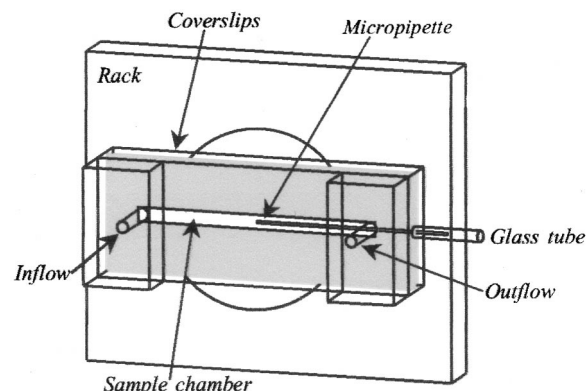


FIG. 2. The fluid chamber.

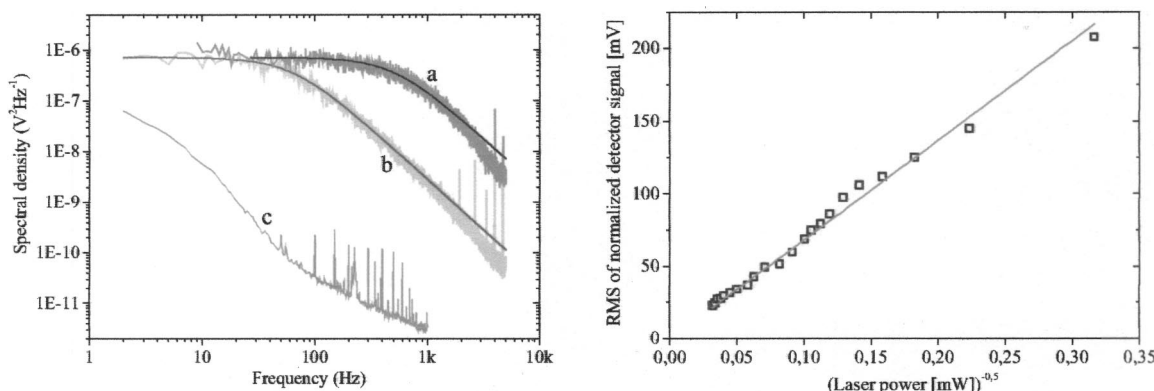


FIG. 3. (Left-hand side) Thermal noise spectra for 3180 nm bead (a) trapped at a laser power of 900 mW (corner frequency  $f_c = 502.9$  Hz, force constant  $k = 94.7$  pN/ $\mu\text{m}$ ), (b) trapped at a laser power of 60 mW (corner frequency  $f_c = 63.1$  Hz, force constant  $k = 11.9$  pN/ $\mu\text{m}$ ), (c) empty trap at a laser power of 60 mW. (Right-hand side) Linear dependency between rms value of the normalized detector signal (proportional to the displacement of the bead inside the trap) and the inverse square root of the laser power.

sures allows reproducible, constant, and smooth liquid flow through the cell.

### III. CALIBRATION AND EXPERIMENTAL PROCEDURE

#### A. Trap stiffness calibration

The stiffness of the trap was determined by measuring the maximum trapping force at different laser powers.<sup>8</sup> We used polystyrene beads with a diameter of 3180 nm (Sphero-tech, IL) covalently coated with streptavidin (binding capacity of 60 pmol biotin/mg particle). For all experiments, the stock solution (0.5% v/w) was diluted 1:1000 with 150 mM NaCl and 10 mM Tris/HCl buffer (*pH* 8.0).

The trapping force  $F$  was calculated via Stokes' friction<sup>8</sup>  $F = -\gamma v$  ( $\gamma = 6\pi\eta r$ ) with velocities up to  $v = 12000$  nm/s for a sphere with radius  $r$  inside an infinite expanded homogenous fluid with a viscosity  $\eta$ . Trapping forces measured at 60 mW, 600 mW, and 900 mW laser power were 16 pN, 105 pN, and 145 pN, respectively. Due to losses in the optical path length we determined a final yield of 20.3% within the optical trap with respect to the laser output. Calibration of the optical trap was realized by moving the liquid cell with respect to the trapped bead at constant velocity where the voltage signal of the quadrant detector can be compared with the actual Stoke's frictional force.<sup>6</sup>

In addition, calibration was checked by computing the noise power spectrum of the detector signal by using a Lorentzian fit. The corner frequency  $f_c$  (Fig. 3 left-hand side) can be related to the force constant  $k = 2\pi\gamma f_c$  of the optical trap potential.

A working distance of 150  $\mu\text{m}$  between bead and cell wall surface made corrections for drag coefficient calculations unnecessary.<sup>8</sup> Additionally, the validity of the equipartition theorem can be reviewed: The detector voltage signal depends linearly on the displacement  $x$  of the bead inside the trap. There is further a linear dependency of the force constant  $k$  on the laser power  $P$ . We observed a linear relation between the root-mean-square (rms) value of the displacement and the inverse square root of the laser power according to the equipartition theorem (Fig. 3 right-hand side):

$\langle x \rangle = (k_B T / k)^{0.5}$  where  $k_B$  and  $T$  are the Boltzmann constant and  $T$  is the absolute temperature, respectively.<sup>6</sup>

#### B. Biotinylation of $\lambda$ -phage double-stranded DNA and coupling to streptavidin-coated beads

Biochemical modification of the  $\lambda$ -DNA is required for force measurements to ensure a tethering process between the DNA and two 3180 nm streptavidin-coated beads. Therefore,  $\lambda$ -dsDNA (Promega Corp., WI) was heated up to 323 K for 5 min to convert the circular form of the DNA into the linearized form, yielding so called "sticky ends" containing 12 free bases at both 5 ft. ends of the  $\lambda$ -DNA. Biotin-14-dCTP (GibcoBRL, Invitrogen Corp., CA) and dATP, dGTP, and dTTP (Amersham Biociences UK Ltd., UK) were added to both 3 ft. ends using Klenow-exo<sup>-</sup> polymerase enzyme (New England Biolabs Inc., MA). After intensive cleaning with Microcon-YM-50 cellulose filters (Amicon Microcon, Millipore Corp., MA) we ended up with modified dsDNA molecules with biotin groups at their 3 ft. ends. The biotinylated  $\lambda$ -DNA was stored as a dilution of 15 pM. DNA binding ligands (YOYO-1, ethidium bromide, and distamycin-A) are used as dilution of 1  $\mu\text{M}$ , respectively.

The buffer was always filtered with syringe filters (0.22  $\mu\text{m}$ , Qualilab, Germany). Additionally the solution of  $\lambda$ -DNA and the solution with streptavidin-coated beads were degassed to prevent spouting air bubbles inside the tubings or the sample chamber while performing an experiment. All experiments were carried out in 10 mM Tris buffer (*pH* 8.0) containing 150 mM NaCl and the respective concentrations of the drug/dye. The concentration of the DNA in the sample chamber was 2 pM.

Briefly, the working procedure was as follows: After filling the cell with buffer, bead solution ( $5 \times 10^{-4}$  % w/v) was injected. Once a bead was trapped, it was transferred to the tip of the micropipette. A second bead stays trapped inside the laser focus. After rinsing the sample chamber with buffer,  $\lambda$ -DNA solution was injected and a flow of 800  $\mu\text{m}/\text{s}$  inducing a drag force of about 24 pN was established.

Once a DNA molecule attaches to the trapped bead, an increased force signal of about 2.5 to 3.0 pN can be detected **31**

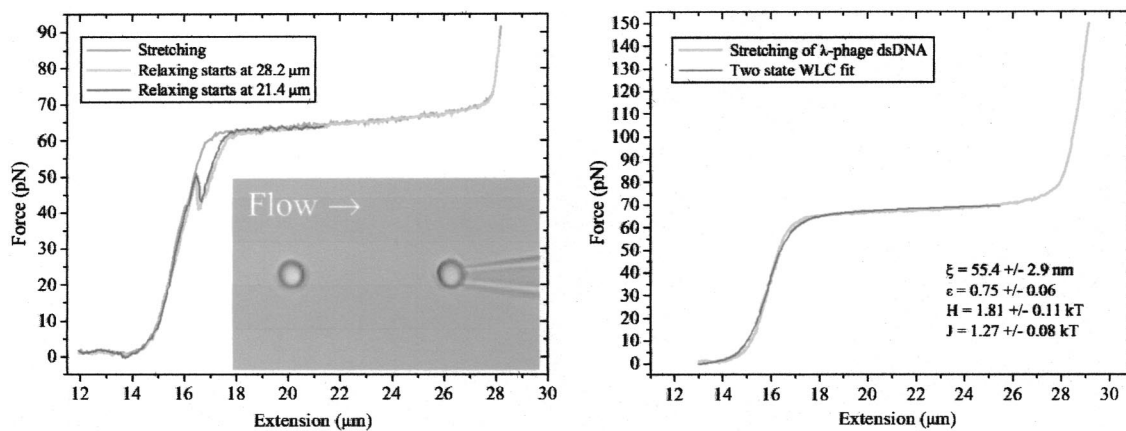


FIG. 4. (Left-hand side) Overstretching of  $\lambda$ -phage dsDNA in a force–extension/relaxation loop. Reproducible force hysteresis effects can be identified during relaxation. Inset: Single video frame obtained during the optical tweezers experiment. A bead ( $3.18 \mu\text{m}$  diameter) coated with streptavidin is held on a micropipette. A second bead (left-hand side) is trapped in the laser beam. A single biotinylated dsDNA molecule is attached to both streptavidin-coated spheres. (Right-hand side) two-state wormlike chain fit of the experimental data of free  $\lambda$ -phage dsDNA elasticity at the B–S transition and force–extension data of stretching dsDNA at higher laser power (900 mW) reveals high precision measurements and an extended force range up to 150 pN.

due to hydrodynamic drag forces of the elongated DNA in the buffer flow. The free end of the DNA was coupled to the bead fixed on the micropipette by reducing the distance to  $11 \mu\text{m}$ , which is smaller than the contour length of the  $\lambda$ -DNA molecule ( $16.4 \mu\text{m}$ ).<sup>11</sup> Tethering of the DNA between the two beads can be checked by a careful extension of the molecule where an attractive force signal indicates proper fixation.

#### IV. RESULTS AND DISCUSSION

Figure 4 (left-hand side) shows three force versus extension/relaxation curves obtained from overstretching a single  $\lambda$ -DNA molecule. The experimental noise of the force experiment even at higher laser power (950 mW) is well below 1.5 pN (Fig. 4, right-hand side) while achieving a maximal force of 150 pN. The noise level is dominated by fluctuations due to mechanical noise and of the flow (<0.2 pN) and laser intensity fluctuations (less than 0.4 pN in a frequency bandwith of 0.1 to 1 Hz at 600 mW). Furthermore, thermal noise caused by Brownian motion has to be considered as well.

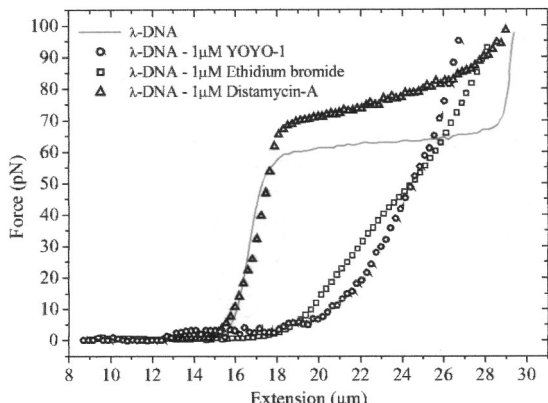


FIG. 5. Changes in the force response of  $\lambda$ -phage dsDNA in the presence of DNA binding agents.  $\lambda$ -phage dsDNA reference, YOYO-1 intercalated  $\lambda$ -DNA, EtBr intercalated  $\lambda$ -DNA, and  $\lambda$ -DNA complexed with Distamycin-A.  
32

The  $B-S$  transition<sup>11</sup> indicated by the plateau is reached at forces of about 65 pN. After the first overstretching (Fig. 4, left-hand side velocity: 30 nm/s); the DNA was relaxed at the same velocity showing a very high reproducibility, except for a small hysteric variation at the onset of the transition from  $B-S$  overstretching to  $B$ -form elasticity. This observation was found to be very reproducible as indicated in the second relaxation curve of Fig. 4 and interpreted as single-stranded nicks of the DNA.<sup>11</sup>

The force–extension curve in the  $B-S$  transition regime was fitted using a “two-state wormlike chain” model<sup>20</sup> (Fig. 4, right-hand side). The values for the persistence length  $\xi$ , the fractional elongation  $\epsilon$ , the free energy difference per segment  $2H$  and the correlation energy between adjacent segments  $J$  were determined to be  $\xi = 55.4 \pm 2.9 \text{ nm}$ ,  $\epsilon = 0.75 \pm 0.06$ ,  $H = 1.81 \pm 0.11 k_B T$ , and  $J = 1.27 \pm 0.08 k_B T$ , respectively, and are in excellent agreement with the results of Ahsan *et al.*<sup>20</sup>

Effects of different DNA binding drugs on the overstretching behavior of DNA were investigated using this optical tweezers setup. In Fig. 5, four force–extension curves are presented, exhibiting the different force responses of  $\lambda$ -DNA to binding of a bis-intercalator (YOYO-1),<sup>14</sup> an intercalator (ethidium bromide),<sup>12,15,17</sup> and a minor groove binder acting as an antitumor drug (distamycin-A).<sup>14</sup>

We could unambiguously show that mechanical properties of DNA vary in the presence of different binding agents, which opens new possibilities to use this setup as a single-molecule biosensor to investigate DNA binding agents and even to identify molecular binding mechanisms.

#### ACKNOWLEDGMENTS

Technical assistance from Christoph Pelargas and Gerd Wiebusch (Bielefeld University) is gratefully acknowledged. The authors thank Martin Hegner and Wilfried Grange (University of Basel, Switzerland) for providing technical advice, biochemical preparation protocols, and functionalized DNA molecules in the early stage of this work.

- <sup>1</sup>A. Ashkin, Phys. Rev. Lett. **24**, 156 (1970).
- <sup>2</sup>A. Ashkin, J. M. Dziedzic, J. E. Bjorkholm, and S. Chu, Opt. Lett. **11**, 288 (1986).
- <sup>3</sup>A. Ashkin, Phys. Rev. Lett. **40**, 729 (1978).
- <sup>4</sup>A. Ashkin, Biophys. J. **61**, 569 (1992).
- <sup>5</sup>A. Ashkin, Proc. Natl. Acad. Sci. U.S.A. **94**, 4853 (1997).
- <sup>6</sup>L. P. Ghislain, N. A. Switz, and W. W. Webb, Rev. Sci. Instrum. **65**, 2762 (1994).
- <sup>7</sup>A. Ashkin and J. M. Dziedzic, Science **235**, 1517 (1987).
- <sup>8</sup>K. Svoboda and S. M. Block, Annu. Rev. Biophys. Biomol. Struct. **23**, 247 (1994).
- <sup>9</sup>S. Yamada, D. Wirtz, and S. C. Kuo, Biophys. J. **78**, 1736 (2000).
- <sup>10</sup>S. M. Block, L. S. Goldstein, and B. J. Schnap, Nature (London) **348**, 6299 (1990).
- <sup>11</sup>S. B. Smith, Y. Cui, and C. Bustamante, Science **271**, 795 (1996).
- <sup>12</sup>D. Anselmetti, J. Fritz, B. Smith, and X. Fernandez-Busquets, Single Mol. **1**, 17 (2000).
- <sup>13</sup>R. Krautbauer, L. H. Pope, T. E. Schrader, S. Allen, and H. E. Gaub, FEBS Lett. **510**, 154 (2002).
- <sup>14</sup>R. Eckel, R. Ros, A. Ros, S. D. Wilking, N. Sewald, and D. Anselmetti, Biophys. J. **85**, 1968 (2003).
- <sup>15</sup>S. Husale, W. Grange, and M. Hegner, Single Mol. **3**, 91 (2002).
- <sup>16</sup>P. Cluzel, A. Lebrun, C. Heller, R. Lavery, J. L. Viovy, D. Chatenay, and F. Caron, Science **271**, 792 (1996).
- <sup>17</sup>E. Krautbauer, S. Fischerlander, S. Allen, and H. E. Gaub, Single Mol. **3**, 97 (2002).
- <sup>18</sup>C. Bustamante, J. C. Macosko, and G. J. Wuite, Nat. Rev. Mol. Cell. Biol. **1**, 130 (2000).
- <sup>19</sup>M. W. Allersma, F. Gittes, M. J. de Castro, R. J. Steward, and C. F. Schmidt, Biophys. J. **74**, 1074 (1998).
- <sup>20</sup>A. Ahsan, J. Rudnick, and R. Bruinsma, Biophys. J. **74**, 132 (1998).

# Molecular Mechanisms and Kinetics between DNA and DNA Binding Ligands

Andy Sischka,\* Katja Toensing,\* Rainer Eckel,\* Sven David Wilking,<sup>†</sup> Norbert Sewald,<sup>†</sup> Robert Ros,\* and Dario Anselmetti\*

\*Experimental Biophysics & Applied Nanosciences, Department of Physics, and <sup>†</sup>Organic and Bioorganic Chemistry, Department of Chemistry, Bielefeld University, 33615 Bielefeld, Germany

**ABSTRACT** Mechanical properties of single double-stranded DNA (dsDNA) in the presence of different binding ligands were analyzed in optical-tweezers experiments with subpiconewton force resolution. The binding of ligands to DNA changes the overall mechanic response of the dsDNA molecule. This fundamental property can be used for discrimination and identification of different binding modes and, furthermore, may be relevant for various processes like nucleosome packing or applications like cancer therapy. We compared the effects of the minor groove binder distamycin-A, a major groove binding  $\alpha$ -helical peptide, the intercalators ethidium bromide, YO-1, and daunomycin as well as the bisintercalator YOYO-1 on  $\lambda$ -DNA. Binding of molecules to the minor and major groove of dsDNA induces distinct changes in the molecular elasticity compared to the free dsDNA detectable as a shift of the overstretching transition to higher forces. Intercalating molecules affect the molecular mechanics by a complete disappearance of the B-S transition and an associated increase in molecular contour length. Significant force hysteresis effects occurring during stretching/relaxation cycles with velocities  $>10$  nm/s for YOYO-1 and  $>1000$  nm/s for daunomycin. These indicate structural changes in the timescale of minutes for the YOYO-DNA and of seconds for the dauno-mycin-DNA complexes, respectively.

## INTRODUCTION

The interaction of ligands with double-stranded DNA is fundamental for many intracellular processes. Especially proteins that bind to specific DNA target sequences control a variety of processes such as regulation, transcription, and translation. Small binding ligands with reduced or no sequence specificity are often able to interfere with those processes because they are capable of changing mechanical properties of the DNA strands and are, therefore, frequently used in cancer therapy (Hurley, 2002). Because of the complex double-helical structure of DNA, different binding modes are possible. Besides covalent binding there are several classes of specific or unspecific noncovalent binding modes: intercalation between basepairs (Reha et al., 2002), bisintercalation (Krishnamoorthy et al., 2002), minor groove binding (Reddy et al., 2001), major groove binding (Niidome et al., 1996; Eckel et al., 2003), a combination of those (Larsson et al., 1994), and binding via nonclassical modes (Lipscomb et al., 1996).

Intercalation is characterized by noncovalent stacking between adjacent basepairs via interaction with  $\pi$ -orbitals of these basepairs (Graves and Velea, 2000) and often combined with hydrogen bonding (Reha et al., 2002). Intercalation extends and frequently partially unwinds the DNA double strands, having large impact on the structure of the nucleosome (McMurray et al., 1991). Furthermore, side

groups of intercalating parts of few ligands also influence the binding process and accordingly can cause sequence selective behavior.

Selective binding to the narrow minor groove of AT-rich sequences by van der Waals interaction, formation of hydrogen bonds, and electrostatic interaction is characteristic for minor groove binders (Reddy et al., 2001). Electrostatic interaction is characteristic for major groove binders (especially helical peptide ligands) as well (Eckel et al., 2003). Minor groove binding drugs, for instance, can interfere with the specific binding of regulatory proteins by changing the local bending of DNA (Zimmer and Wähnert, 1986), or disrupt the nucleosome in a selective way (Fitzgerald and Anderson, 1999).

Detailed information about the structural aspects of binding are given by x-ray diffraction (Coste et al., 1999) and NMR spectroscopy (Gelascio and Lippard, 1998). Additionally, procedures to detect binding properties by investigating contour lengths of ligand-DNA complexes by means of scanning force microscopy (SFM) techniques (Coury et al., 1996) have been introduced by placing those complexes onto a treated surface accessible for SFM survey.

Over the last 15 years different ultrasensitive techniques have been developed that allow measurements of inter- and intramolecular forces at the single-molecule level. Most common techniques are based on atomic force microscopy (AFM) (Binnig et al., 1986) and optical tweezers (Ashkin, 1970, 1997; Ashkin et al., 1986; Svoboda and Block, 1994). Recent works cover AFM force spectroscopy of single DNA molecules (Rief et al., 1999; Clausen-Schaumann et al., 2000) as well as of ligand-DNA complexes (Krautbauer et al.,

Submitted December 17, 2003, and accepted for publication October 13, 2004.

Address reprint requests to Dario Anselmetti, Universität Bielefeld, Fakultät für Physik, Universitätsstrasse 25, 33615 Bielefeld, Germany. E-mail: dario.anselmetti@physik.uni-bielefeld.de.

© 2005 by the Biophysical Society

0006-3495/05/01/404/08 \$2.00

doi: 10.1529/biophysj.103.036293

2000; Anselmetti et al., 2000; Krautbauer et al., 2002a; Eckel et al., 2003), demonstrating their significant implications while investigating mechanical properties of ligand-complexed DNA observable in force-extension measurements.

Optical tweezers systems with their superior force sensitivity compared to AFM were utilized for measurements of elastic responses of immobilized single- and double-stranded DNA molecules (Smith et al., 1996; Wuite et al., 2000; Williams et al., 2001; Wenner et al., 2002; Sischka et al., 2003), whereas optical fiber setups were used for probing the molecular extension of a ligand complexed double-stranded DNA (Cluzel et al., 1996).

Most recently, optical tweezers experiments yield and reveal changes in the mechanical and elastic properties of double-stranded DNA molecules in the presence of binding ligands (Bennink et al., 1999; Husale et al., 2002; Sischka et al., 2003; Tessmer et al., 2003).

In this work a set of DNA binding agents was investigated, including a multitude of binding modes such as the minor groove binder distamycin-A and the supposed major groove binding  $\alpha$ -helical peptide Ac-(Leu-Ala-Arg-Leu)<sub>3</sub>-NH-linker, intercalators ethidium bromide, YO-1, and daunomycin, and the bisintercalator YOYO-1. Distinct and characteristic changes within the mechanical response of DNA up to forces of 100 pN were identified and attributed to the corresponding binding mechanisms.

## MATERIALS AND METHODS

Our single-beam optical-tweezers instrumentation was described recently (Sischka et al., 2003). Briefly, an infrared laser (1064 nm) combined with a commercial inverse microscope achieves maximum trapping forces of 150 pN at a laser power output up to 900 mW. The stability of the optical-tweezers system is based on dedicated optical and flow-system components allowing calibrated and precise force-extension measurements with a force resolution of 0.4 pN at 600 mW during a broad variety of experiments.

For all experiments we took streptavidin-coated polystyrene microspheres (Spherotech, Libertyville, IL) with a diameter of 3.18  $\mu\text{m}$ , which we used in a diluted suspension of  $5 \times 10^{-4}$  % w/v.  $\lambda$ -DNA was biochemically modified (Sischka et al., 2003) to ensure tethering to the beads at the beginning of each force measurement.

Beads,  $\lambda$ -DNA, and binding ligands were dissolved in 10 mM Tris buffer (Sigma, Traufkirchen, Germany) (pH 8.0) containing 150 mM NaCl (Sigma). The concentration of  $\lambda$ -DNA was 15 pM whereas the binding ligands distamycin-A (Sigma), Ac-(Leu-Ala-Arg-Leu)<sub>3</sub>-NH-linker, ethidium bromide (Merck, Darmstadt, Germany), YO-1 (Molecular Probes, Eugene, OR), daunomycin (Sigma), and YOYO-1 (Molecular Probes) were used at a total concentration of 1  $\mu\text{M}$ , respectively. All experiments were performed at 20°C.

## RESULTS AND DISCUSSION

In Fig. 1, the mechanical response to an external force of free  $\lambda$ -DNA and  $\lambda$ -DNA complexed with distamycin-A (minor groove binder), the  $\alpha$ -helical peptide Ac-(Leu-Ala-Arg-Leu)<sub>3</sub>-NH-linker (major groove binder), ethidium bromide, YO-1, daunomycin (intercalators), and YOYO-1 (bisintercalator) are presented. During these force measurements,

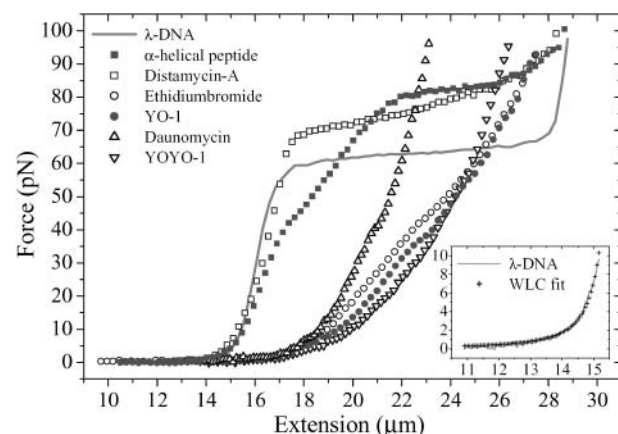


FIGURE 1 Single  $\lambda$ -phage DNA molecule and  $\lambda$ -DNA molecule complexed with minor groove binder (distamycin-A), major groove binder ( $\alpha$ -helical peptide Ac-(Leu-Ala-Arg-Leu)<sub>3</sub>-NH-linker), intercalators (daunomycin, YO-1, ethidium bromide), and bisintercalator (YOYO-1), respectively, exhibit different elasticity curves indicating individual mechanical properties (force fingerprints). Total concentration of each binding ligand was 1  $\mu\text{M}$ , and stretching velocity was 100 nm/s. (Inset) Worm-like-chain model fit on a free  $\lambda$ -DNA in the low-force regime up to 10 pN.

a trap stiffness of 88 pN/ $\mu\text{m}$  combined with a molecular loading rate of 8.8 pN/s was established. Molecular extensions were converted from piezo stage movements using the given trap stiffness and the actual measured forces. To quantify the elastic properties of all measured curves in the medium- and low-force regime, we determined the molecule length at a constant external force of 40 pN as well as the contour and persistence length with the extended worm-like chain model (WLC) (Marko and Siggia, 1995; Bouchiat et al., 1999) in the lower force regime with an upper force limit of 10 pN (Table 1).

$$F = \frac{k_B T}{\xi} \left( \frac{1}{4} \frac{1}{(1 - x/L_0)^2} - \frac{1}{4} + \frac{x}{L_0} + \sum_{i=2}^{i=7} a_i \left( \frac{x}{L_0} \right)^i \right). \quad (1)$$

$F$  denotes the applied force,  $\xi$  the persistence length,  $x$  the end-to-end distance,  $L_0$  the DNA contour length, and  $a_i$  numerical coefficients (Bouchiat et al., 1999), respectively.

In the following, we discuss the experimental findings of the measured elasticity curves of Fig. 1.

## Free dsDNA

The elastic response of a single  $\lambda$ -DNA molecule under an external force shows a distinct plateau, which was first attributed to a structural change from the dsDNA B-form to the overstretched S-form (Cluzel et al., 1996). Based on data obtained by experiments with different ionic strength, temperature, and pH conditions, Wenner et al. (2002) proposed a model where the overstretching plateau was attributed to

**TABLE 1 Molecular parameters for DNA-ligand complexes**

Complex	Binding mode	Molecule length			
		at 40 pN	WLC contour length	WLC persistence length	Oversretching transition
Free dsDNA	—	16.4 $\mu\text{m}$	16.0 $\mu\text{m}$	40.0 nm	62–65 pN at 18–27 $\mu\text{m}$
Distamycin-A	Minor groove	16.7 $\mu\text{m}$	16.3 $\mu\text{m}$	26.7 nm	70–85 pN at 18–27 $\mu\text{m}$
$\alpha$ -Helical peptide	Major groove	17.1 $\mu\text{m}$	16.5 $\mu\text{m}$	29.4 nm	80–85 pN at 22–27 $\mu\text{m}$ ; crossover at 17–22 $\mu\text{m}$
Ethidium bromide	Intercalating	22.5 $\mu\text{m}$	20.4 $\mu\text{m}$	20.7 nm	No transition
YO-1	Intercalating	23.2 $\mu\text{m}$	19.8 $\mu\text{m}$	29.2 nm	No transition
Daunomycin	Intercalating	20.9 $\mu\text{m}$	19.8 $\mu\text{m}$	28.1 nm	No transition
YOYO-1	Bisintercalating	23.5 $\mu\text{m}$	21.8 $\mu\text{m}$	11.8 nm	No transition

Molecular parameters extracted from worm-like-chain model fit of experimental data of free double-stranded  $\lambda$ -DNA and dsDNA complexed with distamycin-A,  $\alpha$ -helical peptide Ac-(Leu-Ala-Arg-Leu)<sub>3</sub>-NH-linker, ethidium bromide, YO-1, daunomycin, and YOYO-1. The concentration of each binding ligand was set to 1  $\mu\text{M}$ , respectively.

a force-induced melting process where at the end of the oversretching process short helical domains of the DNA hold large melted strands together (Williams et al., 2001, 2002; Wenner et al., 2002). In the following we term this plateau “oversretching transition”. Further elongation results in a strongly increasing elastic response corresponding to a nonequilibrium melting process (Rief et al., 1999).

In our experiments we observed the oversretching transition at 64 pN up to an extension of 28  $\mu\text{m}$  (170% of dsDNA contour length), which is in good agreement with the results of other groups under similar conditions such as temperature, ionic strength, and pH value (Cluzel et al., 1996; Williams et al., 2001, 2002). The extended worm-like chain model yielded a contour length of 16.0  $\mu\text{m}$  and a persistence length of 40 nm (Table 1) consistent with previous studies (Husale et al., 2002; Wenner et al., 2002). On the basis of the molecular length at a force of 40 pN, we found a value of 16.4  $\mu\text{m}$ , resulting in a  $\lambda$ -DNA (48,502 basepairs) basepair distance of 0.338 nm/basepair, in excellent agreement with previous studies (Husale et al., 2002; Tessmer et al., 2003).

### Minor groove binders

The minor groove binder distamycin-A has only a small effect on the molecular length of the  $\lambda$ -DNA; at an extension force of 40 pN we observe a slightly increased value of 16.7  $\mu\text{m}$  and a WLC contour length of 16.3  $\mu\text{m}$ . In contrast to the results for the free dsDNA, the oversretching transition is shifted to higher force values (from 64 pN to 70–85 pN), and a drastic change in the persistence length from 40.0 to 26.7 nm can be observed. Noncovalent binding of distamycin-A to the minor groove of dsDNA is characterized by a combination of electrostatic, van der Waals, and bifurcated hydrogen bondings with a strong preference for AT-rich regions (Coll et al., 1987), which stabilize the double strands and resist the force-induced melting. AFM force spectroscopy studies with the minor groove binder netropsin and  $\lambda$ -DNA exhibit a comparable increase in the oversretching transition (Krautbauer et al., 2002a). Due to the distamycin-

A concentration of 1  $\mu\text{M}$  in our experiments a 1:1 binding motif is expected to be dominant with a high binding constant of  $10^7$ – $10^8 \text{ M}^{-1}$  and a preference of binding to AT-rich regions (Pelton and Wemmer, 1989; Bielawski et al., 2001). Previous experiments with poly(dG-dC) ds-DNA and distamycin-A resulted in a slight lowering of the plateau value of the oversretching transition (Eckel et al., 2003). This phenomenon in combination with the observation of a distinct decreased binding affinity for GC-rich regions ( $K_{\text{association}} = 2 \times 10^5 \text{ M}^{-1}$ ; Bielawski et al., 2001) is indicative for different binding modes for AT and GC.

Solid-state NMR studies show that distamycin-A in the 1:1 motif effects a significant narrowing of the minor groove from 9.4 to 7.0 Å (Olsen et al., 2003). We observe a decreased persistence length, corresponding to an increased bending flexibility. For netropsin, where structural data result in a widening of the minor groove, an increased persistence length is described (Tessmer et al., 2003). This is an indication for a direct dependence of the persistence length of dsDNA complexed with minor groove binder and structural changes of the groove.

### Major groove binders

The elastic response curve of  $\lambda$ -DNA complexed with the  $\alpha$ -helical peptide Ac-(Leu-Ala-Arg-Leu)<sub>3</sub>-NH-linker, which binds in the major groove (Niidome et al., 1996; Eckel et al., 2003), is characterized by an intersected transition (between 17 and 22  $\mu\text{m}$ ) between the elastic stretching of B-DNA at low forces and the less pronounced oversretching transition (22–27  $\mu\text{m}$ ) at 80–85 pN. Similar to distamycin-A, the force extension curve exhibits a merging of the oversretching transition into the nonequilibrium melting transition at extensions beyond 28  $\mu\text{m}$ . The molecule length at 40 pN and the WLC contour length is slightly increased to 17.1 and 16.5  $\mu\text{m}$ , respectively, and a reduced persistence length of 29.4 nm was calculated. This observation can be associated with an electrostatic binding along with a compensation of the negatively charged DNA backbone by the guanidino groups of the peptide (Niidome et al., 1996), which neu-

tralizes the intrinsic charge and extends the flexibility of the complexed dsDNA.

Recent investigations (Eckel et al., 2003) did not reveal the intersected transition within the complex of Ac-(Leu-Ala-Arg-Leu)<sub>3</sub>-NH-linker and poly(dG-dC) dsDNA, so we implicate our results to a different binding behavior of Ac-(Leu-Ala-Arg-Leu)<sub>3</sub>-NH-linker between GC-rich and AT-rich regions.

Recently,  $\lambda$ -DNA complexed with SYBR-Green I (Molecular Probes) has been investigated using a dual-beam optical-tweezers setup (Husale et al., 2002). Because SYBR-Green I is a major groove binder, the elasticity curve exhibits similarities to our results, such as a decreased persistence length, a faint and tilted overstretching plateau around 1.5 fractional extensions (f.e.) of B-DNA, and a characteristic intersected transition in the range between 1.1 and 1.35 f.e. (18–22  $\mu\text{m}$ ).

## Intercalators

The effect of three different DNA monointercalating agents ethidium bromide, YO-1, and daunomycin, and the bisintercalating agent YOYO-1 was investigated. For all intercalators it was found that the plateau attributed to the overstretching transition completely disappeared, the molecule length at 40 pN and the WLC contour length increased, and the persistence length was considerably reduced compared to free dsDNA (see Table 1). In contrast to groove binding, intercalation is additionally stabilized by ionic interaction between a positively charged group (a protonated imino group in ethidium bromide and YO-1, and a protonated amino group in daunomycin and YO-1) of the intercalator and the negatively charged phosphate DNA backbone. This unspecific electrostatic binding of the intercalators reduces the net charge and extends the flexibility of the DNA, which explains the decrease of the persistence length.

### Ethidium bromide and YO-1

The binding of ethidium bromide to dsDNA is structurally characterized by an increase of the basepair distance by 0.34 nm/per molecule (Coury et al., 1996). The contour length 20.4  $\mu\text{m}$  indicates that on average every fourth intercalation site has been occupied by an ethidium bromide molecule, a result that was also found by Husale et al. (2002). The corresponding persistence length is reduced to 20.7 nm, which is in excellent agreement with recent results (Tessmer et al., 2003; Husale et al., 2002). The intercalator YO-1, which has been investigated by AFM techniques (Eckel et al., 2003), is characterized by a smaller reduction of the persistence length to 29.2 nm, whereas the contour length (19.8  $\mu\text{m}$ ) is almost equal to that of ethidium bromide. Force-extension curves of dsDNA complexed with ethidium bromide or YO-1 exhibit no hysteresis effects for stretching and relaxing velocities between 100 and 8000 nm/s.

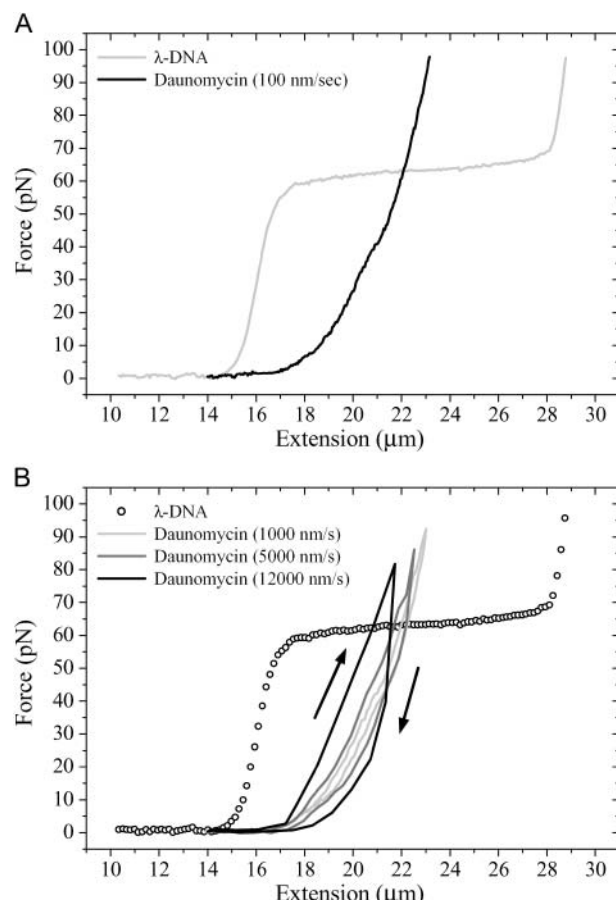


**FIGURE 2** (A) Force-extension curves of a single  $\lambda$ -phage DNA molecule and in the presence of DNA intercalator daunomycin (1  $\mu\text{M}$ ) obtained at a stretching velocity of 100 nm/s. (B) At higher velocities, daunomycin intercalated DNA reveals distinct hysteresis effects during extension relaxation cycles.

### Daunomycin

$\lambda$ -DNA complexed with daunomycin (also known as cerubidine or daunorubicin in medical chemotherapy; Fig. 2 A), recently investigated with AFM force spectroscopy (Eckel et al., 2003), exhibits an increase of the contour length to 19.8  $\mu\text{m}$  and a decrease of the persistence length to 28.1 nm. Daunomycin, like other anthracyclines, is stabilized during intercalation by its electron-deficient anthraquinone part, with hydrogen bonds and electrostatic interaction additionally enhancing the binding stability between the minor groove of the dsDNA and the amino sugar part of daunomycin (Wang et al., 1987). This explains the large resistance of daunomycin complexed dsDNA against an external force, indicated by a steep rise within the force-extension curve that yields a molecular length of 20.9  $\mu\text{m}$  at 40 pN.

During extension/relaxation at cycle velocities beyond 1000 nm/s, we identified distinct hysteresis effects (Fig. 2 B). To our knowledge this is the first observation of non-

equilibrium processes for monointercalating substances. This hysteresis finding is highly reproducible and can therefore not be attributed to melting hysteresis effects as reported (Krautbauer et al., 2002b).

### YOYO-1

Similar to daunomycin, dsDNA complexed with the bisintercalating agent YOYO-1 exhibits distinct force hysteresis effects and is characterized by an increase of the contour length to 21.8  $\mu\text{m}$  and a strong decrease of the persistence length to 11.8 nm (Fig. 3 A). These results have been obtained during stretching experiments down to velocities of 10 nm/s and at YOYO-1 concentrations of 1  $\mu\text{M}$ . Similar to other intercalators the increase of the contour length can be explained by intercalating between adjacent basepairs. However, YOYO-1 stacks two aromatic ring systems (connected by an aliphatic diamine “backbone”) into two intercalation sites causing a “clamp-like” binding motif. We relate the strong decrease of the persistence length to two protonated amino and two protonated imino groups at one YOYO-1 molecule that reduce the intrinsic charge of the DNA backbone and strongly increase its flexibility.

The force hysteresis was found to depend on the cycle velocity and the applied maximum force (Fig. 3, B and C) and is consistent with results of Bennink et al. (1999). All force hysteresis effects were found to be highly reproducible during stretching and relaxation and can, therefore, not be attributed to a melting hysteresis effect. The observed hysteresis is accompanied by a shift of the elasticity curve to smaller extension values with increased experimental velocities.

### Retention force decay and hysteresis effects of daunomycin and YOYO-1

To investigate the hysteresis phenomenon in more detail we carried out the following experiment: while monitoring the force, a  $\lambda$ -DNA molecule in the presence of 1  $\mu\text{M}$  daunomycin or YOYO-1 was rapidly overstretched (12,000 nm/s, 5000 nm/s, and 2000 nm/s) to different maximum forces. After stopping the extension, we observed an exponential decay of the retention force to a lower stable value (Fig. 4 A). During the force decay, the trapped bead is retreated toward the center of the optical trap, causing an elongation of the stretched DNA given by the trap stiffness divided by the force difference. In these experiments we observed elongations of <300 nm.

The relative force decays increase with the stretching velocities and are independent from the maximum retention force (Fig. 4 B). For dsDNA complexed with YOYO-1 the time constants derived from exponential fits show an almost linear dependence from the maximum retention forces and were independent from stretching velocities (Fig. 4 C). Values from 0.26 s for a maximal retention force of 10 pN to

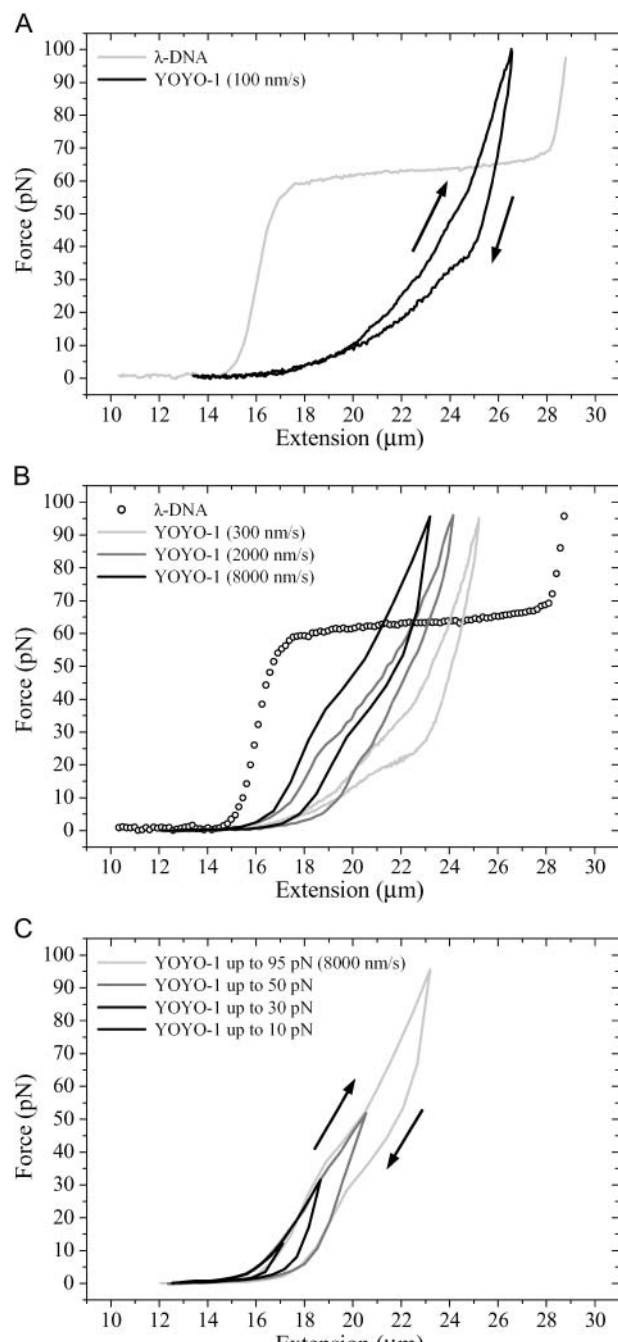


**FIGURE 3** (A) YOYO-1 (1  $\mu\text{M}$ ) bisintercalated  $\lambda$ -phage DNA molecule reveals hysteresis effects during extension/relaxation loop even at low stretching and relaxing velocities. (B) At increased velocities, elasticity curves are shifted to lower extension values. (C) Hysteresis effects at different maximum forces during stretching/relaxation loops of YOYO-1 bisintercalated  $\lambda$ -phage DNA.

1.21 s for 83 pN were observed. For daunomycin the linear dependence was only found for retention forces <45 pN, the values range from 0.13 s at 10 pN to 0.68 s at 45 pN. For higher forces the decay times are constant, which indicates changes in the molecular extension process.

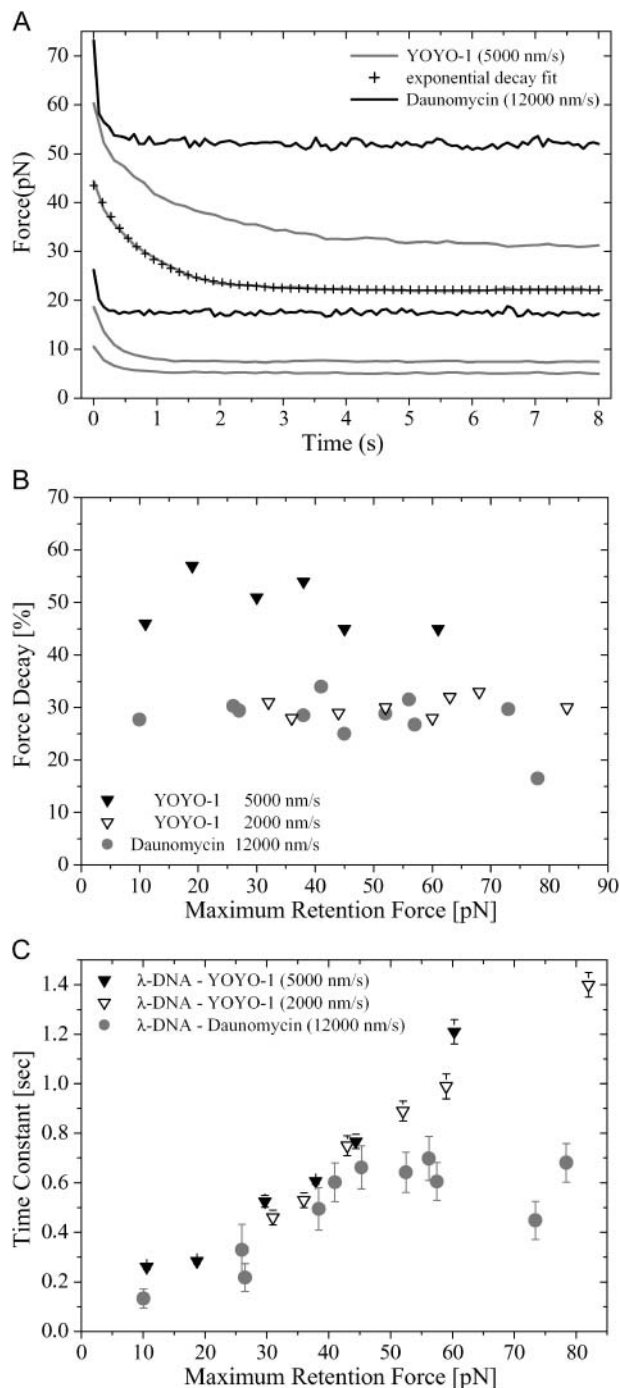


FIGURE 4 (A) Fast stretching of YOYO-1 bisintercalated and daunomycin intercalated  $\lambda$ -phage DNA with a velocity of 5000 nm/s and 12,000 nm/s, respectively, to a maximum force and immediate stopping unveils an exponential decay of the retention force with time. (B) Percentage of exponential decay of the retention force as a function of maximum retention force for YOYO-1 and daunomycin. (C) Relaxation time as a function of maximum retention force for YOYO-1 and daunomycin. Due to high-extension velocity for daunomycin, short-time data acquisition implicates less data averaging, which effects more statistical noise and larger error bars.

The observed hysteresis and retention force decays suggest that the dsDNA strands complexed with these two intercalators are not in equilibrium at the given pulling speed. Rief et al. introduce a model based on a coupled two-level system for biopolymer extensibility, where segments of the molecule undergo conformational changes (Rief et al., 1998). Under an external force the length of each segment changes based on thermodynamics. With this model the hysteresis effects and the retention force can be explained. For YOYO-1 the process of segment elongation is remarkably slow. Pulling velocities of 10 nm/s with a molecular extension of a few microns result in a timescale of minutes, whereas for daunomycin the transition from equilibrium to the nonequilibrium state is in the timescale of seconds.

This elongation of the segments can in principle be attributed to force-induced changes in the molecular structure or to intercalation of additional molecules into the stretched DNA. Because of the high association constant of YOYO-1 ( $10^{12}$  M<sup>-1</sup>; Larsson et al., 1994) and even for the lower constant of daunomycin ( $10^5$  M<sup>-1</sup>; Coury et al., 1996), both intercalators may associate to dsDNA by electrostatic interaction in a fast (for our experiments, undetectable) timescale, but the intercalation itself (especially those of both aromatic ring systems of YOYO-1 into dsDNA) takes place on a much slower timescale, as can be inferred from the calculated time constants.

## CONCLUSIONS

Mechanical properties of  $\lambda$ -DNA (dsDNA) complexed with different binding ligands were analyzed in single-molecule optical-tweezers experiments. The differences between binding modes, such as minor groove binding, major groove binding, and (bis)intercalation could be distinguished by analyzing the mechanical response of a single dsDNA molecule to an applied external force. Different binding properties of the minor and major groove binder for AT- and GC-rich regions could be identified upon comparing our measurement with recently published AFM results. The persistence length of DNA complexed with minor groove binders might be related to changes in the width of the minor groove: narrowing results in a decreased persistence length, a topic to be investigated in more detail in the future.

Force hysteresis effects during stretching/relaxation cycles and retention force decays were found for the bisintercalator YOYO-1 and for the intercalator daunomycin, which we relate to a slow force-induced elongation of DNA segments. This can be attributed to a structural change or the intercalation of additional molecules to the stretched dsDNA. The observation that the other binding ligands investigated (i.e., distamycin-A, the  $\alpha$ -helical peptide Ac-(Leu-Ala-Arg-Leu)<sub>3</sub>-NH-linker, ethidium bromide, and YO-1) lack force hysteresis still remains to be explained. It could be, for these ligands, that the applied force induces no additional time-

dependent change in molecular conformation, but it is also possible that the said effect takes place on a much faster timescale than our experiment (milliseconds, or even faster). In further experiments with very high stretching velocities this question will be addressed. Experiments like our retention force-decay measurements with the force-clamp technique should be able to give quantitative data to describe this fundamental slow structural transition process.

For daunomycin we found in the decay time analysis an unexpected transition from a linear to a constant dependence on the maximal retention force at 45 pN. This gives an interesting hint to a change in the elongation process from a low- to a high-force regime, which will be addressed in further experiments.

We thank Martin Hegner and Wilfried Grange for support during the setup of the optical-tweezers system and Peter Reimann for helpful discussions.

We gratefully acknowledge funding from the collaborative research project SFB 613 from the Deutsche Forschungsgemeinschaft (DFG).

## REFERENCES

- Anselmetti, D., J. Fritz, B. Smith, and X. Fernandez-Busquets. 2000. Single molecule DNA biophysics with atomic force microscopy. *Single Mol.* 1:17–23.
- Ashkin, A. 1970. Acceleration and trapping of particles by radiation pressure. *Phys. Rev. Lett.* 24:156–159.
- Ashkin, A., J. M. Dziedzic, J. E. Bjorkholm, and S. Chu. 1986. Observation of a single-beam gradient force optical trap for dielectric particles. *Opt. Lett.* 11:288–290.
- Ashkin, A. 1997. Optical trapping and manipulating of neutral particles using lasers. *Proc. Natl. Acad. Sci. USA.* 94:4853–4860.
- Bennink, M. J., O. D. Schärer, R. Kanaar, K. Sakata-Sogawa, J. M. Schins, J. S. Kanger, B. G. de Groot, and J. Greve. 1999. Single-molecule manipulation of double-stranded DNA using optical tweezers: interaction studies of DNA with RecA and YOYO-1. *Cytometry.* 36:200–208.
- Bielawski, K., S. Wolczynski, and A. Bielawska. 2001. DNA-binding properties and cytotoxicity of extended aromatic bisamidines in breast cancer mcf-7 cells. *Pol. J. Pharmacol.* 53:143–147.
- Binnig, G., C. F. Quate, and C. Gerber. 1986. Atomic force microscope. *Phys. Rev. Lett.* 56:930–933.
- Bouchiat, C., M. D. Wang, J. F. Allemand, T. Strick, S. M. Block, and V. Croquette. 1999. Estimating the persistence length of a worm-like chain molecule from force-extension measurements. *Biophys. J.* 76:409–413.
- Clausen-Schaumann, H., M. Rief, C. Tolksdorf, and H. E. Gaub. 2000. Mechanical stability of single DNA molecules. *Biophys. J.* 78:1997–2007.
- Cluzel, P., A. Lebrun, C. Heller, R. Lavery, J. L. Viovy, D. Chatenay, and F. Caron. 1996. DNA: an extensible molecule. *Science.* 271:792–794.
- Coll, M., C. A. Frederick, A. H.-J. Wang, and A. Rich. 1987. A bifurcated hydrogen-bonded conformation in the d(AT) base pairs of the DNA dodecamer d(CGCAAATTCGCG) and its complex with distamycin. *Proc. Natl. Acad. Sci. USA.* 84:8385–8389.
- Coste, F., J. M. Malinge, L. Serre, W. Shephard, M. Roth, M. Leng, and C. Zelwer. 1999. Crystal structure of a double-stranded DNA containing a cisplatin interstrand cross-link at 1.63 Å resolution: hydration at the platinated site. *Nucleic Acids Res.* 27:1837–1846.
- Coury, J. E., L. McFail-Isom, L. D. Williams, and L. A. Bottomley. 1996. A novel assay for drug-DNA binding mode, affinity, and exclusion number: scanning force microscopy. *Proc. Natl. Acad. Sci. USA.* 93:12283–12286.
- Eckel, R., R. Ros, A. Ros, S. D. Wilking, N. Sewald, and D. Anselmetti. 2003. Identification of binding mechanisms in single molecule-DNA complexes. *Biophys. J.* 85:1968–1973.
- Fitzgerald, D. J., and J. N. Anderson. 1999. Selective nucleosome disruption by drugs that bind in the minor groove of DNA. *J. Biol. Chem.* 274:27128–27138.
- Gelasco, A., and S. J. Lippard. 1998. NMR solution structure of a DNA dodecamer duplex containing a cis-diamminéplatinum(II) d(GpG) intrastrand cross-link, the major adduct of the anticancer drug cisplatin. *Biochemistry.* 37:9230–9239.
- Graves, D. E., and L. M. Velea. 2000. Intercalative Binding of Small Molecules to Nucleic Acids. *Curr. Org. Chem.* 4:915–929.
- Hurley, L. H. 2002. DNA and its associated processes as targets for cancer therapy. *Nat. Rev. Cancer.* 2:188–200.
- Husale, S., W. Grange, and M. Hegner. 2002. DNA mechanics affected by small DNA interacting ligands. *Single Mol.* 3:91–96.
- Krautbauer, R., H. Clausen-Schaumann, and H. E. Gaub. 2000. Cisplatin changes the mechanics of single DNA molecules. *Angew. Chem. Int. Ed.* 39:3912–3915.
- Krautbauer, R., S. Fischerländer, S. Allen, and H. E. Gaub. 2002a. Mechanical fingerprints of DNA drug complexes. *Single Mol.* 3:97–103.
- Krautbauer, R., L. H. Pope, T. E. Schrader, S. Allen, and H. E. Gaub. 2002b. Discriminating small molecule DNA binding modes by single molecule force spectroscopy. *FEBS Lett.* 510:154–158.
- Krishnamoorthy, G., G. Duportail, and Y. Mely. 2002. Structure and dynamics of condensed DNA probed by 1,1'-(4,4,8,8-tetramethyl-4,8-diazaundecamethylene)bis[4-[[3-methylbenz-1,3-oxazol-2-yl]methylene]-1,4-dihydroquinolinium] tetraiodide fluorescence. *Biochemistry.* 41:15277–15287.
- Larsson, A., C. Carlsson, M. Jonsson, and B. Albinsson. 1994. Characterization of the binding of the fluorescent dyes YO and YOYO to DNA by polarized light spectroscopy. *J. Am. Chem. Soc.* 116:8459–8465.
- Lipscomb, L. A., F. X. Zhou, S. R. Presnell, R. J. Woo, M. E. Peek, R. R. Plaskon, and L. D. Williams. 1996. Structure of a DNA-porphyrin complex. *Biochemistry.* 35:2818–2823.
- Marko, J. F., and E. D. Siggia. 1995. Stretching DNA. *Macromolecules.* 28:8759–8770.
- McMurray, C., E. W. Small, and K. E. van Holde. 1991. Binding of ethidium to the nucleosome core particle. 2. Internal and external binding modes. *Biochemistry.* 30:5644–5652.
- Niidome, T., N. Ohmori, A. Ichinose, A. Wada, H. Mihara, T. Hirayama, and H. Aoyagi. 1996. Binding of cationic alpha-helical peptides to plasmid DNA and their gene-transfer abilities into cells. *J. Biol. Chem.* 272:15307–15312.
- Olsen, G. L., E. A. Louie, G. P. Drobny, and S. Th. Sigurdsson. 2003. Determination of DNA minor groove width in distamycin-DNA complexes by solid-state NMR. *Nucleic Acids Res.* 31:5084–5089.
- Pelton, J. G., and D. E. Wemmer. 1989. Structure characterization of a 2:1 distamycin A d(CGCAAATTGGC) complex by two-dimensional NMR. *Proc. Natl. Acad. Sci. USA.* 86:5723–5727.
- Reddy, B. S. P., S. K. Sharma, and J. W. Lown. 2001. Recent developments in sequence selective minor groove DNA effectors. *Curr. Med. Chem.* 8:475–508.
- Reha, D., M. Kabelac, F. Ryjacek, J. Sponer, J. E. Sponer, M. Elstner, S. Suhai, and P. Hobza. 2002. Intercalators. 1. Nature of stacking interactions between intercalators (ethidium, daunomycin, ellipticine, and 4',6-diaminide-2-phenylindole) and DNA base pairs. Ab initio quantum chemical, density functional theory, and empirical potential study. *J. Am. Chem. Soc.* 124:3366–3376.
- Rief, M., J. M. Fernandez, and H. E. Gaub. 1998. Elastically coupled two-level systems as a model for biopolymer extensibility. *Phys. Rev. Lett.* 81:4764–4767.
- Rief, M., H. Clausen-Schauman, and H. E. Gaub. 1999. Sequence-dependent mechanics of single DNA molecules. *Nat. Struct. Biol.* 6:346–349.

- Sischka, A., R. Eckel, K. Tönsing, R. Ros, and D. Anselmetti. 2003. Compact, microscope based optical tweezers system for molecular manipulation. *Rev. Sci. Instrum.* 74:4827–4831.
- Smith, S. B., Y. Cui, and C. Bustamante. 1996. Overstretching B-DNA: the elastic response of individual double-stranded and single-stranded DNA molecules. *Science*. 271:795–799.
- Svoboda, K., and S. M. Block. 1994. Biological applications of optical forces. *Annu. Rev. Biophys. Biomol. Struct.* 23:247–285.
- Tessmer, I., C. G. Baumann, G. M. Skinner, J. E. Molloy, J. G. Hoggett, S. J. B. Tendler, and S. Allen. 2003. Mode of drug binding to DNA determined by optical tweezers force spectroscopy. *J. Mod. Optics*. 50: 1627–1636.
- Wang, A. H., G. Ughetto, G. J. Quigley, and A. Rich. 1987. Interactions between an anthracycline antibiotic and DNA: molecular structure of daunomycin complexed to d(CpGpTpApCpG) at 1.2-A resolution. *Biochemistry*. 26:1152–1163.
- Wenner, J. R., M. C. Williams, I. Rouzina, and V. A. Bloomfield. 2002. Salt dependence of the elasticity and overstretching transition of single DNA molecules. *Biophys. J.* 82:3160–3169.
- Williams, M. C., J. R. Wenner, I. Rouzina, and V. A. Bloomfield. 2001. Effect of pH on the overstretching transition of double-stranded DNA: evidence for force-induced DNA melting. *Biophys. J.* 80:874–881.
- Williams, M. C., I. Rouzina, and V. A. Bloomfield. 2002. Thermodynamics of DNA interactions from single molecule stretching experiments. *Acc. Chem. Res.* 35:159–166.
- Wuite, G. J. L., R. J. Davenport, A. Rappaport, and C. Bustamante. 2000. An integrated laser trap/flow control video microscope for the study of single biomolecules. *Biophys. J.* 79:1155–1167.
- Zimmer, Ch., and U. Wähnert. 1986. Nonintercalating DNA-binding ligands: specificity of the interaction and their use as tools in biophysical, biochemical and biological investigations of the genetic material. *Prog. Biophys. Mol. Biol.* 47:31–112.

# **3 SMFS Affinity Ranking of Native and Synthetic Point-Mutated Transcription Factors**

## **3.1 Introduction**

Molecular recognition reactions like the interaction between DNA and effector proteins play a major role in many biological processes. The term molecular recognition, as opposed to the mostly sequence-unspecific interactions discussed in chapter 2, here is understood as the sequence-specific interaction of a receptor (e.g. DNA) and a ligand (e.g. a transcription factor). The forces mediating this sequence recognition, however, are very much the same as for unspecific interactions, namely, electrostatic, hydrophobic, ion-dipole and dipole-dipole interactions and hydrogen bonds: The high selectivity for certain binding sequences results solely from their combination and complementarity. In addition to thermodynamic and kinetic parameters, the complex interplay of these forces is of special importance to elucidate the relation between structure and function. In this context, SMFS can be considered an efficacious technique with single molecule sensitivity which is complementary to established integral methods. Techniques like, e.g., microcalorimetry or surface plasmon resonance yield valuable information about binding kinetics and thermodynamics, but these data are necessarily mean values, averaged over a whole ensemble of molecules. SMFS facilitates the measurement of mechanical behavior at the single molecule level and gives immediate access to the dynamics of molecular recognition.

The following work concentrates on the molecular recognition of regulatory DNA sequences from the (*E.coli*) genome by the transcription factor PhoB. The binding of peptide fragments (native and point mutants) from the DNA recognition helix of PhoB and the native protein itself to the PhoB binding sequence of *E.coli* DNA was studied

by SMFS. Two questions should be answered by the single molecule experiments:

- What is the minimal sequence to ensure specific binding to the target sequence, and what are the contributions of the protein environment to enhance binding specificity and kinetics?
- What is the contribution of single amino acids from the binding sequence to the specificity of the interaction, and how do point mutations affect the binding rates?

This introductory section will address the general role of molecular recognition in transcription regulation (chapter 3.1.1) before introducing in more detail the actual system which is of concern here, namely the transcription factor PhoB (chapter 3.1.2). Chapter 3.1.3 will establish the relation between the forces obtained in intermolecular SMFS experiments and important kinetic and structural data which characterize the molecular recognition process. These results will be derived within the framework of the standard theory (cf. chapter 5 for a critical evaluation).

### 3.1.1 Molecular Recognition in Transcription Regulation

One of the most remarkable characteristics of life is the ability of living organisms to respond and adapt to changing environmental conditions. Even simple prokaryotes like *E. coli* can vary the rate of synthesis of many proteins by a factor of  $10^3$  according to the circumstances. In higher multicellular organisms, the genome of highly specialized and diversified cells is the same; diversification into different cell types is mainly due to different levels of transcription for certain proteins, triggered by the secretion of hormones and growth factors. This adaptability to external signals is a matter of gene expression control. (The term gene expression subsumes the transcription of a gene into mRNA, the mRNA processing (splicing etc.), and the translation of the mRNA information into a protein sequence at the ribosome.)

The principal and most important stage at which gene activity is controlled is transcription (this holds for prokaryotes and eukaryotes). In the case of prokaryotes, one can roughly distinguish between positive regulation, effected by activator proteins, and negative regulation, mediated by repressors. The target is the initiation of transcription, when RNA polymerase binds to specific promoter sequences on the DNA. The regulatory proteins bind to control sequences located a few base pairs upstream; the combination of control sites and structural genes to be transcribed is called an “operon”. A repressor can bind to the control site in a way that prevents the RNA polymerase from binding to the promoter, or bind to two different sites upstream, forming a DNA loop which also

prevents transcription from the DNA template. Activator proteins, on the other hand, may bend the DNA strand such that the promoter site becomes easily accessible for the RNA polymerase and enhance transcription in this way. (The situation in eukaryotes is different in some respects: several proteins usually interact and compile to influence transcription.) The specific binding of transcription factors to DNA control sequences

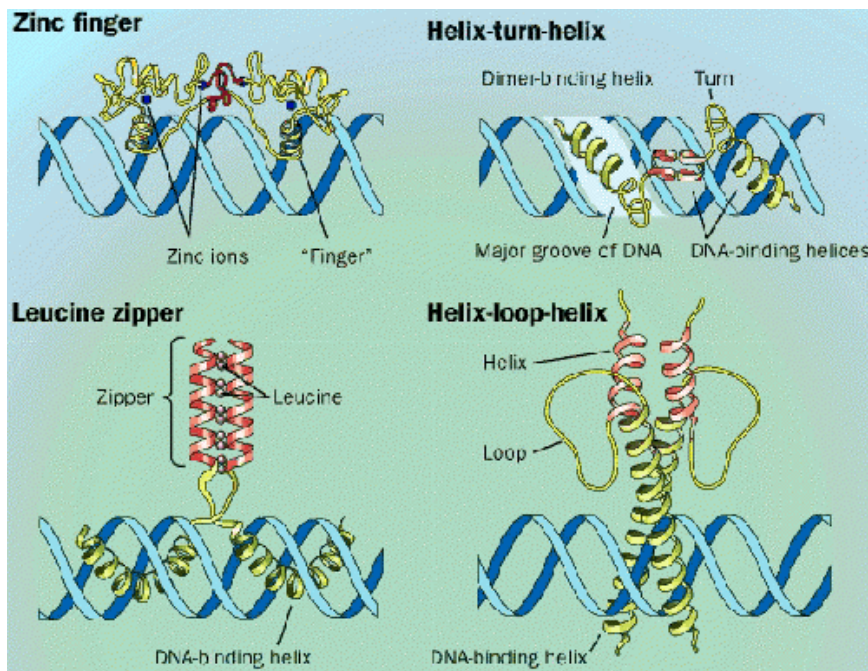


Figure 3.1: Different transcription factor binding motives

(typically 6-20 nucleotides long) is the crucial step in the regulation of gene expression. The interaction with the DNA strand takes place in the major groove, since here the interaction does not interfere with the base pairing: Hydrogen bonds are formed between donor and acceptor groups from the DNA and the regulator protein, and hydrophobic residues approximate under release of water. Many transcription factors bind their specific sequences via an  $\alpha$  helix interacting with the major groove; a special class of these proteins features a so-called *helix – turn – helix (HTH)* motive, where two helices are joined via a *turn* (7-9 amino acids of length). The first helix is the recognition helix, the second stabilizes the binding by mostly unspecific interactions. The DNA binding domain of the transcription factor PhoB (discussed in the following section) is an example of a *HTH* motive. Other, closely related structures which also feature a recognition helix are the zinc finger and leucine zipper motives encountered in eukaryotes (Fig. 3.1).

### 3.1.2 The Transcription Factor PhoB

Phosphorus is an important element in metabolism, being part of membrane lipids, nucleic acids and complex carbohydrates. Bacteria like *E. coli* can make use of any phosphorus source that occurs in nature. The genes coding for the proteins involved in phosphorus assimilation, like, e.g., alkaline phosphatase or the phosphate transporter Pst, are all controlled by a two-component regulatory system which consists of the membrane protein PhoR as the sensor and the transcription factor PhoB as the response regulator. Fig. 3.2 (a) shows the situation if the environmental phosphate concentration

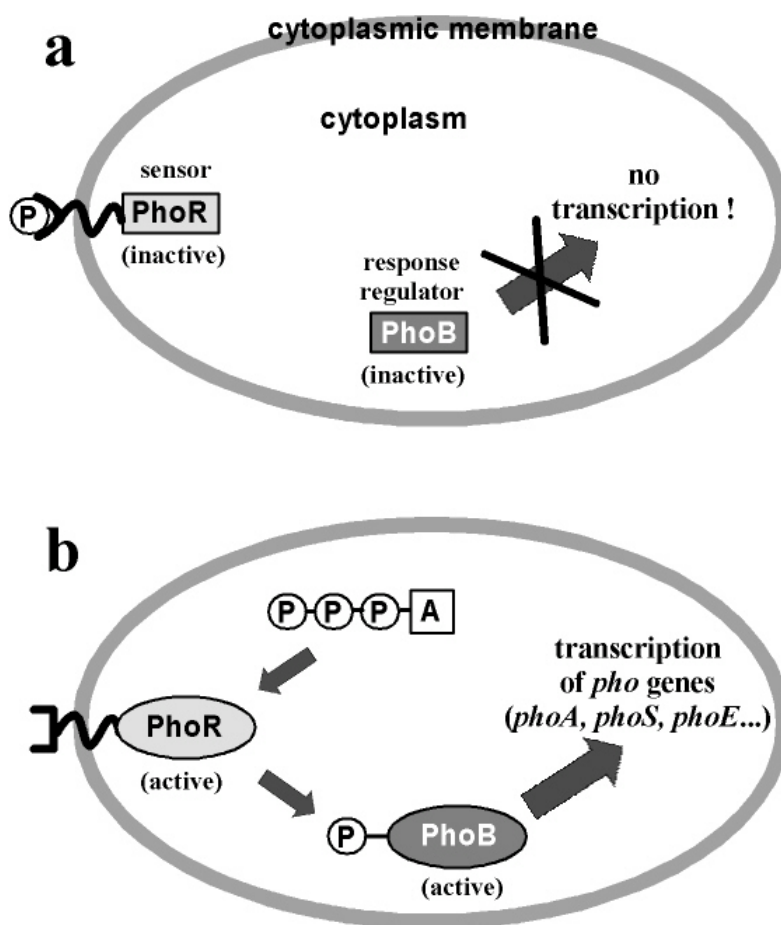


Figure 3.2: The PhoB/PhoR two-component regulatory system in (*E. coli*) (a) at high, (b) at low environmental phosphate concentration. (For details cf. text.)

is high: phosphate is bound to the periplasmic domain of the sensor protein PhoR, and PhoR is inactive. In response to low phosphate concentrations ( $< 4 \mu\text{mol l}^{-1}$ ) in the environment (Fig. 3.2 (b)) a phosphate ion dissociates from the PhoR periplasmic

domain. This causes a conformational change, activating a protein kinase transmitter domain in the cytosolic region of PhoR. The activated transmitter domain transfers an ATP  $\gamma$ -phosphate to a histidine in the transmitter domain. This phosphate is then transferred to an aspartic acid in the response regulator PhoB. Phosphorylated PhoB then activates, by interaction with the  $\sigma^{70}$  subunit of the RNA polymerase [66], the transcription of genes encoding proteins that help the cell to respond to low phosphate, including *phoA*, *phoS*, and *phoE* [67, 68, 69, 70]. If the phosphate concentration increases above the threshold value, PhoB is dephosphorylated by PhoR, and the binding affinity of PhoB to the *pho* box is lowered again.

PhoB (*E.coli*) is a 25 kDa protein consisting of 229 amino acids which belongs to the class of *winged helix – turn – helix (HTH)* proteins. It is composed of an N-terminal regulatory domain (124 amino acids) and a C-terminal DNA binding domain (99 amino acids). Both domains are joined via a linker of six amino acids. For both domains the crystal structure is known [70]. The DNA binding domain consists of seven  $\beta$ -sheets and three  $\alpha$ -helices in the order  $\beta^1\beta^2\beta^3\beta^4\alpha^1\beta^5\alpha^2\alpha^3\beta^6\beta^7$  [70]. The structure of the DNA binding domain is shown in Fig. 3.3. Deletion mutants consisting solely of the DNA binding domain are active.

The *HTH*-motif in PhoB consists of the DNA recognition helix  $\alpha^3$ , which binds to

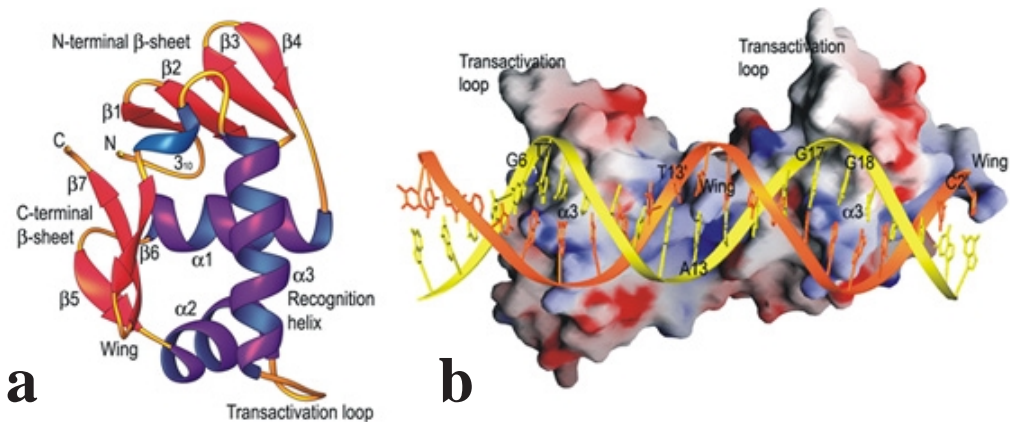


Figure 3.3: (a) DNA binding domain of the transcription factor PhoB from (*E.coli*) (b) Two PhoB DNA binding domains bound to DNA.

the DNA major groove, and the helix  $\alpha^2$ , which stabilizes the DNA-protein interaction, joined by a *loop* between  $\alpha^3$  and  $\alpha^2$ , which here replaces the *turn* commonly found in other proteins of the *HTH* class. This loop, also termed “transactivation loop”, is essential for the activation of transcription: He interacts with the  $\sigma^{70}$  subunit of the

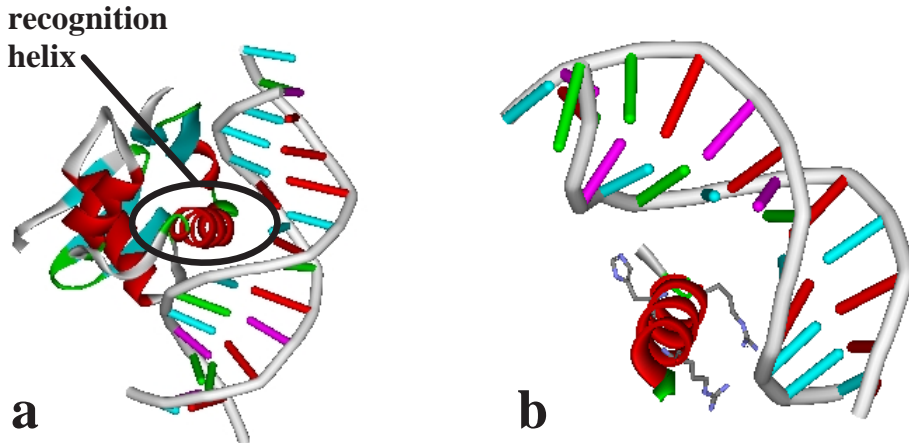


Figure 3.4: (a) PhoB DNA binding domain bound to DNA. The recognition helix  $\alpha^3$  from which the peptide fragments were taken is highlighted. (b) Indication of the three cationic amino acids in the recognition helix that were replaced by alanine in the alanine scan.

RNA polymerase. The specific recognition of the regulatory DNA sequence is mediated via van der Waals forces and hydrogen bonds between the hydrophilic amino acids like arginine, glutamine, serine, and tyrosine and the DNA base pairs. Positively charged residues like lysine and arginine stabilize the binding via unspecific electrostatic interactions with the negatively charged DNA backbone.

The *pho* boxes of the individual operons show slight variations, the consensus sequence being [66]: 5'-CTGT**CATA**(A/T)A(T/A)CTGT**CA**(C/T)-3' (the two binding sites for PhoB are highlighted). For the SMFS experiments reported in the following, the *pho* box of the *pst* operon promoter was used. Fig. 3.4 (a) shows the interaction of the PhoB DNA binding domain with DNA; the position of the recognition helix is indicated. In order to study the contributions of single amino acids to the binding, peptide fragments (20 amino acids of length) representing the recognition helix were synthesized. The following sequence represents the protein PhoB; the peptide fragment mimicking the  $\alpha^3$ -helix is highlighted:

```
MARRILVVEDEAPIREMVCVLEQNGFQPVEAEDYDSAVNQLNEPWPDLLLDW
MLPGGSGIQFIKHLKRESMTRDIPVVMLTARGEEDRVRGLETGADDYITKPFSP
KELVARIKAVMRRISPMAVEEVIEMQGLSLDPTSHRVMAGEEPELMPTEFKLLH
FFMTHPERVYSREQLLNHVGNTNVYVEDRTVDVHIRRLRKALEPGGHDRM
VQTVRGTYRFSTRF
```

An alanine scan with three amino acids in the helix was performed, i.e., three point

mutants were synthesized with one cationic residue each replaced by alanine. The positions of these residues in the crystal structure of the PhoB-DNA complex are indicated in Fig. 3.4 (b). The sequence of the point mutants is presented in publication IV.

### 3.1.3 Forces and Kinetics in SMFS: The Standard Theory

The primary data that are provided by intermolecular SMFS experiments on ligand-receptor systems are dissociation forces. The question how these forces relate to thermodynamic and kinetic data has long been (and still is) a matter of debate [71]. The former opinion that the rupture forces (or, more precisely, the most probable rupture forces) are a direct measure of bond strength has given way to the finding that the forces are distributed stochastically, and that the distribution varies with the retract velocity of the AFM tip. A breakthrough in SMFS theory was the seminal paper by Evans and Ritchie [12]. They were the first to formulate that the dissociation under an externally applied force corresponds to the thermally activated decay of a metastable state, which can be tackled by classical reaction rate theory [72, 73, 74, 75, 76].

Consider the formation of a bond between a ligand  $L$  and an appropriate receptor  $R$  (this simple formalism applies to the molecular recognition of DNA by peptides or proteins as well as to the interaction between a supramolecular host and guest, cf. chapter 4):



Here,  $[L]$ ,  $[R]$  and  $[L \cdot R]$  designate the concentrations of the free ligand, the free receptor and the complex between the ligand and receptor, respectively. The on-rate  $k_{on}^0$  (measured in  $l \text{ mol}^{-1} \text{s}^{-1}$ ) and off-rate  $k_{off}^0$  (measured in  $\text{s}^{-1}$ ) are the kinetic rates of the forward and backward reactions. The inverse of the off-rate  $\tau = (k_{off}^0)^{-1}$  is a measure for the mean life time of the bond.

When thermal equilibrium is reached ( $t \rightarrow \infty$ ), the forward and backward reactions proceed with equal velocity, and the ratio of reactants to products, the dissociation constant, is given by  $K_D = k_{off}^0/k_{on}^0$ . The relation between the standard free enthalpy (if the reaction is held at constant temperature and pressure, this is the appropriate state function) for the dissociation process and the dissociation constant is the well-known

$$\Delta G^0 = RT \ln K_D. \quad (3.2)$$

Fig. 3.5 (a) shows the free dissociation of a ligand-receptor complex.

The free enthalpy difference is the state function which decides whether the reaction

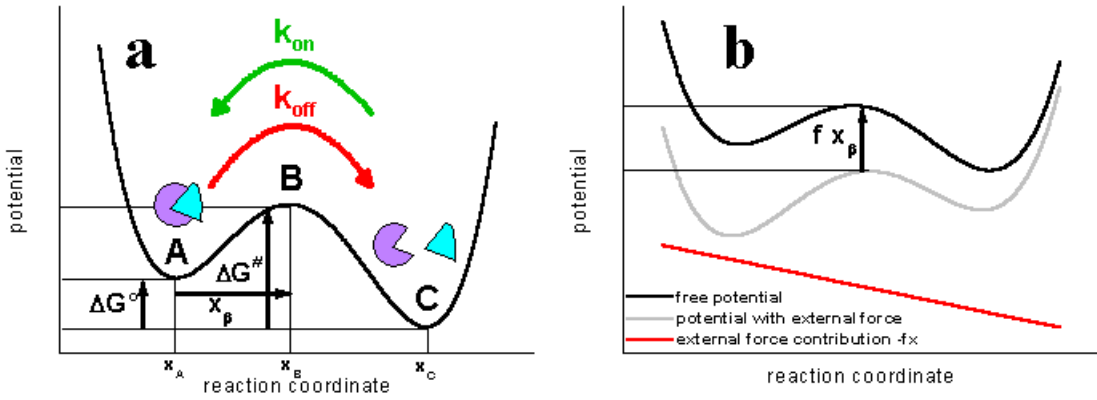


Figure 3.5: (a) Free dissociation of a complex from a metastable bound state via a potential barrier of height  $\Delta G^\ddagger$  to the unbound state. (b) The influence of a constant external force  $f$  on the energy landscape.

proceeds spontaneously ( $\Delta G^0 < 0$ ) or not. The velocity of the dissociation, and hence the off-rate, is a function of the potential barrier (free enthalpy of activation  $\Delta G^\ddagger$ ):

$$k_{off}^0 \propto e^{-\beta \Delta G^\ddagger} \quad (3.3)$$

where  $\beta = 1/k_B T$  ( $k_B$  signifies the Boltzmann constant and  $T$  the temperature).

This relationship, formulated by Arrhenius in 1889 [72], inspired many subsequent works aiming to derive an expression for the proportionality constant. Thermal fluctuations drive the system to overcome the activational barrier; hence, a better understanding of the random thermal particle movement termed “Brownian motion” was essential for the theoretical interpretation [77]. The pathbreaking works by Eyring [73] and Kramers [74] gave the first expressions for rate constants derived by statistical mechanics. Consider (according to Kramers) a particle of mass  $m$  in the potential well  $U(x)$  which experiences a velocity-dependent friction force  $f_R = -m\gamma\dot{x}$  (with the specific damping  $\gamma$ ) and, additionally, a stochastic force  $\xi(t)$ . Inserting this expression into Newton’s force law yields the Langevin equation:

$$m\ddot{x} = -U'(x) - \gamma m\dot{x} + \xi(t) \quad (3.4)$$

The stochastic force  $\xi(t)$  corresponds to white noise to which the fluctuation-dissipation theorem can be applied, i.e. the average net force equals zero and there is no temporal correlation:

$$\langle \xi(t) \rangle = 0, \quad (3.5)$$

$$\langle \xi(t)\xi(t') \rangle = 2m\gamma k_B T \delta(t - t'). \quad (3.6)$$

The stochastic dynamics of the particle at a point  $(x, \dot{x})$  in phase space is a Markovian process (i.e. there is no correlation between  $(x(t'), \dot{x}(t'))$  and  $(x(t), \dot{x}(t))$  for  $|t' - t| > 0$ ). The Klein-Kramers equation describes the temporal development of the probability density in phase space:

$$\frac{\partial \varrho(x, \dot{x}, t)}{\partial t} = \left[ -\frac{\partial}{\partial x}\dot{x} + \frac{\partial}{\partial \dot{x}}\frac{U'(x) + m\gamma\dot{x}}{m} + \frac{\gamma k_B T}{m}\frac{\partial^2}{\partial \dot{x}^2} \right] \varrho(x, \dot{x}, t) \quad (3.7)$$

Now consider a probability flux from the bound state A at  $x_A$  to the free state C at  $x_C$  under the steady state assumption that state A is continuously replenished by particles which have an energy slightly below the height of the activational barrier B at  $x_B$ . The drain for these particles is the free state C. The probability flux  $J$  across the barrier then is given by the product of the off-rate and the number of particles in the bound state A:

$$k_{off}^0 = \frac{J}{n_A} \quad (3.8)$$

Three assumptions are made in order to establish the flux equation:

(I) The particles in the bound state A are in thermal equilibrium; the corresponding probability density at  $x \approx x_A$  (with the partition function  $Z$ ) is given by

$$\varrho(x, \dot{x}) = \frac{1}{Z} \exp\left(-\beta \left[\frac{1}{2}m\dot{x}^2 + U(x)\right]\right). \quad (3.9)$$

(II) The probability density at the barrier can be derived from equation 3.7 by finding the maximum ( $\partial \varrho / \partial t = 0$ ). Using the vibrational frequency  $\omega_B^2 = -U''(x_B)/m > 0$  and the harmonic potential  $U(x) = U(x_B) - 1/2m\omega_B^2(x - x_B)^2$ , the expression for  $x \approx x_B$  is

$$\left[ -\frac{\partial}{\partial x}\dot{x} - \frac{\partial}{\partial \dot{x}}[\omega_B^2(x - x_B) - \gamma\dot{x}] + \frac{\gamma k_B T}{m}\frac{\partial^2}{\partial \dot{x}^2} \right] \varrho(x, \dot{x}) = 0. \quad (3.10)$$

which is known as the stationary Fokker-Planck equation.

(III) The free state C is a particle drain, which corresponds to

$$\varrho(x, \dot{x}) \approx 0. \quad (3.11)$$

for  $x > x_B$ . Equations 3.9-3.11 allow the determination of the number of particles in the bound state  $n_A = \int_A dx d\dot{x} \varrho(x, \dot{x})$  and the flux across the barrier  $J = \int_{-\infty}^{+\infty} d\dot{x} \dot{x} \varrho(x_B, \dot{x})$ . For  $n_A$ , the result is

$$n_A = \frac{2\pi k_B T}{m\omega_0 Z} e^{-\beta U(x_A)}, \quad (3.12)$$

where again a harmonic potential  $U(x) = U(x_A) + \frac{1}{2}m\omega_0^2(x - x_A)$  is assumed. The flux is

$$J = \lambda \frac{k_B T}{m\omega_B Z} e^{-\beta U(x_B)} \quad (3.13)$$

where  $\lambda = -\frac{\gamma}{2} + \sqrt{\omega_B^2 + (\gamma/2)^2}$ . Equations 3.8, 3.12 and 3.13 yield the relation between the activational free enthalpy  $\Delta G^\neq$  and the off-rate  $k_{off}^0$  which we are looking for:

$$k_{off}^0 = \frac{\sqrt{\frac{\gamma^2}{4} + \omega_B^2} - \frac{\gamma}{2}}{\omega_B} \frac{\omega_0}{2\pi} e^{-\beta \Delta G^\neq} \quad (3.14)$$

In SMFS experiments, the dissociation of the complex is driven by the application of an external force which adds to the activational barrier [75, 12] (Fig. 3.5 (b)):

$$\Delta G^\neq(f) = \Delta G^\neq - fx_\beta, \quad (3.15)$$

where  $x_\beta = x_B - x_A$  is the difference between the maximum of the potential barrier and the minimum of the metastable bound state along the reaction coordinate. Inserting 3.15 into 3.14 yields an expression for the off-rate as a function of externally applied force:

$$k_{off}(f) = k_{off}^0 e^{\beta f x_\beta} \quad (3.16)$$

If the sensor is retracted from the sample at a constant velocity  $v$ , the force acting on the complex varies temporally according to

$$\dot{f} = k_{eff}v = r, \quad (3.17)$$

where  $k_{eff}$  signifies the effective spring constant for the system which is derived from the spring constant  $k$  of the cantilever and the elasticity of the polymer linker attached to the tip.  $r$  is the so-called *loading rate*. Thus, the external force varies linearly with time and the off-rate is time-dependent.

According to Evans and Ritchie, the dissociation corresponds to a thermally activated decay of the metastable bound state following the kinetics

$$\frac{dp(t)}{dt} = -k_{off}(f(t))p(t), \quad (3.18)$$

where  $p(t)$  is the probability of a bond to survive until a certain point in time  $t$ . Re-association of a broken bond is an exponentially suppressed process [71, 78]. It is assumed that the dissociation probability is only depending on the instantaneously acting force, not on the “history” (i.e.  $df(t)/dt$ ) of the system. This assumption is justified by taking into account that intramolecular thermal relaxation into the metastable state is

much faster (typically  $t_R = 10^{-10} - 10^{-9}$  s [79]) than a change in the applied force  $f(t)$  ( $\approx 10^{-4}$  s · min) and also than the dissociation of the bond.

The second postulate of the standard theory according to Evans and Ritchie concerns the retract velocity dependance of the force  $f(t)$  which is supposed to be of the form

$$f(t) = F(vt) = F(s) \quad (3.19)$$

with  $F(s)$  independent of the retract velocity  $v$ , i.e.  $f(t)$  only depends on the total extension  $s$  of all elastic components (molecules, linker, cantilever etc.), but not on the velocity that determines how fast this extension increases. This assumption seems justified since all elastic components are not far from their equilibrium states under experimental conditions (hence, their “history” does not influence the present state). Equations 3.18 and 3.19 yield an expression for the survival probability of a bond up to a certain force  $f$ :

$$p_v(f) = \exp\left(-\frac{1}{v} \int_{f_{min}}^f df' \frac{k_{off}(f')}{F'(F^{-1}(f'))}\right) \quad (3.20)$$

with  $p_v(f(t)) = p(t)$  and  $p(t = 0) = p_v(f = f_{min}) = 1$ . Here,  $f_{min}$  is the threshold value below which dissociation forces can not be distinguished from thermal flucutations. Additionally, it is assumed that  $F(s)$  is strictly monotonic increasing (for the inverse  $F^{-1}$  to be existent).

Using equations 3.16 and 3.17, the most probable rupture force  $\hat{F}$  at a given loading rate  $r$  can be derived from the maximum of the distribution  $-dp_v(f)/df$ :

$$\hat{F} = \frac{k_B T}{x_\beta} \ln\left(\frac{x_\beta r}{k_{off}^0 k_B T}\right) \quad (3.21)$$

This relation is the basis for dynamic force spectroscopy: SMFS experiments are performed at different retract velocities which give rise to different loading rates. The force distributions obtained for each loading rate are then analyzed by plotting the most probable rupture forces semilogarithmically against the loading rates. From the slope of the linear fit to the data, the molecular reaction length (dissociation length)  $x_\beta$  can be estimated in accordance with equation 3.21. Extrapolation of the regression line to zero force ( $\hat{F} = 0$ ) yields the thermal off-rate  $k_{off}^0$ .

For a critical evaluation of the standard theory and a novel theoretical approach allowing for a heterogeneity of chemical bonds, the reader is referred to chapter 5. It will be demonstrated that Evans’ and Ritchie’s basic assumptions must be modified to yield a more realistic picture of the dissociation process where the rate of dissociation  $k_{off}$  exhibits an intrinsically random distribution.

## 3.2 Publication IV

**Rainer Eckel**, Sven David Wilking, Anke Becker, Norbert Sewald, Robert Ros, and Dario Anselmetti. Single-molecule experiments in synthetic biology: an approach to the affinity ranking of DNA-binding peptides. *Angew. Chem. Int. Ed.* 44 (2005), 3921-3924.

### 3.2.1 Contribution

All experimental work and data analysis performed by the author.

to DNA, the effect that a single amino acid point mutation has upon biological specificity and affinity, and the minimal peptide sequence length to ensure binding specificity. This approach would also aid in the design of artificial proteins that contain a purely synthetic helix-turn-helix (HTH) binding motif.

In this context, it is of considerable interest to elucidate the DNA-binding specificity of synthetic peptides with a primary sequence akin to the binding domain of a transcription factor. We studied a 20-residue peptide that represents the native sequence of a binding epitope of the transcription activator PhoB (*E. coli*) and three single point mutants of this peptide.

PhoB is a transcription activator which, after phosphorylation by PhoR, binds to the phosphate box in the promoter region of the phosphate regulon *pho* and activates the expression of genes involved in phosphate metabolism.<sup>[7–9]</sup> The protein<sup>[9]</sup> consists of a regulatory phosphorylation domain in the N-terminal region (PhoB 1–127) and a DNA-binding domain in the C-terminal region (PhoB 128–229). Deletion experiments showed that PhoB 139–229 binds to double-stranded DNA and recognizes the sequence TGTCA. The NMR solution structure of the regulatory domain and the DNA-binding domain (PhoB126–229),<sup>[10]</sup> as well as the X-ray crystal structure of the complex with DNA have been reported (Figure 1a).<sup>[11]</sup> Structurally, the DNA-binding domain of PhoB belongs to the family of *winged* helix-turn-helix proteins with the topology  $\beta^1\text{-}\beta^2\text{-}\beta^3\text{-}\beta^4\text{-}\alpha^1\text{-}\beta^5\text{-}\alpha^2\text{-}\alpha^3\text{-}\beta^6\text{-}\beta^7$ , in which the rigid turn is replaced by a loop. This family is characterized by an N-terminal four-stranded  $\beta$  sheet ( $\beta^1\text{-}\beta^2\text{-}\beta^3\text{-}\beta^4$ ), one  $\alpha$  helix ( $\alpha^1$ ) connected through a short  $\beta$  sheet ( $\beta^5$ ) to another  $\alpha$  helix ( $\alpha^2$ ), followed by a third  $\alpha$  helix ( $\alpha^3$ ) and a  $\beta$  hairpin ( $\beta^6\text{-}\beta^7$ ). The DNA-recognizing helix  $\alpha^3$  is amphiphilic and is connected to  $\alpha^2$  by a loop.<sup>[12]</sup> The  $\beta$  hairpin ( $\beta^6\text{-turn-}\beta^7$ ) is often called the *recognition wing*.<sup>[13]</sup>

The single amino acid residues of DNA-binding peptides and proteins contribute differently to affinity and specificity. Whereas cationic side chains (Lys, Arg) often form sequence-independent ionic interactions with the phosphate backbone, the sequence information of the DNA is read through hydrogen bonds and van der Waals interactions with the peptide. Binding of the recognition helix  $\alpha^3$  of PhoB takes place in the DNA major groove.<sup>[11]</sup> Arg201 interacts through a hydrogen bond with the carbonyl oxygen atom of a guanine base while Arg193, His198, Arg200, and Arg203 form salt bridges with phosphate groups. Furthermore, van der Waals contacts with Thr194 and Val197 are involved in specific recognition. Arg219 in the *recognition wing* is bound to deoxyribose moieties through hydrogen bonds.

In the work reported herein, the contribution that single amino acid residues in the DNA-binding helix  $\alpha^3$  contribute to intermolecular affinity was investigated on the single-molecule level. We synthesized peptides in which the amino acid residues that interact with the DNA phosphate backbone in the X-ray crystal structure through salt bridges were individually exchanged by alanine (Table 1). The synthesized peptides comprised the native sequence PhoB(190–209) as well as the point-mutated peptides PhoB(190–209) R193A, PhoB(190–209) H198A and PhoB(190–209) R203A. Accord-

## DNA–Peptide Complexes

### Single-Molecule Experiments in Synthetic Biology: An Approach to the Affinity Ranking of DNA-Binding Peptides\*\*

Rainer Eckel, Sven David Wilking, Anke Becker,  
Norbert Sewald,\* Robert Ros, and Dario Anselmetti\*

Gene expression in eukaryotes is controlled at the transcriptional level by the specific binding of transcription factors to defined DNA sequences. In this way, cell growth, differentiation, and development are regulated. The possibility to influence and control cell metabolism through modified synthetic transcription factors<sup>[1–4]</sup> offers fascinating prospects for molecular cell biology in the framework of biomimetics and synthetic biology.<sup>[5,6]</sup> The design and synthesis of biologically active artificial enzymes and new protein-based materials can be investigated by the combination of bioorganic bottom-up synthesis and single-molecule affinity nanotechnology. With this approach important questions can be addressed, such as the extent to which a single recognition helix contributes to the specific binding of a complete protein

[\*] Dipl.-Chem. R. Eckel, Priv.-Doz. Dr. R. Ros, Prof. Dr. D. Anselmetti  
Experimental Biophysics and Applied Nanoscience  
Bielefeld University  
Universitätsstraße 25, 33615 Bielefeld (Germany)  
Fax: (+49) 521-106-2959  
E-mail: dario.anselmetti@physik.uni-bielefeld.de  
Dipl.-Chem. S. D. Wilking, Prof. Dr. N. Sewald  
Organic and Bioorganic Chemistry  
Bielefeld University  
Universitätsstraße 25, 33615 Bielefeld (Germany)  
Fax: (+49) 521-106-8094  
E-mail: norbert.sewald@uni-bielefeld.de  
Priv.-Doz. Dr. A. Becker  
Genetics  
Bielefeld University (Germany)

[\*\*] The authors thank the Deutsche Forschungsgemeinschaft (SFB 613) for financial support, Tanja Beschnitt for help with DNA preparation, and Kay Lofthouse for a careful reading of the manuscript.

 Supporting information for this article is available on the WWW under <http://www.angewandte.org> or from the author.

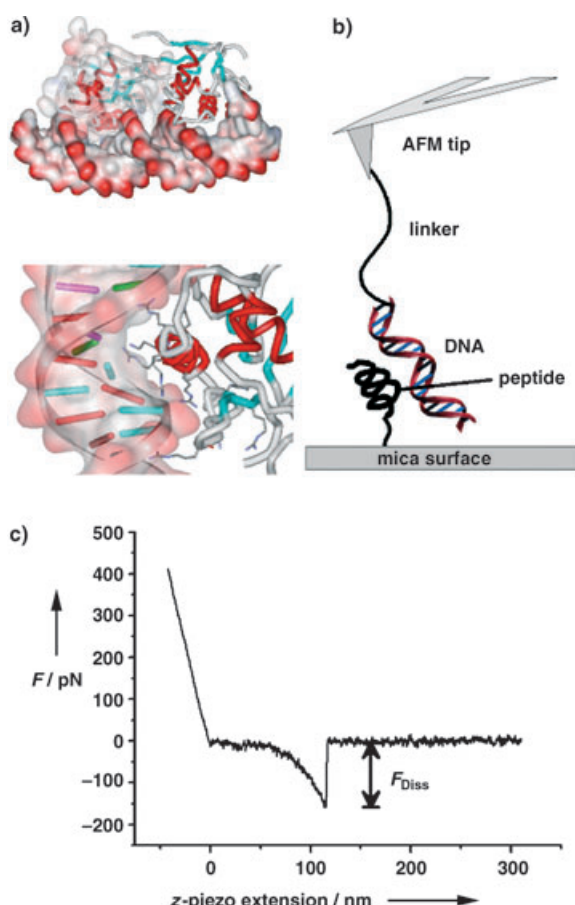


**Figure 1.** a) Upper image: X-ray crystal structure of the 2:1 complex of PhoB(124–229) with DNA;<sup>[10]</sup> lower image: Section from the X-ray crystal structure showing the recognition helix  $\alpha^3$ ; b) force spectroscopy setup (schematic representation); c) typical force–distance curve (only retractive part shown).

**Table 1:** Synthesized peptides from the epitope PhoB(190–209).

Mutation	Peptide Sequence	$k_{\text{off}}$ [s <sup>-1</sup> ] <sup>[a]</sup>	$x_{\beta}$ [Å] <sup>[a]</sup>
–	Ac-VEDRTVDVH <del>I</del> RRLRKALEPG-Linker	$3.1 \pm 2.1$	$6.8 \pm 1.2$
R193A	Ac-VED <del>A</del> TVDVH <del>I</del> RRLRKALEPG-Linker	$0.071 \pm 0.053$	$9.3 \pm 2.6$
H198A	Ac-VEDRTVDV <del>A</del> IRRLRKALEPG-Linker	$49.5 \pm 21.2$	$7.2 \pm 3.5$
R203A	Ac-VEDRTVDVH <del>I</del> RRLK <del>A</del> KALEPG-Linker	no binding	no binding

[a]  $k_{\text{off}}$ : dissociation rate constant for the peptide–DNA complex;  $x_{\beta}$ : molecular reaction length.

ing to CD spectroscopy measurements, all peptides exhibit an  $\alpha$ -helical structure. N-terminal functionalized fragments of the PhoB helix  $\alpha^3$  were synthesized on the solid phase with 2-chlorotriptylresin preloaded with a suitable linker according to the Fmoc/tBu protection scheme.<sup>[14]</sup> The peptides were purified by HPLC with acetonitrile/water/TFA gradients. The interaction of the synthesized peptides with the corresponding DNA was investigated with AFM force spectroscopy.

A broad affinity range for specific molecular recognition between single binding partners from  $10^{-5} \text{ M}$ <sup>[15]</sup> to  $10^{-15} \text{ M}$ <sup>[16,17]</sup> can be investigated with single-molecule force spectroscopy. The deflection of a micro-fabricated force sensor (cantilever) is used to detect forces in the pico-Newton range. The AFM

principle permits investigation of molecular binding forces under physiological conditions, and AFM force spectroscopy has found applications in the study of a variety of specific biological receptor–ligand interactions<sup>[16–22]</sup> as well as in supramolecular host–guest systems.<sup>[15]</sup> The direct investigation of specific, native protein–DNA interactions has been reported recently.<sup>[23–25]</sup>

In our studies reported herein, we applied AFM single-molecule force spectroscopy to study the specific binding between the peptides listed in Table 1 and the DNA target sequence. Each peptide was covalently immobilized to an amino-functionalized mica surface in a directed manner with the short C-terminal linker 1,8-diamino-3,6-dioxaoctane and the cross-linker BS<sup>3</sup> (bis(sulfosuccinimidyl)suberate; Figure 1b). This immobilization prevents unfolding of the peptide caused by physisorption on the surface. PCR-amplified genomic DNA containing the 600-bp PhoB binding motif from *E. coli* was chosen as the binding partner, and was bound to an AFM tip with a bifunctional polyethylene glycol (PEG) linker (molar mass: 3400 g mol<sup>-1</sup>, corresponding to an average length of 30 nm).<sup>[26]</sup> The application of the PEG linker serves various purposes. First, it adds steric flexibility to the system and ensures that dissociation occurs far from the surface. Second, the linker facilitates the distinction between single and multiple dissociation events, and decreases non-specific adhesion. Third, the elastic stretching of the linker ensures a gradual increase in force until the point of bond rupture, and allows precise measurement of the molecular elasticity of the complex (Figure 1c). As the elasticity is determined for each rupture event individually, variations in the entropic portion of the rupture peaks are included and do not affect the statistical interpretation.

Compilation of the rupture forces to histograms and statistical analysis of the resulting force distribution yields the most probable dissociation forces at a given retract velocity. Each histogram represents the analysis of 2000 force curves; the binding probabilities given in the figures (Figure 2 and Supporting Information) refer to the ratio of rupture events divided by the total number of force curves recorded (for example, 300 binding events out of 2000 force curves results in a binding probability of 15%). The maximum of the force distribution was taken as the most probable dissociation force.

Competition experiments were performed to determine if binding between the peptides and the DNA target sequence occurs specifically. For each mutant, a series of force spectroscopy experiments in standard buffer solution (100 mM Na<sub>2</sub>HPO<sub>4</sub>, 50 mM NaCl, pH 7.4) was followed by a series of experiments with an excess of free binding partner (peptide or DNA) as competitor in solution. This was followed by washing the sample with standard buffer and then performing another series of experiments in standard buffer. Figure 2 shows the results of the competition for the native peptide: part (a) shows the force distribution in standard buffer solution, with a total binding probability of  $\approx 33\%$ ; part (b) shows the competition with free peptide in

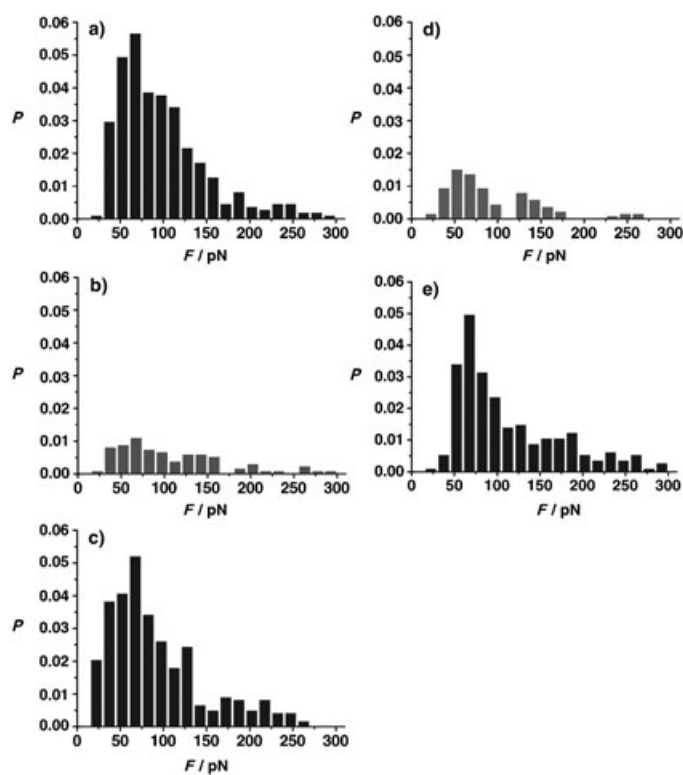


**Figure 2.** Competition experiments with the native peptide sequence: a) force spectroscopy experiment in standard buffer solution (100 mM NaH<sub>2</sub>PO<sub>4</sub>, 50 mM NaCl, pH 7.4) without competitor; b) experiment in buffer solution with an excess of free peptide as competitor; c) experiment after washing with standard buffer solution; d) experiment in buffer solution with excess of free DNA as competitor; e) as in c).

buffer solution, in which a significant decrease in total binding probability is apparent; part (c) illustrates how the original binding probability and activity of the interaction is restored after washing the sample in standard buffer; part (d) shows the analogous competition experiment with excess free DNA in buffer solution, and part (e) illustrates the reactivation of the interaction. In additional control experiments with EBNA DNA fragments, which lack the PhoB binding sequence, no binding was observed at all (data not shown; EBNA = Epstein–Barr virus nuclear antigen). These results clearly prove that the binding of the peptide with the native sequence takes place specifically at the binding sequence on the DNA.

The same conclusion applies to the results of the competition experiments performed with the peptide mutants R193A and H198A. Again, competition was successful both with free peptide and with free DNA as competitor (Supporting Information). For H198A, however, the total binding probability was distinctly lower than those of the native peptide and the mutant R193A. In contrast, binding experiments with the mutant R203A yielded very few binding events, rendering statistical analysis impossible. In summary, there is evidence that the native sequence and the mutants R193A and H198A specifically recognize the PhoB target sequence. As it was doubted recently that short peptide sequences with only one  $\alpha$  helix are capable of specific DNA binding,<sup>[1]</sup> our results are quite remarkable given that the 20-

residue peptides represent a rather small epitope from the binding domain of the protein.

Dynamic force spectroscopy experiments were performed with the native sequence and the mutants R193A and H198A to obtain information on the dissociation kinetics and energy landscapes. In force-induced thermally driven dissociation of a metastable molecular complex,<sup>[27–29]</sup> the measured dissociation forces depend on the temporal force evolution on the complex, commonly referred to as the loading rate. It is given as the product of the molecular elasticity and the retract velocity of the cantilever. In our experiments, the molecular elasticity was determined by fitting the last 20 data points prior to bond rupture in the force–distance curve. The retract velocity was varied in the range of 10–6000 nm s<sup>-1</sup>.

The results of the dynamic experiments are shown in Figure 3. The dissociation forces (derived from analysis of the

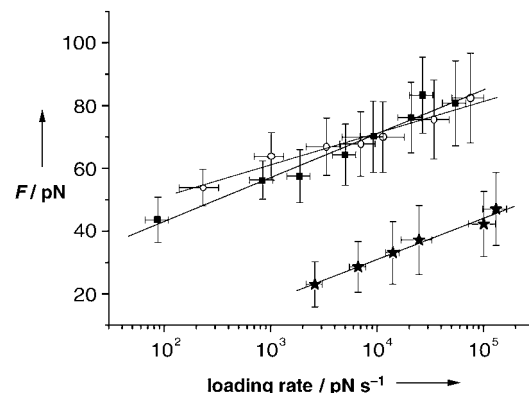


**Figure 3.** Dynamic force spectroscopy: ■ = native sequence; ○ = R193A; \* = H198A.

respective force histograms) are plotted logarithmically against the loading rate. The linear fit of the data provides two important parameters. First, extrapolation to zero external force  $F=0$  gives the thermal off-rate  $k_{\text{off}}$ . For the native sequence, the thermal off-rate amounts to  $k_{\text{off}}=(3.1 \pm 2.1)$  s<sup>-1</sup> (Table 1), which corresponds to a time constant (lifetime) for complex dissociation of  $\tau=(320 \pm 220)$  ms. The complex between DNA and the mutant R193A, interestingly, dissociates more slowly, with  $k_{\text{off}}=(0.071 \pm 0.053)$  s<sup>-1</sup>, indicating a longer complex lifetime of  $\tau=(14.1 \pm 10.5)$  s. In contrast, the mutant H198A exhibits a considerably higher off-rate:  $k_{\text{off}}=(49.5 \pm 21.2)$  s<sup>-1</sup>, corresponding to a shorter lifetime of  $\tau=(20 \pm 8)$  ms. This is not surprising, as in mutant H198A the basic residue His 198 from the native sequence was replaced by alanine. Hence, the charge-controlled contribution to the binding of the peptide with DNA should be decreased. Surprisingly, the mutant R193A, in which Arg 193 was replaced by an alanine, exhibits a lower off-rate and consequently, a longer complex lifetime than the native peptide sequence. This result can presumably be attributed to an enhanced  $\alpha$ -helical conformation of the peptide in solution, a finding which will be examined more closely in future experiments. In comparison with recent single-molecule experiments with complete transcription-activating proteins bearing a HTH DNA-binding motif,

which exhibit lower dissociation rates ( $2 \times 10^{-4}$  to  $1.3 \times 10^{-2} \text{ s}^{-1}$ )<sup>[23]</sup> and lifetimes (100–1000 s), this interesting fact indicates the presence and importance of cooperative binding effects—an issue which must be addressed in the future as well.

The affinity of a ligand to its receptor, represented in the case of a 1:1 kinetics by the dissociation equilibrium constant  $K_D = k_{\text{off}}/k_{\text{on}}$ , is governed by the dissociation rate  $k_{\text{off}}$ .<sup>[22]</sup> Assuming diffusion-controlled association with a typical on-rate constant of  $k_{\text{on}} = 10^5 \text{ M}^{-1} \text{ s}^{-1}$ <sup>[24,30–32]</sup> for the binding of a peptide to the target DNA, equilibrium constants of  $K_D = 3 \times 10^{-6} \text{ M}$  (native sequence),  $K_D = 7 \times 10^{-8} \text{ M}$  (mutant R193A), and  $K_D = 5 \times 10^{-5} \text{ M}$  (mutant H198A) can be estimated. According to  $\Delta G^\circ = RT \ln K_D$ , the corresponding Gibbs' free energy differences of complex formation can be estimated to  $\Delta G^\circ = -31 \text{ kJ mol}^{-1}$  (native sequence),  $\Delta G^\circ = -41 \text{ kJ mol}^{-1}$  (mutant R193A), and  $\Delta G^\circ = -25 \text{ kJ mol}^{-1}$  (mutant H198A).

From the inverse slope of the linear fit to the data (Figure 3), a molecular reaction length  $x_\beta$  can be obtained as a second parameter, which amounts to values of  $6.8 \pm 1.2 \text{ \AA}$  for the native peptide and  $7.2 \pm 3.5 \text{ \AA}$  for the mutant H198A (Table 1). However, for peptide R193A, which exhibits the longest complex lifetime, a larger value of  $x_\beta = 9.3 \pm 2.6 \text{ \AA}$  is found. This is consistent with the previous results, as it indicates that the final activation barrier is located late along the reaction coordinate. This suggests the possibility for the complex to re-associate (assuming microscopic reversibility) over a larger distance along the reaction coordinate, which corresponds to a longer lifetime of the complex.

In summary, the specific interaction of synthetic peptides that comprise only the recognition helix of a transcription activator with DNA could be investigated for the first time at the single-molecule level. The molecular binding forces observed for single peptide–DNA complexes upon induced dissociation were analyzed quantitatively with AFM force spectroscopy. Competition experiments have proven the specific binding of two peptide mutants to DNA. The results of dynamic force spectroscopy experiments indicate a dependence of the binding forces on external load, which is consistent with thermally driven dissociation. These experiments yield values for the dissociation rates of the corresponding complexes, which allow a direct affinity ranking of synthetic peptides with single point mutations. Furthermore, our results indicate the importance of peptide length, cooperative binding effects, and the contribution of single point mutations to the specific binding of (synthetic) peptides to DNA. These results prove the potential of combining chemical synthesis strategies for biomimetics (synthetic biology) with the high sensitivity of AFM single-molecule force spectroscopy to investigate, quantify, and control the mechanisms and properties of molecular recognition processes (molecular nanotechnology).

Received: January 14, 2005

Revised: March 3, 2005

Published online: May 20, 2005

**Keywords:** molecular recognition · peptides · point mutations · scanning probe microscopy · single-molecule studies

- 
- [1] M. E. Vázquez, A. M. Caamaño, J. L. Mascarenas, *Chem. Soc. Rev.* **2003**, *32*, 338–349.
  - [2] M. E. Vázquez, A. M. Caamaño, J. Martínez-Costas, L. Castedo, J. L. Mascarenas, *Angew. Chem.* **2001**, *113*, 4859–4861; *Angew. Chem. Int. Ed.* **2001**, *40*, 4723–4725.
  - [3] A. M. Caamaño, M. E. Vázquez, J. Martínez-Costas, L. Castedo, J. L. Mascarenas, *Angew. Chem.* **2000**, *112*, 3234–3237; *Angew. Chem. Int. Ed.* **2000**, *39*, 3104–3107.
  - [4] C. Melander, R. Burnett, J. M. Gottesfeld, *J. Biotechnol.* **2004**, *112*, 195–220.
  - [5] P. Ball, *Nanotechnology* **2005**, *16*, R1–R8.
  - [6] S. A. Benner, *Nature* **2003**, *421*, 118–118.
  - [7] S.-K. Kim, S. Kimura, H. Shinagawa, A. Nakata, K.-S. Lee, B. L. Wanner, K. Makino, *J. Bacteriol.* **2000**, *182*, 5596–5599.
  - [8] K. Makino, H. Shinagawa, M. Amemura, A. Nakata, *J. Mol. Biol.* **1986**, *190*, 37–44.
  - [9] K. Makino, M. Amemura, T. Kawamoto, K. Kimura, H. Shinagawa, A. Nakata, M. Suzuki, *J. Mol. Biol.* **1996**, *259*, 15–26.
  - [10] Brookhaven Data Base: 1QQI. 2004.
  - [11] A. G. Blanco, M. Sola, F. X. Gomis-Rüth, M. Coll, *Structure* **2002**, *10*, 701–713.
  - [12] H. Okamura, S. Hanaoka, A. Nagadoi, K. Makino, Y. Nishimura, *J. Mol. Biol.* **2000**, *295*, 1225–1236.
  - [13] E. Martínez-Hackert, A. M. Stock, *J. Mol. Biol.* **1997**, *269*, 301–312.
  - [14] S. D. Wilking, N. Sewald, *J. Biotechnol.* **2004**, *112*, 109–114.
  - [15] R. Eckel, R. Ros, B. Decker, J. Mattay, D. Anselmetti, *Angew. Chem.* **2005**, *117*, 489–492; *Angew. Chem. Int. Ed.* **2005**, *44*, 484–488.
  - [16] E.-L. Florin, V. T. Moy, H. E. Gaub, *Science* **1994**, *264*, 415–417.
  - [17] G. U. Lee, D. A. Kidwell, R. J. Colton, *Langmuir* **1994**, *10*, 354–357.
  - [18] U. Dammer, O. Popescu, P. Wagner, D. Anselmetti, H.-J. Güntherodt, G. N. Misevic, *Science* **1995**, *267*, 1173–1175.
  - [19] T. Strunz, K. Oroszlan, R. Schäfer, H.-J. Güntherodt, *Proc. Natl. Acad. Sci. USA* **1999**, *96*, 11277–11282.
  - [20] R. Ros, F. Schwesinger, D. Anselmetti, M. Kubon, R. Schäfer, A. Plückthun, L. Tiefenauer, *Proc. Natl. Acad. Sci. USA* **1998**, *95*, 7402–7405.
  - [21] U. Dammer, M. Hegner, D. Anselmetti, P. Wagner, M. Dreier, W. Huber, H.-J. Güntherodt, *Biophys. J.* **1996**, *70*, 2437–2441.
  - [22] F. Schwesinger, R. Ros, T. Strunz, D. Anselmetti, H.-J. Güntherodt, A. Honegger, L. Jermutus, L. Tiefenauer, A. Plückthun, *Proc. Natl. Acad. Sci. USA* **2000**, *97*, 9972–9977.
  - [23] F. W. Bartels, B. Baumgarth, D. Anselmetti, R. Ros, A. Becker, *J. Struct. Biol.* **2003**, *143*, 145–152.
  - [24] B. Baumgarth, F. W. Bartels, D. Anselmetti, A. Becker, R. Ros, *Microbiology* **2005**, *151*, 259–268.
  - [25] F. Kühner, L. T. Costa, P. M. Bisch, S. Thalhammer, W. M. Heckl, H. E. Gaub, *Biophys. J.* **2004**, *87*, 2683–2690.
  - [26] P. Hinterdorfer, W. Baumgartner, H. Gruber, K. Schilcher, H. Schindler, *Proc. Natl. Acad. Sci. USA* **1996**, *93*, 3477–3481.
  - [27] G. I. Bell, *Science* **1978**, *200*, 618–627.
  - [28] E. Evans, K. Ritchie, *Biophys. J.* **1997**, *72*, 1541–1555.
  - [29] R. Merkel, P. Nassoy, A. Leung, K. Ritchie, E. Evans, *Nature* **1999**, *397*, 50–53.
  - [30] M. Schlosshauer, D. Baker, *Protein Sci.* **2004**, *13*, 1660–1669.
  - [31] M. Vijayakumar, K.-W. Wong, G. Schreiber, A. R. Fersht, A. Szabo, H.-X. Zhou, *J. Mol. Biol.* **1998**, *278*, 1015–1024.
  - [32] O. G. Berg, R. B. Winter, P. H. von Hippel, *Biochemistry* **1981**, *20*, 6929–6948.
-

### 3.3 SMFS Studies with the Native Protein PhoB: The Role of the Protein Environment

Recently, SMFS experiments with the DNA binding domain (PhoB(126-229)) of the PhoB protein were performed that give insight into the contribution of the protein environment to molecular recognition. The protein PhoB was expressed in *E. coli* and isolated using standard biochemical methods (cf. chapter 3.3.1). The binding of the protein to the target DNA was demonstrated in an EMSA (electrophoretic mobility shift assay) experiment (Fig. 3.6): Adding protein to the Cy3-labeled target DNA effects a clearly visible shift, corresponding to a larger mass resulting from the protein-DNA complex. The EMSA experiment gives evidence for the formation of a protein-DNA

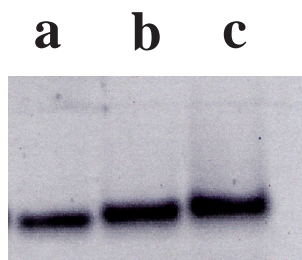


Figure 3.6: EMSA (electrophoretic mobility shift assay) of the PhoB protein (buffer: 20 mM Na-HEPES, 500 mM NaCl, 1 mM EDTA, 50 mM MESNA, pH 8.5). DNA labeled with Cy3. (a) 1  $\mu$ M DNA. (b) 1  $\mu$ M DNA + 0.5  $\mu$ g protein. (c) 1  $\mu$ M DNA + 1.1  $\mu$ g protein.

complex, but it does not indicate whether the binding observed is specific, i.e. if the protein binds to its specific target sequence on the DNA. In order to probe the binding specificity, SMFS experiments were performed. The resulting force histograms are shown in Fig. 3.7.

The first three measurement series (Fig. 3.7 (a)-(c)) were all performed at a loading rate of 2300 pN s<sup>-1</sup> using the same AFM tip functionalized with the target DNA; the protein was immobilized on the sample surface via a Cys residue. The first series (Fig. 3.7 (a)) corresponds to experiments in standard buffer (100 mM Na<sub>2</sub>HPO<sub>4</sub>, 50 mM NaCl, pH 7.4; the same buffer was used for the experiments with the synthetic peptides mimicking the PhoB recognition helix, cf. publication IV). In the second series, a 10-fold excess of free DNA in standard buffer was added to the sample, intended to serve as a competitor of the DNA at the AFM tip. As can be inferred from the histogram (Fig. 3.7 (b)), the total unbinding probability was decreased significantly by adding the competitor DNA. After washing the sample with standard buffer, another series of experiments

was performed (Fig. 3.7 (c)). The total unbinding probability amounted to the value from the first series, which indicates that the system could be fully reactivated. Fig. 3.7

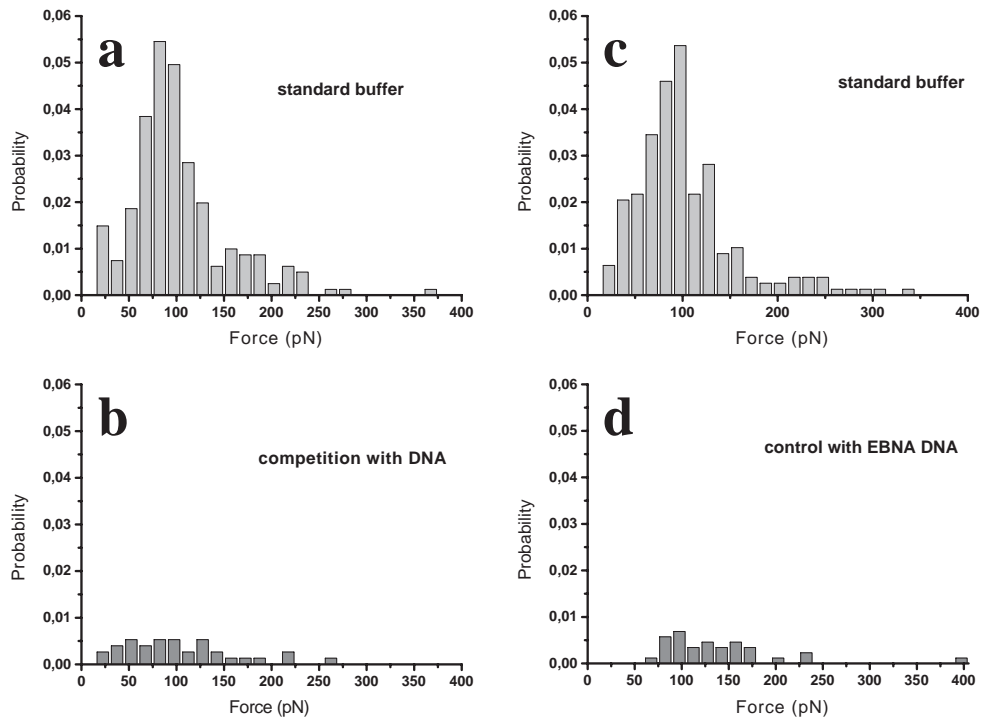


Figure 3.7: SMFS experiments with the PhoB protein (shown are force histograms; loading rate:  $2300 \text{ pN s}^{-1}$ ). (a) Experiment in standard buffer ( $100 \text{ mM Na}_2\text{HPO}_4$ ,  $50 \text{ mM NaCl}$ , pH 7.4). (b) Competition with excess DNA. (c) Experiment after washing with standard buffer. (d) Control experiment with EBNA (Epstein-Barr virus nuclear antigen) DNA.

(d) shows an experiment with EBNA (Epstein-Barr virus nuclear antigen) DNA (which features no PhoB target sequence) as a negative control. The histogram shows that almost no dissociation events could be detected in this experimental series. These experiments demonstrate that the PhoB protein which was isolated is active and binds specifically to its target sequences on the *pho* box. Dynamic force spectroscopy experiments were performed with a view to extract kinetic and structural information about the protein-DNA complex. The resultant force - loading rate plot is shown in Fig. 3.8, together with the plot for the native peptide sequence PhoB(190-209) (publication IV) for comparison. The results for the thermal off-rate  $k_{off}$  and the reaction length  $x_\beta$  for the protein and the peptide are compared in the table 3.1. The value of  $x_\beta$  is lower

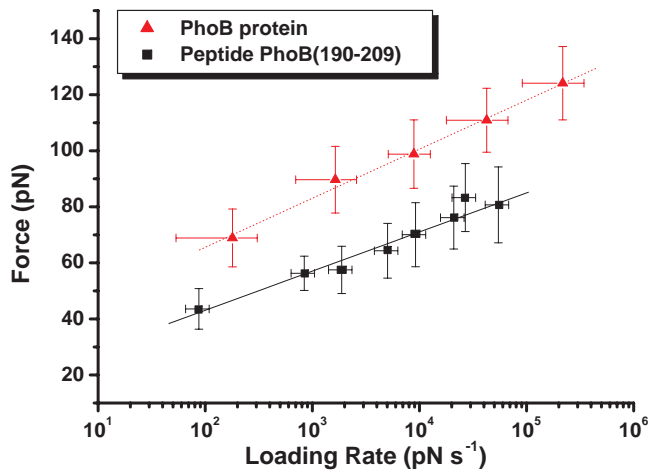


Figure 3.8: Dynamic force spectroscopy results for the PhoB protein and comparison with the results for the peptide PhoB(190-209).

System	$x_\beta$ (nm)	$k_{off}$ ( $s^{-1}$ )	$\tau$ (s)
Protein PhoB(126-229)	$0.24 \pm 0.17$	$(2.41 \pm 2.15) \cdot 10^{-3}$	415
Peptide PhoB(190-209)	$0.68 \pm 0.12$	$3.1 \pm 2.1$	0.32

Table 3.1: Dynamic force spectroscopy parameters for the DNA binding domain of the protein PhoB and the peptide PhoB(190-209)

for the protein than for the peptide, corresponding to a later activation barrier. It is a remarkable finding that the thermal off-rate for the complex formed by the DNA and the PhoB DNA binding domain is three orders of magnitude lower than for the peptide representing only the recognition helix. The off-rate corresponds to a life time for the complex of 415 s, as opposed to only 320 ms for the peptide-DNA complex. This clear difference can be attributed to the protein environment encompassing the recognition helix  $\alpha^3$ , and especially to the helix  $\alpha^2$ , which is missing in the peptide sequence. The helix  $\alpha^2$  is known to stabilize the complex by additional formation of non-specific, mainly electrostatic, interactions. It can be concluded from the data that the helix  $\alpha^3$  is the part of the binding domain which ensures binding specificity, whereas the rest of the protein is responsible for a further boost in binding strength once the target sequence has been identified by the recognition helix.

### 3.3.1 Materials and Methods

**PhoB DNA binding domain.** The target protein (PhoB(126-229), the PhoB DNA binding domain from *E. coli*) was expressed as a fusion protein containing a chitin binding domain and a modified *Mth* RIR 1 intein. The corresponding DNA fragment was received from the genomic DNA (*E. coli*) and the primers PhoB-CF-*Nde*I and PhoB-CF-*Sap*I via PCR. For purification, the protein was bound to chitin beads and the intein-mediated cleaving was induced by a reduction agent. For expression, the plasmid was cloned into the *E. coli* ER2655 strain and the bacteria cultivated at 37°C. The isolated protein was ligated with cysteine, dialysed against phosphate buffer (100 mM Na<sub>2</sub>HPO<sub>4</sub>, 50 mM NaCl, pH 7.4) and the concentration determined via Bradford assay.

**DNA.** For construction of the EcoPho1.1 plasmid, a 268 bp *Hind*III-*Eco*RI fragment encoding the *pho* box from the *pst* operon promoter was cloned into a pUC18 plasmid. The SH-labeled DNA fragments (360 bp) were amplified via PCR using *Taq* polymerase (PeqLab), SH-M13uni and SH-M13rev primers and the EcoPho1.1 plasmid. The DNA was purified using a PCR cleanup kit (Qiagen) and the concentration determined by UV spectrometry. SH-labeled EBNA DNA (321 bp) was amplified following the same protocol, using SH-M13uni and SH-M13rev primers and *Taq* polymerase.

**Sample preparation.** Gold surfaces (11·11 mm<sup>2</sup>, Arrandee) were incubated with 0.01 μM protein in phosphate buffer (100 mM Na<sub>2</sub>HPO<sub>4</sub>, 50 mM NaCl, pH 7.4) for 1 h at 25°C. Subsequently, the sample was washed with buffer solution. Modified samples were stable for 2 days if stored at 4°C.

**AFM tip modification.** For AFM force spectroscopy, Si<sub>3</sub>N<sub>4</sub> cantilevers (Microlevers, Veeco Instruments) were dipped in concentrated nitric acid for activation and incubated with a solution of 2% aminopropyltriethoxysilane (Sigma-Aldrich) in dry toluene for 2 h at ambient temperature. After silanization, the cantilevers were washed with toluene and incubated with 1 mM N-hydroxysuccinimide-poly(ethyleneglycol)-maleimide (Shearwater Polymers) in water for 30 min. The cantilevers were washed with phosphate buffer (100 mM Na<sub>2</sub>HPO<sub>4</sub>, 50 mM NaCl, pH 7.4) and functionalized by incubating them overnight at 4 °C with 10 ng μl<sup>-1</sup> of the DNA target sequence bearing a sulphydryl group in phosphate buffer. The functionalized cantilevers were washed with buffer and used for force spectroscopy experiments. Modified tips were stored at 4 °C and remained usable for one week at least. Prior to use in experiment, the modified tips were washed with buffer solution.

**SMFS measurements.** Force spectroscopy experiments were performed using a com-

mercial AFM head (Multimode IIIa, Veeco Instruments) at room temperature. Acquisition of the cantilever deflection force signal and the vertical piezo movement was controlled by a 16 bit AD/DA card (PCI 6052E, National Instruments) and a high-voltage amplifier (600H, NanoTechTools) via a home-built software based on LabView (National Instruments). The deflection signal was low-pass filtered ( $< 4$  kHz) and box averaged by a factor of 5. The spring constants of all AFM cantilevers were calibrated via the thermal fluctuation method with an absolute uncertainty of approximately 15%. The values obtained ranged from 15.4 to 19.3 pN nm $^{-1}$ . All experiments were performed in phosphate buffer solution (100 mM Na<sub>2</sub>HPO<sub>4</sub>, 50 mM NaCl, pH 7.4). For the competition experiments, a solution of 200 ng  $\mu$ l $^{-1}$  unlabeled *pho* box DNA in buffer solution was used. In dynamic force spectroscopy experiments, the retract velocity of the piezo element was varied while keeping the approach velocity constant. For dynamic force spectroscopy experiments, typically 2000 force curves were recorded at the retract velocities 50, 500, 1000, 3000 and 5000 nm s $^{-1}$ .

**Data analysis.** Analysis of the force-distance curves measured was performed with a Matlab program (MathWorks) and corrected to display the actual molecular distances calculated from the z piezo extension, which is especially important for soft cantilevers. The elasticity of the molecular system was obtained from the slope of the force-distance curves (corrected to molecular extension) on the last 20 data points prior to detachment of the cantilever. The loading rate then was given by the system elasticity times the retract velocity.

# 4 SMFS of Molecular Recognition in Supramolecular Guest-Host Systems

## 4.1 Introduction

The striking precision of molecular recognition in biological systems like the one discussed in chapter 3 has inspired a vastness of synthetic compounds which aim at mimicking this aspect of living systems, giving rise to a new field of research generally termed “supramolecular chemistry”. Calixarenes are a class of supramolecular compounds which, properly functionalized, can serve as a host for small guest ligands like, e.g., ammonium ions that are precisely tailored to fit accurately into the cavity provided by the calixarene. Due to their easy synthetic accessibility, calixarenes have gained importance in recent years as simple model systems for molecular recognition.

An interesting question is whether the forces that mediate the very low affinity in such supramolecular aggregates can be measured at the single molecule level by techniques like SMFS. The work presented here will show that it can, and, moreover, that it is possible to get kinetic and structural information on the systems that cannot be extracted by other techniques. These data even allow the affinity ranking of guest molecules that differ in size.

Another property which makes calixarenes important is the possibility to functionalize them at their “upper rim”. Introducing a suited photoisomerizable group, it is possible to make the access to the host cavity photoswitchable. The second part of this work deals with the first SMFS experiments on such a photoswitchable host receptor.

Chapter 4.1.1 of the introduction will give a short definition of supramolecular systems in general. In 4.1.2, the class of compounds which are of major concern here, namely, the resorc[4]arenes, will be introduced. Chapter 4.1.3 will shortly address the issue of molecular optical switches and present a novel photoswitchable resorc[4]arene which can serve as a supramolecular host system.

### 4.1.1 Supramolecular Chemistry

The field of supramolecular chemistry is commonly defined as a chemistry “beyond the molecule” [80, 81], i.e. the chemistry of designed intermolecular interactions. From a certain point of view, also molecular recognition in biological systems could be viewed as a part of supramolecular chemistry, since the forces involved are basically the same. The difference arises from the word “design”: Supramolecular systems are often inspired by nature, but they are usually constituted from simpler building blocks which are accessible by conventional chemical bottom-up synthesis. Sometimes the aim is to mimic a certain biological function; examples for this strategy are, e.g., synthetic ion channels, siderophores, or even the DNA-binding peptide fragments discussed in chapter 3. In many cases, however, the intention is not to imitate an already existing biological system, but to tailor new supramolecular architectures *de novo*, like, e.g., in phase transfer agents, liquid crystals, or photoswitchable host-guest systems.

The leading principle of supramolecular design is complementarity: The interactions between the species that ought to assemble must be tuned and optimized. Often chelate and macrocyclic effects are helpful, especially in the synthesis of host-guest architectures. Studies of the binding strength and selectivity provide an insight into how a given receptor might be improved; the conclusions from thermodynamic and kinetic data provide a feedback that guides the synthesis of a second, improved generation of compounds. Eventually, the properties of the supramolecular system become so finely adjusted that technological application comes into reach. In this context, the study of supramolecular interactions at the level of individual molecules can yield important information.

### 4.1.2 Calixarenes and Resorc[4]arenes

Calix[n]arenes are a family of synthetic macrocyclic receptors consisting of cyclic arrays of  $n$  phenol moieties linked by methylene groups. They are formed by condensation of alkylphenols and formaldehyde [82, 83]. and provide a receptor cavity which can be functionalized additionally at the upper and lower rim of the macrocycle. Their goblet-like conformations have earned them their name (from *calix*, latin for wine-cup). A vast number of these compounds have been synthesized and their properties, e.g. structure and complex formation with ionic and neutral guest molecules, have been studied [84]. Also phenol derivatives like resorcinol (1,3-dihydroxybenzene) can undergo condensation reactions with formaldehyde, giving rise to mostly tetrameric macrocycles called “resorc[4]arenes”. Fig. 4.1 shows a cavitand, i.e. a resorc[4]arene linked at

the upper rim via ether bridges. There are two major modes of interaction between

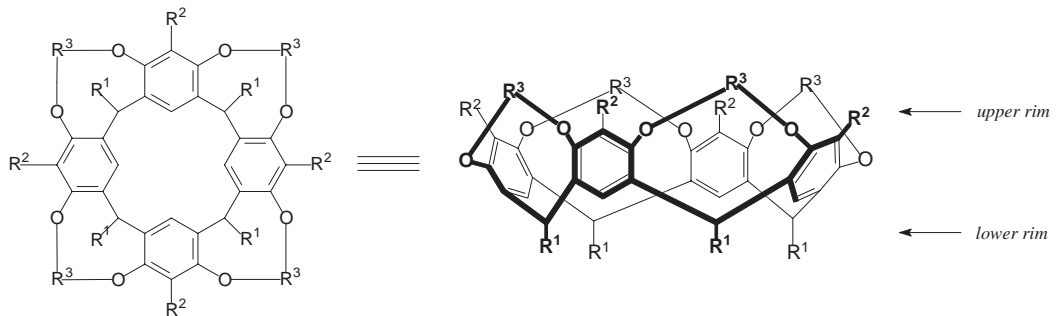


Figure 4.1: A resorc[4]arene cavitand

a resorcarene cavity and a positively charged guest. Firstly, the oxygen atoms at the upper rim (or, in the case of the cavitand, the chaplet formed by the ether oxygen atoms) can form coordinative (in the case of a metal cation) or hydrogen (in the case of ammonium) bonds with the cation; this interaction resembles the action of a crown ether. The aromatic cavity, however, is also capable of binding to the cationic guest via so-called  $\pi$ -cation interactions. These are believed to arise from favorable electrostatic interactions between the electron deficient cation and the electron-rich aromatic ring. Fig. 4.2 (a) shows a gas-phase structure of the complex of a resorc[4]arene cavitand bound to an ethylammonium ion, calculated using the B3LYP/3-21G\* density functional. Resorc[4]arenes can be functionalized with alkylsulfides at the lower rim for

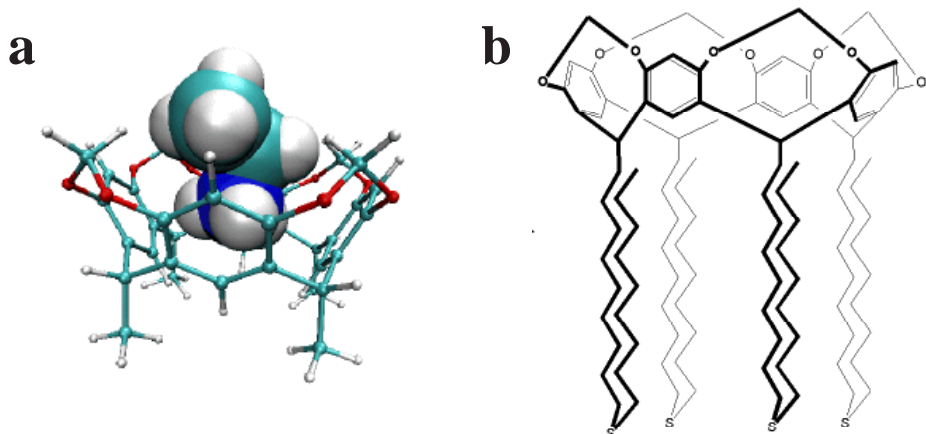


Figure 4.2: (a) Complex between a resorc[4]arene cavitand and an ethylammonium ion; (b) Resorc[4]arene cavitand functionalized for self assembly

immobilization. Fig. 4.2 (b) shows a system which is capable of self assembly on flat gold surfaces.

### 4.1.3 Molecular Optical Switches

The possibility to modulate a certain physical property of a molecule by an external stimulus, e.g. light or an electric field, is of growing importance for the manufacturing of molecular or supramolecular functional devices. Great efforts are made to find dynamic molecular systems which can be switched reversibly between different states. In recent years, a variety of means to address molecular switches has been developed; among these are electrical [85], chemical [86] and even mechanical stimuli [87]. (The mechanical addressing of nanoobjects will be discussed in more detail in chapter 6.1.1.) A very successful way of switching molecules, however, is by light. The basic requirement for an optical molecular switch is a photochromic group, i.e., the molecule must occur in two energetically not too different electronic states  $|a\rangle$  and  $|b\rangle$  (bistability), where configuration  $|a\rangle$  can be switched to configuration  $|b\rangle$  by irradiating the molecule with a certain wavelength  $\lambda_a$ , and the reverse process ( $|b\rangle \rightarrow |a\rangle$ ) must be triggered by irradiation with another wavelength  $\lambda_b$ . The configurations  $|a\rangle$  and  $|b\rangle$  must be stable without permanent irradiation and the switching process must be fast and repeatable without photochemical damage of the molecule. Examples for compounds fulfilling these requirements are, e.g., the so-called fulgides [88], diarylethene [89] and dithienylethene (cf. Fig. 4.3) derivatives.

There are examples for the optical switching of many different molecular properties.

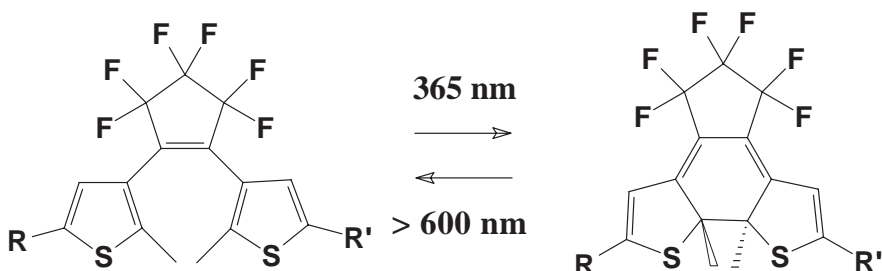


Figure 4.3: A photochromic group (dithienylethene).

Compounds consisting of a donor and acceptor group for excitational energy, linked by a fulgide moiety, are known where the state of the fulgide (i.e. closed, conjugated or open, “disrupted”  $\pi$  system) decides whether the energy transfer can proceed from the donor to the acceptor group via an energetically intermediate state of the fulgide or not [88]. Other simple examples for switchable “molecular wires” are dithienylethenes which mediate the electron transfer between a suited donor and acceptor [90]. Much research is also done on photochromic biomolecules [91, 92]. The integration of photoisomer-

izable groups into biomolecules facilitates the switching of functions like biocatalysis, electron transfer or the specific binding to substrates. Notably, also the primary process of vision is based on the action of the molecular switch 11-cis-retinal. Even the functionalization of peptides or protein fragments which recognize specific DNA sequences (very similar to the ones discussed in chapter 3!) with photoswitchable groups has been achieved [93, 94]. This might lead the way to synthetic transcription factors that can be addressed by application of a light pulse. Recently, also the reversible photoswitching of a GFP-like fluorescent protein was reported which might serve as a valuable tool in future single molecule fluorescence imaging or even as the basis of a high-density optical data storage [95].

An important property of supramolecular systems (like the calixarenes discussed in

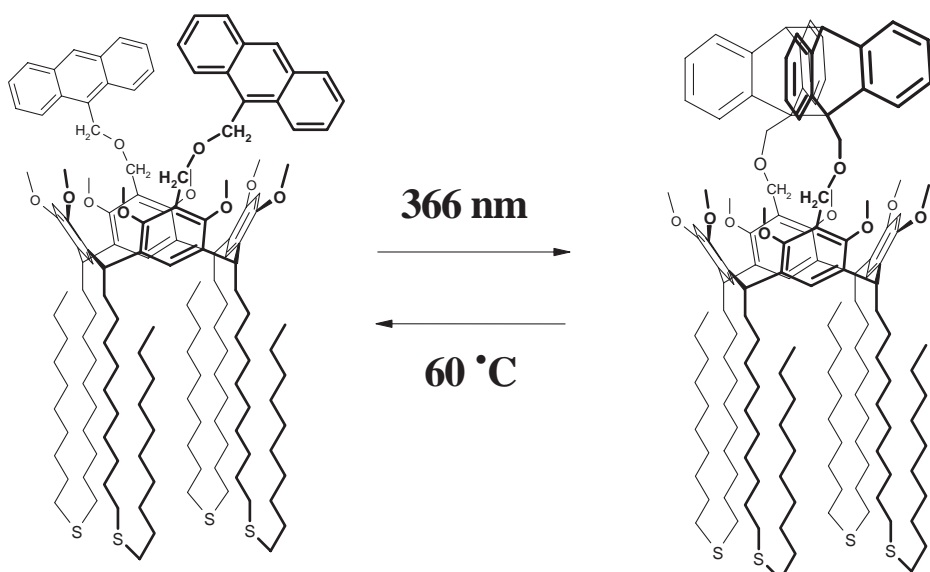


Figure 4.4: Design of a resorc[4]arene photoswitch for self-assembly.

the previous chapter) which can be modulated by optical switching is the affinity to a certain guest molecule. In such a system, the information “ligand bound to cavity” or “cavity empty” can be stored in a single molecule; if the optical switching is reversible, the system can be set and reset. A photoswitchable resorc[4]arene was designed which bears a photoisomerizable group at the upper rim, consisting of two anthryl (anthracene) groups in the open form and a closed anthraquinone-like ring system in the closed form (Fig. 4.4). By irradiation at 360-370 nm, the transition from the open to the closed isomer, a [4+4] photodimerization, is effected. Re-opening of the ring is possible by irradiation below 270 nm or by the transfer of thermal energy. In the open form, the compound presents a cavity for the specific binding of ammonium ions, in the closed

configuration, the cavity is blocked. The affinity modulation of this supramolecular optical switch was studied with SMFS.

## 4.2 Publication V

**Rainer Eckel**, Robert Ros, Björn Decker, Jochen Mattay, and Dario Anselmetti. Supramolecular chemistry at the single molecule level. *Angew. Chem. Int. Ed.* 44 (2005), 484-488.

### 4.2.1 Contribution

All experimental work and data analysis performed by the author.

**Supramolecular Chemistry at the Single-Molecule Level\*\***

Rainer Eckel, Robert Ros, Björn Decker,  
Jochen Mattay,\* and Dario Anselmetti\*

In supramolecular chemistry<sup>[1]</sup> synthetically designed organic constituents interact noncovalently, in a directed and specific way to form host–guest complexes of higher complexity. The ability to tailor the molecular interplay with respect of chemical design, specificity, and molecular switching opens up the development of new molecular materials for artificial molecular recognition, molecular organization, and self-assembly. We have used mechanical single-molecule force spectroscopy to investigate the binding of individual resorc[4]arene-ligand host–guest complexes. By using diluted samples of the host and guest molecules that are modified with a long linker which is attached to an atomic force microscope (AFM) tip, we were able to prevent multiple binding and to observe single host–guest unbinding events in a supramolecular system for the first time. The molecular binding forces, their dependence on external loading rates, the rate of dissociation, and the molecular cavity length directly relate to the molecular properties of the supramolecular species and are consistent with an activated decay of a metastable bound state, a finding already established for biological receptor–ligand complexes. This result allows new insights into the mechanisms, kinetics, and thermodynamics of intermolecular association in chemistry and biology, and opens new possibilities in the investigation, design, and development of synthetic receptor systems.

Calixarenes are model receptor systems providing synthetic receptor cavities for the inclusion of small cationic guests, such as alkali-metal or ammonium ions.<sup>[2–5]</sup> Organic cations, such as ammonium ions, play a significant role in molecular recognition processes in nature (e.g. in protein side chains). Calix[n]arenes, generally, are a class of macrocyclic compounds formed by the base-catalyzed condensation of *n*-phenol derivatives and formaldehyde.<sup>[2,3]</sup> The resorc[4]arenes<sup>[6,7]</sup> considered herein are calixarenes formed from four

[\*] Dipl.-Chem. R. Eckel, Priv.-Doz. Dr. R. Ros, Prof. Dr. D. Anselmetti  
Experimental Biophysics and Applied Nanoscience  
Bielefeld University  
Universitätsstrasse 25, 33615 Bielefeld (Germany)  
Fax: (+49) 521-106-2959  
E-mail: dario.anselmetti@physik.uni-bielefeld.de  
Dipl.-Chem. B. Decker, Prof. Dr. J. Mattay  
Organic Chemistry  
Bielefeld University  
Universitätsstrasse 25, 33615 Bielefeld (Germany)  
Fax: (+49) 521-106-6417  
E-mail: mattay@uni-bielefeld.de

[\*\*] Financial support from the Deutsche Forschungsgemeinschaft (SFB 613) is gratefully acknowledged.

 Supporting information for this article is available on the WWW under <http://www.angewandte.org> or from the author.

resorcinol building blocks linked by methine groups. This structure leaves degrees of freedom for rotation around the methine C–C bonds, which results in five discernible conformations: crown ( $C_{4v}$ ), boat ( $C_{2v}$ ), chair ( $C_{2h}$ ), diamond ( $C_s$ ), and saddle ( $D_{2d}$ ). A means to constrain this conformational flexibility in resorc[4]arenes is to link the hydroxy groups at the upper rim of the molecule, to form ether bridges. In this way, the molecule is fixed in the crown conformation, a so-called cavitand,<sup>[8]</sup> and the rigid cavity of this host serves as a template for the inclusion of small guest ions. The binding of cations to the resorc[4]arene cavitand is facilitated by ion-dipole interactions, although hydrogen bonds and cation- $\pi$  interactions between the positive charge of the ion and the cavitand with the aromatic rings also have considerable influence.<sup>[9]</sup> The specificity of the binding is governed by the steric complementarity of the host and guest: only cations small enough to fit into the tailored cavity are recognized by the resorc[4]arene cavitand receptor. In our experiments the 2,8,14,20-tetra-(10-(decylthio)decyl) cavitand, which has a calculated cavity width of 0.7 nm, serves as a host and its specific recognition of ammonium ions and ammonium-ion derivatives is tested (Figure 1).<sup>[9]</sup>

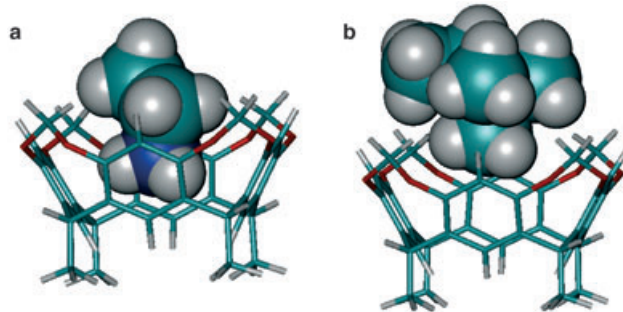


**Figure 1.** Gas-phase structure for the complex formed by the cavitand with a) an ethyl ammonium ion and b) an ethyl trimethyl ammonium ion. Structure optimized at the B3LPY/3-21G\* level.

To investigate these interactions we applied single-molecule force spectroscopy, a method which uses the deflection of an AFM cantilever to measure minute forces in the pico-Newton (pN) range under physiological conditions. In combination with its sub-nanometer spatial resolution, single-molecule force spectroscopy provides, in contrast to standard ensemble experiments, a potent tool to address and manipulate single molecules and investigate forces within and between individual molecules, to yield information about the molecular energy landscape. During the last fifteen years, AFM spectroscopy and related single-molecule techniques based on ultra-sensitive force probes have found applications in the study of molecular recognition and of the specific bond formation in a variety of systems, such as biotin–streptavidin/avidin,<sup>[10,11]</sup> antibody–antigen,<sup>[12–15]</sup> selectin–ligand,<sup>[16]</sup> DNA–protein,<sup>[17]</sup> between individual strands of DNA,<sup>[18,19]</sup> and cell-adhesion proteoglycans.<sup>[20]</sup>

Similarly, host–guest interactions in supramolecular systems have been investigated on  $\beta$ -cyclodextrin–ferrocene<sup>[21–23]</sup> and [18]crown-6–ammonium systems.<sup>[24,25]</sup> In both cases

single-molecule host–guest interaction could only be identified by a statistical analysis of the measured force distribution histograms, however, with no evidence of a loading-rate-dependent force spectrum, which could account for a thermally driven unbinding and give access to the energy landscape of this interaction. In contrast to these experiments, we used diluted cavitand monolayers on a gold surface in a 1:40 mixture with didecylsulfide. The guest ions (ammonium, trimethyl ammonium, and triethyl ammonium, each carrying one additional functional group) were covalently attached to the AFM tip with a flexible poly(ethylene glycol) (PEG) linker (Figure 2). This method introduces more steric flexi-

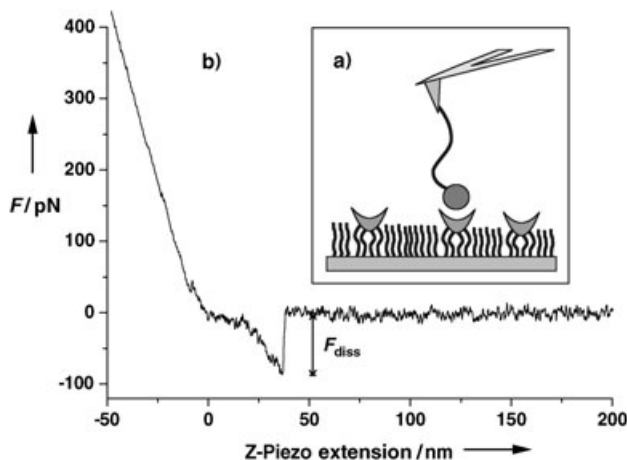


**Figure 2.** Force spectroscopy: a) schematic setup. The cavitand is immobilized together with didecylsulfide in a 1:40 mixture on a gold substrate. The (tetraorganyl) ammonium residue (shaded circle), is attached to an  $\text{Si}_3\text{N}_4$  AFM tip by a flexible polymer linker. b) Typical force–distance curve (only retractive trace shown). The stretching of the PEG linker over a certain distance prior to bond rupture (tip detachment and relaxation of the cantilever) indicates an unbinding event.

bility which facilitates complex formation and supports binding of a single host–guest pair and its proper identification. The functionalized AFM tip was repetitively approached to and retracted from the cavitand surface (in ethanol) at an adjustable but constant velocity.

Molecular unbinding events could be identified by plotting the force response of the AFM cantilever against the z-position of the piezo actuator (of the cavitand surface; Figure 2). The elastic stretching of the PEG spacer before the point of detachment, which shows an elasticity curve in accordance with the wormlike-chain polymer-elasticity model, served as the criterion to discriminate real single-binding events from unspecific adhesion. Since the molecular unbinding process is of stochastic nature, rupture forces from many rupture events (typically 200) were compiled in a force histogram. The mean value resulting from a single-nodal Gaussian fit to the histogram distribution is the most probable unbinding force. The experimental error is based on the statistical error (standard variation) and the uncertainty in the effective spring constant of the cantilever; the errors given

below for the thermal dissociation (off rate) at zero force and the width of the binding pocket are derived from these values by error propagation.

Figure 3 shows three force histograms for the binding of the cavitand to ammonium, trimethyl ammonium, and

triethyl ammonium residues. The histograms show the unbinding probability  $P$  versus force  $F$  in pN. The histograms for ammonium (a,c,e) show a broad distribution with a peak around 100 pN. The histograms for trimethyl ammonium (d,f) show a narrower distribution with a peak around 100 pN. The histograms for triethyl ammonium (g,i) show a very narrow distribution with a peak around 100 pN. The histograms for ammonium in ethanol (a,d,g) show a higher unbinding probability than the histograms for ammonium in ethanol saturated with free ions (b,e,h). The histograms for triethyl ammonium in ethanol (g) show a lower unbinding probability than the histograms for triethyl ammonium in ethanol saturated with free ions (i).

According to the thermally driven unbinding theory of an activated decay of a metastable bound state<sup>[26,27]</sup> the measured forces are not constant and depend on the temporal force evolution on the molecular complex, which is referred to as the loading rate, and can be calculated from the experimental velocity multiplied by the molecular elasticity. The elasticity of the molecular system was obtained from the slope of the force–distance curves (corrected for molecular extension) for the last 20 data points prior to detachment of the cantilever. The loading rate then was given by the system elasticity multiplied by the retract velocity.

With dynamic force spectroscopy (force-loading-rate plots) details about the kinetics of the binding and information concerning the length scale of the interaction can be extracted. The results for the natural thermal off-rates are presented in Figure 4, yielding  $k_{\text{off}} = (0.99 \pm 0.81) \text{ s}^{-1}$  for the ammonium and  $k_{\text{off}} = (1.87 \pm 0.75) \times 10^{-2} \text{ s}^{-1}$  for the trimethyl ammonium residue, resulting in a bond lifetime of  $\tau = 1.01 \text{ s}$  (for the ammonium residue) and  $\tau = 53.5 \text{ s}$  (trimethyl ammonium residue). This finding,

together with the results of the competition experiments, indicate that the trimethyl ammonium residue fits more

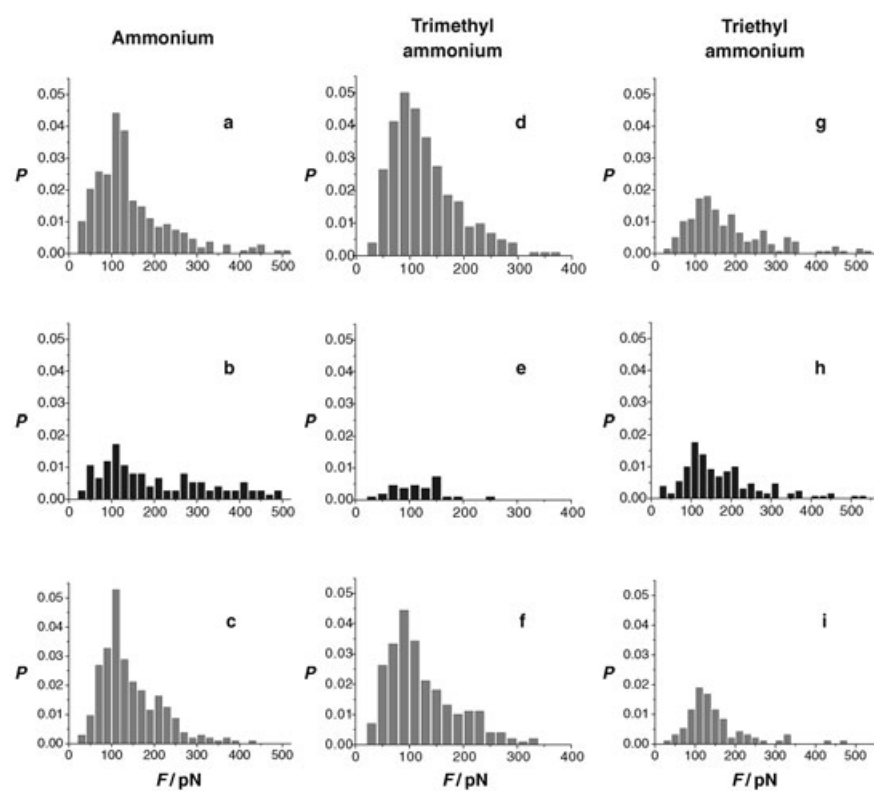


**Figure 3.** Force spectroscopy experiments in ethanol (a,d,g), in ethanol saturated with the respective free ions (b,e,h), washing with ethanol restored the original unbinding probability  $P$  (c,f,i).

triethyl ammonium residues and the corresponding competition experiments. The total unbinding probability (that is, the total number of identified rupture events divided by the number of approach–retract cycles) for the ammonium and trimethyl ammonium residues both amount to approximately 25 %. As a control experiment for validating the specificity of the host–guest interaction, free ammonium or tetramethyl ammonium ions were added to the solvent as competing ligands. In both cases the total (integrated) unbinding probability was significantly reduced. The effect was stronger for solvent saturated with the tetramethyl ammonium ion (Figure 3b,e). After washing tip and sample again with the original solvent (ethanol without competitor), the systems could be reactivated to their full former unbinding functionality (Figure 3c,f). This effect of the free ions competing with the modified ions linked to the AFM tip demonstrates the specificity of the molecular recognition between the host and guest.

For the triethyl ammonium residue, the results are different. From Figure 3, it can be seen that the integrated unbinding probability is much lower for this system than for the ammonium or tetramethyl ammonium ions, whereas the

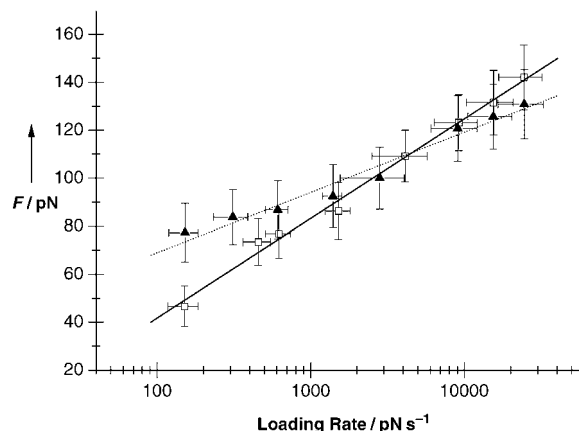


**Figure 4.** The unbinding forces, plotted logarithmically against the corresponding loading rates, for the binding of the ammonium ( $\square$ ) and trimethyl ammonium ( $\blacktriangle$ ) residues to the resorc[4]arene cavitand. For details see text.

tightly into the receptor cavity, that is, its complexation is accompanied by a greater rise in binding affinity than for ammonium. In receptor–ligand interactions, the interaction affinity (equilibrium constant of dissociation  $K_{\text{diss}} = k_{\text{off}}/k_{\text{on}}$ ) is mostly dominated (and varied) by the reaction off-rate  $k_{\text{off}}$ , whereas the values for the reaction on-rate  $k_{\text{on}}$  do not exhibit such a drastic variation.<sup>[13]</sup> Assuming a diffusion-limited association with a typical on-rate for a ligand binding to a receptor pocket of  $k_{\text{on}} = 10^5 \text{ M}^{-1} \text{s}^{-1}$ ,<sup>[13,28]</sup> we can deduce equilibrium constants of  $K_{\text{diss}} = 0.99 \text{ s}^{-1}/10^5 \text{ M}^{-1} \text{s}^{-1} \approx 10^{-5} \text{ M}$  for ammonium ions and  $K_{\text{diss}} = 2 \times 10^{-2} \text{ s}^{-1}/10^5 \text{ M}^{-1} \text{s}^{-1} = 2 \times 10^{-7} \text{ M}$  for trimethyl ammonium ions. From the equilibrium constants for these host–guest systems the Gibbs' free energy difference  $\Delta G = RT \ln K_{\text{diss}}$  can be derived, which gives a rough estimate of the related binding energies of  $\Delta G \approx -28 \text{ kJ mol}^{-1}$  (ammonium) and  $\Delta G \approx -38 \text{ kJ mol}^{-1}$  (trimethyl ammonium). These values for  $\Delta G$  correspond well with calorimetric or NMR spectroscopic data obtained for related supramolecular systems, such as cyclodextrins<sup>[23,29]</sup> and water-soluble cavitands.<sup>[30]</sup> This aspect is important for two reasons: 1) it shows that AFM force spectroscopy can be used to investigate single-molecule affinity interactions in a broad affinity range of ten orders of magnitude ( $10^{-15} \text{ M}$  (biotin-streptavidin) to  $10^{-5} \text{ M}$  (this work)), and 2) that this technique allows the estimation of equilibration constants and related binding energies of single (supra)molecular complexes. This factor is of broad interest, since a determination of reaction equilibrium constants and associated binding energies of ionic binding partners with a wide variation in solubility, for example, by NMR spectroscopic titration experiments, is extremely difficult to accomplish, and no corresponding values for our system are known to us.

From the inverse slope of the loading-rate dependency the molecular reaction lengths (width of binding pocket) can be extracted yielding  $x_\beta = (0.22 \pm 0.04) \text{ nm}$  for ammonium, and  $x_\beta = (0.38 \pm 0.06) \text{ nm}$  for the trimethyl ammonium ions. These values are qualitatively comparable with calculated van der Waals diameters of 0.3 nm for ammonium and 0.6 nm for trimethyl ammonium.<sup>[9]</sup> Therefore we can conclude that the steric complementarity of the host and guest plays an important role in the interaction, with cation–π interactions contributing considerably to the molecular binding mechanism. This finding is also consistent for the interaction of the trimethyl ammonium residue with the cavitand because a the positive-charge distribution has been shown to reside on the hydrogen atoms of the methyl groups.<sup>[31,31]</sup>

In summary, we could show that the specific interaction and dissociation of single guest molecules and their host receptors in supramolecular systems are consistent with an activated decay of a metastable bound state and obey the laws of thermally driven unbinding, as predicted theoretically and verified in biological ligand–receptor systems. The measured reaction lengths were compatible with the calculated van der Waals diameters of the corresponding guest ligands, and give a rough estimate of how deep a ligand enters the receptor site of a calixarene cavitand. The measured single-molecule kinetic reaction rates are consistent with the expected nature of a moderate-affinity host–guest interaction, whereas a clear affinity ranking between the probed host ligands by

single-molecule force spectroscopy was possible for the first time.

Received: July 21, 2004

**Keywords:** atomic force microscopy · calixarenes · host–guest systems · single molecules · supramolecular chemistry

- [1] a) J.-M. Lehn, *Supramolecular Chemistry*, VCH, Weinheim, 1995; b) F. Vögtle, *Supramolecular Chemistry*, Wiley, Chichester, 1991; c) J. L. Atwood, J. E. D. Davies, D. D. Macnicol, F. Vögtle, J.-M. Lehn, *Comprehensive Supramolecular Chemistry*, Pergamon, New York, 1996; d) J. W. Steed, J. L. Atwood, *Supramolecular Chemistry*, Wiley, Chichester, 2000; e) E. Fischer, *Ber. Dtsch. Chem. Ges.* **1894**, 27, 2985–2993; f) P. Ehrlich, *Klin. Jahrb.* **1897**, 6, 299–326; g) A. Werner, *Ber. Dtsch. Chem. Ges.* **1907**, 40, 15–69.
- [2] C. D. Gutsche, *Calixarenes*, Royal Society of Chemistry, Cambridge, 1989.
- [3] C. D. Gutsche, *Calixarenes Revisited*, Royal Society of Chemistry, Cambridge, 1998.
- [4] J. Vicens, V. Böhmer, *Calixarenes. A Versatile Class of Macroyclic Compounds*, Kluwer, Dordrecht, 1991.
- [5] L. Mandolini, R. Ungaro, *Calixarenes in Action*, Imperial College Press, London, 2000.
- [6] V. Böhmer, *Angew. Chem.* **1995**, 107, 785–818; *Angew. Chem. Int. Ed. Engl.* **1995**, 34, 713–745.
- [7] P. Timmerman, W. Verboom, D. N. Reinhoudt, *Tetrahedron* **1996**, 52, 2663–2704.
- [8] D. J. Cram, S. Karbach, H. E. Kim, C. B. Knobler, E. F. Maverick, J. L. Ericson, R. C. Helgeson, *J. Am. Chem. Soc.* **1988**, 110, 2229–2237.
- [9] A. B. Rozhenko, W. W. Schoeller, M. C. Letzel, B. Decker, C. Agena, J. Mattay, unpublished results.
- [10] G. U. Lee, D. A. Kidwell, R. J. Colton, *Langmuir* **1994**, 10, 354–357.
- [11] E.-L. Florin, V. T. Moy, H. E. Gaub, *Science* **1994**, 264, 415–417.
- [12] P. Hinterdorfer, W. Baumgartner, H. Gruber, K. Schilcher, H. Schindler, *Proc. Natl. Acad. Sci. USA* **1996**, 93, 3477–3481.
- [13] F. Schwesinger, R. Ros, T. Strunz, D. Anselmetti, H.-J. Güntherodt, A. Honegger, L. Jermutus, L. Tiefenauer, A. Plückthun, *Proc. Natl. Acad. Sci. USA* **2000**, 97, 9972–9977.
- [14] U. Dammer, M. Hegner, D. Anselmetti, P. Wagner, M. Dreier, W. Huber, H.-J. Güntherodt, *Biophys. J.* **1996**, 70, 2437–2441.
- [15] R. Ros, F. Schwesinger, D. Anselmetti, M. Kubon, R. Schäfer, A. Plückthun, L. Tiefenauer, *Proc. Natl. Acad. Sci. USA* **1998**, 95, 7402–7405.
- [16] J. Fritz, A. G. Katopodis, F. Kolbinger, D. Anselmetti, *Proc. Natl. Acad. Sci. USA* **1998**, 95, 12283–12288.
- [17] F. W. Bartels, B. Baumgarth, D. Anselmetti, R. Ros, A. Becker, *J. Struct. Biol.* **2003**, 143, 145–152.
- [18] G. U. Lee, L. A. Chrisey, R. J. Colton, *Science* **1994**, 266, 771–773.
- [19] T. Strunz, K. Oroszlan, R. Schäfer, H.-J. Güntherodt, *Proc. Natl. Acad. Sci. USA* **1999**, 96, 11277–11282.
- [20] U. Dammer, O. Popescu, P. Wagner, D. Anselmetti, H.-J. Güntherodt, G. N. Misevic, *Science* **1995**, 267, 1173–1175.
- [21] H. Schönher, M. W. J. Beulen, J. Bügler, J. Huskens, F. C. J. M. van Veggel, D. N. Reinhoudt, G. J. Vancso, *J. Am. Chem. Soc.* **2000**, 122, 4963–4967.
- [22] S. Zapotoczny, T. Auletta, M. R. de Jong, H. Schönher, J. Huskens, F. C. J. M. van Veggel, D. N. Reinhoudt, G. J. Vancso, *Langmuir* **2002**, 18, 6988–6994.
- [23] T. Auletta, M. R. de Jong, A. Mulder, F. C. J. M. van Veggel, J. Huskens, D. N. Reinhoudt, S. Zou, S. Zapotoczny, H. Schönher,

- G. J. Vancso, L. Kuipers, *J. Am. Chem. Soc.* **2004**, *126*, 1577–1584.
- [24] S. Kado, K. Kimura, *J. Am. Chem. Soc.* **2003**, *125*, 4560–4564.
- [25] S. Kado, K. Yamada, K. Kimura, *Langmuir* **2004**, *20*, 3259–3263.
- [26] G. I. Bell, *Science* **1978**, *200*, 618–627.
- [27] E. Evans, K. Ritchie, *Biophys. J.* **1997**, *72*, 1541–1555.
- [28] M. Schlosshauer, D. Baker, *Protein Sci.* **2004**, *13*, 1660–1669.
- [29] L. A. Godínez, L. Schwartz, C. M. Criss, A. E. Kaifer, *J. Phys. Chem. B* **1997**, *101*, 3376–3380.
- [30] T. Haino, D. M. Rudkevich, A. Shivanuk, K. Rissanen, J. Rebek, Jr., *Chem. Eur. J.* **2000**, *6*, 3797–3805.
- [31] C. A. Deakyne, M. Meot-Ner (Mautner), *J. Am. Chem. Soc.* **1985**, *107*, 474–479.
- [32] H. J. Schneider, T. Schiestel, P. Zimmermann, *J. Am. Chem. Soc.* **1992**, *114*, 7698–7703.

### 4.3 SMFS Experiments with a Photoswitchable Resorc[4]arene

In recent experiments, the photochemical switching of the resorc[4]arene presented in chapter 4.1.3 was investigated at the single molecule level by SMFS. These experiments proved that the switching of the anthracene moiety at the resorc[4]arene upper rim by means of heat and ultraviolet (UV) irradiation is remarkably efficient and, moreover, reversible.

Fig. 4.5 presents the UV absorption spectrum of the resorc[4]arene photoswitch. Prominent are the peaks between 310 and 400 nm in the near UV, which are due to excitations into different vibrational energy levels of the excited electronic state of the anthryl group aromatic ring system which is covalently linked to the upper rim of the molecule. Optical switching, i.e. the transition to the closed form of the resorc[4]arene, proceeds from this excited state. The absorption below 300 nm (which both isomers show) is due to excitations of the cavity macrocycle and does not lead to photoisomerization.

Fig. 4.6 schematically shows the design of the SMFS experiments with the resorc[4]arene

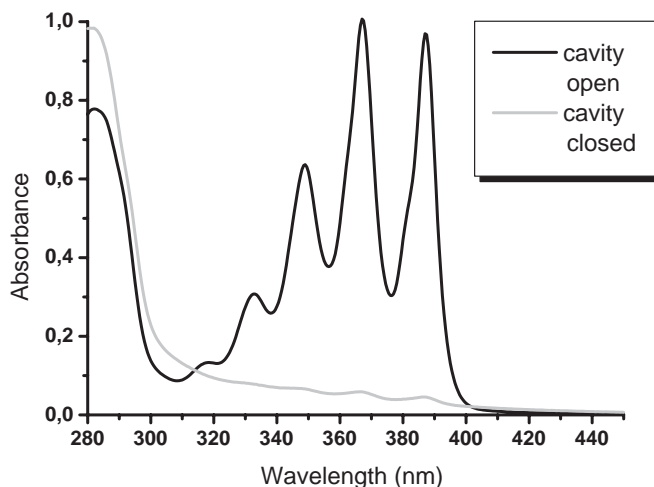


Figure 4.5: UV absorption spectrum of the resorc[4]arene photoswitch in the open and closed forms. The peaks in the near UV for the open form are a characteristic of the anthracene moieties.

photoswitch. In principle, the same setup was used as for the experiments on the resorc[4]arene cavitand complexes with different (tetraorganyl)ammonium guests reported in publication V. A self-assembled monolayer consisting of the resorc[4]arene function-

alized with four didecylsulfide linkers at the lower rim and the free sulfide in a ratio of 1:40 covered a gold surface, an ammonium ion was attached via an organic residue and a PEG linker to the AFM tip. The switching from closed to open form was achieved by heating the sample to 60°C for 2 h, the cavity was closed by irradiating with a UV lamp at  $(368 \pm 7)$  nm for 5 min.

Five series of SMFS experiments were performed (Fig. 4.7). The first series was mea-

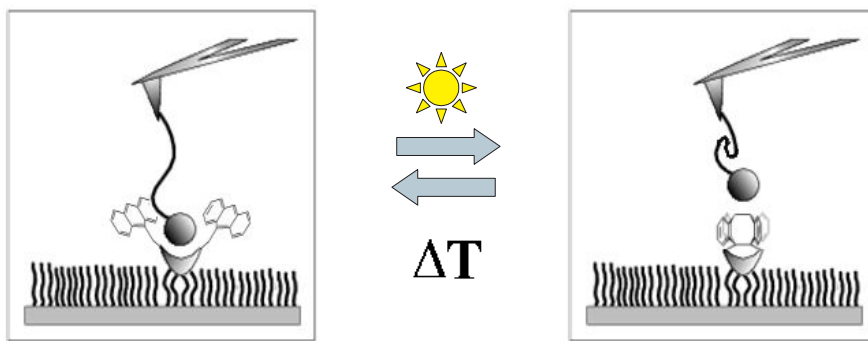


Figure 4.6: Scheme of the SMFS experiments with the resorc[4]arene photo-switch

sured on the open form (Fig. 4.7 (a)), i.e. after heating. The number of rupture events was high enough to analyze them by fitting a Gaussian to the histogram, yielding an overall binding probability of 9.1% and a most probable force of 101 pN at a loading rate of  $5260 \text{ pN s}^{-1}$ . Then the sample was irradiated with UV light, and subsequently a new SMFS series was recorded, resulting in the histogram shown in Fig. 4.7 (b). It is evident that the probability of dissociation (and hence, binding) events was significantly lowered after irradiation (to 0.9%); the very small number of events that still could be detected might be due either to incomplete closing or to gradual re-opening of the system. For the next series (Fig. 4.7 (c)), the sample was heated again for two hours. The resulting force histogram, which is very similar to the first one (total unbinding probability of 9.6%), clearly indicates that the re-opening was successful. In the next experimental series, a competition experiment was performed, where the ethanolic solution was exchanged by an ethanolic solution saturated with ammonium chloride (Fig. 4.7 (d)). The free, unfunctionalized ions compete for binding sites with the ions linked to the AFM tip. The competition lowered the overall binding probability significantly (to 1.4%), though not to the extent which was observed after UV radiation (Fig. 4.7 (b)). After washing the sample with ethanol, a last SMFS series was performed (4.7 (e)). The overall binding probability for the open system without competitor could be recovered (9.5%).

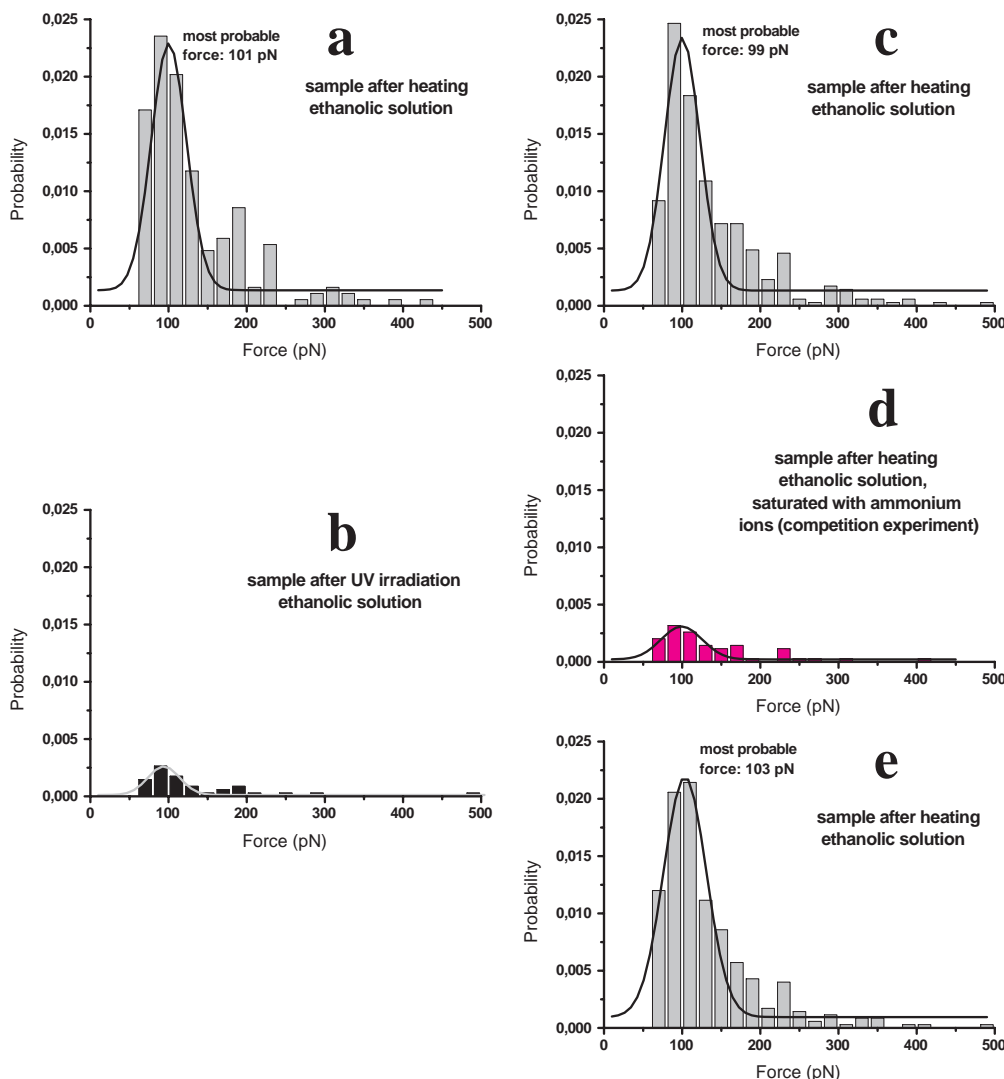


Figure 4.7: SMFS experiments with the resorc[4]arene photoswitch. (a) Experiment after heating the sample to 60°C for 2 h. (b) Experiment after irradiating the sample at 368 nm for 5 min. (c) Experiment after renewed heating the sample for 2 h. (d) Competition experiment in ethanol saturated with free ammonium as competitor. (e) Experiment after washing the sample with ethanol to remove bound free ammonium. All experiments were performed with the same tip and sample (loading rate: 5260 pN).

These experiments prove four statements:

- The resorc[4]arene can be switched between two different isomers.
- The switching is reversible.
- One of the two isomers has a high affinity to ammonium, the other one almost none.
- The binding of the ammonium-functionalized AFM tip to the high-affinity isomer can be hindered by adding competing free ammonium, i.e. the binding observed is ammonium-specific.

These findings can be explained if one adopts the hypothesis for the photochemical behavior of the resorc[4]arene compound which was formulated a priori (Fig. 4.4).

### 4.3.1 Materials and Methods

**Sample preparation.** Gold coated sample substrates ( $11 \cdot 11 \text{ mm}^2$ , Arrandee) were incubated with 2,8,14,20-tetra-(10-(decylthio)decyl) resorc[4]arene and didecylsulfide in a molar ratio of 1:40, solubilized in ethanol/chloroform (1:1), by heating to  $60^\circ\text{C}$  for at least 16 h, which is essential for obtaining highly ordered monolayers [96].

**Tip preparation.**  $\text{Si}_3\text{N}_4$  tips (Microlevers, Veeco) were functionalized with APTES and a bifunctional PEG linker according to the protocol described in chapter 3.3.1. The cantilevers were washed with water and functionalized by incubating them overnight at room temperature with a 1 mM ethanolic solution of 2-mercaptoethylamine hydrochloride (Sigma-Aldrich). Modified tips were stored at  $4^\circ\text{C}$  and remained usable for at least one week. Prior to use in experiment, the cantilevers were washed with ethanol.

**SMFS experiments.** SMFS experiments were performed using the same equipment and setup already described in chapter 3.3.1. Spring constants in the range from 13.8 to 17.9  $\text{pN nm}^{-1}$  were obtained for the cantilevers. All experiments were performed in ethanol. For competition experiments, a saturated ethanolic solution of ammonium chloride was used. Force-distance traces were recorded at a retract velocity of  $1000 \text{ nm s}^{-1}$ .

**Photoisomerization.** The switching from closed to open form was performed by heating the sample to  $60^\circ\text{C}$  for 2 h. Closing the cavity was achieved by irradiation for 5 min with a quartz halogen UV light source (Norland Opticure 4 light gun) which yields  $50 \text{ mW cm}^{-2}$  in the spectral range from 340 to 400 nm. An optical filter (( $368.3 \pm 7.1$ ) nm, UV-PIL, Schott) was prefixed to the UV source.

# 5 An Improved Theory for SMFS Analysis: Heterogeneity of Chemical Bonds

## 5.1 Introduction

The standard theory for the analysis of SMFS experiments which was described in chapter 3.1.3 has experienced several extensions and improvements in the past decade [13, 78, 97, 98, 99, 100, 101]. Nevertheless, in all these theories the physical interpretation of the dissociation process essentially remained unaltered.

In 2003, an optimized method for the analysis of SMFS experiments was proposed [102]. Consider a given data set consisting of  $N_v$  rupture forces  $f_n$  ( $n = 1, \dots, N_v$ ;  $f_n > f_{min}$  for all  $n$ ) measured at a given retract velocity  $v$ . The true probability of bond survival  $p_v(f)$  can be estimated to

$$\tilde{p}_v(f) = \frac{1}{N_v} \sum_{n=1}^{N_v} \Theta(f_n - f) \quad (5.1)$$

where  $\Theta(x) = \int_{-\infty}^x \delta(y)dy$  is the Heaviside step function ( $\Theta(x < 0) = 0$ ,  $\Theta(x = 0) = 1/2$ ,  $\Theta(x > 0) = 1$ ). For  $N \rightarrow \infty$ ,  $\tilde{p}_v(f) \rightarrow p_v(f)$ . For every finite number of rupture events  $N_v$  formula 5.1 is the best estimate for  $p_v(f)$  without any further assumptions. It allows an estimate of the “true” integral in equation 3.20:

$$\tilde{g}_v(f) = -v \ln \tilde{p}_v(f) \quad (5.2)$$

It follows from Evans’ and Ritchie’s assumptions 3.18 and 3.19 that the expression in equation 5.2 must be, apart from statistic fluctuations, *independent* of the pulling velocity  $v$ . The force distributions resulting from different retract velocities, plotted in a diagram  $-v \ln \tilde{p}_v(f)$  against  $f$ , should collapse to a single master curve.

The application of the method to experimental data [103] clearly proved that this is

not the case! This result was verified by extending the analysis to data obtained for a large variety of different ligand-receptor systems (publications IV and V, [25]), even to experiments which were performed using a micropipette rather than an AFM as the force transducer [104].

It can be concluded that the basic postulates of the standard theory must be taken to the test. Since assumption 3.19 is confirmed by the experiment, it must be postulate 3.18 which is the reason for the observed inconsistencies. It could be shown [103] that neither a variation of the threshold value  $f_{min}$  nor the assumption of multiple metastable states can explain the deviations from the predicted master curve satisfactorily.

In this work (publication VI), a new and promising approach is presented which postulates a heterogeneity of chemical bonds to account for the observed inconsistencies. The assumptions 3.18 and 3.19 are basically left unaltered, but an intrinsic random variation of the force-dependent off-rate is allowed for. If  $k_{off}$  varies from experiment to experiment, it is no longer permitted to compare the experimental function  $\tilde{p}_v(f)$  with  $p_v(f)$ ; only a comparison to the value  $\bar{p}_v(f)$  which is an average over the statistically distributed off-rates  $k_{off}(f)$  is feasible.

An intrinsic random distribution of the rate of dissociation  $k_{off}(f)$  due to a heterogeneity of chemical bonds can be justified by several reasons not all of which must needs be present in a real SMFS experiment:

1. Modulations of the local ionic strength or pH due to random fluctuations of the local molecular environment;
2. different conformations of a molecule due to thermally activated structural fluctuations;
3. geometrical variations like, e.g., different orientations of the complex relative to the direction of the applied pulling force;
4. mis-interpretation of nonspecific adhesion as “true” specific binding events;
5. different binding domains of a receptor molecule.

These ideas can be quantified using an ansatz of the form  $k_{off}(f) = k_{off}^0(f; \vec{\lambda})$ . The set of parameters  $\vec{\lambda}$  is randomly distributed with a probability density  $\varrho(\vec{\lambda}, \vec{\mu})$  where  $\vec{\mu}$  is a set of fit parameters. Using equations 3.16 and 3.17, it follows from 3.20 that

$$p_v(f; \vec{\lambda}) = \exp \left[ -\frac{k_{off}^0 k_B T}{x_\beta r} \left( \exp \left( \frac{x_\beta f}{k_B T} \right) - 1 \right) \right] \quad (5.3)$$

and

$$\bar{p}_v(f; \vec{\mu}) = \frac{\int d\vec{\lambda} \varrho(\vec{\lambda}, \vec{\mu}) p_v(f; \vec{\lambda})}{\int d\vec{\lambda} \varrho(\vec{\lambda}, \vec{\mu}) p_v(f_{min}; \vec{\lambda})} \quad (5.4)$$

This means that the proposed bond heterogeneity gives rise to the randomization of the two parameters  $k_{off}^0$  and  $\alpha = x_\beta/k_B T$ , i.e.  $\vec{\lambda} = (k_{off}^0, \alpha)$ .

It can be shown (publication VI) that randomization of  $k_{off}^0$  does not improve the consistency of the theory with experimental data. A randomization of the linker elasticity as proposed by Friedsam et al. [98, 24] essentially corresponds to a randomization of the off-rate and does not explain the phenomenon.

Thus,  $k_{off}^0$  is taken as a fix parameter and counted among the set of parameters  $\vec{\mu} = (k_{off}^0, a, \sigma)$  which determine a (truncated) Gaussian probability distribution of the form

$$\varrho(\alpha; a, \sigma) = N \exp \left[ -\frac{(\alpha - a)^2}{2\sigma^2} \right] \Theta(\alpha) \quad (5.5)$$

where  $a$  and  $\sigma$  approximately correspond to the mean and variance of  $\alpha$  if the relative width  $\sigma/a$  is sufficiently small and  $N$  is a normalization constant. The best fit to the experimental data was achieved using this distribution (publication VI). Additional parameters taking nonlinearities or multiple metastable states into account as well as a simultaneous randomization of  $k_{off}^0$  and  $\alpha$  did not yield a significantly better fit. In summary, it turns out that the crucial fit parameter is the dispersion of the effective dissociation length  $x_\beta$ , a quantity which cannot be determined by the standard method. Even though the standard theory neglects the bond heterogeneity, it is still appropriate to use it for the evaluation of the parameters  $k_{off}^0$  and  $a$ . If the most probable rupture force is determined numerically using the new theory from  $d^2\bar{p}_v(f_0)/df^2 = 0$  and equation 5.4,  $\hat{F}$  still is to a very good approximation given as a linear function of  $\ln(r)$ , though with a somewhat more complicated dependence on the parameters  $(k_{off}^0, a, \sigma)$ . This is also the reason why the inconsistency of the standard theory could not be detected in the  $\hat{F}$  against  $\ln(r)$  plots.

It can be shown that the molecular reaction length  $x_\beta$  can still be determined fairly well even by the standard method, whereas the new theory is clearly superior when it comes to the evaluation of  $k_{off}^0$ .

## 5.2 Publication VI

Martin Raible, Mikhaylo Evstigneev, Frank Wilco Bartels, **Rainer Eckel**, M. Nguyen-Duong, Rudolf Merkel, Robert Ros, Dario Anselmetti, and Peter Reimann. Theoretical analysis of single-molecule force spectroscopy experiments: heterogeneity of chemical bonds. Accepted by *Biophys. J.*

### 5.2.1 Contribution

The author participated substantially in the efforts to explain the heterogeneity of chemical bonds postulated by the novel theory in terms of experimental facts (chapters IVa, VIII). Furthermore, he provided part of the experimental data which were used for the  $-v \ln \tilde{p}_v(f)$  against  $f$  plots (Fig. 5 and 6).

# Theoretical analysis of single-molecule force spectroscopy experiments: heterogeneity of chemical bonds

M. Raible<sup>(1)</sup>, M. Evstigneev<sup>(1)</sup>, F. W. Bartels<sup>(2)</sup>, R. Eckel<sup>(2)</sup>, M. Nguyen-Duong<sup>(3)</sup>, R. Merkel<sup>(3)</sup>, R. Ros<sup>(2)</sup>, D. Anselmetti<sup>(2)</sup>, and P. Reimann<sup>(1)\*</sup>

<sup>(1)</sup>Theoretische Physik, Universität Bielefeld, 33615 Bielefeld, Germany

<sup>(2)</sup>Experimentelle Biophysik, Universität Bielefeld, 33615 Bielefeld, Germany

<sup>(3)</sup>Institute of Thin Films and Interfaces, Research Centre Jülich, 52425 Jülich, Germany

(Dated: October 10, 2005)

We show that the standard theoretical framework in single-molecule force spectroscopy by Evans and Ritchie [Biophys. J. 72, 1541 (1997)] has to be extended in order to consistently describe the experimental findings. The basic amendment is to take into account heterogeneity of the chemical bonds via random variations of the force dependent dissociation rates. This results in a very good agreement between theory and rupture data from several different experiments.

PACS numbers: 82.37.Np, 33.15.Fm, 87.15.By

## I. INTRODUCTION

Dynamic force spectroscopy is a widely used tool for investigating binding properties of biomolecular complexes at the atomic scale by means of the dissociation of single chemical bonds under an external force [1, 2]. Since the first reported ligand-receptor experiments [3–5] the technique has rapidly evolved into a quantitative single molecule binding assay technology giving access to binding forces, molecular elasticities, reaction off-rates, and binding energy landscapes with a sensitivity of single point mutations for single molecule affinity ranking. Essentially, the molecular complex of interest is connected via suitable linkers (spacer molecules) to an atomic force microscope (AFM), see Fig. 1, or a micropipette-based force probe and pulled apart at a constant speed  $v$  while monitoring the acting forces until the chemical bond ruptures.

Since the molecular dissociation process is of stochastic nature, the theoretical interpretation of the observed rupture forces is a non-trivial task: upon repeating the same experiment at the same pulling velocity  $v$  several times, the rupture forces are found to be distributed over a wide range, see Fig. 2. Furthermore, for different pulling velocities  $v$  different such distributions are obtained. Hence, neither a single rupture event nor the average rupture force at any fixed pulling velocity can serve as a meaningful characteristic quantity of a given chemical bond strength.

On the other hand, direct molecular dynamics simulations of the forced dissociation process are still very far from reaching experimentally realistic conditions due to the limited accessible time-scale [6–9]. Hence, non-trivial theoretical modeling steps are unavoidable.

The main breakthrough in solving the puzzle came with the hallmark papers by Bell in 1978 [10] and by

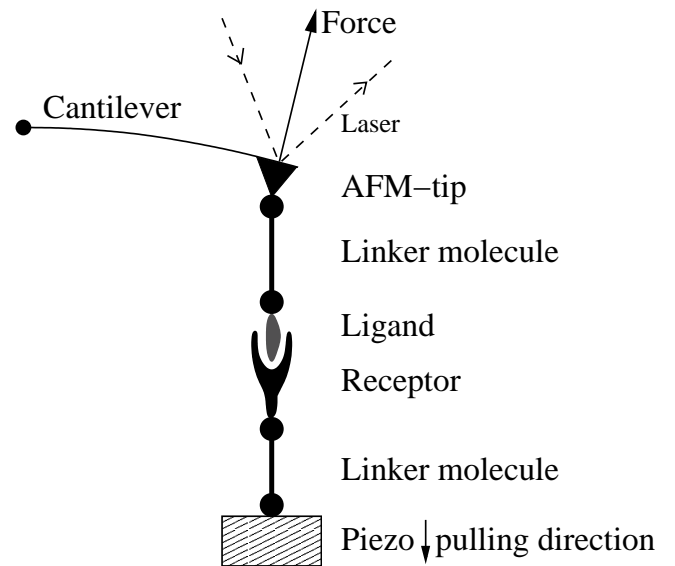


FIG. 1: Schematic illustration of dynamic AFM force spectroscopy: a single chemical bond, e.g. in a ligand-receptor complex, is connected via two flexible linker molecules with the tip of an AFM cantilever and a piezoelectric element. The latter “pulls down” the attached linker molecule at some constant velocity  $v$ . The resulting elastic reaction force of the cantilever can be determined from the deflection of a laser beam. The main quantity of interest is the force value at the moment when the bond dissociates.

Evans and Ritchie in 1997 [11], recognizing that a forced bond rupture event is a thermally activated decay of a metastable state that can be described within the general framework of reaction rate theory [12].

While Evans and Ritchie’s original theoretical approach has been extended and refined in several important directions [1, 2, 13–19], the essential physical picture – henceforth called *standard theory* – has remained unchanged and has been the basis for evaluating the observed rupture data of all experimental investigations

\*E-mail: reimann@physik.uni-bielefeld.de

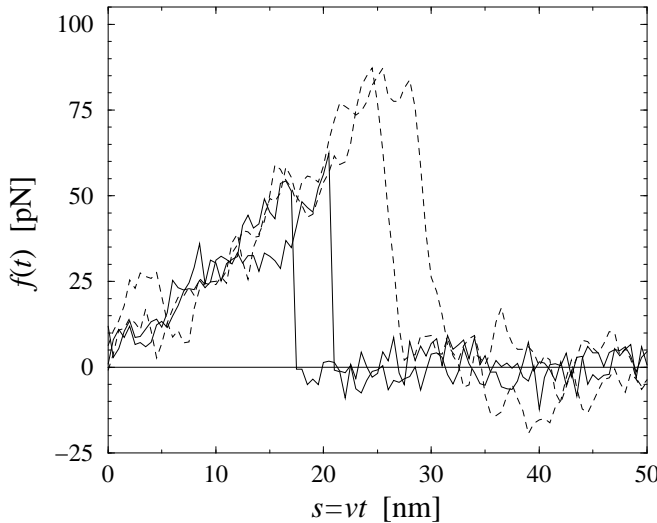


FIG. 2: Force-extension curves of 4 representative single-molecule pulling experiments, 2 with pulling velocity  $v = 100$  nm/s (solid) and 2 with  $v = 5000$  nm/s (dashed), obtained by dynamic AFM force spectroscopy for the DNA fragment *expE1/E5* and the regulatory protein ExpG [24]. The abrupt drop of  $f(t)$  indicates dissociation of the chemical bond between *expE1/E5* and ExpG. Apart from noise effects, the forces  $f(t)$  prior to dissociation (relevant in (1)) collapse quite well to a single force-extension master-curve  $F(s)$ , cf. (2). It can be noted that for a given pulling velocity, the rupture forces are distributed over a considerable range and that larger pulling velocities result in larger average dissociation forces.

ever since [1, 2]. In Sect. II we present this so-called standard theory and its underlying assumptions in more detail. In Sect. III we evaluate rupture data from several different experiments and we show that all of them are incompatible with the basic assumptions of the standard theory. In the central Sect. IV we propose an extension of the standard theory which leads to a very good agreement with the experiments. The basic new idea is to take into account heterogeneity of the chemical bonds by means of a simple and natural phenomenological ansatz to quantify the proposed randomness of the dissociation rates. In Sect. V we show that our theory is largely independent of the details of this phenomenological ansatz. In Sect. VII the previously established standard data analysis procedure is reconsidered from the viewpoint of the new theory. The final Sect. VIII contains our summary and conclusions.

## II. THE STANDARD THEORY

### A. Assumptions

The *standard theory*, which is at the heart of all recent experimental and theoretical studies in the field of single-molecule force spectroscopy [1, 2], is mainly due to Evans

and Ritchie [11]. Adopting the common concepts and notions of equilibrium (static) reaction rate theory [12], a rupture event is viewed as a thermally activated decay of a metastable state, governed by a reaction kinetics

$$\dot{p}(t) = -k(f(t)) p(t) , \quad (1)$$

where  $p(t)$  is the probability of bond survival up to time  $t$  and  $k(f)$  the dissociation rate in the presence of a pulling force  $f$ .

A first assumption implicit in (1) is that the applied force  $f(t)$  changes slowly compared to the molecular relaxation into the accompanying equilibrium of the metastable bound state and also compared to the typical duration of thermally activated transition and decay processes. Second, rebinding after dissociation is neglected because of an immediate separation of the two molecules after their dissociation, see Sect. III B .

Another main ingredient of the standard theory regards the dependence of the force  $f(t)$  in (1) on the pulling velocity  $v$ . Namely, it is assumed that

$$f(t) = F(vt) , \quad (2)$$

where the function  $F(s)$  is independent of  $v$ . In other words, the instantaneous force  $f(t)$  only depends on the externally imposed total extension  $s = vt$  of all elastic components of the setup (molecules, linkers, AFM-cantilever, etc.), but not on the velocity  $v$  at which this extension increases. The theoretical justification is that under realistic conditions all elastic components remain close to their accompanying/instantaneous equilibrium states and hence their previous history does not matter. An experimental verification is provided by Fig. 2, see also [20].

Supplementing the *standard theory* – consisting in the basic assumptions (1) and (2) – by certain additional approximations gives rise to the so-called *standard method* for analyzing rupture force distributions. A more detailed discussion of this method is postponed to Sect. VII.

### B. Implications

Combining (1) and (2), a straightforward calculation yields for the probability  $p_v(f)$  of bond survival up to a force  $f$  (defined via  $p_v(f(t)) = p(t)$ ) the result

$$p_v(f) = \exp \left\{ -\frac{1}{v} \int_{f_{\min}}^f df' \frac{k(f')}{F'(F^{-1}(f'))} \right\} \quad (3)$$

where  $f_{\min}$  denotes the threshold below which rupture events cannot be distinguished from fluctuations in the experiment (e. g.  $f_{\min} \approx 20$  pN in Fig. 2). Accordingly,  $f \geq f_{\min}$  is henceforth tacitly understood in relations like (1) and (3). Furthermore, we assumed  $F(s)$  to be monotonically increasing so that its inverse  $F^{-1}$  exists [21]. For the rest, the force-extension characteristic  $F(s)$  may

be completely arbitrary and the rate  $k(f)$  may describe a completely general activated decay of a metastable state in a high-dimensional potential energy landscape [19, 22]. The only prerequisite for (3) is the validity of (1) and (2). The latter, in turn, is basically tantamount to the requirement of quasi-equilibrium of the entire setup in Fig. 1 (bound complex, linkers, AFM) for all times prior to bond dissociation.

Eq. (3) implies that the function  $-v \ln p_v(f)$  is independent of the pulling velocity  $v$ , resulting in a single master curve, onto which the data points should collapse for all pulling velocities [23]. Next, this conclusion will be used to check the consistency of the standard theory (1), (2) with the experimental data.

### III. INCONSISTENCY WITH EXPERIMENTAL FINDINGS

#### A. Evaluation of experimental data

Given a set of  $N_v$  experimentally observed rupture forces  $f_n$  at a fixed pulling velocity  $v$  ( $n = 1, \dots, N_v$ ,  $f_n > f_{\min}$  for all  $n$ ), we can infer the following estimate  $\tilde{p}_v(f)$  for the “true” bond survival probability  $p_v(f)$ :

$$\tilde{p}_v(f) = \frac{1}{N_v} \sum_{n=1}^{N_v} \Theta(f_n - f) . \quad (4)$$

Here,  $\Theta(x) := \int_{-\infty}^x \delta(y) dy$  is the Heaviside step function with the convention

$$\Theta(0) = 1/2 . \quad (5)$$

By definition,  $\tilde{p}_v(f) \rightarrow p_v(f)$  for  $N_v \rightarrow \infty$  (with probability 1), and for any finite  $N_v$ , (4) is in fact the best estimate for  $p_v(f)$  that can be inferred from the given data without additional a priori assumptions about the system.

In Fig. 3 we have evaluated  $-v \ln(\tilde{p}_v(f))$  for different pulling velocities  $v$  according to (4) for the same experimental system as in Fig. 2 (rupture data obtained by dynamic AFM force spectroscopy for the DNA fragment *expE1/E5* and the regulatory protein ExpG [24]).

In contrast to Eq. (3), the functions  $-v \ln(\tilde{p}_v(f))$  evaluated from the experimental data using Eq. (4) at different values of  $v$  do not collapse onto a single master curve. Rather, increasing the velocity results in an increased value of this function for sufficiently high forces. In view of the very strong dependence of the experimental curves  $-v \ln(\tilde{p}_v(f))$  on the pulling velocities  $v$ , we conclude that the experimental findings are incompatible with (3) and hence with the basic assumptions (1) and (2) of the standard theory [20].

In order to check if this finding depends on the chosen experimental system, we have also evaluated dynamic AFM force spectroscopy data for the dissociation of another DNA fragment from the regulatory protein ExpG

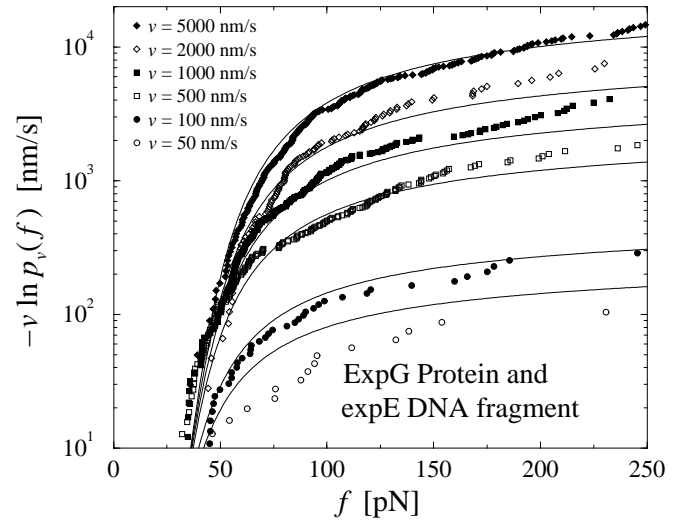


FIG. 3: Symbols: The functions  $-v \ln(\tilde{p}_v(f))$  for different pulling velocities  $v$ , obtained according to (4) from the same experiment [24] as in Fig. 2. Each depicted point corresponds to one rupture event at  $f = f_n$  and hence a step of the piecewise constant function (4). Only  $f_n$  above  $f_{\min} = 20$  pN have been taken into account, see below (3). The number  $N_v$  of experimental data points for the 6 different velocities  $v$  in (4) are:  $N_{50\text{nm/s}} = 20$ ,  $N_{100\text{nm/s}} = 44$ ,  $N_{500\text{nm/s}} = 179$ ,  $N_{1000\text{nm/s}} = 208$ ,  $N_{2000\text{nm/s}} = 108$ ,  $N_{5000\text{nm/s}} = 253$ . A few very small or large  $f_n$  are omitted in this plot for the sake of better visibility of the remaining symbols. Solid lines: Theoretical functions  $-v \ln(\bar{p}_v(f))$  for the same pulling velocities  $v$  as the symbols, using to (9), (11)-(19). For more details see Sect. IV.

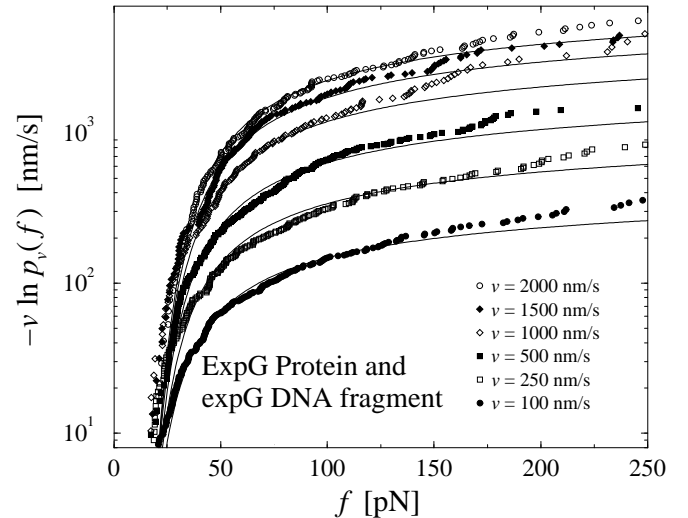


FIG. 4: Same as in Fig. 3 but for dynamic AFM force spectroscopy data by Bartels et al. [24] for the dissociation of the DNA fragment *expG1/G4* from the regulatory protein ExpG. Symbols: The functions  $-v \ln(\tilde{p}_v(f))$  for different pulling velocities  $v$ , obtained according to (4) and taking into account only  $f_n$  above  $f_{\min} = 10$  pN. Solid lines: Theoretical functions  $-v \ln(\bar{p}_v(f))$  for the same pulling velocities  $v$  as the symbols, using (9), (11)-(16), (20).

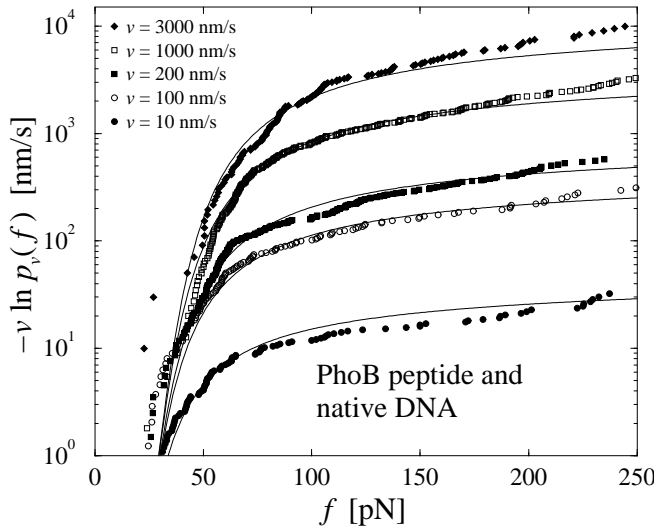


FIG. 5: Same as in Fig. 3 but for dynamic AFM force spectroscopy data by Eckel et al. [25] for the dissociation of the PhoB peptide (wild type) of *E. coli* from the DNA target sequence. Symbols: The functions  $-v \ln(\tilde{p}_v(f))$  for different pulling velocities  $v$ , obtained according to (4) and taking into account only  $f_n$  above  $f_{\min} = 20$  pN. Solid lines: Theoretical functions  $-v \ln(\bar{p}_v(f))$  for the same pulling velocities  $v$  as the symbols, using (9), (11)-(16), (21).

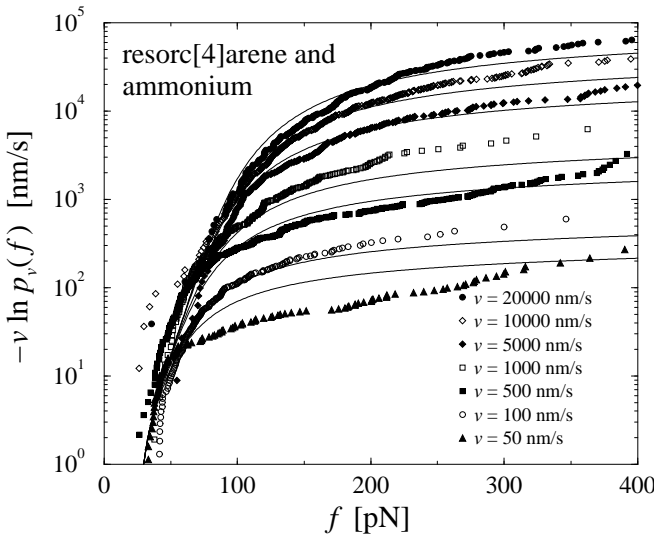


FIG. 6: Same as in Fig. 3 but for dynamic AFM force spectroscopy data by Eckel et al. [26] for the dissociation of a calixaren host molecule (resorc[4]arene) from cationic guest (ammonium). Symbols: The functions  $-v \ln(\tilde{p}_v(f))$  for different pulling velocities  $v$ , obtained according to (4) and taking into account only  $f_n$  above  $f_{\min} = 25$  pN. Solid lines: Theoretical functions  $-v \ln(\bar{p}_v(f))$  for the same pulling velocities  $v$  as the symbols, using (9), (11)-(16), (22).

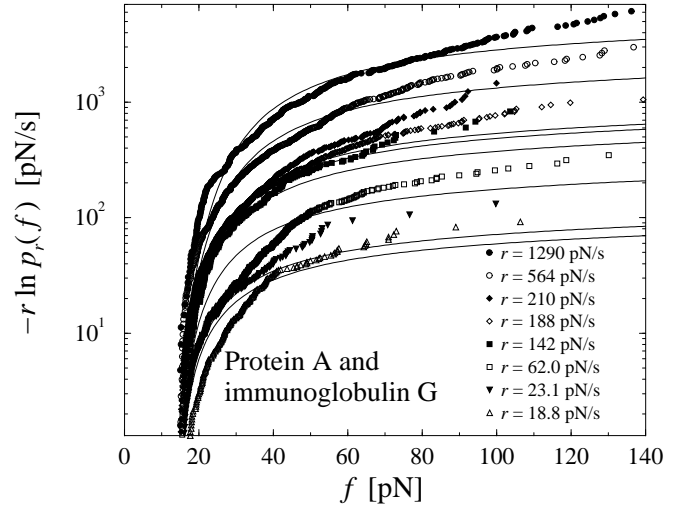


FIG. 7: Same as in Fig. 3 but for micropipette-based force probe data by Nguyen-Duong et al. [19] for the dissociation of immunoglobulin of type G from protein A. Symbols: The functions  $-r \ln(\tilde{p}_r(f))$  for different loading rates  $r$ , see below (6), taking into account only  $f_n$  above  $f_{\min} = 15$  pN. Solid lines: Theoretical functions  $-r \ln(\bar{p}_r(f))$  for the same loading rates  $r$  as the symbols, using (7), (9), (11)-(16), (23).

(see Fig. 4), a PhoB peptide (wild type) from the corresponding DNA target sequence (see Fig. 5), and a cationic guest molecule from a supramolecular calixaren host molecule (see Fig. 6). Since essentially the same linkers have been used in all those AFM-experiments, the force extension curves always look similar to those in Fig. 2. For more experimental details we refer to [24–26].

Furthermore, we have evaluated in Fig. 7 rupture data observed by means of a micropipette-based force probe for the dissociation of a rabbit immunoglobulin of type G from protein A, see [19] for the experimental details. In doing so, we have employed as an additional assumption a linear force-extension characteristic

$$F(s) = \kappa s , \quad (6)$$

where  $\kappa$  is the effective elastic spring constant of the entire setup (bound complex, red blood cell, micorbeads, etc.). Moreover, instead of different pulling velocities  $v$ , we considered different loading rates

$$r := \dot{f}(t) = \kappa v \quad (7)$$

of the force  $f(t)$  in (2). The reason for this modification is that in the experiment from [19], rupture data both for different  $v$  and different  $\kappa$  are available and can be simultaneously evaluated in this way. Namely, by exploiting that  $F'(s) \equiv \kappa$  (independent of  $s$ ) and renaming  $p_v(f)$  as  $p_r(f)$  we can again conclude from (3) that  $-r \ln(\tilde{p}_r(f))$  should be independent of  $r$ .

In all the different experimental systems in Figs. 3–7 we thus recover the same kind of incompatibility with (3) and hence with the basic assumptions (1) and (2) of the standard theory.

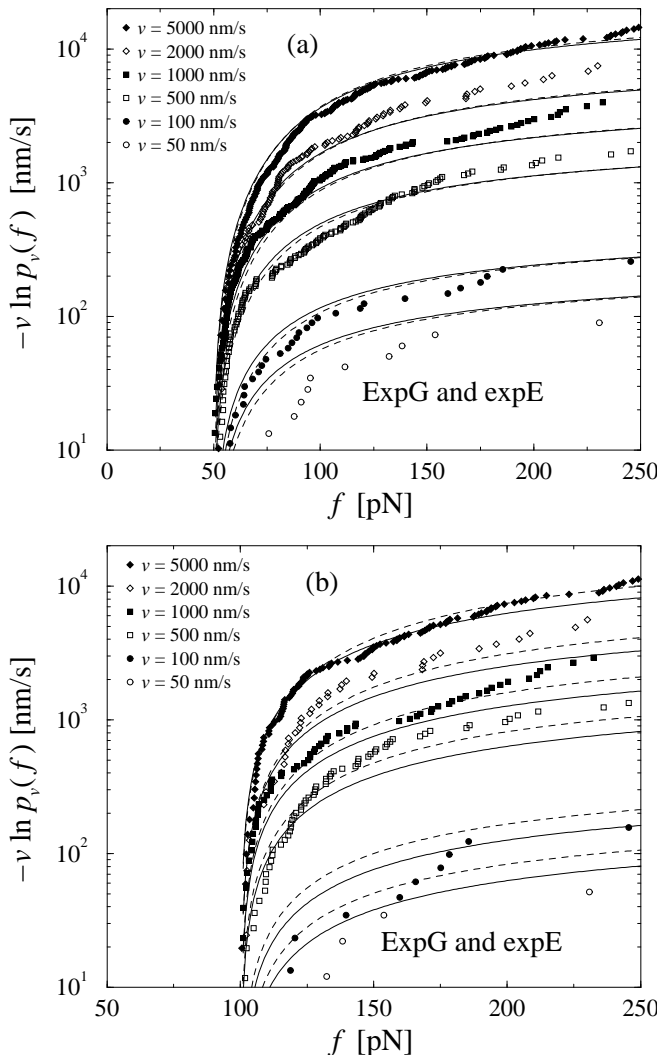


FIG. 8: Symbols: Same as in Fig. 3 except that in (a) only  $f_n$  above  $f_{\min} = 50$  pN and in (b) only  $f_n$  above  $f_{\min} = 100$  pN have been taken into account. The solid lines are the corresponding theoretical functions  $-v \ln(\bar{p}_v(f))$  using (9), (11)-(19). Dashed lines: same as solid lines but after refitting the parameters  $k_0$ ,  $\alpha_m$ ,  $\sigma$  to the given data subset, resulting in  $k_0 = 0.000020 \text{ s}^{-1}$ ,  $\alpha_m = 0.19 \text{ pN}^{-1}$ ,  $\sigma = 0.095 \text{ pN}^{-1}$  for (a), and in  $k_0 = 0.017 \text{ s}^{-1}$ ,  $\alpha_m = 0.091 \text{ pN}^{-1}$ ,  $\sigma = 0.040 \text{ pN}^{-1}$  for (b).

### B. Unsuccessful explanations

Since the incompatibility between experimental findings and the standard theory is essentially of the same character in all the different cases evaluated in Figs. 3-7, we concentrate on one of them, namely, the system from Fig. 3. Moreover, since (2) is verified experimentally by Fig. 2, we can focus on (1) to pinpoint the leakage of the standard theory and possibly repair it.

We first note that only  $f(t)$ -curves surpassing  $f_{\min} = 20$  pN in Fig. 2 have been taken into account in Fig. 3. Hence, rebinding after dissociation would require a huge

and hence extremely unlikely random fluctuation [1, 2] and has indeed never been observed in the experiment at hand. Moreover, upon increasing  $f_{\min}$  we did not observe any clear tendency towards a better data collapse than in Fig. 3, see Fig. 8. In other words, rebinding events are indeed negligible.

Concerning the accompanying equilibrium assumption implicit in (1), the most convincing possibility leading to its failure is the existence of several metastable (sub-) states of the bound complex with relatively slow transitions between them [11, 15, 16, 27] and possibly several different dissociation pathways [28] (see also Sect. VI B). As discussed in detail in [20] one indeed gets a spreading of  $-v \ln(p_v(f))$  for different  $v$  in this way. This spreading is, however, qualitatively quite different from that in Fig. 3 for a generic model with a few “internal states”. With more complex networks of “internal states” – and a concomitant flurry of fit parameters in the form of transition rates between them – a satisfactory fit to the data in Figs. 3-7 may well be possible, but their actual existence in all the different experimental systems seems quite difficult to justify.

For further unsuccessful attempts to quantitatively explain the non-collapse of the data to a single master curve in Figs. 3-7 see [20].

## IV. HETEROGENEITY OF CHEMICAL BONDS

### A. Basic Idea

We now come to the central point of our paper. Namely, we propose *heterogeneity of the chemical bonds* as an explanation of the experimental findings in Figs. 3-7. Basically, this means that (1) and (2) remain valid except that the force dependent dissociation rate  $k(f)$  is subjected to random variations upon repeating the pulling experiment. As a consequence, the experimentally determined  $\tilde{p}_v(f)$  from (4) should not be compared with the function  $p_v(f)$  from (3) but rather with its average with respect to the probability distribution of the rates  $k(f)$ , henceforth denoted as  $\bar{p}_v(f)$ .

At first glance, such an intrinsic randomness of the dissociation rate  $k(f)$  might appear unlikely in view of the fact that, after all, it are always the same species of molecules which are dissociating. Yet, possible physical reasons for such random variations of the dissociation rate  $k(f)$  might be:

- (i) Random variations and fluctuations of the local molecular environment by ions, water and solvent molecules locally modulate ionic strength, pH and electric fields which may influence the dissociation process of the molecular complex [29].
- (ii) Structural fluctuations due to thermal activation may lead to different conformations of a (macro-) molecule [30, 31].
- (iii) Orientational fluctuations of the molecular complex relative to the direction of the applied pulling force

may amount to different dependences of the rate  $k$  on  $f$ . In addition, the linker molecules may be attached to the complex at different positions, but also many other random geometrical variations may be possible (cf. Fig. 1).

(vi) Even more importantly, in a number of dissociation events one is actually not pulling apart the specific molecular complex of interest but rather some different, unspecific chemical bond. In a small but not necessarily negligible number of such unspecific events, the force-extension-curve may still look exactly like in Fig. 2 and hence it is impossible to eliminate those events from the experimental data set.

We remark that not all those general reasons may be pertinent to the specific experimental data in Figs. 3-7 and that there may well exist additional sources of randomness which we overlooked so far. Their detailed quantitative modeling is a daunting task beyond the scope of our present work and also beyond the present possibilities of experimental verification. Rather, we will resort to the ad hoc ansatz that all those different sources of randomness approximately sum up to an effective Gaussian distribution with two fit parameters, see Eq. (16) below. Furthermore, we will verify that moderate variations of this Gaussian ansatz indeed leave our main conclusions practically unchanged, see Sect. V.

## B. Formalization

To quantify the basic qualitative ideas from the previous Sect. IV A, the usual starting point will be some parametric ansatz for the functional form of the rate,  $k(f) = k(f; \vec{\lambda})$ , with a set of parameters  $\vec{\lambda}$ . These parameters are randomly distributed according to a certain (conditional) probability density  $\rho(\vec{\lambda}; \vec{\mu})$ , which itself depends on some fit parameters  $\vec{\mu}$ . In such a case, the parametric  $\vec{\lambda}$ -dependence of  $k(f) = k(f; \vec{\lambda})$  is inherited by  $p_v(f) = p_v(f; \vec{\lambda})$  via (3), yielding

$$p_v(f; \vec{\lambda}) = \exp \left\{ -\frac{1}{v} \int_0^f df' \frac{k(f'; \vec{\lambda})}{F'(F^{-1}(f'))} \right\}. \quad (8)$$

The relevant  $\bar{p}_v(f)$ , to which the experimentally determined  $\tilde{p}_v(f)$  from (4) should be compared (cf. beginning of Sect. IV A), follows by averaging with respect to the probability distribution of the rates, i. e.

$$\bar{p}_v(f; \vec{\mu}) = \frac{\int d\vec{\lambda} \rho(\vec{\lambda}; \vec{\mu}) p_v(f; \vec{\lambda})}{\int d\vec{\lambda} \rho(\vec{\lambda}; \vec{\mu}) p_v(f_{\min}; \vec{\lambda})}. \quad (9)$$

The denominator accounts for the fact that rupture forces below  $f_{\min}$  cannot be distinguished from thermal fluctuations and other artifacts (see Fig. 2) and therefore are missing in the experimental data set. Hence  $\bar{p}_v(f; \vec{\mu})$  is restricted to  $f \geq f_{\min}$  and must be normalized to unity for  $f = f_{\min}$  [32].

Finally, the fit parameters  $\vec{\mu}$  are determined so that  $\bar{p}_v(f; \vec{\mu})$  reproduces the experimentally observed  $\tilde{p}_v(f)$  as closely as possible. The resulting optimal parameters  $\vec{\mu}$  yield an estimate for the heterogeneity of the chemical bonds in the form of the probability distribution  $\rho(\vec{\lambda}; \vec{\mu})$  of the rates  $k(f; \vec{\lambda})$ .

In practice, one has to choose a cost function to quantify the “fitness” or “quality” of a given  $\bar{p}_v(f; \vec{\mu})$  with respect to the experimental data  $\tilde{p}_v(f)$ . A natural choice, which we will use in the following, is

$$Q(\vec{\mu}) := \sum_{n,v} [\tilde{p}_v(f_n) - \bar{p}_v(f_n; \vec{\mu})]^2 \quad (10)$$

where the sum runs over all experimentally observed rupture forces  $f_n$  and all pulling velocities  $v$ . The main argument in favor of the cost function (10) is that it attributes the same “importance” to each rupture event, independent of the velocity  $v$  at which it has been observed. Its main shortcoming is that if one artificially partitions the data for one pulling velocity  $v$  into two subsets, then the resulting minimizing parameters  $\vec{\mu}$  will not remain the same for these subsets in general. A more detailed discussion of this issue will be given elsewhere [33].

## C. Model functions

To further substantiate these ideas, assumptions about the functional form of the force-extension characteristic  $F(s)$ , the dissociation rate  $k(f, \vec{\lambda})$ , and the probability density  $\rho(\vec{\lambda}; \vec{\mu})$  are unavoidable.

According to Fig. 2, the force-extension characteristic is approximately linear,

$$F(s) = \kappa s, \quad \kappa \simeq 3 \text{ pN/nm}, \quad (11)$$

cf. Eq. (6).

Further, we adopt the standard approximation [1, 2, 10, 11]

$$k(f) = k_0 e^{\alpha f} \quad (12)$$

where  $k_0$  is the force-free dissociation rate and  $e^{\alpha f}$  is supposed to capture the dominating Arrhenius-type dependence of the decay rate on the applied force [12]. In doing so, the parameter  $\alpha$  can be identified with the dissociation length, that is, the distance  $\Delta x$  between the potential minimum and the (unstable) transition state, projected along the force direction and measured in units of the thermal energy:

$$\alpha = \Delta x / k_B T, \quad (13)$$

see also Sect. VI B below.

Introducing (11) and (12) into (8) yields the simplified expression

$$p_v(f; \vec{\lambda}) = \exp \left\{ -\frac{k_0}{v \kappa} \frac{e^{\alpha f} - 1}{\alpha} \right\}. \quad (14)$$

The above proposed heterogeneity of the chemical bonds in general amounts to a randomization of the two parameters  $k_0$  and  $\alpha$  in (12), i.e.  $\vec{\lambda} = (k_0, \alpha)$ . In view of the exponential function in (12) we can expect that the randomness of  $\alpha$  has a much stronger effect than that of  $k_0$ . Hence, we first consider  $k_0$  as fixed and only  $\alpha$  as random parameter, i. e.

$$\vec{\lambda} = \alpha . \quad (15)$$

The corresponding probability distribution is thus of the form  $\rho(\alpha; \vec{\mu})$ . A particularly simple and natural choice is the truncated Gaussian

$$\rho(\alpha; \vec{\mu}) = \mathcal{N} \exp\{-(\alpha - \alpha_m)^2 / 2\sigma^2\} \Theta(\alpha) \quad (16)$$

with  $\vec{\mu} = (\alpha_m, \sigma)$ . Negative  $\alpha$ -values in (12) appear quite unphysical and hence are suppressed by the factor  $\Theta(\alpha)$ , while  $\mathcal{N}$  is a normalization constant, whose explicit value is actually not needed in (9). The remaining truncated Gaussian may be viewed as a poor man's guess in order to effectively take into account the many different possible sources of bond randomness mentioned in Sect. IV A. The parameters  $\alpha_m$  and  $\sigma$  approximate the mean and the dispersion of  $\alpha$ , provided the relative dispersion  $\sigma/\alpha_m$  is sufficiently small. Otherwise, the actual mean value

$$\bar{\alpha} = \bar{\alpha}(\vec{\mu}) := \int d\alpha \alpha \rho(\alpha; \vec{\mu}) \quad (17)$$

may exceed the most probable value  $\alpha_m$  of the density in (16) quite notably.

Since  $k_0$  is considered fixed (cf. Eq. (15)), this parameter effectively moves from the set  $\vec{\lambda}$  into the set  $\vec{\mu}$ , i.e. we are left with three fit parameters

$$\vec{\mu} = (k_0, \alpha_m, \sigma) . \quad (18)$$

The standard theory (1), (2) with (11), (12) is recovered from (16) for  $\sigma \rightarrow 0$ , thus leaving only two fit parameters  $\vec{\mu} = (k_0, \alpha)$ , and hence  $\bar{p}_v(f) \rightarrow p_v(f)$  with  $\alpha = \alpha_m$ .

#### D. Application to experimental data

The fit to the five experimental data sets in Figs. 3-7 along the lines described in the previous section is very good in the first three cases and still satisfactory in the two remaining cases.

For the corresponding fit parameters in (18) we have obtained the following results.

For *expE1/E5* and *ExpG* (Figs. 2, 3):

$$k_0 \simeq 0.0033 \text{ s}^{-1}, \alpha_m \simeq 0.13 \text{ pN}^{-1}, \sigma \simeq 0.07 \text{ pN}^{-1} . \quad (19)$$

For *expG1/G4* and *ExpG* (Fig. 4):

$$k_0 \simeq 0.0026 \text{ s}^{-1}, \alpha_m \simeq 0.13 \text{ pN}^{-1}, \sigma \simeq 0.17 \text{ pN}^{-1} \quad (20)$$

For *PhoB* peptide and *DNA* (Fig. 5):

$$k_0 \simeq 0.00038 \text{ s}^{-1}, \alpha_m \simeq 0.14 \text{ pN}^{-1}, \sigma \simeq 0.10 \text{ pN}^{-1} \quad (21)$$

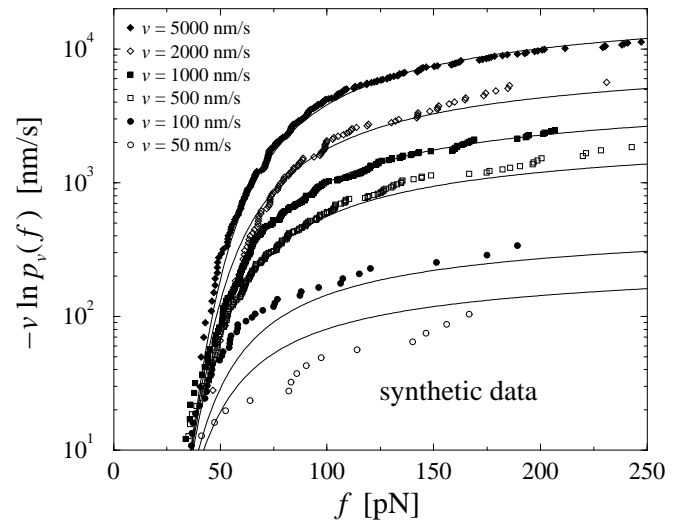


FIG. 9: Same as in Fig. 3 but for synthetic rupture data (symbols), sampled numerically according to (9), (11)-(19). The velocities  $v$  and the number of rupture events  $N_v$  for each  $v$  are identical to those in Fig. 3.

For resorc[4]arene and ammonium (Fig. 6):

$$k_0 \simeq 0.092 \text{ s}^{-1}, \alpha_m \simeq 0.057 \text{ pN}^{-1}, \sigma \simeq 0.031 \text{ pN}^{-1} \quad (22)$$

For immunoglobulin G and protein A (Fig. 7):

$$k_0 \simeq 0.014 \text{ s}^{-1}, \alpha_m \simeq 0.22 \text{ pN}^{-1}, \sigma \simeq 0.14 \text{ pN}^{-1} \quad (23)$$

As already mentioned, essentially the same linkers have been used for all the AFM-experiments in Figs. 3-6, hence the force extension curves always look similar to those in Fig. 2. Accordingly, (11) has been employed throughout (19)-(22).

In all cases, the relative dispersion  $\sigma/\alpha_m$  is comparable to or smaller than unity. Hence the mean  $\alpha$ -value, given by  $\bar{\alpha}$  in (17), is always close to the most probable  $\alpha$ -value, given by  $\alpha_m$  in (16).

Since the experiments are conducted at room temperature, the typical dissociation length  $\overline{\Delta x} := \bar{\alpha} k_B T$  (cf. (13)) resulting from (19)-(23) with  $\bar{\alpha} \simeq \alpha_m$  are:

$$\overline{\Delta x} = 0.54 \text{ nm for } \textit{expE1/E5} \text{ and } \textit{ExpG}.$$

$$\overline{\Delta x} = 0.54 \text{ nm for } \textit{expG1/G4} \text{ and } \textit{ExpG}.$$

$$\overline{\Delta x} = 0.58 \text{ nm for } \textit{PhoB} \text{ and } \textit{DNA}.$$

$$\overline{\Delta x} = 0.24 \text{ nm for } \textit{resorc[4]arene} \text{ and } \textit{ammonium}.$$

$$\overline{\Delta x} = 0.92 \text{ nm for } \textit{immunoglobulin G} \text{ and } \textit{protein A}.$$

#### E. Synthetic data, fluctuations, systematic deviations

By means of a random number generator, synthetic rupture data can be easily produced numerically, which satisfy (1), (2), (11)-(19) *exactly*. The resulting Fig. 9 is indeed strikingly similar to Fig. 3.

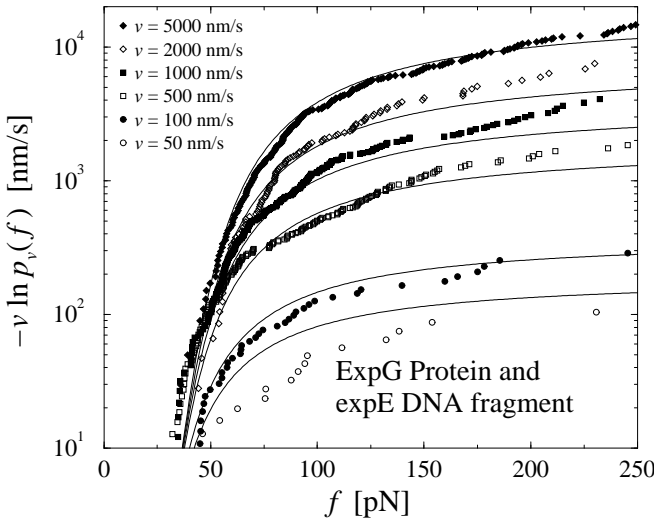


FIG. 10: Symbols: Same experimental data as in Fig. 3. Solid lines: Theoretical functions  $-v \ln p_v(f)$  for the same pulling velocities  $v$  as the symbols, using (9), (11)-(15), (24), and (25).

Fig. 9 also provides a feeling for the typical statistical fluctuations due to the finite numbers  $N_v$  of rupture events at a given pulling speed  $v$ .

It seems plausible that all deviations between experiment and theory in Fig. 3 can be attributed to such purely statistical uncertainties with the exception of the small but systematic deviations at large forces  $f$ . Note that the same type of systematic deviations at large  $f$  are also apparent in Figs. 4-7.

We come back to those systematic deviations in Sect. VI, while the statistical fluctuations will be addressed in more detail elsewhere [33].

## V. OTHER RATE DISTRIBUTIONS

In this section, we discuss variations and generalizations of our model function ansatz (16) for the probability density quantifying the bond heterogeneity, while modifications of the ansatz for the dissociation rate (12) itself are postponed to the subsequent Sect. VI. Like in Sect. III B, we focus on one experimental system, namely the data for *expE1/E5* and ExpG from Fig. 3. Throughout this section,  $\mathcal{N}$  denotes normalization constants.

### A. Distribution of $\alpha$

In the following, we discuss modifications of the probability distribution (16) for  $\alpha$  in several paradigmatic ways, while keeping  $k_0$  fixed and the ansatz for the dissociation rate (12) unchanged.

(i) Gaussian distribution, but in contrast to (16) with-

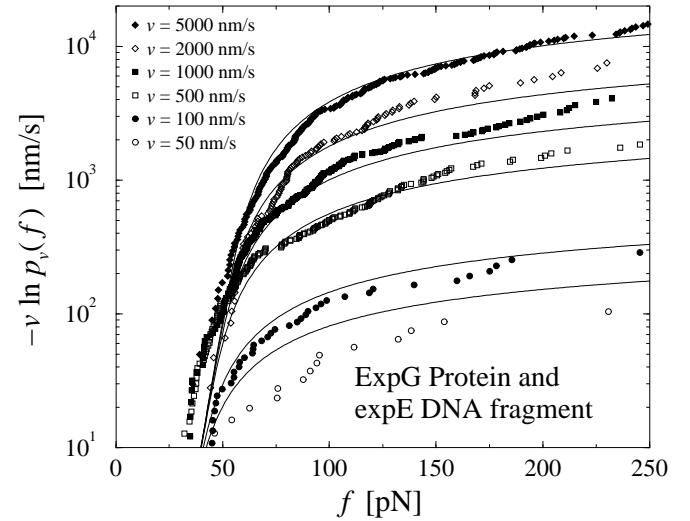


FIG. 11: Symbols: Same experimental data as in Fig. 3. Solid lines: Theoretical functions  $-v \ln p_v(f)$  for the same pulling velocities  $v$  as the symbols, using (9), (11)-(15), (26), and (27).

out suppressing negative  $\alpha$ -values, i.e.

$$\rho(\alpha; \vec{\mu}) = \mathcal{N} \exp\{-(\alpha - \alpha_m)^2 / 2\sigma^2\}. \quad (24)$$

The fit to the experimental data in Fig. 10 is practically identical to that in Fig. 3 and also the corresponding fit parameters

$$k_0 \simeq 0.0038 \text{ s}^{-1}, \alpha_m \simeq 0.13 \text{ pN}^{-1}, \sigma \simeq 0.07 \text{ pN}^{-1}, \quad (25)$$

are essentially the same as in (19). The obvious reason for the good agreement is the smallness of the Gaussian tail with negative  $\alpha$ -values. In other words, the suppression of negative  $\alpha$ -values in (16) is not an essential point for small-to-moderate relative dispersions  $\sigma/\alpha_m$ .

(ii) Parabolic distribution of  $\alpha$  between the limiting values  $\alpha_l$  and  $\alpha_r$  of the form

$$\rho(\alpha; \vec{\mu}) = \mathcal{N} (\alpha - \alpha_l)(\alpha_r - \alpha) \Theta(\alpha - \alpha_l) \Theta(\alpha_r - \alpha). \quad (26)$$

The fit to the experimental data is shown in Fig. 11 and is of the same quality as in Fig. 3, except for small forces. For the corresponding fit parameters  $\vec{\mu} = (k_0, \alpha_l, \alpha_r)$  we obtained

$$k_0 \simeq 0.0042 \text{ s}^{-1}, \alpha_l \simeq -0.002 \text{ pN}^{-1}, \alpha_r \simeq 0.26 \text{ pN}^{-1} \quad (27)$$

Thus,  $k_0$  is comparable to the result in (19) and also mean and dispersion of the parabolic distribution (26) are close to those of the truncated Gaussian (16).

(iii) Box distribution of  $\alpha$  the form

$$\rho(\alpha; \vec{\mu}) = \mathcal{N} \Theta(\alpha - \alpha_l) \Theta(\alpha_r - \alpha). \quad (28)$$

The fit to the experimental data in Fig. 12 is slightly worse than in Fig. 3. For the corresponding fit parameters  $\vec{\mu} = (k_0, \alpha_l, \alpha_r)$  we obtained

$$k_0 \simeq 0.0048 \text{ s}^{-1}, \alpha_l \simeq 0.033 \text{ pN}^{-1}, \alpha_r \simeq 0.23 \text{ pN}^{-1} \quad (29)$$

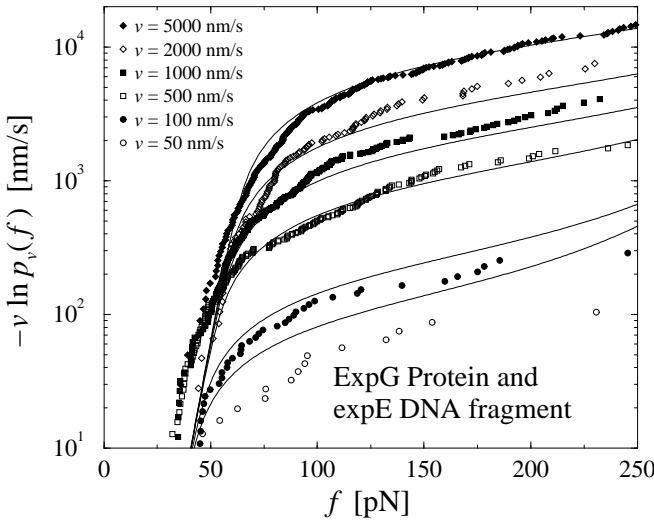


FIG. 12: Symbols: Same experimental data as in Fig. 3. Solid lines: Theoretical functions  $-v \ln p_v(f)$  for the same pulling velocities  $v$  as the symbols, using (9), (11)-(15), (28), and (29).

Again,  $k_0$  is comparable to the result in (19) and also mean and dispersion of the box distribution (28) are close to those of the truncated Gaussian (16).

All in all, for the above modification (i)-(iii) and several further variations of the distribution (16) of dissociation rates (12) which we tried out, the resulting fit parameters were always comparable to those in (19) and the agreement with the experimental data was comparable to or worse than that in Fig. 3, but never significantly better.

### B. Randomization of $k_0$

In a first step, we keep  $\alpha$  in (12) fixed and instead randomize  $k_0$  according to a truncated Gaussian distribution of the form (cf. (16))

$$\rho(\vec{\lambda}; \vec{\mu}) = \mathcal{N} \exp\{-(k_0 - q)^2/2\sigma_k^2\} \Theta(k_0) \quad (30)$$

with random parameters  $\vec{\lambda} = k_0$  and fit parameters  $\vec{\mu} = (q, \sigma_k, \alpha)$ . The fit to the experimental data is shown in Fig. 13 and is clearly considerably worse than in Fig. 3. For the corresponding fit parameters  $\vec{\mu} = (q, \sigma_k, \alpha)$  we obtained the result

$$q \simeq 0.0064 \text{ s}^{-1}, \sigma_k \simeq 4.0 \text{ s}^{-1}, \alpha \simeq 0.05 \text{ pN}^{-1}. \quad (31)$$

While the most probable dissociation rate  $q$  and the parameter  $\alpha$  are still comparable to  $k_0$  and  $\alpha_m$  in (19), the relative dispersion  $\sigma_k/q$  of the dissociation rate distribution takes the quite unlikely value of about 1000. The latter is in accordance with our above guess (see above (15)) that randomizing  $\alpha$  has a much stronger effect than randomizing  $k_0$  in (12) due to the exponentiation.

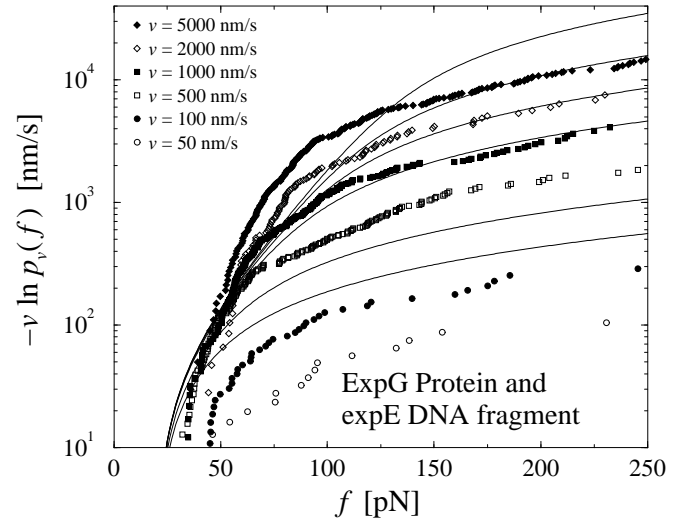


FIG. 13: Symbols: Same experimental data as in Fig. 3. Solid lines: Theoretical functions  $-v \ln (\bar{p}_v(f))$  for the same pulling velocities  $v$  as the symbols, using (9), (11)-(15), (30), and (31).

In view of the bad agreement between theory and experiment in Fig. 13 and the prediction that the dissociation rate  $k_0$  will vary by factors of 1000 between different realizations of the same chemical bond, we conclude that varying  $k_0$  instead of  $\alpha$  does not admit a satisfactory theoretical description of the experimental reality.

We remark that under the assumptions (11) and (12), the quantities  $k_0$  and  $\kappa$  appear in the combination  $k_0/\kappa$  in (14). Hence, a randomization of the linker stiffness, as considered in [34, 35], is basically equivalent to a randomization of  $k_0$  and does not satisfactorily explain our present experimental findings.

As a next step, we consider a simultaneous randomization of  $k_0$  and  $\alpha$ . Specifically, we employed a distribution function of the form (cf. (16), (28))

$$\rho(\vec{\lambda}; \vec{\mu}) = \mathcal{N} \Theta(k_0 - k_l) \Theta(k_r - k_0) \times \exp\{-(\alpha - \alpha_m)^2/2\sigma^2\} \Theta(\alpha) \quad (32)$$

with random parameters  $\vec{\lambda} = (k_0, \alpha)$  (cf. (15)) and fit parameters  $\vec{\mu} = (k_l, k_r, \alpha_m, \sigma)$  (cf. (18)). The resulting fit to the experimental data in Fig. 14 is practically indistinguishable from that in Fig. 3. For the corresponding fit parameters we obtained the result

$$\begin{aligned} k_l &\simeq 1.2 \cdot 10^{-11} \text{ s}^{-1}, k_r \simeq 0.0091 \text{ s}^{-1}, \\ \alpha_m &\simeq 0.13 \text{ pN}^{-1}, \sigma \simeq 0.07 \text{ pN}^{-1}. \end{aligned} \quad (33)$$

These parameters are also very similar to those in (19).

In other words, the agreement with the experimental data and the quantitative numbers hardly change in spite of the two extra fit parameters.

The main conclusion of this subsection is that randomizing  $k_0$  is of no use.

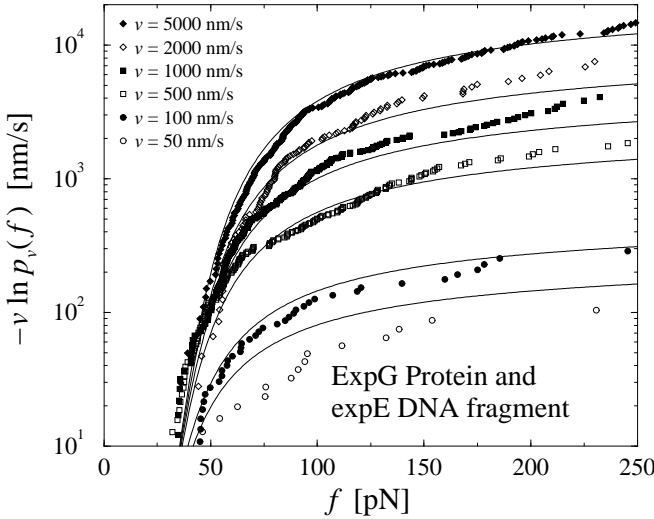


FIG. 14: Symbols: Same experimental data as in Fig. 3. Solid lines: Theoretical functions  $-v \ln(p_v(f))$  for the same pulling velocities  $v$  as the symbols, using (9), (11)-(15), (32), and (33).

A second basic observation of this section is that variations of the rate  $k_0$  in (12), or equivalently of  $\kappa$  in (11), have a much weaker effect than variations of  $\alpha$ . The same conclusion is corroborated by comparison of the solid and dashed lines in Fig. 8 and by the huge variations of the linker stiffness in the works [34, 35], and is naturally explained by the discussion preceding Eq. (15).

Conversely, this implies that estimating  $k_0$  from experimental data is much more “critical”, i.e. accompanied by a much larger uncertainties, than estimating  $\alpha$ .

## VI. GENERALIZED DISSOCIATION RATES

Complementary to the previous Sect. V, in this section we address modifications of the dissociation rate (12), while keeping the ansatz for the probability density (16) unchanged. In doing so, the main motivation is the observation from Sect. IV E that Figs. 3-7 exhibit a small but still significant systematic underestimation of the experimental data by the theoretical lines for large forces  $f$ . Accordingly, the basic criterion for the subsequent variations of the dissociation rate will be to further reduce those small deviations between theory and experiment. As usual, we focus on one experimental data for *expE1/E5* and ExpG from Fig. 3.

Throughout this section, the following simple argument plays a crucial role. If one modifies the force dependent dissociation rate  $k(f)$  of a given chemical bond such that it becomes larger than before for all  $f$ -values, then the survival probability  $p_v(f)$  up to the force  $f$  will obviously become smaller than before for any  $f$ -value. The same property is inherited by  $\bar{p}_v(f)$  after averaging over the random variations of the dissociation rate  $k(f)$ ,

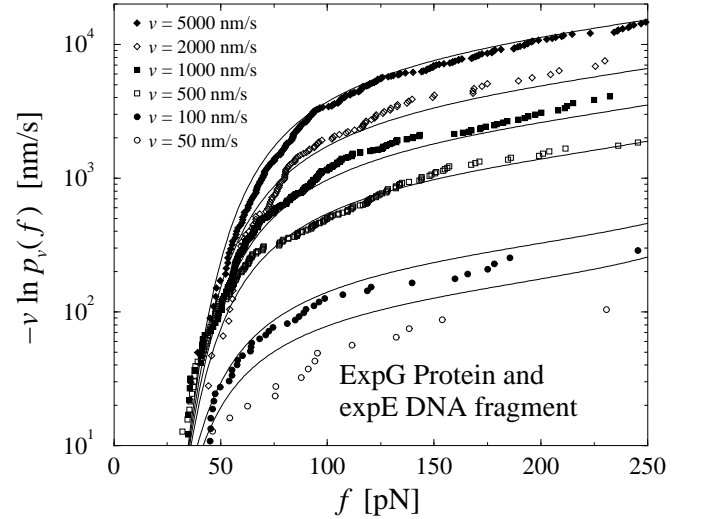


FIG. 15: Symbols: Same experimental data as in Fig. 3. Solid lines: Theoretical functions  $-v \ln(\bar{p}_v(f))$  for the same pulling velocities  $v$  as the symbols, using (8), (9), (11), (16), (34)-(36).

cf. (9). Since  $\bar{p}_v(f)$  is decreasing from 1 towards 0 as  $f$  increases from  $f_{min}$  towards  $\infty$ , the resulting property of the function  $-v \ln(\bar{p}_v(f))$  is to become larger than before. The opposite behavior results if the rate  $k(f)$  is modified so that it becomes smaller than before for all  $f$ -values.

Hence, in order to reduce the above mentioned deviations between experiment and theory, we are seeking for physical mechanisms which systematically *increase the dissociation rates*  $k(f)$ , especially for large forces  $f$ .

### A. Nonlinear generalization of Bell’s rate

First, we generalize Bell’s ansatz (12) for the dissociation rate [10] according to

$$k(f) = k_0 e^{\alpha f + \gamma f^2}. \quad (34)$$

A straightforward calculation shows that a negative contribution to  $\gamma$  arises from the nonlinear corrections to the so far adopted leading order approximation  $\Delta U(f) = \Delta U_0 - \Delta x f$  for the effective potential barrier that has to be surmounted by thermal activation in the presence of an external pulling force  $f \geq 0$ , see also the discussion above Eq. (13) and in Sect. VI B. According to the general argument at the beginning of this section it follows that including nonlinear corrections of the potential barrier  $\Delta U(f)$  does not improve the agreement between theory and experiment but rather worsens it.

So, in order to further improve our theory, a mechanism which generates positive  $\gamma$ -values is required. For instance, such a positive value of  $\gamma$  may be caused by deformations of the polymer linkers attached to the ligand-receptor complex (see Fig. 1), such that an increasing

force  $f$  leads to an alignment of the reaction coordinate with the force direction. Since the supposed rotation of the reaction coordinate is caused by the component of the force perpendicular to it and larger values of  $\alpha$  correspond to a close alignment of the reaction coordinate and the force direction from the beginning of the pulling process (cf. item (iii) in Sect. IV A),  $\gamma$  is a decreasing function of  $\alpha$ .

In the absence of a quantitative model for the mechanisms of bond heterogeneities mentioned in Sect. IV A, we quantify the above mentioned decreasing behavior of  $\gamma$  as a function of  $\alpha$ , together with further possibly existing mechanisms contributing to  $\gamma$  in (34), by the heuristic ad hoc ansatz

$$\gamma = \beta_0^2 \exp(-2(\alpha/\alpha_m)^2), \quad (35)$$

where  $\beta_0$  is an additional fit parameter and  $\alpha$  is randomly distributed according to (16).

In other words, our generalized model involves still the usual single random parameter (15), while the original fit parameters (18) are now extended to  $\vec{\mu} = (k_0, \alpha_m, \sigma, \beta_0)$ . The fit to the experimental data along these lines in Fig. 15 is of the same quality as in Fig. 3, except that the agreement for large forces  $f$  is now indeed slightly better. For the corresponding fit parameters we obtained the result

$$\begin{aligned} k_0 &\simeq 0.0031 \text{ s}^{-1}, \alpha_m \simeq 0.13 \text{ pN}^{-1}, \\ \sigma &\simeq 0.08 \text{ pN}^{-1}, \beta_0 \simeq 0.010 \text{ pN}^{-1}. \end{aligned} \quad (36)$$

Again, these results for  $k_0$ ,  $\alpha_m$ , and  $\sigma$  are close to those in (19).

In conclusion, the slight systematic deviations between theory and experiment in Figs. 3-7 can be reduced by means of a physically meaningful generalization of the force-dependent dissociation rate (34) (non-linear corrections in the exponent) with a single additional fit parameter.

## B. Intermediate energy barriers

Although the chemical reaction path, in the simplest case, proceeds from a bound metastable state across an energy barrier (activated state) towards a dissociated product state, in more general cases there may exist additional intermediate metastable states separated by additional intermediate energy barriers [11, 15, 16, 27].

The simplest example of such a situation with one intermediate state is sketched in Fig. 16. At small forces  $f$  the population of this state is small and the dissociation is effectively governed by a decay rate of the form  $k(f) = k_0 e^{\alpha f}$ , where  $\alpha$  is the distance between the first and the last extremum of the potential  $U_0(x)$  divided by the thermal energy  $k_B T$ , cf. (12), (13). On the other hand, the decay is always limited by the escape rate across the outer energy barrier  $k'_0 e^{\alpha' f}$  with  $k_0 < k'_0$  and  $\alpha > \alpha'$ . At larger forces this becomes the effective

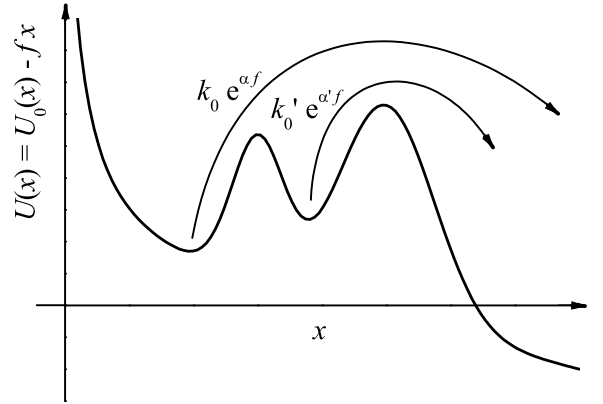


FIG. 16: Sketch of the relevant dissociation rates of a chemical bond whose reaction coordinate  $x$  experiences a reaction potential  $U(x)$  with an intermediate energy barrier.

decay rate, because most of the population is now in the intermediate metastable state. Altogether, we thus have  $k(f) = k_0 e^{\alpha f}$  for small forces and  $k(f) = k'_0 e^{\alpha' f} < k_0 e^{\alpha f}$  for larger forces.

According to the general argument at the beginning of this section it follows that such a modification of  $k(f)$  due to the presence of an additional intermediate energy barrier cannot lead to an improved agreement between experiment and theory. It only can lead to an increased curvature of the theoretical lines in Figs. 3-7, while a better agreement would require that the curvatures decrease.

In Fig. 16 we have tacitly assumed that upon increasing the “tilt”  $f$ , the two minima exchange their roles (local vs. global minima) before the two barriers exchange their roles (local vs. global maxima). One can easily see that our final conclusions remains valid also in the opposite situation. Moreover, the conclusions persist also in the case of more than one intermediate state.

The same conclusion is once more confirmed by Fig. 8. If there were an intermediate state present along the dissociation pathway, then the rate law  $k(f) = k_0 e^{\alpha f}$  which governs the small- $f$  regime would become less and less relevant with increasing  $f_{min}$ , while the large- $f$  law  $k(f) = k'_0 e^{\alpha' f}$  would become more and more dominant. Hence one should see a systematic increase of the fit parameter  $k_0$  with increasing  $f_{min}$ , while  $\alpha_m$  should systematically decrease. Comparing the fit parameters (19) for  $f_{min} = 20 \text{ pN}$  (Fig. 3) with those for  $f_{min} = 50 \text{ pN}$  and  $f_{min} = 100 \text{ pN}$  in Fig. 8, such a systematic tendency is not observed.

In conclusion, the experimental data in Figs. 3-7 do not imply the existence of intermediate states within the framework of our present theoretical description.

Note the difference between this conclusion and the one from [20], mentioned also in Sect. III B. There, it has been shown that within the framework of the stan-

dard theory, it is not possible to explain the very strong disagreement of the experimental curves  $-v \ln(\tilde{p}_v(f))$  for different pulling velocities  $v$  in Figs. 3-7 by taking into account intermediate states.

## VII. COMPARISON WITH THE STANDARD METHOD

In this section we discuss some practical aspects of experimental data evaluation in the light of our extension of the standard theory, thereby also providing a further strong argument in favor of our new theory.

While our main quantity of interest so far was  $-v \ln(\bar{p}_v(f))$ , traditionally one mostly considers rupture force distributions  $-d\bar{p}_v(f)/df$ , and similarly for  $\tilde{p}_v(f)$ . Fig. 17 illustrates a well-known problem of the standard theory (1), (2) supplemented by (11), (12) in this context (see e.g. Ref [30, 31]): the dotted theoretical curves and the experimental rupture force histograms have opposite skewness and agree very badly after fitting  $k_0$  and  $\alpha = \alpha_m$  according to the so-called standard method, as described in more detail in the next paragraph. On the other hand, our generalized theory has the correct skewness and agrees very well with the experimental histograms in Fig. 17, thus quantitatively confirming the qualitative arguments in [30, 31].

The most probable rupture force  $f^*$  by definition maximizes the rupture force distribution  $-d\bar{p}_v(f)/df$  within the regime  $f \geq f_{min}$ , implying

$$f^* = \max\{f_{min}, f_0^*\} \quad \text{with} \quad d^2\bar{p}_v(f_0^*)/df^2 = 0. \quad (37)$$

For the standard theory (1), (2) with (11), (12) it readily follows that

$$f^* = \max\{f_{min}, \alpha^{-1} \ln(\alpha \kappa v / k_0)\}. \quad (38)$$

Accordingly, in many experimental studies one traditionally plots  $f^*$  versus  $\ln v$  and determines  $k_0$  and  $\alpha$  according to (38) by means of a (piecewise) linear fit, where  $f^*(v)$  is estimated for each pulling velocity  $v$  by way of fitting a Gaussian with four parameters  $c_1, \dots, c_4$  of the form

$$y(f) = c_1 \exp(-c_2(f - c_3)^2) + c_4 \quad (39)$$

to the experimentally observed rupture force histogram. This procedure is commonly referred to as the *standard method*. Along these lines we determined the fit parameters  $k_0$  and  $\alpha_m = \alpha$  used for the dotted curves in Fig. 17.

Note the difference between our present notions of standard method and standard theory. The *standard theory* consists in the assumptions (1), (2) about the rupture process (often supplemented by the assumptions (11) and (12)). The *standard method* consists in fitting Gaussians (39) to the experimental histograms of rupture force distributions and using the resulting most probable rupture

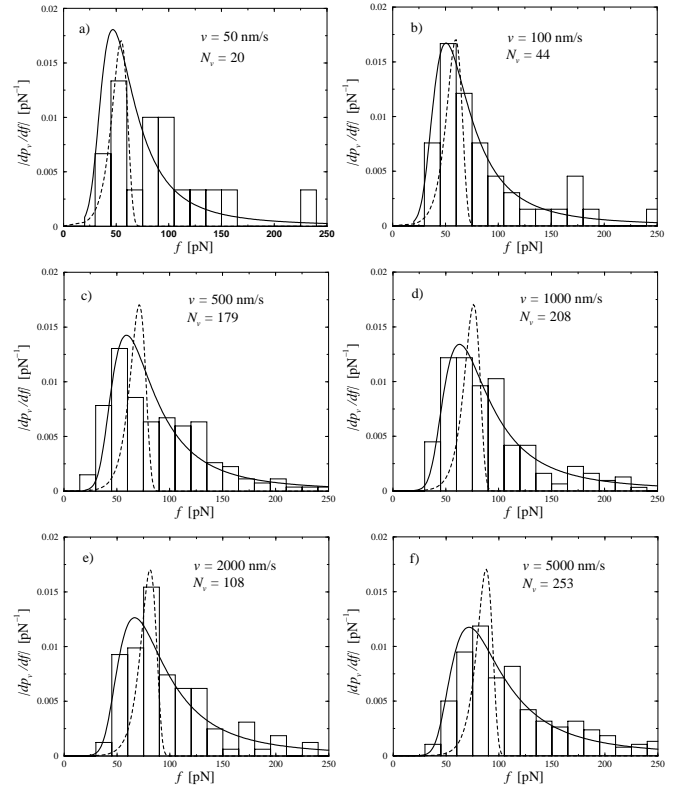


FIG. 17: Histograms: Same experimental rupture data as in Fig. 3 but represented as rupture force distributions. Solid lines: Theoretical curves  $-d\bar{p}_v(f)/df$  according to (9), (11)-(19). Dotted lines: same but for  $k_0 = 0.011 \text{ s}^{-1}$ ,  $\alpha_m = 0.14 \text{ pN}^{-1}$ ,  $\sigma = 0 \text{ pN}^{-1}$ ,  $f_{min} = 0$  (see main text) and with  $-d\bar{p}_v(f)/df$  divided by a factor 3 for better visibility of the other curves.

forces  $f^*$  to determine  $\alpha$  and  $k_0$  according to formula (38).

The standard theory, together with the common ansätze (11), (12), implies formula (38). We will now demonstrate that *the standard method may still be a satisfactory approximation although the standard theory is not*.

Within our generalized theory, Eq. (37) is no longer tractable analytically but easily solved numerically, see Fig. 18.

While the mean  $\alpha$ -value, given by  $\bar{\alpha}$  in (17), and the most probable  $\alpha$ -value, given by  $\alpha_m$  in (16), are quite similar if the relative dispersion  $\sigma/\alpha_m$  is comparable to or smaller than unity, they may notably differ for larger dispersions. In Fig. 18 we have kept  $\alpha_m$  fixed and compared the resulting curves for different ratios  $\sigma/\alpha_m$  and thus different dispersions  $\sigma$ , hence implicitly varying  $\bar{\alpha}$  as well. Complementary, in Fig. 19 we have kept  $\bar{\alpha}$  fixed while varying  $\sigma$  and hence also  $\alpha_m$  in such a way that their ratio  $\sigma/\alpha_m$  was still the same as in Fig. 18.

Finally, in Fig. 20 we again kept  $\bar{\alpha}$  fixed like in Fig. 19, but now we did not determine  $f^*$  by numerically solving

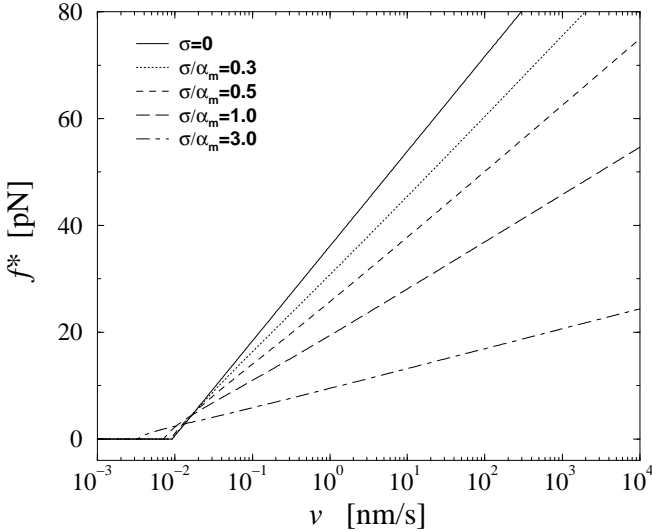


FIG. 18: Most probable rupture force  $f^*$  versus pulling velocity  $v$  (logarithmic scale) by solving (37) numerically with (9),  $f_{\min} = 0$ , (11)-(16),  $k_0$  and  $\alpha_m$  from (19), and 5 different values of  $\sigma$ . For  $f_{\min} > 0$ , the maximum of the plotted curves and  $f_{\min}$  yield  $f^*$ .

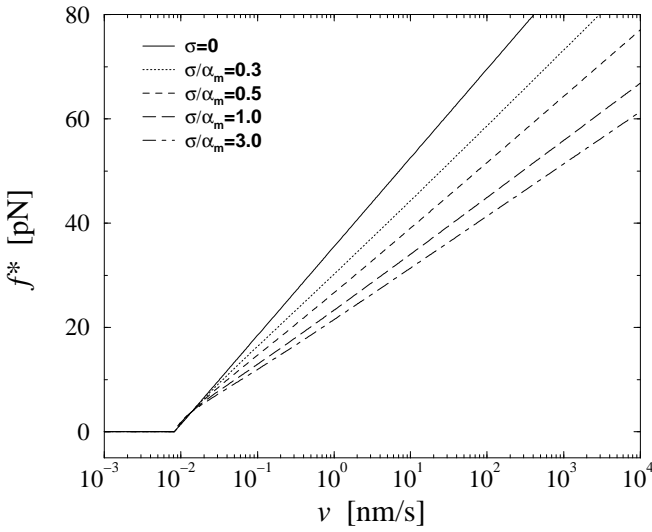


FIG. 19: Same as Fig. 18, except that  $\bar{\alpha}$  in (17) rather than  $\alpha_m$  in (16) has been kept fixed to the value  $0.135 \text{ pN}^{-1}$ .

(37) but rather by fitting Gaussians of the form (39) to the actual rupture force distributions  $-d\bar{p}_v(f)/df$  in the spirit of the standard method.

In all three Figs. 18-20, the curves for  $\sigma = 0$  (solid lines) are almost identical and represent the prediction (38) of the standard theory (see discussion below 18)). Surprisingly, even for  $\sigma > 0$ , in all three figures  $f^*$  still remains in very good approximation (but not rigorously) a (piecewise) linear function of  $\ln v$ . However, in general the dependence of these curves on the parameters  $k_0$ ,  $\alpha_m$  or  $\bar{\alpha}$ , and  $\sigma$  is much more complex than for the standard

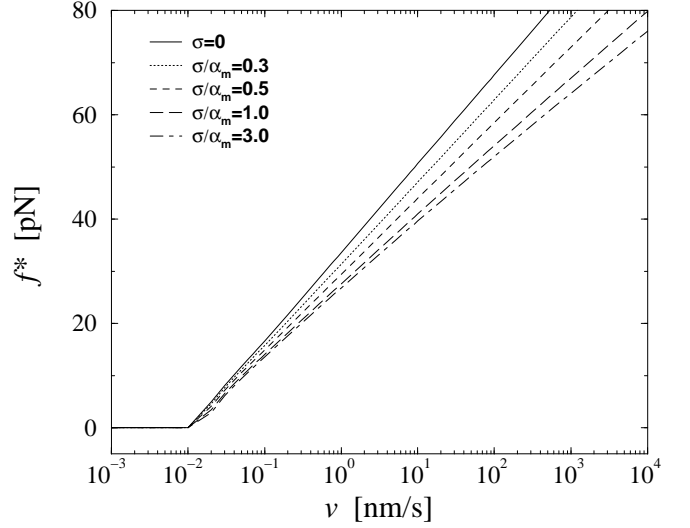


FIG. 20: Same as Fig. 19, except that  $f^*$  was not determined according to (37) but rather by fitting the rupture force distributions  $-d\bar{p}_v(f)/df$  by Gaussians (39). (The fit was performed on the interval  $0 \leq f \leq 250 \text{ pN}$ .)

theory in (38).

Curiously enough, the increasing agreement of the different curves when proceeding from Fig. 18 to Fig. 20 implies, that if one estimates  $f^*$  in the traditional spirit by fitting Gaussians (39) to the rupture force distributions then the dependence of this fit on the dispersion  $\sigma$  is approximately negligible. Hence one still can approximately determine  $k_0$  and  $\bar{\alpha}$  by means of the standard method, since the error of the underlying standard theory and of the Gaussian fitting procedure almost compensate each other!

E.g. the parameters  $k_0$ ,  $\bar{\alpha}$  which can be inferred from the 5 functions in Fig. 20 via (38) remain between  $k_0 = 0.0046 \text{ s}^{-1}$ ,  $\bar{\alpha} = 0.13 \text{ pN}^{-1}$  and  $k_0 = 0.0033 \text{ s}^{-1}$ ,  $\bar{\alpha} = 0.19 \text{ pN}^{-1}$ , i.e. quite close to their actual values  $k_0 = 0.0033 \text{ s}^{-1}$ ,  $\bar{\alpha} = 0.135 \text{ pN}^{-1}$ .

In other words, the inconsistency of the standard theory as unraveled in our present work could not be discovered in the traditional  $f^*$  versus  $\ln v$  plots. Conversely, such plots still remain “admissible” from the viewpoint of our present generalized theory in order to approximately determine  $k_0$  and  $\bar{\alpha}$ , while  $\sigma$  (and hence  $\alpha_m$ ) can only be estimated by means of a more elaborate data analysis.

## VIII. SUMMARY AND CONCLUSIONS

The theory by Evans and Ritchie [11] plays a key role in the field of single-molecule force spectroscopy. While extended in several important directions, their basic assumptions (1), (2) have been taken over in all subsequent theoretical and experimental works in this field, reflected also by the almost 400 citations of that paper.

In Sects. II, III we demonstrated that the incompatibility of this standard theory with experimental findings – originally unraveled in [20] – is a general feature of many different experimental systems. The qualitative similarity of Figs. 3–7 suggests that this incompatibility is in fact universal.

The central part of our present work is represented by Sect. IV, where we show how the problem can be cured. Namely, we explain and remedy the discrepancy between experiment and theory by postulating heterogeneities of the chemical bonds in extension of the standard theory. In the simplest case, the single new fit parameter of the generalized theory is the dispersion of the effective dissociation lengths. The resulting very good agreement with the experimental data corroborates that the proposed heterogeneity of the chemical bonds is ubiquitous in dynamic force spectroscopy experiments and that our model equations (9), (11)–(16) constitute a faithful model for the interpretation of these experimental data.

At the same time, another long-known problem of the standard data analysis procedure is resolved in Sect. VII, namely the notoriously bad agreement between experimentally observed and theoretically calculated rupture force distributions (Fig. 17). Since this procedure builds on the standard theory and since the rupture force distribution from Sect. VII is basically the derivative of the survival probability from Sects. 4, it seems possible that the two problems of the standard theory treated in those two sections are essentially two sides of the same coin, though we have not been able to explicitly demonstrate such a connection.

A main open problem is a more detailed understanding and quantitative modeling of the bond heterogeneities instead of the rather qualitative arguments in Sect. IV A and ad hoc ansätze like in (16). On the other hand, in Sect. V A we could demonstrate that the specific quantitative form of those ansätze does not matter very much. Moreover, such a detailed modeling of the many different potential sources of bond randomness would probably go beyond the present possibilities of experimental verification.

In view of our numerous unsuccessful previous attempts to explain the experimental findings, see Sect. III B and [20], we believe that our present explanation indeed captures an important real effect in such experiments. In particular, the fact that the experimental curves in Figs. 3–7 are typically increasing with increasing pulling velocity  $v$ , seems difficult or even impossible to explain quantitatively in a different way. While the standard theory predicts no such  $v$ -dependence at all, most physically meaningful alternative explanations lead just to the opposite  $v$ -dependence than observed experimentally [20]. That an explanation is both physically meaningful and in quantitative agreement with the experiment seems to be an important requirement to us. E.g. it may be easily possible to fit the curves in Fig. 3–7 by some ad hoc mathematical ansatz with a few fit parameters but without a physical basis. An example of

such an ansatz is a scaling function with certain scaling exponents. The fragility of such a satisfactory *quantitative* agreement between theory and experiment is once more illustrated by Sect. V B.

Since our central theoretical quantity,  $-v \ln(\bar{p}_v(f))$ , is very different from the traditional observables considered in the context of dynamic force spectroscopy (cf. Sect. VII), it may be worth to summarize the effects of our three basic fit parameters  $k_0$ ,  $\alpha_m$ ,  $\sigma$  (cf. (18)) on the shape of this function. The qualitative effect of the force free dissociation rate  $k_0$  and of the most probable dissociation length  $\alpha_m$  in units of  $kT$  can still be inferred from (14), yielding

$$-v \ln(\bar{p}_v(f)) \approx \frac{k_0}{\kappa \alpha_m} (e^{\alpha_m f} - 1). \quad (40)$$

Plotted on a logarithmic scale, like in Figs. 3–15, the small- $f$  regime is thus dominated by a logarithmic asymptotic of the form  $\ln(f k_0 / \kappa)$ , crossing over for large  $f$  towards a linear asymptotics of the form  $\alpha_m f$ . The remaining parameter  $\sigma$ , representing the random dispersion of the dissociation lengths  $\alpha$  in units of  $kT$ , mainly determines the spreading of the functions  $-v \ln(\bar{p}_v(f))$  upon variation of the pulling speed  $v$ . In particular, for  $\sigma \rightarrow 0$  this spreading disappears and our new theory reduces to the standard theory (with  $\alpha = \alpha_m$ ).

The remaining small systematic differences between theory and experiment at large forces  $f$  in Figs. 3–7 have been explained in Sect. VI A by means of a simple physical mechanism, giving rise to one further fit parameter. This mechanism would support the physical reason (iii) to explain bond heterogeneities in Sect. IV A, namely geometrical variations of the entire setup in Fig. 1 which are changing upon increasing the external load  $f$  on the bound complex.

According to the conclusions of Sect. V A, variations of  $k_0$ , or equivalently, of  $\kappa$  in (12), have a much weaker effect than variations of  $\alpha$ . Further closely related conclusion are: (i) Randomization of the linker stiffness [34, 35] is of no help to explain the experimental observations in Figs. 3–7. (ii) Small-to-moderate variations of the force extension curves are of little importance in Figs. 3–7. Only for the rigorous arguments in Sect. II A no such variations are admissible, see also Fig. 2. (iii) Estimating  $k_0$  from experimental data is accompanied by a much larger uncertainty than estimating the mean value  $\alpha_m$  and the dispersion  $\sigma$  of the random distribution governing  $\alpha$ . In fact, (12) suggests that not  $k_0$  itself but rather  $\ln k_0$  should be considered as the natural fit parameter complementing  $\alpha_m$  and  $\sigma$ .

### Acknowledgement

We thank Ralf Eichhorn for providing Fig. 1. This work was supported by the Deutsche Forschungsgemeinschaft under SFB 613 and RE 1344/3-1, the Alexander

- 
- [1] R. Merkel, Phys. Rep. **346**, 343 (2001)
- [2] E. Evans, Annu. Rev. Biomol. Struct. **30**, 105 (2001)
- [3] E.-L. Florin, V. T. Moy, and H. E. Gaub, Science **264**, 415 (1994)
- [4] G. Lee, L. A. Chrisey, and R. J. Colton, Science **266**, 771 (1994)
- [5] U. Dammer, U., O. Popescu, P. Wagner, D. Anselmetti, H.-J. Gntherodt, G. N. Misevic, Science **267**, 1173 (1995)
- [6] S. Izrailev, S. Stepaniants, M. Balsara, Y. Oono, and K. Schulten, Biophys. J. **72**, 1568 (1997)
- [7] J. R. Gullingsrud, R. Braun, and K. Schulten, J. Comput. Phys. **151**, 190 (1999)
- [8] E. Paci, A. Caflisch, A. Plückthun, and M. Karplus, J. Mol. Biol. **314**, 589 (2001)
- [9] B. Heymann and H. Grubmüller, Biophys. J. **81**, 1295 (2001)
- [10] G. I. Bell, Science **200**, 618 (1978)
- [11] E. Evans and K. Ritchie, Biophys. J. **72**, 1541 (1997)
- [12] P. Hänggi, P. Talkner, and M. Borkovec M., Rev. Mod. Phys. **62**, 251 (1990)
- [13] M. Rief, J. M. Fernandez, and H. E. Gaub, Phys. Rev. Lett. **81**, 4764 (1998)
- [14] J. Shillcock and U. Seifert, Phys. Rev. E **57**, 7301 (1998)
- [15] R. Merkel, P. Nassoy, A. Leung, K. Ritchie, and E. Evans, Nature **397**, 50 (1999)
- [16] T. Strunz, K. Oroszlan, I. Schumakovitch, H.-J. Güntherodt, and M. Hegner M., Biophys. J. **79**, 1206 (2000)
- [17] B. Heymann and H. Grubmüller H., Phys. Rev. Lett. **84**, 6126 (2000)
- [18] U. Seifert U., Phys. Rev. Lett. **84**, 2750 (2000)
- [19] N. Nguyen-Duong, K. W. Koch, and R. Merkel, Europhys. Lett. **61**, 845 (2003)
- [20] M. Raible, M. Evstigneев, P. Reimann, F. W. Bartels, and R. Ros, J. Biotechnology **112**, 13 (2004)
- [21] If  $F(s)$  were decreasing within a certain interval of  $s$ -values, this would imply a mechanical instability and hence the coexistence of yet at least two further stable branches of  $F(s)$ . These two stable branches would furthermore imply hysteresis and hence an incompatibility with the assumption discussed below (2).
- [22] A. Sain and M. Wortis, Phys. Rev. E **70**, 031102 (2004)
- [23] M. Evstigneev and P. Reimann, Phys. Rev. E **68**, 045103 (2003)
- [24] F. W. Bartels, B. Baumgarth, D. Anselmetti, R. Ros, and A. Becker, J. Struct. Biol. **143**, 145 (2003)
- [25] R. Eckel, S. D. Wilking, A. Becker, N. Sewald, R. Ros, and D. Anselmetti, Angew. Chem. (Intl. Edition) **44**, 3921 (2005).
- [26] R. Eckel, R. Ros, B. Decker, J. Mattay, and D. Anselmetti, Angew. Chem. (Intl. Edition) **44**, 484 (2005).
- [27] I. Derényi, D. Bartolo, and A. Ajdari, Biophys. J. **86**, 1263 (2004)
- [28] D. Bartolo, I. Derényi, and A. Ajdari, Phys. Rev. E **65**, 051910 (2002)
- [29] R. A. Vijayendran, D. E. Leckband, Analytical Chemistry, **73**, 471 (2001)
- [30] D. A. Simson, M. Strigl, M. Hohenadl, and R. Merkel, Phys. Rev. Lett. **83**, 652 (1999);
- [31] M. Strigl, D. A. Simson, C. M. Kacher, and R. Merkel, Langmuir **15**, 7316 (1999)
- [32] Note that rupture events at  $f < f_{\min}$ , though not detectable by the specific experiment at hand, do occur in actual reality and hence  $f_{\min}$  does *not* play any role regarding the validity range or functional form of (8) (in contrast to (3)).
- [33] M. Raible et al., unpublished.
- [34] C. Friedsam, A. K. Wehle, F. Kühner, and H. E. Gaub, J. Phys.: Condens. Matter **15**, S1709 (2003)
- [35] F. Kühner, L. T. Costa, P. M. Bisch, S. Thalhammer, W. M. Heckl, and H. E. Gaub, Biophys. J. **87**, 2683 (2004)

# 6 Mechanical Emission Control of Individually Addressed Nanocrystals

## 6.1 Introduction

Mechano-optical switching of single nanoobjects serves as a new and promising concept for probing and manipulating matter in nanoscale science. In this work, a combined atomic force microscopy and total internal reflection fluorescence microscopy setup was used to control the fluorescence emission of an individual semiconductor nanocrystal (“quantum dot”). The aim was to combine a single nanocrystal and a quenching AFM tip to a mechanically switchable nanophotonic device.

The first introductory chapter (6.1.1) gives a short review of mechanical switching at the nanoscale. Chapter 6.1.2 will introduce semiconductor nanocrystals, a novel type of tunable fluorophore with multiple applications which has several advantages over classical organic dyes. Quantum dots are suited for radiationless energy transfer experiments, e.g. fluorescence quenching, a topic addressed in more detail in chapter 6.1.3. Chapter 6.1.4 will present an overview of fluorescence microscopy techniques with single molecule resolution, before chapter 6.1.5 focusses on the method of total internal reflection fluorescence microscopy in more detail.

### 6.1.1 Mechanical Switching of Single Nanoobjects

Nanomechanical switches hold promises for many future applications in science and technology. Here, a “mechanical switch” shall be strictly defined by the mechanism which is used to bring about the change in a physical property, not by the property to be switched (just as in chapter 4.1.3 where optical switches were discussed). Nevertheless, the mechanical switching of nanoscale objects is mostly related to a second property of interest, be it electronic, chemical or optical.

The past years have seen the design of a number of so-called nanoelectromechanical devices where the mechanically controlled modulation of electrical properties like the conductance of a single nanoobject could be achieved. Some systems are based upon manipulation with a scanning probe tip. For example, the mechanical interaction between an STM tip and a single Cu TBP porphyrin molecule was used to change the configuration of the molecule by rotating single “legs” of the porphyrin around their  $\sigma$  bonds, resulting in a drastical change in tunneling current [87]. In a recent experiment, the decrease in conductance of a single oligothiophene molecule upon mechanical stretching was demonstrated [105]. Other devices draw upon the nanomechanical oscillations of single molecules. Thus, a strong coupling between the center-of-mass motion of a single C<sub>60</sub> molecule and the conductance of the fullerene mediated by single-electron hopping was observed in a nanoscale transistor [106]. Similar experiments were performed where the vibration-assisted tunneling of electrons in single C<sub>140</sub> transistors could be observed [107]. Recently, also the interplay between the guitar-string-like oscillation modes of a single carbon nanotube and an electrical high-frequency component was studied [108].

There are, however, only few examples for optomechanical switching of a nanoscale property. A groundbreaking experiment which combined mechanical and optical switching of a single macromolecule to a cycle was reported by Hugel et al. [109]. A polymer chain consisting of photoswitchable azobenzenes was subjected to SMFS experiments, inducing a stretching of the molecule, and subsequently to optical excitation, causing an electronic transition in the photoisomerizable azobenzene. In these experiments, the efficiency of an optomechanical energy conversion in a single molecule device could be analyzed for the first time.

### 6.1.2 Semiconductor Nanocrystals

The optical properties of solids usually do not depend on their size; quantum-mechanical effects do not play a role until the size of an object becomes comparable to the characteristic length scale which determines the coherence of its wave function. If, however, the dimensions of a crystal become very small, the physical properties of the system become size-dependent due to quantum confinement. Heisenberg’s uncertainty principle states that if a particle is confined to a region of length  $\Delta x$ , its momentum  $p_x$  can only be determined within the range of an uncertainty

$$\Delta p_x \sim \frac{\hbar}{\Delta x} \quad (6.1)$$

where  $\hbar = h/2\pi$  is Planck's constant. For a particle of mass  $m$ , the confinement in the  $x$  direction gives rise to an additional kinetic energy of magnitude

$$E_{confinement} = \frac{(\Delta p_x)^2}{2m} \sim \frac{\hbar^2}{2m(\Delta x)^2} \quad (6.2)$$

which will become significant if it is comparable to (or greater than) the kinetic energy of the particle due to thermal motion in the  $x$  direction, i.e. if

$$\frac{\hbar^2}{2m(\Delta x)^2} > \frac{1}{2}k_B T \quad (6.3)$$

or, in terms of the confinement length,

$$\Delta x \sim \sqrt{\frac{\hbar^2}{mk_B T}}. \quad (6.4)$$

This is equivalent to stating that  $\Delta x$  must be of the same order of magnitude as the de Broglie wavelength  $\lambda = h/p_x$  for the particle. A similar estimate holds for the optical properties of solids. For semiconducting solids, the Bohr radius of an exciton, i.e. an electron-hole pair generated by the absorption of a photon, is given by the expression

$$a_0 = \frac{\hbar^2 \epsilon}{e^2} \left( \frac{1}{m_e} + \frac{1}{m_h} \right) \quad (6.5)$$

where  $\epsilon$  is the material's dielectricity constant,  $e$  the elementary charge, and  $m_e$  and  $m_h$  the effective masses of the electrons and holes, respectively. In bulk semiconductors, this quantity is very large in comparison to the atomic scale (typically,  $a_0 \approx 5\text{-}50$  nm). Drastic changes in the optical properties only occur if the system gets confined to a value  $\Delta x \approx a_0$  in one (quantum well), two (quantum wire), or even three (quantum dot) dimensions. A consequence of the confinement are changes in the corresponding densities of states. Within the framework of the particle in a box model, bulk matter exhibits a continuous energy spectrum ( $\varrho(E) \sim \sqrt{E}$ ). Quantum wells (free in two dimensions) feature a quantized "staircase", ( $\varrho(E) = \text{const.}$ ), quantum wires (free in one dimension) a quasi-discrete ( $\varrho(E) \sim 1/\sqrt{E}$ ) and quantum dots (no degree of freedom left) a discrete energy spectrum. Thus, a nanocrystal quantum dot can be considered a three-dimensional quantum well with no degrees of freedom and "zero-dimensional" properties where excitons are completely localized. The energy levels for such a system with dimensions ( $d_x, d_y, d_z$ ) can be approximated by the solution of the Schrödinger equation for the 3-D particle in a box (with infinite barriers):

$$E(n_x, n_y, n_z) = \frac{\pi^2 \hbar^2}{2m} \left( \frac{n_x^2}{d_x^2} + \frac{n_y^2}{d_y^2} + \frac{n_z^2}{d_z^2} \right) \quad (6.6)$$

with the quantum numbers  $n_x$ ,  $n_y$ ,  $n_z$  and  $m$  as the effective exciton mass.

Semiconductor nanocrystal quantum dots can be prepared via epitaxial growth or by organometallic synthesis from colloidal solutions. For highly monodisperse nanocrystal solutions, a typical procedure is based on the (quick) injection of metal and chalcogenide precursors into a hot, strongly coordinating solvent (e.g. trioctylphosphineoxide, TOPO) which induces nucleation. The crystal growth can be influenced by temperature control. Typical metal-chalcogenide combinations for nanocrystal quantum dots are, e.g., CdSe or InGaAs, which are often modified by growing a shell around the semiconductor nucleus (e.g. ZnS) which is surrounded by a self-assembled layer of solvent molecules. Fig. 6.1 (a) is a schematic representation of such a coated core-shell quantum dot.

In colloidal solutions, the possibility to tune the optical properties of a semiconductor

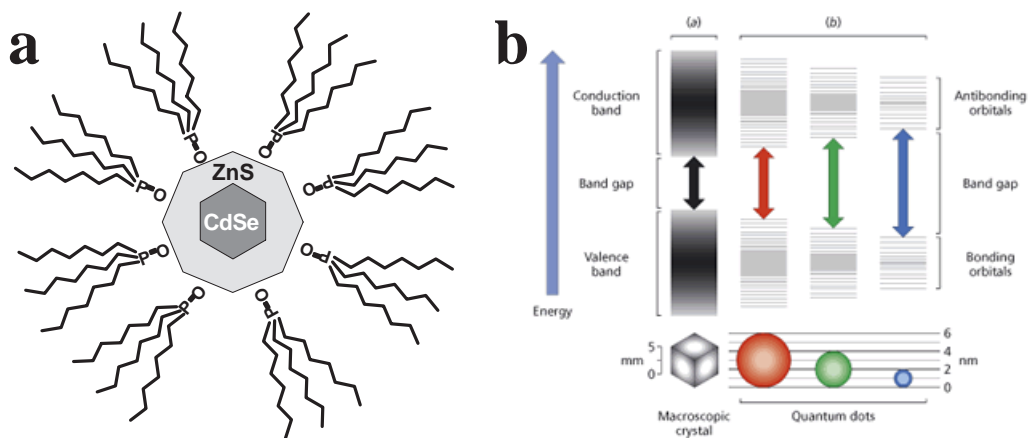


Figure 6.1: (a) Colloidal nanocrystal quantum dot consisting of a CdSe core and a ZnS shell, coated with a layer of TOPO molecules. (b) Bandgap tuning.

nanocrystal can be easily demonstrated. As the size of a nanocrystal decreases (Fig. 6.1 (b)), the energy gap (in the bulk semiconductor the separation between the continuous conduction and valence bands) increases (the nanocrystal, consisting of less and less atoms, approximates atomic behaviour). Typically, nanocrystal energy gaps vary between 2.5 eV (red emission) and 1 eV (blue emission).

Using single molecule fluorescence techniques (cf. the following chapter), it is possible to study the optical dynamics of single nanocrystal quantum dots. In contrast to organic dye molecules which exhibit bleaching after several  $10^6$  excitation-, emission cycles (a process which is often induced by triplet-triplet interaction with oxygen molecules and the subsequent reaction of the dye with singlet oxygen), nanocrystal quantum dots

are significantly more photostable and can be observed far longer. In single quantum dots, another striking dynamic process can be investigated which occurs on timescales between  $10^{-4}$  to  $10^3$  s and is called fluorescence intermittency or, familiarly spoken, “blinking”: The fluorescence emission under continuous excitation of a semiconductor nanocrystal is not constant over time, but turns on and off intermittently, giving rise to a characteristic flare [110]. The on- and off-times are characteristically distributed and can be analyzed, e.g. by their noise-power spectra [111]. The main reason for this blinking behaviour is thought to be the electron-hole ejection and recombination kinetics. In the on-state, electrons are excited from the core of the quantum dot, in the off-state, they are located far from the holes, and they recombine with the holes during the new on-state. The electron transport in semiconductor nanocrystals is a tunneling process, and from the measured life time  $\tau$ , a minimal electron-hole distance of 2-4 nm can be estimated. The corresponding kinetics observes a potential law

$$P(\tau) \propto \frac{1}{\tau^m} \quad (6.7)$$

since a local excitation exhibiting a single-exponential life time dependence is weighted with an exponential distribution of rate constants (corresponding to the distribution of potential depths in the excited state etc.). This means that the blinking dynamics can be characterized only by a distribution of life times (not by a single one). In other words: The blinking life time is a complex function of the experimental details, for there are always events which are to fast (or to slow) to be observed in a given experiment [112, 113]. Fluorescence intermittency is an intrinsically dynamic phenomenon and very sensitive to fluctuations in the nano-environment of the nanocrystal quantum dot. This theoretical difficulty can be turned into an experimental virtue, since the blinking statistics of individual nanocrystals provide valuable information about their nano-environment. In this way, semiconductor nanocrystals can serve as active reporters.

Quantum dots, just like “classical” fluorophores (e.g. organic dyes), can also be used in radiationless energy transfer experiments. Their fluorescence emission may be quenched by bringing them into the near proximity of suited quenching agents (e.g., gold surfaces or gold nanocrystals); this topic will be addressed in more detail in the following chapter. They can also be used as donors or acceptors in fluorescence resonant energy transfer (FRET) experiments, based on the radiationless energy transfer from a donor fluorophore to an acceptor fluorophore at nanoscale distances. Moreover, they can, at least in principle, be chemically derivatized in order to enhance their biocompatibility. All these interesting properties give rise to a vast multitude of different applications, a few of which shall at least be shortly indicated. Due to the non-degeneration of the

ground state, only one exciton is necessary to yield a population inversion in a quantum dot, which makes them possible candidates for laser action [114]. They are also discussed as single photon sources with strong quantum correlations among photons [115, 116] and might someday find application in quantum communication. Finally, their remarkable photostability, their brightness and their function as local position markers also make them ideal fluorescence labels for many biological applications [117, 118, 119].

### 6.1.3 Fluorescence Quenching

The term fluorescence quenching refers to every process which tends to decrease the fluorescence intensity emitted by an excited fluorophore. Quenching can be induced by a variety of different mechanisms.

The deactivation of the excited-state fluorophore  $F^*$  by collision with another molecule diffusing in solution (the quenching agent or quencher  $Q$ ) is called *collisional* or *dynamic quenching* if the molecules survive the collision chemically unaltered. Examples for collisional quenchers are oxygen, nitric oxide, halogens, amines, and electron-deficient molecules such as acrylamide and quinones. If the fluorophore is continually excited and the system undisturbed in any other respect, an equilibrium is reached where the concentration of excited fluorophores  $[F^*]$  does not change any longer, i.e.  $d[F^*]/dt = 0$ . This equilibrium will be reached with or without quenching agent  $Q$  present in solution. Since the fluorescence intensities with or without quencher,  $I_Q$  and  $I_0$ , are proportional to the concentrations of the excited fluorophores  $F_Q^*$  and  $F_0^*$ , we obtain the following Stern-Volmer equation:

$$\frac{I_0}{I_Q} = 1 + k_Q \tau_0 [Q] = 1 + K_{S-V} [Q] \quad (6.8)$$

where  $k_Q$  denotes the bimolecular quenching constant,  $\tau_0$  the un-quenched lifetime of the excited state, and  $K_{S-V}$  the so-called Stern-Volmer quenching constant. It results that collisional quenching also influences the mean lifetime of the excited-state fluorophore. A special type of dynamic quenching is quenching by fluorescence resonant energy transfer (FRET): The excited-state fluorophore transfers its fluorescence energy radiationless to the quencher which gets excited. This can happen if the emission of the fluorophore donor and the absorption spectrum of the quenching acceptor have a great overlap (resonance). The excited-state quencher can lose its energy either by fluorescence at a different wavelength or by dark decay. This energy transfer process is strongly distance-dependent ( $\propto R^{-6!}$ ) and typically occurs if the donor and acceptor molecules come closer than 10 nm (and if the emitting and receiving dipoles are properly oriented).

A different quenching mechanism is ground state complex formation, also called *static quenching*. In the first step, a nonfluorescent complex is formed between the ground-state fluorophore and the quencher, induced by hydrophobic and electrostatic interactions. The complex may absorb the exciting radiation, resulting in an excited heterodimer (exciplex), but it shows a dark decay to the ground state, since it has different electronic properties than its component molecules. For static quenching, one obtains (note the similarity to the Stern-Volmer equation)

$$\frac{I_0}{I_Q} = 1 + \left( \frac{[F]_0}{[F][Q]} - \frac{1}{[Q]} \right) [Q] = 1 + K_A [Q] \quad (6.9)$$

where  $[F]_0$  designates the total fluorophore concentration,  $[F]$  and  $[Q]$  the respective concentrations of free fluorophore and quencher, and  $K_A$  the association constant of the complex. Quenching by ground-state complex formation exhibits an exponential distance dependence and is also very dependent on the temperature.

Another type of fluorescence quenching can be observed if the excited state of the fluorophore opens a pathway for a chemical reaction. In this case, the quenching is mostly irreversible, so it is more appropriate to speak of photobleaching. Both intramolecular (e.g. pericyclic reactions) and intermolecular reactions (e.g. induced by singlet oxygen) can occur.

All quenching pathways discussed so far always require the presence of another molecule as the quencher. A different (and more complicated) situation arises when the quenching agent is represented by a metallic surface [120, 121, 122]. The metal significantly influences the absorption and emission properties of a nearby fluorophore; interactions between the exciting electromagnetic field, the metal interface, and the oscillating dipole of the fluorophore must be taken into account. Firstly, the rate of excitation can be significantly altered via local variations of the electric field. By changing the geometry of the quenching solid, these variations can span several orders of magnitude; this effect is due to the excitation of surface plasmons at the metal interface. The oscillating dipole of the fluorophore can likewise induce an electromagnetic field in the metal surface which, on its part, may de- or increase the radiative decay rate. Secondly, the metal surface provides additional pathways for electromagnetic decay; energy can easily be dissipated in the metallic solid. Thirdly, a thin enough metallic layer ( $< 50$  nm) causes polarization of the emitted radiation and, hence, concentration to a narrow angular range due to intermediate surface plasmon excitation. All these processes may act to enhance or inhibit (quench) the excitation or fluorescence emission of a fluorophore located in the vicinity. For the experiments reported in this work the fluorescence quenching of a Cd/Se semiconductor nanocrystal by a vicinal gold surface was exploited.

### 6.1.4 Single Molecule Fluorescence Microscopy

The study of single molecules and nanoobjects via fluorescence microscopy and spectroscopy is a very fast developing field of interdisciplinary research at the frontier between physics, chemistry and biology [26, 123, 124]. As in scanning probe techniques, to which single molecule fluorescence methods are in many respects complementary, distributions of molecular properties instead of average ensemble values are obtained, and the dynamics of individual molecules can be investigated directly.

The crucial task in these experiments is to isolate the fluorescence signal of individual molecules from the background of the surrounding medium (e.g. a polymer matrix). This requirement is best fulfilled by laser excitation of the sample, where the molecules can be excited very selectively and the light scattered by the sample can be separated easily from the fluorescence signal. With an appropriate optical setup, it is possible to observe the laser-induced fluorescence emission of individual molecules. The requirements for fluorescence spectroscopy of single molecules can be summarized as follows:

- A small excitation volume containing only a small number of molecules or, else, a wide-field epifluorescence setup with sufficient sensitivity;
- a low contamination of the sample by interfering molecules/objects;
- a high spectral selectivity to ensure that only the molecules of interest are excited;
- an experimental setup providing high optical sensitivity and quantum efficiency, capable to detect the fluorescence signal of single molecules with a sufficient signal-to-noise ratio (and separated from the background fluorescence of the sample).

Basically, two major classes of detectors for single molecule fluorescence can be distinguished: single element detectors, which are used mostly in scanning or near field setups, and array detectors, which are more often used in wide-field applications. Among single element detectors, commonly specialized avalanche photodiodes (APDs), so-called SPADs (single photon avalanche photodiodes), are employed to count single photons [125]. These feature high quantum efficiencies ( $> 60\%$ ) in the visible spectral range and are often equipped with on-board amplification and cooling units which effectively reduce dark counts. SPADs have mostly replaced the microchannel plate photomultiplier tube (PMT) as the photon counter of choice for single molecule applications.

Array detectors (cameras) are essentially two-dimensional arrays of many photon counting devices. In intensified frame transfer charge-coupled device (CCD) cameras, the photons are detected by a multialkali photocathode. The emitted photon is amplified

in a microchannel plate which is coupled to the photocathode via a glass fiber bundle. The electron cascade hits a phosphorus screen and emits new photons which are converted by a front-illuminated Si CCD detector into electrons. The resulting electrical signal is then digitized by a fast analog-to-digital converter (ADC). An advantage of this configuration is that the signal from the primary photon is amplified before the read-out, which would otherwise add to the signal and make the detection of single photons limited by read-out noise. Back-illuminated frame-transfer CCD cameras can use even faster ADCs. In contrast to front-illuminated cameras, however, back-illuminated devices are limited to brighter fluorophores because of the increased read-out noise. A general limitation with cameras as compared to single element detectors is their lower temporal resolution which is due to the read-out times for the CCD array. For the experiments described in publication VII, a front-illuminated Si CCD camera (I-Pentamax, Princeton Instruments) was used to detect fluorescence light.

Concerning the microscope setup, there are essentially two different approaches. Scanning methods, which include confocal and near-field optical microscopy, rely on the possibility to illuminate the sample with a very small spot which is scanned over the sample (or vice versa, i.e. the excitation spot is fixed and the sample scanned). The small illumination volume significantly reduces background luminescence. For scanning applications, single element detectors can be used which facilitate high temporal resolution. A disadvantage is that it is not possible to observe motion of single nanoobjects over larger distances. In confocal microscopy [26], a collimated laser beam is reflected by a dichroitic beam splitter and through an infinity-corrected microscope objective with a high numerical aperture (NA) such that the laser gets focussed to a tiny spot at the sample plane whose size is limited by diffraction (spot diameters are typically around  $10^2$  nm). The emitted and backscattered light is recollected and collimated by the objective and passes the dichroitic beamsplitter. Residual laser light is filtered out and the fluorescence focussed by the tube lens through a pinhole aperture which is located at the image plane of the microscope. The pinhole serves as a filter for light emanating from out-of-focal planes; this leads to greatly improved axial resolution (“confocal advantage”).

A different scanning technique which can be adopted for single molecule studies is scanning near-field optical microscopy (SNOM) [27], which is basically a scanning probe method (cf. chapter 2.1.1). It operates in the near-field of an aperture with a diameter much smaller than the wavelength of visible light (typically 50 nm). Hence, the optical resolution is not limited by diffraction. If the metal-coated optical fiber which serves as the near-field light source is placed very close to the sample surface and the radiation

propagating through its small aperture is detected within an axial distance of the order of the aperture diameter, the detected spot size will correspond to the size of the aperture.

Wide-field methods for single molecule imaging do not require the generation of a small spot. A big advantage is the possibility to observe many fluorophores at a time; the drawback of the method is the obligatory use of comparably slow array detectors whose maximum frame acquisition rates are limited (typical value: 50 ms). In its simplest configuration (epifluorescence), a laser illuminates an area several microns in diameter, much like in traditional light microscopy. Residual excitation light is filtered out and the fluorescence light from the sample passed on to an array detector (bright single fluorophores can even be observed by the adapted eye). A requirement for epifluorescence is that the (uncollimated!) laser beam is expanded in order to illuminate a larger area-of-interest on the sample.

A refined wide-field technique exploits the exponential decay of the evanescent field which goes with the total internal inflection at a high-index to low-index boundary, effecting a significant decrease in background noise. This method, called total internal reflection fluorescence microscopy (TIRFM) [29], was used in the experiments discussed in publication VII and is discussed in greater detail in the following chapter.

### 6.1.5 Total Internal Reflection Fluorescence Microscopy (TIRFM)

In total internal reflection microscopy, fluorophores are selectively illuminated and excited in a very small excitational volume which is adjacent to a high refractive index to low refractive index interface (usually, glass to water). In this region, an evanescent wave (penetration depth typically below 200 nm) is induced which results from the total reflection of an incident laser beam at the interface. If fluorophores are immobilized in the near proximity of the sample surface, they can be considered as a third medium, and the total reflection is frustrated (hindered), i.e. the evanescent wave can transport energy and excite the fluorophores. Since this is only possible at distances within the evanescent wave's penetration depth, this mode of excitation significantly reduces background luminescence emitted from fluorophores in the farther environment, e.g. in solution. Fig. 6.2 shows a schematic representation of a TIRFM setup.

To explain the TIRFM principle in more detail, consider a plane interface of two media with the refractive indices  $n_1$  and  $n_2$ . In the general case, a light beam propagating through medium (1) and meeting the interface at an incident angle  $\theta_1$  is partially refracted (transmitted, passes the interface) and partially reflected (where incident angle

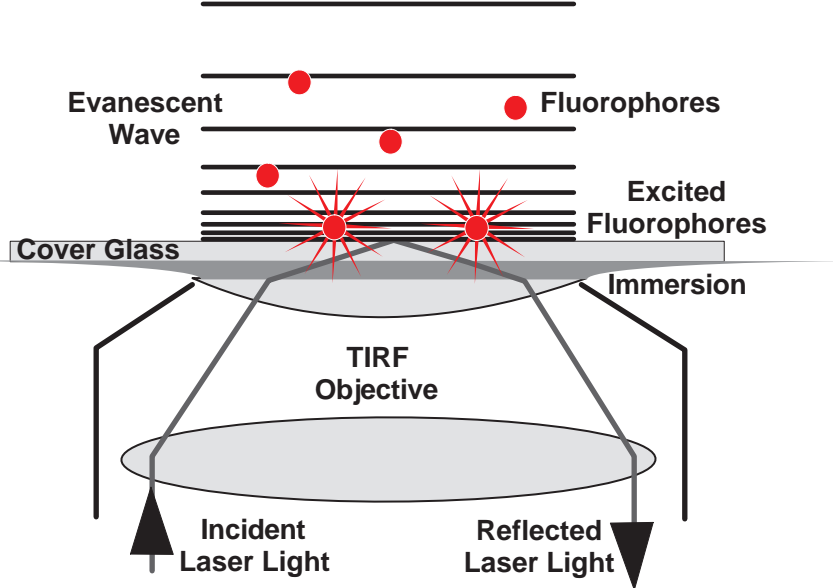


Figure 6.2: Principle of TIRFM.

= reflection angle). The transmitted beam is refracted at an angle  $\theta_2$  according to Snell's law:

$$n_1 \sin \theta_1 = n_2 \sin \theta_2. \quad (6.10)$$

Now let (1) the medium of higher refractive index. (Typical values for a cover glass (1) - aqueous solution (2) interface would be  $n_1 = 1.52$  and  $n_2 = 1.33$ , respectively.) With increasing incident angle (relative to the normal), the portion of the reflected light increases at the expense of the refracted part (cf. Fresnel's formulae). At a critical incident angle  $\theta_c$ , the refraction angle reaches  $90^\circ$  ( $\sin \theta_2 = 1$ ), and if the critical angle is exceeded, total internal reflection is observed. The critical angle is given by

$$\theta_c = \sin^{-1} \left( \frac{n_2}{n_1} \right). \quad (6.11)$$

For  $\theta_1 > \theta_c$ , Snell's law must be generalized to allow for imaginary values. Abbreviating  $W = \sin \theta_1 / \sin \theta_c$  and introducing the angle  $\theta_t$ , one can define

$$\cos \theta_t = \sqrt{\left( 1 - \frac{\sin^2 \theta_1}{\sin^2 \theta_c} \right)} = \sqrt{(1 - W^2)} = iQ \quad (6.12)$$

where  $Q$  represents a real number. We now make an ansatz for the electric field in medium (2) in the case of incident angles  $\theta_1 > \theta_c$ :

$$\mathbf{E}(\mathbf{r}, t) = \mathbf{E}_{20} \exp [-i(\omega t - \mathbf{k}_2 \cdot \mathbf{r})]. \quad (6.13)$$

Using  $\mathbf{k}_2 = k_2(\cos \theta_t \mathbf{e}_x + \sin \theta_t \mathbf{e}_y)$  with the unit normal vectors  $\mathbf{e}_x$  and  $\mathbf{e}_y$ ,  $x$  being the perpendicular distance from the interface in medium (2), we obtain an expression for the electric field of the evanescent wave

$$\mathbf{E}(\mathbf{r}, t) = \mathbf{E}_{20} \exp(-k_2 Qx) \exp[-i(\omega t - k_2 W y)]. \quad (6.14)$$

The wave propagates along the interface. In the optically thinner medium (2), it is damped exponentially with the penetration depth

$$d = \frac{2\pi}{k_2 Q} = \frac{\lambda_1}{2\pi} \left( n_1^2 \sin^2 \theta_1 - n_2^2 \right)^{-1/2} \quad (6.15)$$

where  $\lambda_1$  is the wavelength of the incident, sinusoidal wave. These results also correspond to an exponential decay of the evanescent field intensity.

Since the normal component of the Poynting vector is purely imaginary,

$$\langle \mathbf{S} \rangle \cdot \mathbf{e}_N = \langle \mathbf{E} \times \mathbf{H} \rangle \cdot \mathbf{e}_N = \text{Re} \left[ \frac{c\epsilon_0\epsilon_r}{2|\mathbf{E}|^2 iQ} \right] = 0, \quad (6.16)$$

there is no transport of energy across the interface by the evanescent wave. The situation changes, however, if a second interface is established not far away from the first one (within the penetration depth of the evanescent wave). If the third medium (e.g. a fluorophore) has a higher refractive index than the second ( $n_3 > n_2$ ), the wave can pass the second interface and propagate sinusoidally into medium (3). Energy transport (and excitation of fluorophores) is now possible. The phenomenon, called “frustrated TIR”, bears a certain resemblance to the quantum mechanical tunnel effect.

The reduced sample thickness which is illuminated in TIR fluorescence microscopy gives rise to reduced background fluorescence and facilitates the use of lower laser powers for excitation. The technique has found applications for biological samples quite a long time [126], but only recently in the study of single fluorophores [28, 29]. Essentially, there are two different setups for a TIR microscope. The first possibility couples a laser, incident under the critical angle  $\theta_c$ , into an index-matching prism which is connected to a glass coverslip [29]. An alternative is coupling the laser through the utmost edge of a high-NA microscope objective (“through-the-objective TIR”) [28]. Since the laser in a TIRFM experiment is not collimated, it is possible to switch a setup between epifluorescence and TIR by simply adding a translatable mirror (or a double prism) into the optical path. By translating this device, the laser may be coupled either through the center or through the edge of a TIRFM objective [127]. A comparable setup was used for the experiments reported in the following.

## 6.2 Publication VII

**Rainer Eckel**, Volker Walhorn, Christoph Pelargus, Jörg Martini, Thomas Nann, Dario Anselmetti, and Robert Ros. Nanocrystal Light Switch. Submitted to *Small*.

### 6.2.1 Contribution

All experimental work and data analysis performed by the author.

## Nanocrystal Light Switch\*\*

Rainer Eckel, Volker Walhorn, Christoph Pelargus, Jörg Martini, Thomas Nann,  
Dario Anselmetti, and Robert Ros\*

[\*] Dipl. Chem. R. Eckel, Dipl. Phys. V. Walhorn, Dipl. Ing. (FH) Ch. Pelargus,  
Dipl. Phys. J. Martini, Prof. Dr. D. Anselmetti, Priv.-Doz. Dr. R. Ros  
Experimental Biophysics and Applied Nanosciences, Faculty of Physics  
Bielefeld University, Universitätsstr. 25, 33615 Bielefeld, Germany  
Fax: +49-(0)521-106-2959  
E-mail: rros@physik.uni-bielefeld.de

Priv.-Doz. Dr. Th. Nann  
Freiburg Materials Research Center (FMF)  
University of Freiburg

[\*\*] Financial support from the Deutsche Forschungsgemeinschaft (SFB 613) is gratefully acknowledged.

In single molecule manipulation techniques the physical concepts of optical switching<sup>[1-3]</sup> and optomechanics<sup>[4]</sup> as well as the local energy transfer (i.e. quenching and fluorescence resonant energy transfer (FRET)<sup>[5]</sup>) between single nanoobjects open fascinating means of controlling and manipulating matter on the nanometer scale<sup>[6-8]</sup>. Single semiconductor nanocrystals (“quantum dots”) exhibit remarkable resistance to photobleaching, can be derivatized in a biocompatible way and allow tuning of their spectroscopical properties<sup>[9;10]</sup>. Furthermore, these nanosystems are not only isolated position markers, but can be regarded as active reporters which interact with their microenvironment and carry information about their local vicinity, for example in their blinking frequency<sup>[11;12]</sup>. Due to these qualities, nanocrystal fluorescence markers for biological applications have been designed in recent years, and new assays based on their energy-transfer properties have been developed<sup>[13-16]</sup>. In this context, the external control and switching of single nanocrystal fluorescence

emission is a significant step towards a better control of functional properties of matter on the single molecule level. In this letter, we report on the first external, mechano-optical emission control of a single nanoobject by means of an AFM tip functionalized with gold nanoparticles. Moreover, it was possible to fully control the light emission state of a single nanocrystal from emitting (blinking) to quenched (dark) by mechanically approaching and retracting the tip which invokes quenching.

Our experimental setup combines total internal reflection fluorescence microscopy (TIRFM)<sup>[17;18]</sup> with the piezo-controlled nanometer-sensitive movement of an atomic force microscope (AFM)<sup>[19]</sup> (Fig. 1). Previously the lifetimes of single dye molecules in the presence of an AFM tip have been investigated with a comparable combination of AFM and confocal microscopy<sup>[20]</sup>. Because our focus is on the mechanical switching of a single fluorophore, we use CdSe/ZnS nanocrystals, which are resistant to photobleaching and whose emission can be recovered after quenching. An AFM tip, which has been functionalized covalently with gold nanoparticles, serves as an appropriate and effective quenching agent. The nanocrystals are immobilized in submonolayer coverage on a cover glass so that single emitters can be clearly discriminated and resolved. Our mechano-optical setup combines a home-built AFM-head which is mounted on a 3D-piezo stage (Physik Instrumente AG) with an inverted optical microscope (Axiovert S100, Carl Zeiss) equipped with a TIRFM lens (100x, NA = 1.45; Olympus). The setup is controlled via a home-made LabVIEW-based software (National Instruments). The TIRFM mode significantly reduces optical background noise. For excitation we illuminate the sample using an Ar<sup>+</sup> laser beam (488 nm, cw, @ 10 mW). A dichroic mirror and an optical bandpass filter (580/75 nm) separate excitation and emission light; in order to prevent optical crosstalk between the exciting and the AFM laser, an appropriate bandpass filter (670/20 nm) is mounted on the quadrant diode position detector. Fluorescence detection is realized with a high speed CCD camera (I-PentaMAX, Roper) equipped with a 512x512 pixel chip, microchannel plate image intensifier and a 5 MHz 12 bit A/D converter.

Luminescent CdSe/ZnS nanocrystals were prepared according to a previously published procedure<sup>[21]</sup> and exhibited an emission maximum at 585 nm. Briefly: A solution of Cd-stearate and trioctylphosphineselenide in trioctylphosphine (TOP) was swiftly injected into

a hot mixture of trioctylphosphineoxide (TOPO) and hexadecylamine. After several minutes of reaction, the mixture was quenched by adding cold butanol. The yielded nanocrystals were redispersed in TOPO. Diethylzinc and hexamethyldisilathiane in TOP were injected dropwise at elevated temperature. The reaction was terminated after one day and the resulting CdSe/ZnS nanocrystals were purified and resuspended in chloroform. The nanocrystals were immobilized by dilution in heptane and subsequent incubation and drying on a cleaned (treated with caroic acid, UVO cleaner) glass coverslip. Spherical Gold nanoparticles (average diameter: 5 nm) were synthesised by reduction of HAuCl<sub>4</sub> in the presence of citric acid in water<sup>[22]</sup>. The gold nanoparticles were used as synthesized. Silicon nitride AFM tips (Veeco) were amino-functionalized with 3-mercaptopropyltriethoxysilane and incubated with a suspension of the gold nanoparticles. It could be shown that these gold particles effectively quench the nanocrystal emission when applied to the sample in aqueous suspension<sup>[23]</sup>.

Fig. 2a shows the general experimental setup when the AFM tip is withdrawn from the sample surface. Nanocrystals immobilized on the cover glass surface are excited by the evanescent field emanating from a totally reflected laser beam and exhibiting fluorescence emission. When the AFM tip, as shown in Fig. 2b, is brought into near proximity of the nanocrystal, significant quenching of the single fluorophore emission induced by the quenching agent at the AFM tip is expected. The fluorescence emission time trace of a single nanocrystal and the corresponding z-position of the AFM-tip is shown in Fig. 2c (cf. also the supplementary video); z = 0 in AFM tip travel is equivalent with physical contact between AFM tip and the sample surface (total piezo travel: ca. 35 nm). Two regimes can clearly be distinguished: When the tip is removed from the nanocrystal on the sample surface, the system shows the known blinking characteristics typical for a single nanocrystal; if brought into near proximity, the emission of the nanocrystal is effectively quenched. The corresponding on- and off-time (cut-off threshold at 50 % of maximum intensity) distributions are shown in Fig. 3a and Fig. 3b for the withdrawn and approached tip, respectively. In Fig. 3c and 3d the cumulated probabilities (step functions) for on- and off-times for each of the two cases are shown. Both the on-time distributions and the step functions are significantly different with respect to the AFM-tip position. For the

withdrawn tip (Fig. 3c), the total on-time sums up to 79,8 % of the total time, i.e. the probability of finding the nanocrystal in the bright state is 79,8 %, as opposed to only 1 % for the experiment when the tip is approached (Fig. 3d). We found that “negative” control of the nanocrystal emission is possible, i.e. an external stimulus (the quenching agent) brought in close contact with the nanocrystal causes effective quenching, whereas the typical blinking behavior is re-established upon mechanical removal of the quenching agent.

We have presented a new means of switching the fluorescence emission of a single nanocrystal by external, mechanical intervention of an AFM tip. This technique represents a major step on the way to addressing and controlling molecular individuals in complex biological systems. Applications of the general concept ranging from microarrays to the manipulation of single reporter molecules are conceivable. Important information about dynamic processes (e.g. protein folding) is accessible via local energy transfer techniques<sup>[24]</sup>. AFM force spectroscopy yields complementary data, for example the force response of folded systems to the application of an external stress<sup>[25]</sup> or the adhesion forces between individual ligand-receptor pairs<sup>[26-31]</sup>. The combination of both approaches promises to be a valuable tool for the investigation of important features of molecular individuals such as folding pathways or molecular recognition.

## References

- [1] B. Lounis, W. E. Moerner, *Nature* **2000**, *407* 491-493.
- [2] D. M. Chudakov, V. V. Verkhusha, D. B. Staroverov, E. A. Souslova, S. Lukyanov, K. A. Lukyanov, *Nature Biotechnol.* **2004**, *22* 1435-1439.
- [3] S. Habuchi, R. Ando, P. Dedecker, W. Verheijen, H. Mizuno, A. Miyawaki, J. Hofkens, *Proc.Natl.Acad.Sci.USA* **2005**, *102* 9511-9516.
- [4] T. Hugel, N. B. Holland, A. Cattani, L. Moroder, M. Seitz, H. E. Gaub, *Science* **2002**, *296* 1103-1106.
- [5] T. Förster, *Ann.Phys.* **1948**, *2* 55-75.
- [6] L. Stryer, R. P. Haugland, *Proc.Natl.Acad.Sci.USA* **1967**, *58* 719-726.
- [7] P. R. Selvin, *Nature Struct.Biol.* **2000**, *7* 730-734.

- [8] T. Ha, Th. Enderle, D. F. Ogletree, D. S. Chemla, P. R. Selvin, S. Weiss, *Proc.Natl.Acad.Sci.USA* **1996**, 93 6264-6268.
- [9] C. B. Murray, D. J. Norris, M. G. Bawendi, *J.Am.Chem.Soc.* **1993**, 115 8706-8715.
- [10] M. A. Hines, P. Guyot-Sionnest, *J.Phys.Chem.* **1996**, 100 468-471.
- [11] M. Nirmal, B. O. Dabbousi, M. G. Bawendi, J. J. Macklin, J. K. Trautman, T. D. Harris, L. E. Brus, *Nature* **1996**, 383 802-804.
- [12] X. Brokman, J.-P. Hermier, G. Messin, P. Desbiolles, J.-P. Bouchaud, M. Dahan, *Phys.Rev.Lett.* **2005**, 90 120601-1-120601-4.
- [13] D. M. Willard, L. L. Carillo, J. Jung, A. Van Orden, *Nano Lett.* **2001**, 1 469-474.
- [14] E. Oh, M.-Y. Hong, D. Lee, S.-H. Nam, H. C. Yoon, H.-S. Kim, *J.Am.Chem.Soc.* **2005**, 127 3270-3271.
- [15] Z. Gueroui, A. Libchaber, *Phys.Rev.Lett.* **2004**, 93 166108-1-166108-4.
- [16] L. Dyadyusha, H. Yin, S. Jaiswal, T. Brown, J. J. Baumberg, F. P. Booy, T. Melvin, *Chem.Commun.* **2005**, 2005 3201-3203.
- [17] T. Funatsu, Y. Harada, M. Tokunaga, K. Saito, T. Yanagida, *Nature* **1995**, 374 555-559.
- [18] R. M. Dickson, D. J. Norris, Y.-L. Tzeng, W. E. Moerner, *Science* **1996**, 274 966-968.
- [19] G. Binnig, C. F. Quate, C. Gerber, *Phys.Rev.Lett.* **1986**, 56 930-933.
- [20] W. Trabesinger, A. Kramer, M. Kreiter, B. Hecht, U. P. Wild, *Appl.Phys.Lett.* **2002**, 81 2118-2120.
- [21] T. Nann, *Chem.Commun.* **2005**, 2005 1735-1736.
- [22] W. Bücking, T. Nann, *IEE Proc.Nanobiotechnology* **2005**, submitted .
- [23] B. Nikoobakht, C. Burda, M. Braun, M. Hun, M. A. El-Sayed, *Photochem.Photobiol.* **2002**, 75 591-597.
- [24] S. Weiss, *Nat.Struct.Biol.* **2000**, 7 724-729.
- [25] M. Rief, M. Gautel, F. Oesterhelt, J. M. Fernandez, H. E. Gaub, *Science* **1997**, 276 1109-1112.
- [26] G. U. Lee, L. A. Chrisey, R. J. Colton, *Science* **1994**, 266 771-773.
- [27] E.-L. Florin, V. T. Moy, H. E. Gaub, *Science* **1994**, 264 415-417.
- [28] U. Dammer, O. Popescu, P. Wagner, D. Anselmetti, H.-J. Güntherodt, G. N. Misevic, *Science* **1995**, 267 1173-1175.
- [29] R. Ros, F. Schwesinger, D. Anselmetti, M. Kubon, R. Schäfer, A. Plückthun, L. Tiefenauer, *Proc.Natl.Acad.Sci.USA* **1998**, 95 7402-7405.

- [30] R. Eckel, S. D. Wilking, A. Becker, N. Sewald, R. Ros, D. Anselmetti, *Angew.Chem.Int.Ed.* **2005**, *44*, 3921-3924; *Angew.Chem.* **2005**, *117*, 3989 –3993.
- [31] R. Eckel, R. Ros, B. Decker, J. Mattay, D. Anselmetti, *Angew.Chem.Int.Ed.* **2005**, *44*, 484-488; *Angew.Chem.* **2005**, *117*, 489-492.

## Figure Captions

**Fig. 1.** Single light emission control experiment (schematics). The complete setup is placed on an inverted microscope. A laser beam is projected via a TIRF objective lens at an angle of total reflection onto the cover glass. The evanescent wave protruding less than 50 nm beyond the interface excites fluorophores immobilized on the sample surface. Surface occupancy is low so as to enable the addressing of individual fluorophores. Fluorescence emission from the surface is recorded by a CCD camera. An AFM head is positioned on top of the microscope. The AFM tip is functionalized with nanoparticles known to effectively quench the fluorophore's fluorescence emission when brought into proximity.

**Fig. 2.** (a) TIRFM image of a single nanocrystal. The AFM tip is withdrawn ~35 nm from the sample surface. The fluorophore at the surface is excited and emits fluorescence light. (b) TIRFM image of the same nanocrystal if the quenching agent is positioned in close proximity. The fluorescence from the individual fluorophore is quenched. (c) Traces of the AFM piezo stage (upper part) and the concomitant fluorescence emission (lower part) of an individual nanocrystal fluorophore. Each data point corresponds to a 50 ms video frame. A low position value signifies proximity to the sample surface. When the tip is positioned close to the nanocrystal on the surface, the fluorescence emission is almost totally quenched. When the tip is redrawn, the blinking fluorescence emission typical for single nanocrystals is restored. As can be inferred from the traces, it was possible to repeatedly switch the fluorescence emission of a single dot from emitting (bright) to quenched (dark) state by simply approaching and retracting the tip.

**Fig. 3.** Statistics for single nanocrystal quenching experiments. Fig. 3a shows part of the on- and off-time histogram (threshold: 50 % of maximum intensity) for the experiment with AFM tip withdrawn. The distribution of the off-times is much narrower than for the on-times, most off-times have durations of only 50 or 100 ms. The situation is reversed for the

experiment with tip approached (3b); no on-times longer than 100 ms could be detected. Fig. 3c and Fig. 3d show the cumulated probabilities (total duration times normalized to one) as step functions for the cases tip withdrawn and tip approached, respectively. The probability of the nanocrystal being in the dark state is 20.2 % for tip withdrawn and 99.0 % for tip approached.

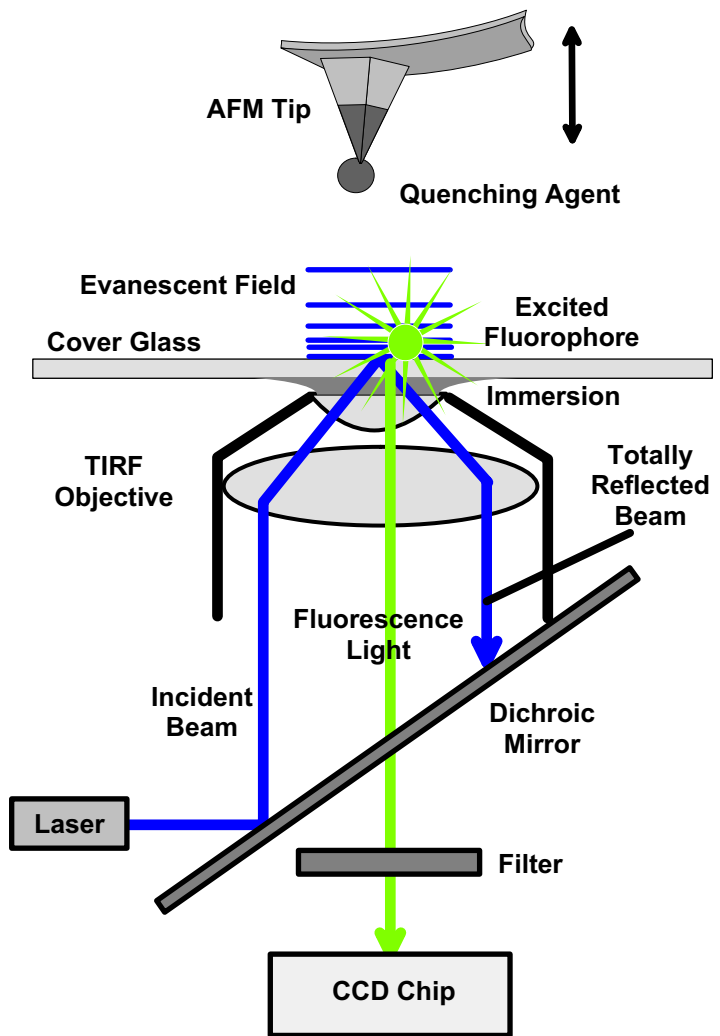


**Fig. 1**

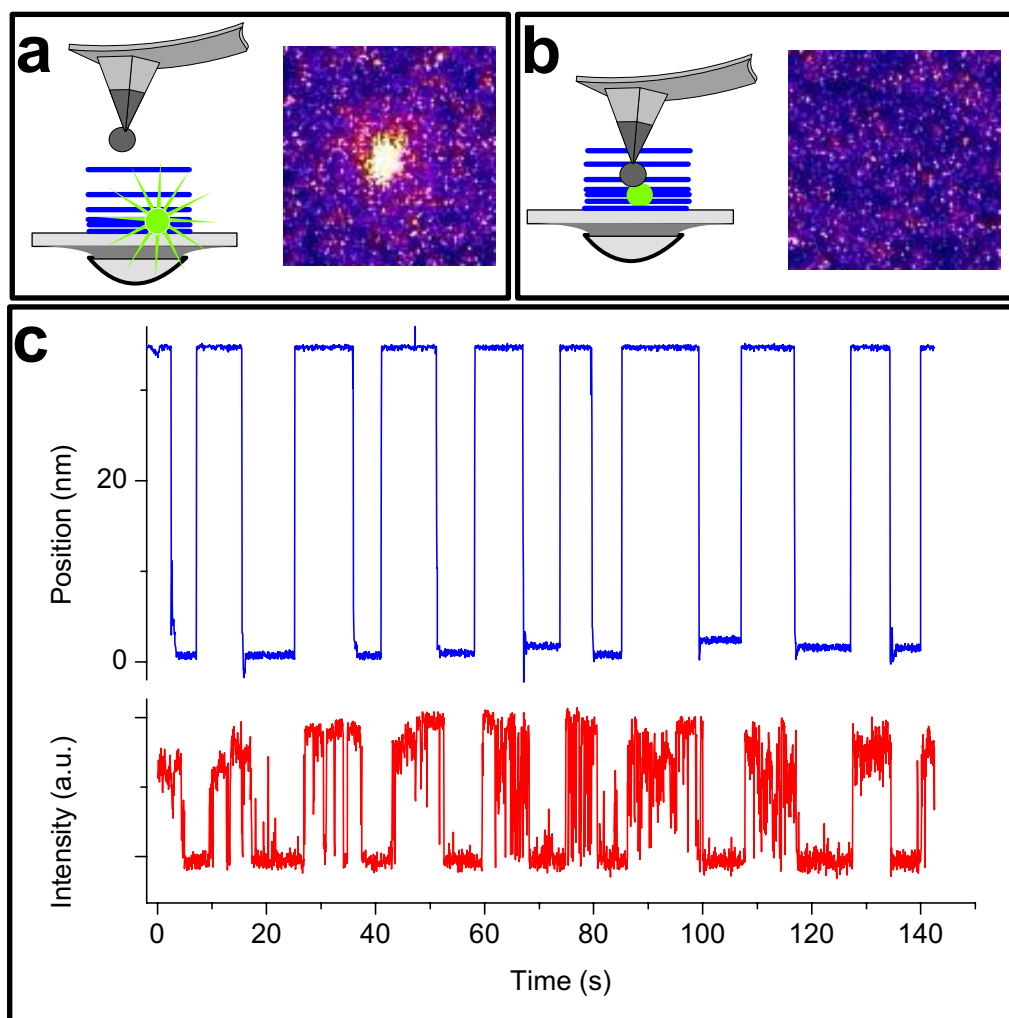
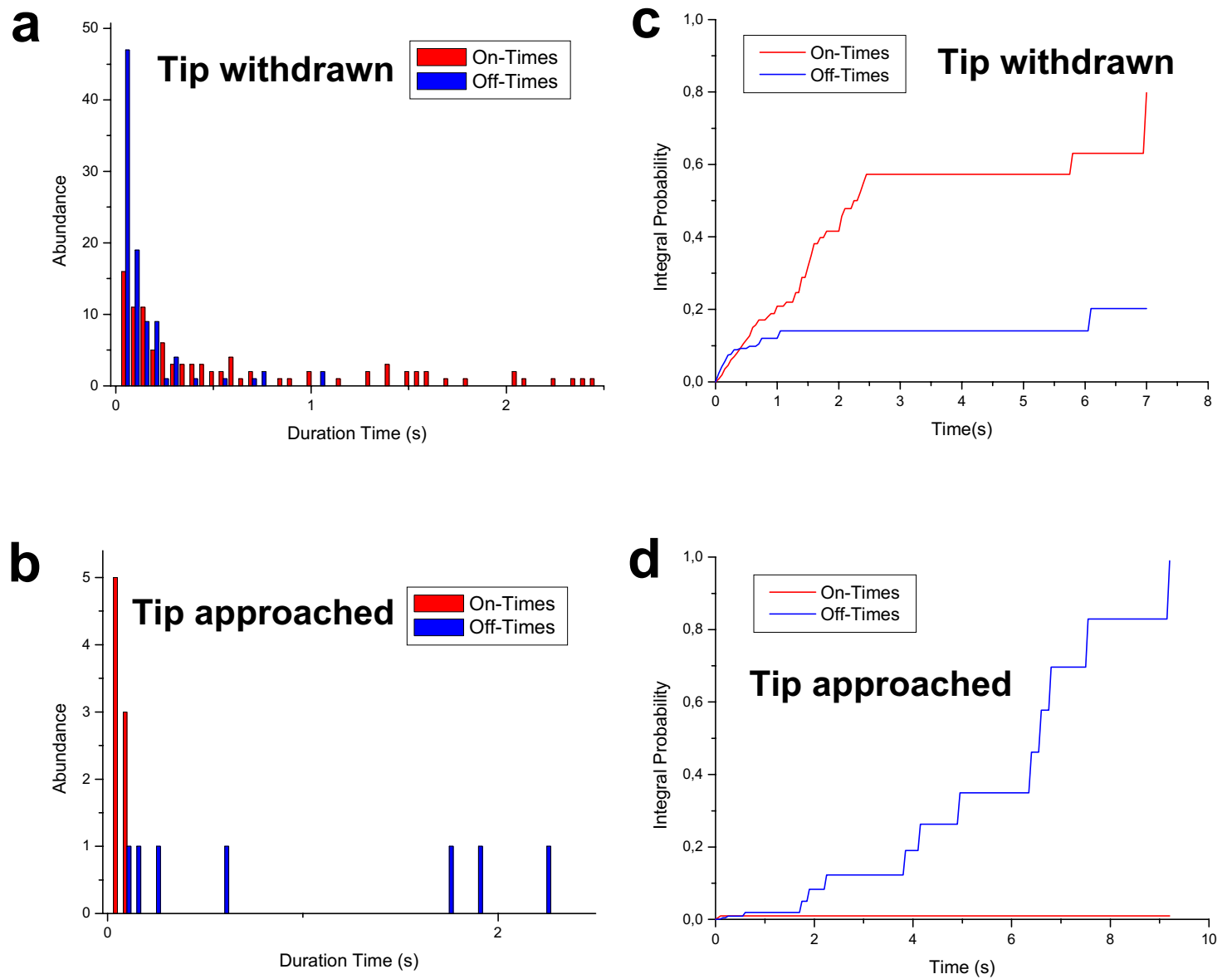


**Fig. 2**



## 6.3 Publication VIII

**Rainer Eckel**, Volker Walhorn, Christoph Pelargus, Jörg Martini, Thomas Nann, Dario Anselmetti, and Robert Ros. Combined TIRF-AFM Setup: Controlled Quenching of Individual Quantum Dots. Submitted to *Proc. SPIE*.

### 6.3.1 Contribution

The author designed and assembled the TIRFM setup for the combined AFM-TIRFM experiment (Fig.2) and performed the experimental work and analysis.

# Combined TIRF-AFM Setup: Controlled Quenching of Individual Quantum Dots

Rainer Eckel<sup>1\*</sup>, Volker Walhorn<sup>1\*</sup>, Christoph Pelargus<sup>1</sup>, Jörg Martini<sup>1</sup>, Thomas Nann<sup>2</sup>,  
Dario Anselmetti<sup>1</sup>, and Robert Ros<sup>1†</sup>

<sup>1</sup>Experimental Biophysics and Applied Nanoscience, Bielefeld University, Universitätsstraße 25,  
33615 Bielefeld, Germany

<sup>2</sup>Freiburg Materials Research Center (FMF), University of Freiburg, Stefan-Maier-Straße 21, 79104  
Freiburg, Germany

## ABSTRACT

Single molecules can nowadays be investigated by means of optical, mechanical and electrical methods. Fluorescence imaging and spectroscopy yield valuable and quantitative information about the optical properties and the spatial distribution of single molecules. Force spectroscopy by atomic force microscopy (AFM) or optical tweezers allows addressing, manipulation and quantitative probing of the nanomechanical properties of individual macromolecules. We present a combined AFM and total internal reflection fluorescence (TIRF) microscopy setup that enables ultrasensitive laser induced fluorescence detection of individual fluorophores, control of the AFM probe position in x, y and z-direction with nanometer precision, and simultaneous investigation of optical and mechanical properties at the single molecule level. Here, we present the distance-controlled quenching of semiconductor quantum dot clusters with an AFM tip. In future applications, fluorescence resonant energy transfer between single donor and acceptor molecules will be investigated.

**Keywords:** Single Molecule Manipulation; TIRF; AFM; Quantum Dots

## 1. INTRODUCTION

An important challenge for nanoscale science is the direct manipulation of individual nanoobjects, combined with simultaneous observation of the system's response which can manifest itself in properties like force, conformational change and optical properties. The ambition to measure several physical properties of single nanoobjects at a time requires the combination of conceptually different techniques which have evolved in the past decade. Especially the combination of single molecule fluorescence detection and atomic force microscopy or spectroscopy holds great promises for future investigation.

The observation of individual nanoscale behavior has greatly benefitted from the development of single molecule fluorescence imaging and spectroscopy techniques<sup>1, 2</sup>. Optical single molecule detection with low signal-to-noise ratios is facilitated by the illumination of small excitation volumes with laser light and collection of the emitted fluorescence light via a high numerical aperture objective lens which is coupled to a suitable, highly sensitive detector such as an avalanche photodiode, a photomultiplier tube, or an intensified charge-coupled device (CCD) camera. The confinement of the excitation volume can be achieved via different approaches, the most important being laser scanning confocal microscopy, where the fluorescence emission is focussed by a microscope lens through a pinhole aperture at the image plane, scanning near-field optical microscopy<sup>3</sup>, another scanning method which exploits the evanescent wave field

---

\* Contributed equally to this work.

† rros@physik.uni-bielefeld.de; phone +49-(0)521 1065388; fax +49-(0)521 1062959;  
www.physik.uni-bielefeld.de/biophysik

emanating from a nanoscale aperture, and total internal reflection fluorescence (TIRF) microscopy. TIRF microscopy also makes use of an evanescent wave field which is generated by total internal reflection of an incident laser beam at a high refraction index to low refraction index boundary. The illumination in TIRF microscopy is confined to a small area within the penetration depth of the evanescent wave, resulting in a significantly reduced fluorescence background. The technique, if applied to study single molecules<sup>4; 5</sup>, has the advantage that a complete illumination area enables the observation of many single fluorophores at a time; a slight disadvantage is the necessity to recur to comparably slow array detectors like CCD cameras.

The data obtained in single molecule fluorescence experiments yield direct information about energy changes in a single fluorophore and the transfer of energy which accompanies the interaction between different fluorophores. This information can indicate subpopulations or intermediates that are difficult or impossible to observe in a classical ensemble measurement. Specialized techniques like FRET (fluorescence resonant energy transfer) which require the radiationless interaction of two fluorophores and exhibit a strong distance dependence provide additional data, e.g. about folding pathways or the characteristic length scale of molecular recognition reactions. In this context, semiconductor nanocrystals (quantum dots) as a novel type of fluorescent probe have evoked considerable attention. Their long-term photostability and high excitation cross sections in combination with the possibility to functionalize them in a biocompatible way and attach them to biomolecules make them a promising alternative for optical nanoscale experiments<sup>6-8</sup>.

Single molecule force techniques focus on the mechanical properties of individual nanoobjects and can be regarded as a conceptually different approach which is complementary to optical experiments. They provide important information about the forces which accompany structural rearrangements within a single macromolecule<sup>9-11</sup>, or the forces and kinetics involved in the breaking of single ligand-receptor bonds<sup>12-17</sup>. Whereas in optical<sup>18</sup> or magnetic<sup>19</sup> tweezers the force is transduced via a microbead exposed to an external field, the atomic force microscope (AFM)<sup>20</sup> uses a microfabricated cantilever as mechanical force transducer to which a sharp nano-probe is attached. This technique also be used to address and manipulate single nanoobjects.

The complementarity of single molecule fluorescence and force techniques strongly advises for a combination of the different approaches. The simultaneous measurement of optical and mechanical properties will certainly provide new mechanistic insight into the forces, energies and conformational changes that accompany biomolecular interaction. Up to now, only few experiments which combine mechanical manipulation and fluorescence imaging or spectroscopy have been reported. Lang et al. presented a setup combining TIRF detection and optical trapping of single biomolecules<sup>21</sup>. Recently, also the combination of AFM and confocal microscopy has been reported<sup>22; 23</sup>.

In this work, a combined AFM-TIRF microscopy setup for the manipulation of single nanoobjects and the quantitative probing of biomolecular interactions is introduced which allows simultaneous mechanical manipulation and fluorescence imaging. The controlled quenching of semiconductor quantum dot fluorescence emission by mechanical intervention of an AFM tip is presented.

## 2. INSTRUMENTATION

The experiments are performed on a home-built AFM-head (Fig. 1) using the beam deflection method<sup>24</sup> to read out the cantilever deflection. A laser diode module (HL11, Lisa Laser, Katlenburg, Lindau, Germany, optical power <1mW @ 670 nm) with an integrated collimation optics is directed on a polarizing beam splitter (Linos, Göttingen, Germany). The incident beam is divided into two orthogonally linear polarized beams from which the undiverted is blocked. The other beam passes a  $\lambda/4$  wave plate (Linos, Göttingen, Germany) where the polarisation is changed to circular. A focussing lens  $f = 8$  mm serves to direct the laser on the cantilever as well as to collimate the reflected part of the beam. Passing again the  $\lambda/4$  wave plate the polarisation is changed to linear polarisation which is tilted by  $\pi/2$  referring to the incident beam. This enables the passing of the reflected beam through the beam splitter with virtually no loss of intensity. A dichroic mirror (XF2021, Omega Optical Inc., Brattleboro, USA) allows observation of the cantilever and sample but leaves the deflected laser beam unaffected. A quadrant photodiode (QD50-5T, Centronic, Croydon Surrey, England) serves as position sensitive device. For each segment the induced current is converted to voltage by a single high speed operational amplifier (Burr-Brown OPA655, Texas Instruments, Dallas Texas, USA). These yield high bandwidth performance as well as reasonable signals even for poor cantilever reflectivity. A home-made quadrant detector electronics is used for both generating deflection and lateral signals and further amplification. Optionally an analog 8<sup>th</sup> order Tchebycheff low pass filter ( $f_{\text{cutoff}} = 4$  kHz) can be inserted before the data acquisition hardware. 16-bit

multiplex AD/DA boards and a 16-bit transient recorder are used, respectively, for experiment control and data acquisition (PCI-6036E and PCI-6704, National Instruments, Austin Texas, USA and Spectrum MI.4540, Spectrum GmbH, Grosshadendorf, Germany). The AFM control software is a self-coded LabVIEW program (National Instruments, Austin Texas, USA).

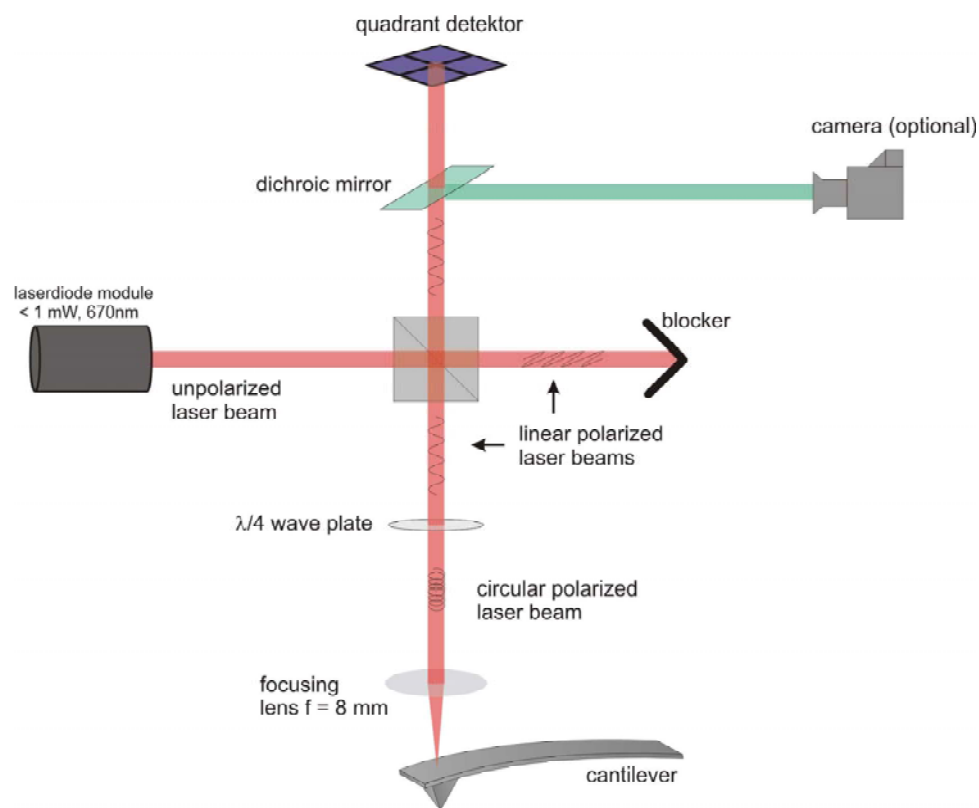


Fig. 1: AFM head setup

Schematic of the optical components of the home-built AFM. A collimated laser beam is linearly polarized and redirected by a beam splitter. Polarisation is changed to circular by a  $\lambda/4$  wave plate. A lens focuses the incident and collimates the reflected laser beam. The  $\lambda/4$  wave plate changes polarisation back to linear. The beam splitter and the dichroic mirror are passed. The cantilever deflection is read out by a quadrant photodiode.

The AFM-head is mounted on a frame bearing the sample stage. This stage consists of a sample holder for 24x24 mm coverslips on a manually driven 2D stage which itself is mounted on a 3D piezo stage (PI 517.3CL, Physik Instrumente GmbH & Co. KG, Karlsruhe, Germany) with travel ranges of 100x100x20  $\mu\text{m}$ . The piezo stage can be operated in open loop (analog) and closed loop mode (analog or digital) via an adequate controller (E516, Physik Instrumente GmbH & Co. KG, Karlsruhe, Germany). The sample stage is mounted on an inverting microscope (Zeiss Axiovert S100, Carl Zeiss, Jena, Germany) such that the microscope lens points to the sample (Fig. 2).

The sample is optically excited by an argon ion laser (cw 50 mW @ 488 nm). To avoid excitation by other laser lines a filter is inserted into the optical path (XF1073 475/40, Omega Optical Inc. Brattleboro, USA). The sample is illuminated from underneath by an objective lens (Olympus Plapo 100X TIRFM, NA=1,45; Olympus, Tokyo, Japan) either in EF (epifluorescence) or TIRF (total internal reflection fluorescence) mode. Fluorescent light is directed from the microscope lens through a band pass filter (HQ 580/80, AHF Analysentechnik, Tübingen, Germany) to a high speed CCD-Camera (I-PentaMAX, Roper Scientific, Trenton, New Jersey, USA). The acquired fluorescence signal is intensified by a micro channel plate intensifier and directed to a 512X512 pixel CCD chip. A 5 MHz 12-bit AD-

converter realizes a frame rate of approximately 20Hz for a full frame. By choosing a region of interest higher frame rates can be achieved.

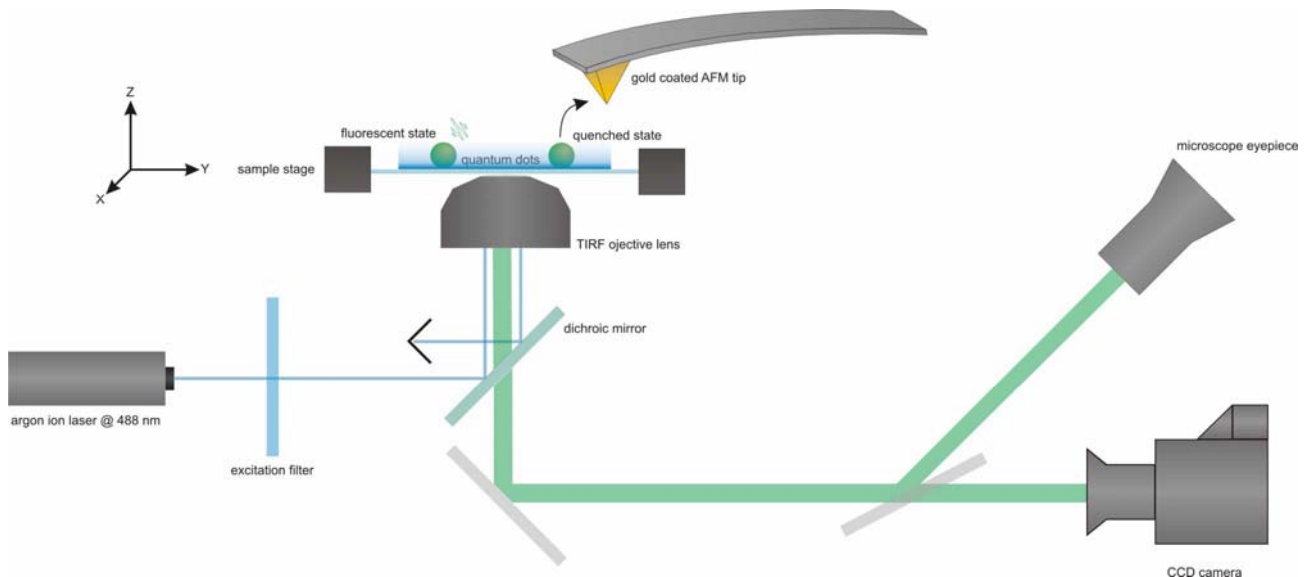


Fig. 2: TIRF setup

Quantum dots on a coverslip are illuminated by an argon ion laser. Fluorescent light is directed via a dichroic mirror to a CCD camera. Switching between the fluorescent and extinguished state is induced by retracting and approaching a gold coated cantilever.

### 3. MATERIALS AND METHODS

Fluorescent CdSe/ZnS nanocrystal quantum dots were prepared following a previously published protocol<sup>25</sup>. In short, a solution of cadmium stearate and trioctylselenide in trioctylphosphine was swiftly injected into a hot mixture of trioctylphosphineoxide and hexadecylamine. The mixture was stirred for several minutes and then quenched by adding cold butanol. The resulting nanocrystals were resuspended in trioctylphosphineoxide. To this dispersion, a solution of diethylzinc and hexamethyldisilathiane in trioctylphosphine was added dropwise at elevated temperature for one day. The CdSe/ZnS nanocrystals obtained in this reaction were purified and redispersed in chloroform. They showed an emission maximum around 585 nm. For immobilization, the semiconductor nanocrystals were diluted in heptane and subsequently dried on a cleaned (treatment with caroic acid, UVO cleaner) glass coverslip. Silicon nitride AFM tips (Microlevers, Veeco Metrology LLC, S. Barbara, California, USA) were coated with a 10 nm gold layer by evaporation. It has been demonstrated that the fluorescence emission of the semiconductor nanocrystals is effectively quenched if brought into contact with gold surfaces<sup>26</sup>.

### 4. RESULTS AND CONCLUSION

To test the TIRF microscopy setup, single quantum dots were detected and their fluorescence emission and fluorescence intermittency (blinking) observed. Fig. 3 shows a time series, taken with a frame rate of 20 Hz, of a  $12 \times 12 \mu\text{m}^2$  frame from a quantum dot experiment. As is evident from the flares in fluorescence intensity, one of the bright spots (termed b) in the frame exhibits the characteristic blinking and can be unambiguously identified as single nanocrystals, the other two spots (a and c) being probably a bunch of several ones.

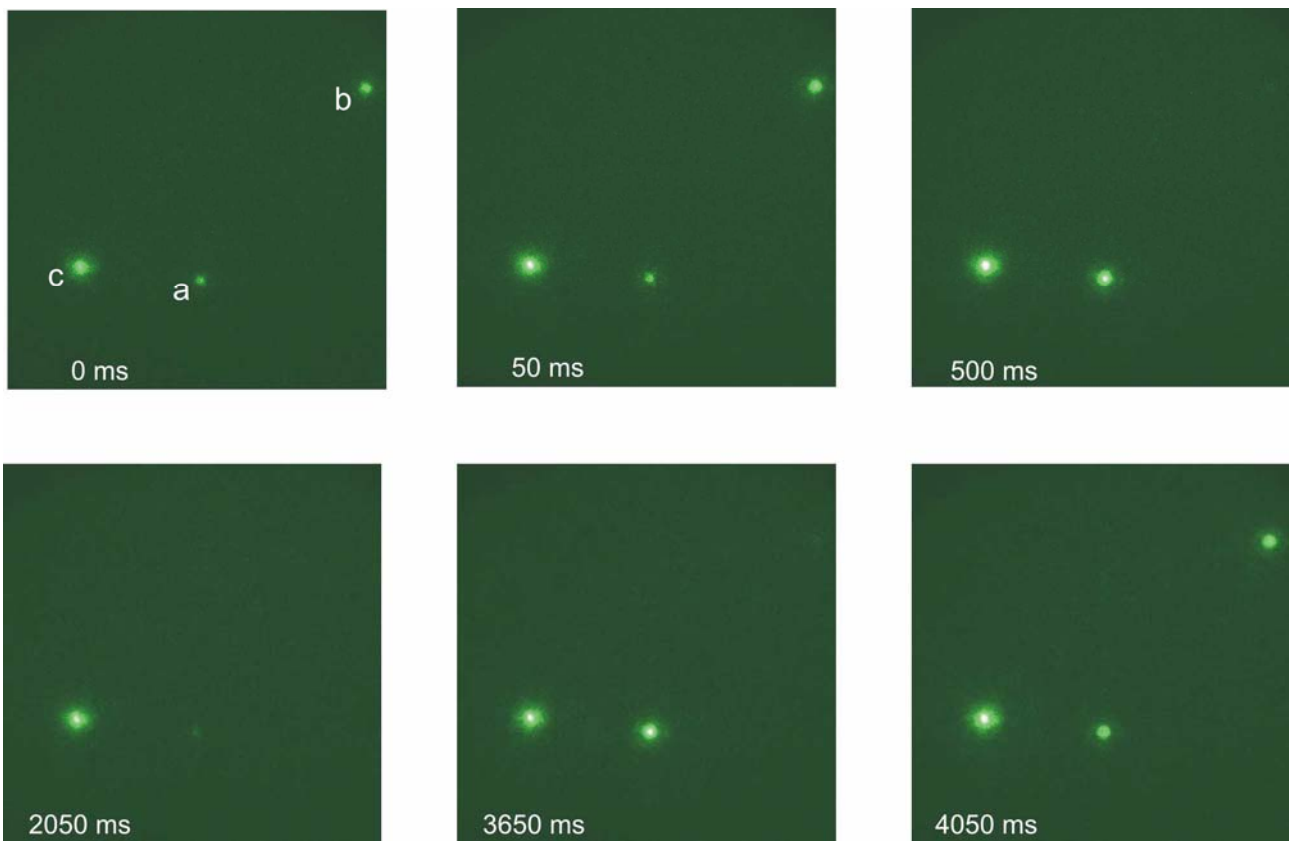


Fig. 3: Optical imaging of semiconductor quantum dots

Successive images of semiconductor quantum dots on a coverslip taken with a frame rate of 20 Hz. The spot marked with (b) represents a single nanocrystal; this can be inferred from the typical blinking behaviour. The spots (a) and (c), however, exhibit only slight fluctuations of intensity and therefore might represent rather an aggregate of several semiconductor quantum dots.

Using the combined TIRF-AFM setup, the mechanical emission control of a small cluster of single quantum dots by means of gold-coated AFM probe has been achieved. In a series of mechano-optical experiments, fluorescence images of the aggregate were taken at a frame rate of 20 Hz while the lateral position of the tip was varied. The results are presented in Fig. 4. The first row demonstrates the respective position of the AFM tip: At (a), which corresponds to the tip position during the first five seconds of the experiment, the tip is separated from the nanocrystal fluorophores by a lateral distance of a half micron; after five seconds (b), the tip has moved laterally into the near proximity of the cluster; the gold surface is now very close to the quantum dots; after another five seconds (c), the tip is removed again. The second row shows fluorescence images of the quantum dot aggregate (frame:  $600 \times 600 \text{ nm}^2$ ) from the time intervals (a), (b) and (c), respectively. The third row presents the plot of intensity against time. It is evident from (b) that approximation of the tip causes effective quenching of the quantum dot fluorescence. Upon withdrawal of the tip (c), the original fluorescence emission from the cluster can only be partly regained; from the corresponding intensity trace and the image, it can be concluded that one of the presumably three single dots has been removed or bleached by the tip. Nevertheless, this experiment clearly proves the capability of the combined TIRF-AFM setup to control the optical properties of single nanoobjects by external, mechanical intervention.

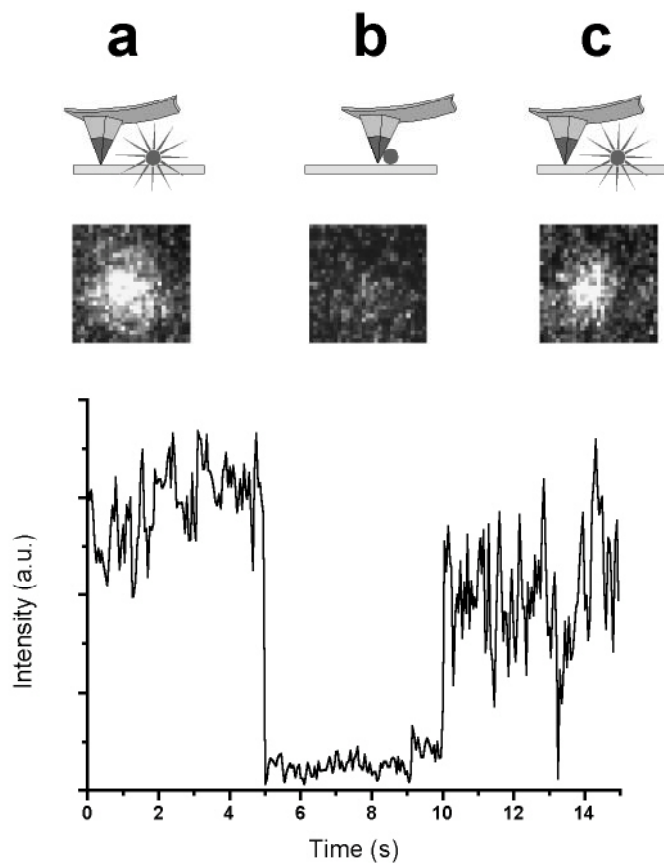


Fig. 4: External emission control of a semiconductor quantum dot cluster.

The fluorescence emission from a bunch of semiconductor nanocrystals (probably three) could be effectively quenched by moving a gold-coated AFM tip into the proximity of the aggregate. The emission of at least some (probably two) nanocrystals could be re-activated upon lateral retraction of the tip. The first row of images shows a schematic of the lateral tip movement, the second a fluorescence image of the aggregate, the third a plot of the fluorescence intensity against time. During the first five seconds of the experiment (a), the tip was not in contact with the aggregate. For the next five seconds (b), the tip was moved laterally and brought into contact with the aggregate. Subsequently, it was removed again (c).

Further improvements of the setup will facilitate the simultaneous AFM topography and fluorescence imaging of the sample. It is planned to address individual fluorophores with different receptors and to perform affinity experiments with these. The next step on the way to simultaneous fluorescence and force spectroscopy on single biomolecules will be the addition of an acceptor fluorophore (instead of a quenching agent) to the AFM tip and, subsequently, the simultaneous measurement of tip position and fluorescence resonant energy transfer between the donor and acceptor. Furthermore, the experiment discussed here resembles an off-switching of the fluorophore and hence a “negative” control; the inverse approach, i.e., a FRET setup with an acceptor fluorophore attached to the sample surface and a donor at the AFM tip, would correspond to a “positive” control of fluorophore emission, i.e., the fluorescence signal is switched on if the external stimulus (the donor fluorophore at the tip) is brought close.

#### ACKNOWLEDGEMENTS

Financial support from the Deutsche Forschungsgemeinschaft (SFB 613) is gratefully acknowledged.

## REFERENCES

1. Moerner,W.E. and Fromm,D.P.: "Methods of single-molecule fluorescence spectroscopy and microscopy", Rev.Sci.Instr., **74**, 3597-3619, 2003.
2. Orrit,M.: "Single-molecule spectroscopy: The road ahead", J.Chem.Phys., **117**, 10938-10946, 2002.
3. Pohl,D.W., Denk,W., and Lanz,M.: "Optical stethoscopy: Image recording with resolution lambda/20", Appl.Phys.Lett., **44**, 651-653, 1984.
4. Funatsu,T., Harada,Y., Tokunaga,M., Saito,K., and Yanagida,T.: "Imaging of single fluorescent molecules and individual ATP turnovers by single myosin molecules in aqueous solution", Nature, **374**, 555-559, 1995.
5. Dickson,R.M., Norris,D.J., Tzeng,Y.-L., and Moerner,W.E.: "Three-dimensional imaging of single molecules solvated in pores of poly(acrylamide) gels", Science, **274**, 966-968, 1996.
6. Larson,D.R., Zipfel,W.R., Williams,R., Clark,S.W., Bruchez,M.P., Wise,F.W., and Webb,W.W.: "Water-soluble quantum dots for multiphoton fluorescence imaging in vivo", Science, **300**, 1434-1436, 2003.
7. Parak,W.J., Gerion,D., Pellegrino,T., Zanchet,D., Micheel,C., Williams,S.C., Boudreau,R., Le Gros,M.A., Larabell,C.A., and Alivisatos,A.P.: "Biological applications of colloidal nanocrystals", Nanotechnology, **14**, R15-R27, 2003.
8. Bruchez Jr.,M., Moronne,M., Gin,P., Weiss,S., and Alivisatos,A.P.: "Semiconductor nanocrystals as fluorescent biological labels", Science, **281**, 2013-2016, 1998.
9. Rief,M., Oesterhelt,F., Heymann,B., and Gaub,H.E.: "Single molecule force spectroscopy on polysaccharides by atomic force microscopy", Science, **275**, 1295-1297, 1997.
10. Rief,M., Gautel,M., Oesterhelt,F., Fernandez,J.M., and Gaub,H.E.: "Reversible unfolding of individual titin immunoglobulin domains by AFM", Science, **276**, 1109-1112, 1997.
11. Eckel,R., Ros,R., Ros,A., Wilking,S.D., Sewald,N., and Anselmetti,D.: "Identification of binding mechanisms in single molecule-DNA complexes", Biophys.J., **85**, 1968-1973, 2003.
12. Florin,E.-L., Moy,V.T., and Gaub,H.E.: "Adhesion forces between individual ligand-receptor pairs", Science, **264**, 415-417, 1994.
13. Lee,G.U., Chrisey,L.A., and Colton,R.J.: "Direct measurement of the forces between complementary strands of DNA", Science, **266**, 771-773, 1994.
14. Ros,R., Schwesinger,F., Anselmetti,D., Kubon,M., Schäfer,R., Plückthun,A., and Tiefenauer,L.: "Antigen binding forces of individually addressed single-chain Fv antibody molecules", Proc.Natl.Acad.Sci.USA, **95**, 7402-7405, 1998.
15. Bartels,F.W., Baumgarth,B., Anselmetti,D., Ros,R., and Becker,A.: "Specific binding of the regulatory protein ExpG to promoter regions of the galactoglucan biosynthesis gene cluster of Sinorhizobium meliloti - a combined molecular biology and force spectroscopy investigation", J.Struct.Biol., **143**, 145-152, 2003.
16. Eckel,R., Ros,R., Decker,B., Mattay,J., and Anselmetti,D.: "Supramolecular chemistry at the single-molecule level", Angew.Chem.Int.Ed., **44**, 484-488, 2005.

17. Eckel,R., Wilking,S.D., Becker,A., Sewald,N., Ros,R., and Anselmetti,D.: "Single-molecule experiments in synthetic biology: An approach to the affinity ranking of DNA-binding peptides", *Angew.Chem.Int.Ed.*, **44**, 3921-3924, 2005.
18. Ashkin,A.: "Optical laser trapping and manipulation of neutral particles using lasers", *Proc.Natl.Acad.Sci.USA*, **94**, 4853-4860, 1997.
19. Smith,S.B., Finzi,L., and Bustamante,C.: "Direct mechanical measurements of the elasticity of single DNA molecules by using magnetic beads", *Science*, **258**, 1122-1126, 1992.
20. Binnig,G., Quate,C.F., and Gerber,C.: "Atomic Force Microscope", *Phys.Rev.Lett.*, **56**, 930-933, 1986.
21. Lang,M.J., Fordyce,P.M., and Block,S.M.: "Combined optical trapping and single-molecule fluorescence", *J.Biol.*, **2**, 2003.
22. Kassies,R., van der Werf,K.O., Lenferink,A., Hunter,C.N., Olsen,J.D., Subramaniam,V., and Otto,C.: "Combined AFM and confocal fluorescence microscope for applications in bio-nanotechnology", *J.Microsc.*, **217**, 109-116, 2005.
23. Owen,R.J., Heyes,C.D., Knebel,D., Rocker,C., and Nienhaus,G.U.: "An integrated instrumental setup for the combination of atomic force microscopy with optical spectroscopy", *Biopolymers*, (**electronic publication ahead of print**), 2005.
24. Meyer,G. and Amer,N.M.: "Novel optical approach to atomic force microscopy", *Appl.Phys.Lett.*, **53**, 1045-1047, 1988.
25. Nann,T.: "Phase-transfer of CdSe@ZnS quantum dots using amphiphilic hyperbranched polyethylenimine", *Chem.Commun.*, **2005**, 1735-1736, 2005.
26. Nikoobakht,B., Burda,C., Braun,M., Hun,M., and El-Sayed,M.A.: "The quenching of CdSe quantum dots photoluminescence by gold nanoparticles in solution", *Photochem.Photobiol.*, **75**, 591-597, 2002.

## 7 Conclusions and Outlook

In this thesis, several different aspects of interaction between single molecules and nanocrystals have been investigated by means of single molecule force spectroscopy and total internal fluorescence microscopy. This chapter is intended to summarize the major conclusions in turn and to give a short outlook.

The sequence-nonspecific interaction between double-stranded DNA and small organic effector molecules at the single molecule level was studied in the first part of this thesis (chapter 2). In publication I, the effects of ligands on the force-induced structural transitions of DNA were detected and analyzed. It could be proven that AFM SMFS is a potent tool to identify and distinguish between the different binding modes intercalation, minor and major groove binding. The recognition of the poly(dG-dC) DNA minor groove by the cytostatic drug distamycin A could be shown to cause a significant shift to lower forces in the B-S plateau which is observed for free DNA. The synthetic amphiphilic peptides Ac-(Leu-Ala-Arg-Leu)<sub>3</sub>-NH<sub>2</sub> (an  $\alpha$ -helix) and Ac-(Aib-Leu-Arg)<sub>4</sub>-NH<sub>2</sub> (a 3<sub>10</sub>- helix) showed a similar, though more pronounced, effect, with a B-S plateau merged and not easily separable from the irrversibel melting transition observed in free DNA. This result gave strong indication that the two peptides, as was formulated as an a priori hypothesis, indeed bind to the DNA major groove. In contrast to this behaviour, no distinct B-S plateau was observed for the complexes of single poly(dG-dC) DNA with the different intercalants daunomycin, ethidium, YO-1 and YOYO-1. These intercalants hinder the partial unwinding which goes with the B-S transition, so the force-distance trace only represents a steady, quasi-exponential increase in force as a function of molecular extension.

In publications II and III, these investigations were repeated, taking advantage of the increased force sensitivity of an optical tweezers setup as compared to an AFM in the low force regime. In these studies, the previously formulated results could be corroborated, extended to further DNA-ligand systems and quantified in terms of molecular elasticity models like the Worm-Like Chain and the Two-State Worm-Like Chain, a

---

model which is well suited for the description of the B-S transition in double-stranded DNA. The fitting of these models to force-extension data yielded parameters which indicate a decrease in persistence length (which is a measure for the intrinsic stiffness of a polymer) in the order free DNA → complex with minor groove binder → complex with intercalant. The effect of the minor groove binders could be due to a narrowing of the groove upon binding. These results clearly show the potential of SMFS experiments for the investigation of intramolecular transitions and the interaction of chain-like polymers with small ligand molecules.

The next part of this work (chapter 3) dealt with the sequence-specific interaction of the transcription factor PhoB (*E. coli*) to the corresponding DNA *pho* box target sequence. In Publication IV, the binding of a peptide fragment representing the DNA recognition helix of the PhoB protein and several point mutants of this peptide sequence to the DNA target was investigated by intermolecular SMFS. The forces of molecular recognition observed for these complexes were analyzed quantitatively, and dynamic force spectroscopy results proved a dependence of the binding forces on external load, yielding values for the molecular reaction (dissociation) length  $x_\beta$  and the thermal off-rate  $k_{off}$  (in accordance with Evans' and Ritchie's standard theory). It could be shown that the wild type peptide and two point mutants with cationic amino acid residues exchanged by alanine bind specifically to the *pho* box, one of the mutants (R193A) even with a lower off-rate than the native sequence. This is the first affinity ranking of synthetic peptides mimicking the function of a protein at the single molecule level.

Recently, also the native protein PhoB (strictly speaking, only the DNA binding domain PhoB(126-229)) could be isolated by biochemical methods and investigated in an SMFS experiment (chapter 3.3). This investigation provides a quantitative answer to the question what contribution the protein environment, especially the stabilizing helix  $\alpha_2$ , adds to binding strength and specificity: According to the dynamic force spectroscopy results, the life time of the DNA-bond is increased by three orders of magnitude in the case of the protein as compared to the wild type peptide PhoB(190-209).

In the future, it is planned to express also the mutant proteins R193A and H198A in *E. coli* and to investigate their DNA-binding via SMFS. Moreover, fluorescence correlation spectroscopy (FCS) and surface plasmon resonance (SPR) experiments, both of which are not feasible with the peptides for different reasons, shall be performed with the proteins, which will hopefully yield comparative and additional data. A further perspective for the more distant future is the integration of photochromic groups into a functional peptide (serving as a prototype of a photoswitchable transcription factor) and its investigation at the single molecule level, using the combined AFM-TIRFM setup

discussed in chapter 6.

The first quantitative SMFS experiments on a supramolecular system, the host-guest complex between a resorc[4]arene cavitand and three different tetra(organyl)ammonium ions, were reported in publication V. Competition experiments proved the specific binding of the guests ammonium and trimethylammonium to the receptor cavity. Dynamic force spectroscopy results showed that the dissociation of the host-guest complex can be formulated as an activated decay of a metastable bound state and analyzed according to the standard theory as a thermally driven unbinding process, in the very same way as for biological receptor-ligand systems. A major difference to molecular recognition in complex biological systems are, however, the significantly higher off-rates and the concomitant lower bond life times. It could be shown that SMFS is capable to detect, quantify and affinity-rank even low-affinity interactions in synthetic supramolecular complexes. Apart from the kinetic data, the experiments also provided structural information in terms of molecular reaction lengths which are in good accordance with the calculated van der Waals diameters for the guest molecules.

A recent experiment (chapter 4.3) was performed on a photoswitchable resorc[4]arene receptor, functionalized at the upper rim of the host cavity by two photochromic anthryl groups. It could be shown in SMFS experiments that the reversible affinity-switching of the receptor molecule by means of UV radiation (open  $\rightarrow$  closed cavity) and heat (closed  $\rightarrow$  open cavity) is possible. Different applications for the photochromic system are conceivable. A self-assembled monolayer of the photoswitchable host molecule studied here may serve as the prototype of a nanoscale re-writable memory. The host molecule may also operate as a switchable trap for ligand molecules, i.e. as a single-molecule tweezers system.

Future experiments in this field will investigate the forces observed in inclusion compounds, where a guest is encased by the interacting cavities of two host molecules at the same time. Other interesting topics are the investigation of pH dependencies and chiral recognition. A long-term goal might be a combined fluorescence-resonant energy transfer (FRET)-SMFS experiment with a fluorophore-labeled host and suitable guest molecules.

The theoretical framework for the analysis of intermolecular SMFS experiments like the ones discussed in chapters 3 and 4 of this thesis was examined in publication VI. Evans' and Ritchie's basic postulates (chapter 3.1.3) were tested using a new method of analysis, which predicted the collapse of the experimental data to a single master curve in a  $-v \ln \tilde{p}_v(f)$  against  $f$  plot. The analysis of the data from publications IV and V proved that this collapse does not occur, and that this inconsistency can only be satisfactorily

explained if one allows for an intrinsic random distribution of the off-rate  $k_{off}$ . This theoretical necessity, translated into the language of the experimentalist, corresponds to a heterogeneity of chemical bonds which can be assigned to random fluctuations in structure, orientation, and local environment of the receptor-ligand complex. It turns out that the new method of analysis based on the heterogeneity of chemical bonds yields similar values for the dissociation length  $x_\beta$  as the standard method, but far better estimates of  $k_{off}$ . This new method will soon be implemented in order to become the new standard for the analysis of SMFS experiments.

While the previously discussed results all dealt with forces of molecular interactions, the last (and most recent) part of this thesis was concerned with a different type of interaction, namely the transfer of excitational energy from a single semiconductor nanocrystal to a quenching agent (gold nanocrystals attached to an AFM tip). This interaction was studied in a home-built, combined AFM-TIRFM setup (described in detail in publication VIII) which allows simultaneous fluorescence microscopy and manipulation of single nanoobjects. Using this combination, the first external, mechano-optical emission control of a single nanoobject by means of a functionalized AFM tip was achieved (publication VII): The emission state of a nanocrystal quantum dot could be switched from emitting (blinking) to dark (quenched) state. The combination of single quantum dot and AFM tip can be considered as a novel type of a nanophotonic switch.

Where to go from here? A very important experimental method based on local energy

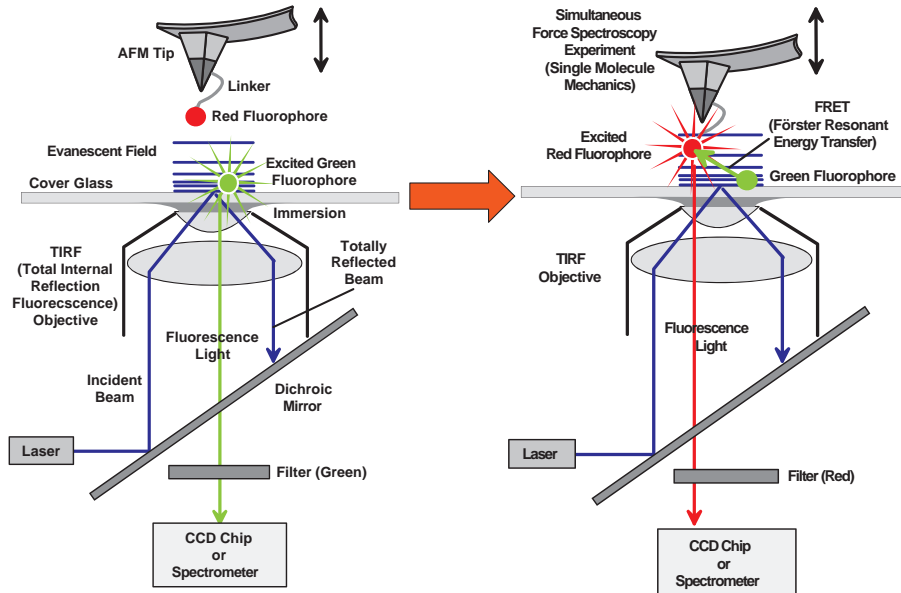


Figure 7.1: Design of a future combined SMFS-FRET experiment.

transfer is fluorescence resonant energy transfer (FRET) where the distance-dependence

of the interaction provides important insight into dynamic processes like the folding pathways of macromolecules or molecular recognition. In this respect, FRET is complementary to SMFS which focusses on forces rather than energies and distances. A combination of the different approaches holds great promise for the study of individual molecules. A conceivable next experimental step can be the addition of an acceptor fluorophore (instead of a quenching agent) to the AFM tip and, subsequently, the simultaneous measurement of tip position and FRET between the donor and acceptor as depicted in Fig. 7.1. Whereas this experiment resembles an off-switching of the fluorophore and hence a “negative” control, the inverse approach, i.e., an inverted FRET setup with an acceptor fluorophore attached to the sample surface and a donor at the AFM tip, would correspond to a “positive” control of fluorophore emission, i.e., the fluorescence signal is switched on if the external stimulus (the donor fluorophore at the tip) is brought close. One can also think of unfolding experiments on single molecules with simultaneous FRET measurement. Certainly the technique will open new possibilities to address and control single fluorophores also in more complex systems.

If it is feasible to draw a general conclusion from this thesis which has dealt with a variety of interactions at the level of single nanoobjects, from very complex ones like the molecular recognition of DNA by large transcription factors down to the interactions experienced by nonspecific DNA binders, supramolecular host-guest systems and semiconductor nanocrystals, it is the finding that the possibilities of investigating and manipulating matter that we already have at our disposal are fascinating, and that the study of physical interaction at the nanoscale will remain a most inspiring subject.

# Bibliography

- [1] G. Binnig, C. F. Quate, C. Gerber. Atomic force microscope. *Phys. Rev. Lett.*, 56(9):930–933, 1986.
- [2] G. Meyer, N. M. Amer. Novel optical approach to atomic force microscopy. *Appl. Phys. Lett.*, 53:1045–1047, 1988.
- [3] A. Kishino, T. Yanagida. Force measurements by micromanipulation of a single actin filament by glass needles. *Nature*, 334:74–76, 1988.
- [4] E. Evans, K. Ritchie, R. Merkel. Sensitive force technique to probe molecular adhesion and structural linkages at biological surfaces. *Biophys. J.*, 68:2580–2587, 1995.
- [5] T. R. Strick, J.-F. Allemand, D. Bensimon, A. Bensimon, V. Croquette. Direct mechanical measurements of the elasticity of a single supercoiled DNA molecule. *Science*, 271:1835–1837, 1996.
- [6] S. B. Smith, L. Finzi, C. Bustamante. Direct mechanical measurements of the elasticity of single DNA molecules by using magnetic beads. *Science*, 258:1122–1126, 1992.
- [7] A. Ashkin. Optical laser trapping and manipulation of neutral particles using lasers. *Proc. Natl. Acad. Sci. USA*, 94:4853–4860, 1997.
- [8] M. Rief, F. Oesterhelt, B. Heymann, H. E. Gaub. Single molecule force spectroscopy on polysaccharides by atomic force microscopy. *Science*, 275:1295–1297, 1997.
- [9] M. Rief, M. Gautel, F. Oesterhelt, J. M. Fernandez, H. E. Gaub. Reversible unfolding of individual titin immunoglobulin domains by AFM. *Science*, 276:1109–1112, 1997.

## Bibliography

---

- [10] P. Cluzel, A. Lebrun, C. Heller, R. Lavery, J.-L. Viovy, D. Chatenay, F. Caron. DNA: An extensible molecule. *Science*, 271:792–794, 1996.
- [11] M. Rief, H. Clausen-Schaumann, H. E. Gaub. Sequence-dependent mechanics of single DNA molecules. *Nat. Struct. Biol.*, 6(4):346–349, 1999.
- [12] E. Evans, K. Ritchie. Dynamic strength of molecular adhesion bonds. *Biophys. J.*, 72:1541–1555, 1997.
- [13] R. Merkel, P. Nassoy, A. Leung, K. Ritchie, E. Evans. Energy landscapes of receptor-ligand bonds explored with dynamic force spectroscopy. *Nature*, 397:50–53, 1999.
- [14] G. U. Lee, D. A. Kidwell, R. J. Colton. Sensing discrete streptavidin-biotin interactions with atomic force microscopy. *Langmuir*, 10:354–357, 1994.
- [15] E.-L. Florin, V. T. Moy, H. E. Gaub. Adhesion forces between individual ligand-receptor pairs. *Science*, 264:415–417, 1994.
- [16] G. U. Lee, L. A. Chrisey, R. J. Colton. Direct measurement of the forces between complementary strands of DNA. *Science*, 266:771–773, 1994.
- [17] T. Strunz, K. Oroszlan, R. Schäfer, H.-J. Güntherodt. Dynamic force spectroscopy of single DNA molecules. *Proc. Natl. Acad. Sci. USA*, 96:11277–11282, 1999.
- [18] J. Fritz, A. G. Katopodis, F. Kolbinger, D. Anselmetti. Force-mediated kinetics of single P-selectin/ligand complexes observed by atomic force microscopy. *Proc. Natl. Acad. Sci. USA*, 95:12283–12288, 1998.
- [19] U. Dammer, O. Popescu, P. Wagner, D. Anselmetti, H.-J. Güntherodt, G. N. Misevic. Binding strength between cell adhesion proteoglycans measured by atomic force microscopy. *Science*, 267:1173–1175, 1995.
- [20] P. Hinterdorfer, W. Baumgartner, H. Gruber, K. Schilcher, H. Schindler. Detection and localization of individual antibody-antigen recognition events by atomic force microscopy. *Proc. Natl. Acad. Sci. USA*, 93:3477–3481, 1996.
- [21] U. Dammer, M. Hegner, D. Anselmetti, P. Wagner, M. Dreier, W. Huber, H.-J. Güntherodt. Specific antigen/antibody interactions measured by force microscopy. *Biophys. J.*, 70:2437–2441, 1996.

- [22] R. Ros, F. Schwesinger, D. Anselmetti, M. Kubon, R. Schäfer, A. Plückthun, L. Tiefenauer. Antigen binding forces of individually addressed single-chain Fv antibody molecules. *Proc. Natl. Acad. Sci. USA*, 95:7402–7405, 1998.
- [23] F. W. Bartels, B. Baumgarth, D. Anselmetti, R. Ros, A. Becker. Specific binding of the regulatory protein ExpG to promoter regions of the galactoglucan biosynthesis gene cluster of *Sinorhizobium meliloti* - a combined molecular biology and force spectroscopy investigation. *J. Struct. Biol.*, 143:145–152, 2003.
- [24] F. Kühner, L. T. Costa, P. M. Bisch, S. Thalhammer, W. M. Heckl, H. E. Gaub. LexA-DNA bond strength by single molecule force spectroscopy. *Biophys. J.*, 87:2683–2690, 2004.
- [25] B. Baumgarth, F. W. Bartels, D. Anselmetti, A. Becker, R. Ros. Detailed studies of the binding mechanism of the *Sinorhizobium meliloti* transcriptional activator ExpG to DNA. *Microbiology*, 151:259–268, 2005.
- [26] W. E. Moerner, D. P. Fromm. Methods of single-molecule fluorescence spectroscopy and microscopy. *Rev. Sci. Instr.*, 74(8):3597–3619, 2003.
- [27] D. W. Pohl, W. Denk, M. Lanz. Optical stethoscopy: Image recording with resolution lambda/20. *Appl. Phys. Lett.*, 44:651–653, 1984.
- [28] T. Funatsu, Y. Harada, M. Tokunaga, K. Saito, T. Yanagida. Imaging of single fluorescent molecules and individual ATP turnovers by single myosin molecules in aqueous solution. *Nature*, 374:555–559, 1995.
- [29] R. M. Dickson, D. J. Norris, Y.-L. Tzeng, W. E. Moerner. Three-dimensional imaging of single molecules solvated in pores of poly(acrylamide) gels. *Science*, 274(5289):966–968, 1996.
- [30] G. Binnig, H. Rohrer, C. Gerber, E. Weibel. Tunneling through a controllable vacuum gap. *Appl. Phys. Lett.*, 40:178–180, 1982.
- [31] G. Binnig, H. Rohrer, C. Gerber, E. Weibel. Surface studies by scanning tunneling microscopy. *Phys. Rev. Lett.*, 49:57–61, 1982.
- [32] J. M. Neumeister, W. A. Ducker. Lateral, normal, and longitudinal spring constants of atomic force microscopy cantilevers. *Rev. Sci. Instr.*, 64:2527–2531, 1994.

- [33] J. P. Cleveland, S. Manne, D. Bocek, P. K. Hansma. A nondestructive method for determining the spring constant of cantilevers for scanning force microscopy. *Rev. Sci. Instr.*, 64(2):403–405, 1993.
- [34] C. T. Gibson, G. S. Watson, S. Myhra. Determination of the spring constants of probes for force microscopy/spectroscopy. *Nanotechnology*, 7:259–262, 1996.
- [35] J. L. Hutter, J. Bechhoefer. Calibration of atomic-force microscope tips. *Rev. Sci. Instr.*, 7:1868–1873, 1993.
- [36] D. A. Walters, J. P. Cleveland, N. H. Thomson, P. K. Hansma, M. A. Wendman, G. Gurley, V. Elings. Short cantilevers for atomic force microscopy. *Rev. Sci. Instr.*, 67(10):3583–3590, 1996.
- [37] A. Roters, D. Johannsmann. Distance-dependent noise measurements in scanning force microscopy. *J. Phys.: Condens. Matter*, 8:7561–7577, 1996.
- [38] S. B. Smith, Y. Cui, C. Bustamante. Overstretching B-DNA: The elastic response of individual double-stranded and single-stranded DNA molecules. *Science*, 271:795–799, 1996.
- [39] T. Strick, J.-F. Allemand, D. Bensimon, V. Croquette. Stress-induced structural transitions in DNA and proteins. *Annu. Rev. Biophys. Biomol. Struct.*, 29:523–543, 2000.
- [40] T. Strick, J.-F. Allemand, D. Bensimon, R. Lavery, V. Croquette. Phase coexistence in a single DNA molecule. *Physica A*, 263:392–404, 1999.
- [41] M. W. Konrad, J. I. Bolonick. Molecular dynamics simulation of DNA stretching is consistent with the tension observed for extension and strand separation and predicts a novel ladder structure. *J. Am. Chem. Soc.*, 118:10989–10994, 1996.
- [42] R. H. Austin, J. P. Brody, E. C. Cox, T. Duke, W. Volkmuth. Stretch genes. *Physics Today*, February 1997:32–38, 1997.
- [43] A. Lebrun, R. Lavery. Modelling extreme stretching of DNA. *Nucleic Acids Res.*, 24(12):2260–2267, 1996.
- [44] J. F. Leger, G. Romano, A. Sarkar, J. Robert, L. Bourdieu, D. Chatenay, J. F. Marko. Structural transitions of a twisted and stretched DNA molecule. *Phys. Rev. Lett.*, 83(5):1066–1069, 1999.

- [45] J. Rouzina, V. A. Bloomfield. Force-induced melting of the DNA double helix. 1. thermodynamic analysis. *Biophys. J.*, 80:882–893, 2001.
- [46] J. Rouzina, V. A. Bloomfield. Force-induced melting of the DNA double helix. 2. effect of solution conditions. *Biophys. J.*, 80:894–900, 2001.
- [47] H. Clausen-Schaumann, M. Rief, C. Tolksdorf, H. E. Gaub. Mechanical stability of single DNA molecules. *Biophys. J.*, 78(4):1997–2007, 2000.
- [48] B. C. Baguley. Nonintercalative DNA-binding antitumour compounds. *Mol. Cell Biochem.*, 43(3):167–181, 1982.
- [49] C. Bailly, J. B. Chaires. Sequence-specific DNA minor groove binders. design and synthesis of netropsin and distamycin analogues. *Bioconj. Chem.*, 9(5):513–538, 1998.
- [50] P. R. Turner, W. A. Denny. The mutagenic properties of DNA minor groove binding ligands. *Mutat. Res.*, 355(1-2):141–169, 1996.
- [51] S. D. Wilking, N. Sewald. Solid pase synthesis of an amphiphilic peptide modified for immobilisation at the C-terminus. *J. Biotechnol.*, 112:109–114, 2004.
- [52] G. N. Hortobagyi. Anthracyclines in the treatment of cancer. *Drugs*, 54(4):1–7, 1997.
- [53] G. Aubel-Saudron, D. Londos-Gagliardi. Daunorubicin and doxorubicin, anthracycline antibiotics, a physicochemical and biological review. *Biochimie*, 66(5):333–352, 1984.
- [54] G. G. Hu, X. Shui, F. Leng, W. Priebe, J. B. Chaires, L. D. Williams. Structure of a DNA-bisdaunomycin complex. *Biochemistry*, 36:5940–5946, 1997.
- [55] A. R. Morgan, J. S. Lee, D. E. Pulleyblank, N. L. Murray, D. H. Evans. Review: Ethidium fluorescence assays, part 1: Physicochemical studies. *Nucleic Acids Res.*, 10(7):547–569, 1979.
- [56] A. R. Morgan, D. H. Evans, G. U. Lee, D. E. Pulleyblank. Review: Ethidium fluorescence assays, part 2: Enzymatic studies and DNA-protein interactions. *Nucleic Acids Res.*, 10(7):571–594, 1979.
- [57] A. N. Glazer, H. S. Rye. Stable dye-DNA intercalation complexes as reagents for high-sensitivity fluorescence detection. *Nature*, 359(6398):859–861, 1992.

## Bibliography

---

- [58] J. F. Marko, E. D. Siggia. Stretching DNA. *Macromolecules*, 28:8759–8770, 1995.
- [59] J. F. Marko. Statistical mechanics of supercoiled DNA. *Phys. Rev. E*, 52(3):2912–2938, 1995.
- [60] J. F. Marko. DNA under high tension: Overstretching, undertwisting, and relaxation dynamics. *Phys. Rev. E*, 57(2):2134–2149, 1998.
- [61] C. Bustamante. Entropic elasticity of lambda-phage dna. *Science*, 265:1599–1600, 1994.
- [62] A. Ahsan, J. Rudnick, R. Bruinsma. Elasticity theory of the B-DNA to S-DNA transition. *Biophys. J.*, 74:132–137, 1998.
- [63] E. Ising. Beitrag zur Theorie des Ferromagnetismus. *Zeitschrift f. Physik*, 31:253–258, 1925.
- [64] P. Cizeau, J.-L. Viovy. Modeling extreme extension of DNA. *Biopolymers*, 42:383–385, 1997.
- [65] H. Zhou, Y. Zhang, Z.-C. Ou-Yang. Elastic property of single double-stranded DNA molecules: Theoretical study and comparison with experiments. *Phys. Rev. E*, 62(1):1045–1058, 2000.
- [66] K. Makino, M. Amemura, T. Kawamoto, K. Kimura, H. Shinagawa, A. Nakata, M. Suzuki. DNA binding of PhoB and its interaction with RNA polymerase. *J. Mol. Biol.*, 259:15–26, 1996.
- [67] K. Makino, H. Shinagawa, M. Amemura, K. Kimura, A. Nakata. Regulation of the phosphate regulon of Escherichia coli - activation of *pstS* transcription in vitro. *J. Mol. Biol.*, 203:85–95, 1988.
- [68] H. Okamura, S. Hanaoka, A. Nagadoi, K. Makino, Y. Nishimura. Structural comparison of the PhoB and OmpR DNA-binding/transactivation domains and the arrangement of PhoB molecules on the phosphate box. *J. Mol. Biol.*, 295:1225–1236, 2000.
- [69] S.-K. Kim, S. Kimura, H. Shinagawa, A. Nakata, K.-S. Lee, B. L. Wanner, K. Makino. Dual transcription regulation of the Escherichia coli phosphate-starvation-inducible *psiE* gene of the phosphate regulon by PhoB and the cyclic

- AMP (cAMP)-cAMP receptor protein complex. *J. Bacteriol.*, 182(19):5596–5599, 2000.
- [70] A. G. Blanco, M. Sola, F. X. Gomis-Rüth, M. Coll. Tandem DNA recognition by PhoB, a two-component signal transduction transcriptional activator. *Structure*, 10:701–713, 2002.
- [71] R. Merkel. Force spectroscopy on single passive biomolecules and single biomolecular bonds. *Physics Reports*, 346:343–385, 2001.
- [72] S. Arrhenius. Über die Reaktionsgeschwindigkeit bei der Inversion von Rohrzucker durch Säuren. *Zeitschrift f. Phys. Chemie*, 4:226–248, 1889.
- [73] H. Eyring. The activated complex in chemical reactions. *J. Chem. Phys.*, 3:107–115, 1935.
- [74] H. A. Kramers. Brownian motion in a field of force and the diffusion model of chemical reactions. *Physica VII*, 4:284–304, 1940.
- [75] G. I. Bell. Models for the specific adhesion of cells to cells. *Science*, 200:618–627, 1978.
- [76] P. Hänggi, P. Talkner, M. Borkovec. Reaction-rate theory: fifty years after Kramers. *Rev. Mod. Phys.*, 62(2):251–341, 1990.
- [77] A. Einstein. Über die von der molekularkinetischen Theorie der Wärme geforderte Bewegung von in ruhenden Flüssigkeiten suspendierten Teilchen. *Ann. Phys.*, 17:549–560, 1905.
- [78] E. Evans. Probing the relation between force-lifetime and chemistry single molecular bonds. *Annu. Rev. Biophys. Biomol. Struct.*, 30:105–128, 2001.
- [79] E. Evans. Energy landscapes of biomolecular adhesion and receptor anchoring at interfaces explored with dynamic force spectroscopy. *Faraday Discuss.*, 111:1–16, 1998.
- [80] J.-M. Lehn. *Supramolecular chemistry*. Verlag Chemie, 1995.
- [81] F. Vögtle. *Supramolecular chemistry*. Wiley and Sons, 1991.
- [82] C. D. Gutsche. *Calixarenes*. Royal Society of Chemistry, 1989.

- [83] C. D. Gutsche. *Calixarenes revisited*. Royal Society of Chemistry, 1998.
- [84] V. Böhmer. Calixarene - Makrocyclen mit (fast) unbegrenzten Möglichkeiten. *Angew. Chem.*, 107:785–818, 1995.
- [85] M. Bermudez, N. Capron, T. Gase, F. G. Gatti, F. Kajzar, D. A. Leigh, F. Zerbetto, S. W. Zhang. Influencing intramolecular motion with an alternating electric field. *Nature*, 406:608–611, 2000.
- [86] R. A. Bissell, E. Cordova, A. E. Kaiser, J. F. Stoddart. A chemically and electrochemically switchable molecular shuttle. *Nature*, 369:133–137, 1994.
- [87] F. Moresco, G. Meyer, K. H. Rieder, H. Tang, A. Gourdon, C. Joachim. Conformational changes of single molecules induced by scanning tunneling microscopy: a route to molecular switching. *Phys. Rev. Lett.*, 86:672–675, 2001.
- [88] J. Walz, K. Ulrich, H. Port, H. C. Wolf, F. Effenberger. Fulgides as switches for intramolecular energy transfer. *Chem. Phys. Lett.*, 213:321–324, 1993.
- [89] M. Irie, Th. Lifka, K. Uchida. Photochromism of single crystalline diarylethenes. *Mol. Cryst. Liqu. Cryst.*, 297:81–84, 1997.
- [90] R. M. Metzger, B. Chen, U. Höpfner, M. V. Lakshmikantham, D. Vuillaume, T. Kawai, X. Wu, H. Tachibana, T. V. Hughes, H. Sakurai, J. W. Baldwin, C. Hosch, M. P. Cava, L. Brehmer, C. J. Ashwell. Unimolecular electrical rectification of hexadecylquinolinium tricyanoquinodimethanid. *J. Am. Chem. Soc.*, 119(43):10455–10466, 1997.
- [91] I. Willner, S. Rubin. Steuerung der Struktur und Funktion von Biomakromolekülen durch Licht. *Angew. Chem.*, 108:419–439, 1996.
- [92] I. Willner. Photoswitchable biomaterials: En route to optobioelectronic systems. *Acc. Chem. Res.*, 30(9):347–356, 1997.
- [93] M. E. Vázquez, A. M. Caamano, J. Martínez-Costas, L. Castedo, J. L. Mascarenas. Design and synthesis of a peptide that binds specific DNA sequences through simultaneous interaction in the major and in the major groove. *Angew. Chem.*, 113(24):4859–4861, 2001.
- [94] M. E. Vázquez, A. M. Caamano, J. L. Mascarenas. From transcription factors to designed sequence-specific DNA-binding peptides. *Chem. Soc. Rev.*, 32:338–349, 2003.

- [95] D. M. Chudakov, V. V. Verkhusha, D. B. Staroverov, E. A. Souslova, S. Lukyanov, K. A. Lukyanov. Photoswitchable cyan fluorescent protein for protein tracking. *Nature Biotechnol.*, 22(11):1435–1439, 2004.
- [96] E. U. Thoden van Velzen, J. F. J. Engbersen, P. J. de Lange, J. W. G. Mahy, D. N. Reinhoudt. Self-assembled monolayers of resorcin[4]arene tetrasulfides on gold. *J. Am. Chem. Soc.*, 117:6853–6862, 1995.
- [97] T. Strunz, K. Oroszlan, I. Schumakovitch, H.-J. Güntherodt, M. Hegner. Model energy landscapes and the force-induced dissociation of ligand-receptor bonds. *Biophys. J.*, 79(3):1206–1212, 2000.
- [98] C. Friedsam, A. K. Wehle, F. Kühner, H. E. Gaub. Dynamic single-molecule force spectroscopy: bond rupture analysis with variable spacer length. *J. Phys.: Condens. Matter*, 15:S1709–S1723, 2003.
- [99] M. Rief, J. M. Fernandez, H. E. Gaub. Elastically coupled two-level systems as a model for biopolymer extensibility. *Phys. Rev. Lett.*, 81(21):4764–4767, 1998.
- [100] O. Braun, A. Hanke, U. Seifert. Probing molecular free energy landscapes by periodic loading. *Phys. Rev. Lett.*, 93(15):158105–1–158105–4, 2004.
- [101] B. Heymann, H. Grubmüller. Dynamic force spectroscopy of molecular adhesion bonds. *Phys. Rev. Lett.*, 84(26):6126–6129, 2000.
- [102] M. Evstigneev, P. Reimann. Dynamic force spectroscopy: Optimized data analysis. *Phys. Rev. E*, 68:045103–1–045103–4, 2003.
- [103] M. Raible, M. Exstigneev, P. Reimann, F. W. Bartels, R. Ros. Theoretical analysis of dynamic force spectroscopy experiments on ligand-receptor complexes. *J. Biotechnol.*, 112:13–23, 2004.
- [104] M. Nguyen-Duong, K. W. Koch, R. Merkel. Surface anchoring reduces lifetime of single specific bonds. *Europhys. Lett.*, 61(6):845–851, 2003.
- [105] B. Q. Xu, X. L. Li, Xiao, X.Y., H. Sakaguchi, N. J. Tao. Electromechanical and conductance switching properties of single oligothiophene molecules. *Nano Lett.*, 5(7):1491–1495, 2005.
- [106] H. Park, J. Park, A. K. L. Lim, E. H. Anderson, A. P. Alivisatos, P. L. McEuen. Nano-mechanical oscillations in a single-C<sub>60</sub> transistor. *Nature*, 407:57–59, 2000.

- [107] A. N. Pasupathy, J. Park, C. Chang, A. V. Soldatov, S. Lebedkin, R. C. Bialczak, J. E. Grose, L. A. K. Donev, J. P. Sethna, D. C. Ralph, P. L. McEuen. Vibration-assisted electron tunneling in C140 transistors. *Nano Lett.*, 5(2):203–207, 2005.
- [108] V. Sazonova, Y. Yaish, H. Üstünel, D. Roundy, T. A. Arlas, P. L. McEuen. A tunable carbon nanotube electromechanical oscillator. *Nature*, 431:284–287, 2004.
- [109] T. Hugel, N. B. Holland, A. Cattani, L. Moroder, M. Seitz, H. E. Gaub. Single-molecule optomechanical cycle. *Science*, 296(5570):1103–1106, 2002.
- [110] M. Nirmal, B. O. Dabbousi, M. G. Bawendi, J. J. Macklin, J. K. Trautman, T. D. Harris, L. E. Brus. Fluorescence intermittency in single cadmium selenide nanocrystals. *Nature*, 383:802–804, 1996.
- [111] M. Pelton, D. G. Grier, P. Guyot-Sionnest. Characterizing quantum-dot blinking using noise power spectra. *Appl. Phys. Lett.*, 85(5):819–821, 2004.
- [112] M. Kuno, D. P. Fromm, H. F. Hamann, A. Gallagher, D. J. Nesbitt. Nonexponential blinking kinetics of single CdSe quantum dots: A universal powerlaw behaviour. *J. Chem. Phys.*, 112(7):3117–3120, 2000.
- [113] R. G. Neuhauser, K. T. Shimizu, W. K. Koo, S. A. Empedocles, M. G. Bawendi. Correlation between fluorescence intermittency and spectral diffusion in single semiconductor quantum dots. *Phys. Rev. Lett.*, 85(15):3301–3304, 2000.
- [114] V. I. Klimov, A. A. Mikhailovsky, S. Xu, A. Malko, J. A. Hollingsworth, C. A. Leatherdale, H.-J. Eisler, M. G. Bawendi. Optical gain and stimulated emission in nanocrystal quantum dots. *Science*, 290:314–317, 2000.
- [115] P. Michler, A. Kiraz, C. Becher, W. V. Schoenfeld, P. M Petroff, L. Zhang, E. Hu, A. Imamoglu. A quantum dot single-photon turnstile device. *Science*, 290:2282–2285, 2000.
- [116] X. Brokman, G. Messin, P. Desbiolles, E. Giacobono, M. Dahan, J.-P. Hermier. Colloidal CdSe/ZnS quantum dots as single-photon sources. *New J. Phys.*, 6(99):1–7, 2004.
- [117] M Bruchez Jr., M. Moronne, P. Gin, S. Weiss, A. P. Alivisatos. Semiconductor nanocrystals as fluorescent biological labels. *Science*, 281:2013–2016, 1998.

- [118] D. R. Larson, W. R. Zipfel, R. Williams, S. W. Clark, M. P. Bruchez, F. W. Wise, W. W. Webb. Water-soluble quantum dots for multiphoton fluorescence imaging in vivo. *Science*, 300:1434–1436, 2003.
- [119] W. J. Parak, D. Gerion, T. Pellegrino, D. Zanchet, C. Micheel, S. C. Williams, R. Boudreau, M. A. Le Gros, C. A. Larabell, A. P. Alivisatos. Biological applications of colloidal nanocrystals. *Nanotechnology*, 14:R15–R27, 2003.
- [120] A. B. Rozhenko, W. W. Schoeller, M. C. Letzel, B. Decker, C. Agena, J. Mattay. Calixarenes as hosts for ammonium cations. a quantum chemical investigation. *J. Am. Chem. Soc.*, submitted:)2, 2004.
- [121] J. Enderlein. Theoretical study of single molecule fluorescence in a metallic nanocavity. *Appl. Phys. Lett.*, 80(2):315–317, 2002.
- [122] K. Vasilev, W. Knoll, M. Kreiter. Fluorescence intensities of chromophores in front of a thin metal film. *J. Chem. Phys.*, 120(7):3439–3445, 2004.
- [123] M. Orrit. Single-molecule spectroscopy: The road ahead. *J. Chem. Phys.*, 117(24):10938–10946, 2002.
- [124] F. Kulzer, M. Orrit. Single-molecule optics. *Annu. Rev. Phys. Chem.*, 55:585–611, 2004.
- [125] L.-A. Li, L. Davis. Single photon avalanche diode for single molecule detection. *Rev. Sci. Instr.*, 64:1524–1530, 1993.
- [126] N. L. Thompson, H. M. McConnell, T. P. Burghardt. Order in supported phospholipid monolayers detected by the dichroism of fluorescence excited with polarized evanescent illumination. *Biophys. J.*, 46:739–747, 1984.
- [127] M. F. Paige, E. J. Bjerneld, W. E. Moerner. A comparison of through-the-objective total internal reflection microscopy and epi-fluorescence microscopy for single-molecule fluorescence imaging. *Single Molecules*, 2:191–201, 2001.

# Acknowledgements

Interdisciplinary work like the one presented in this thesis can only be successful if good collaboration with many other specialist co-workers is guaranteed. I am indebted to several persons to whom I would like to express my thanks.

First of all, I would like to thank Prof. Dr. Dario Anselmetti for his supervision, his inspiration and the possibility to work on the topic of interaction at the nanoscale with its various facets. I am much obliged to his optimism and encouragement. The very same applies to my tutor PD Dr. Robert Ros, whom I also wish to thank for his valuable advice, immediate support and constant interest during this work. I have learned a lot from him.

I am in debt to all colleagues from the Experimental Biophysics group for the excellent working atmosphere. I would like to emphasize the expert support from Christoph Pelargus during the assembly of the TIRFM setup. I owe very much to his optics expertise. Special thanks are due to Volker Walhorn and Jörg Martini who constructed the AFM head, originally designed for SMFS with small cantilevers, which was used in the external emission control experiments. Thanks also to Dr. Frank Bartels for many valuable and inspiring discussions and to my colleagues Wibke Hellmich, Thanh Tu Duong and Jan Regtmeier for the good climate in our office.

I would also like to thank the many collaboration partners in the various projects. I am much obliged to the organic chemists Dr. Björn Decker and Christian Schäfer from Prof. Dr. Jochen Mattay's group who synthesized the resorc[4]arene host molecules. Thanks to both of them for the good collaboration.

Special thanks are also due to Sven David Wilking and Katrin Wollschläger from the chair of Bioorganic Chemistry. Their good cooperation has contributed considerably to the advancement of the peptide-DNA and protein-DNA interaction studies. Thanks also to PD Dr. Anke Becker and Dr. Birgit Baumgarth who provided the *pho* box and PhoB genes.

The novel theoretical approach for SMFS experiments which was tested and interpreted

in this thesis was developed by Prof. Dr. Peter Reimann, Dr. Mykhaylo Evstigneev and Dr. Martin Raible from the chair of condensed matter theory. I am indebted to these persons for the good collaboration and valuable discussions.

Furthermore, I would like to thank PD Dr. Thomas Nann from the Freiburg Materials Research Center (FMF) at Freiburg University for the synthesis and provision of the CdSe/ZnS semiconductor nanocrystals.

This work was performed within the scope of the collaborative research center 613: “physics of single molecule processes and molecular recognition in organic systems”. I would like to thank the Deutsche Forschungsgemeinschaft for financial support.

Besonderer Dank gilt weiterhin meinen Eltern, die mir das Studium ermöglichten und auf deren vielfältige Unterstützung ich auch während der Promotion bauen durfte. Last, but certainly not least I would like to thank my wife Friederike Steffen for her love and support beyond compare.

# Appendix

## List of Publications

- I. RAINER ECKEL, ROBERT ROS, ALEXANDRA ROS, SVEN DAVID WILKING, NORBERT SEWALD, AND DARIO ANSELMETTI. Identification of binding mechanisms in single molecule - DNA complexes. *Biophys. J.* 85 (2003), 1968-1973.
- II. ANDY SISCHKA, RAINER ECKEL, KATJA TOENSING, ROBERT ROS, AND DARIO ANSELMETTI. Compact microscope-based optical tweezers system for molecular manipulation. *Rev. Sci. Instr.* 74, 11 (2003), 4827-4831.
- III. ANDY SISCHKA, KATJA TOENSING, RAINER ECKEL, SVEN DAVID WILKING, NORBERT SEWALD, ROBERT ROS, AND DARIO ANSELMETTI. Molecular mechanisms and kinetics between DNA and DNA binding ligands. *Biophys. J.* 88 (2005), 404-411.
- IV. RAINER ECKEL, SVEN DAVID WILKING, ANKE BECKER, NORBERT SEWALD, ROBERT ROS, AND DARIO ANSELMETTI. Single-molecule experiments in synthetic biology: an approach to the affinity ranking of DNA-binding peptides. *Angew. Chem. Int. Ed.* 44 (2005), 3921-3924.
- IVa. **German edition:** Einzelmolekülexperimente in der synthetischen Biologie - ein Ansatz für das Affinitätsranking DNA-bindender Peptide. *Angew. Chem.* 117 (2005), 3989-3993.
- V. RAINER ECKEL, ROBERT ROS, BJÖRN DECKER, JOCHEN MATTAY, AND DARIO ANSELMETTI. Supramolecular chemistry at the single molecule level. *Angew. Chem. Int. Ed.* 44 (2005), 484-488.
- Va. **German edition:** Supramolekulare Chemie mit einzelnen Molekülen. *Angew. Chem.* 117 (2005), 489-492.

- 
- VI. MARTIN RAIBLE, MIKHAYLO EVSTIGNEEV, FRANK WILCO BARTELS, RAINER ECKEL, M. NGUYEN-DUONG, RUDOLF MERKEL, ROBERT ROS, DARIO ANSELMETTI, AND PETER REIMANN. Theoretical analysis of single-molecule force spectroscopy experiments: heterogeneity of chemical bonds. Accepted by *Biophys. J.*
- VII. RAINER ECKEL, VOLKER WALHORN, CHRISTOPH PELARGUS, JÖRG MARTINI, THOMAS NANN, DARIO ANSELMETTI, AND ROBERT ROS. Nanocrystal light switch. Submitted to *Small*.
- VIII. RAINER ECKEL, VOLKER WALHORN, CHRISTOPH PELARGUS, JÖRG MARTINI, THOMAS NANN, DARIO ANSELMETTI, AND ROBERT ROS. Combined TIRF-AFM setup: Controlled quenching of individual quantum dots. Submitted to *Proc. SPIE*.

Additional publication not treated in this thesis:

- RAINER ECKEL, HONG HUO, HONG-WEI GUAN, XIANG HU, XUN CHE, AND WEI-DONG HUANG. Characteristic infrared spectroscopic patterns in the protein bands of human breast cancer tissue. *Vibrational Spectroscopy* 27, 2 (2001), 165-173.

## Contributions to Conferences

1. RAINER ECKEL, ROBERT ROS, ALEXANDRA ROS, SVEN DAVID WILKING, NORBERT SEWALD, KATJA TOENSING, AND DARIO ANSELMETTI. Effects of small DNA-binding agents on the molecular elasticity of single DNA molecules. *The WE Heraeus Seminar 282: "Single Molecule Dynamics"* June 18 - 21, 2002, Bad Honnef, Germany. (Poster)
2. RAINER ECKEL, ROBERT ROS, ALEXANDRA ROS, SVEN DAVID WILKING, NORBERT SEWALD, AND DARIO ANSELMETTI. Force spectroscopy studies on DNA-ligand complexes: Distinction of different binding modes. *Scanning Probe Microscopies and Organic Materials XI*, September 22 - 24, 2002, Kassel, Germany. (Talk)
3. SVEN DAVID WILKING, RAINER ECKEL, ROBERT ROS, ALEXANDRA ROS, DARIO ANSELMETTI, AND NORBERT SEWALD. Synthesis and first AFM studies of helical DNA-binding model peptides and a DNA-binding fragment of PhoB (E.coli). *6<sup>th</sup> German Peptide Symposium*, March 23 - 26, 2003, Berlin, Germany. (Poster)

4. RAINER ECKEL, ROBERT ROS, ALEXANDRA ROS, SVEN DAVID WILKING, NORBERT SEWALD, AND DARIO ANSELMETTI. Binding of peptides to DNA: an AFM force spectroscopy study. *Scanning Probe Microscopies and Organic Materials XII*, September 24 - 26, 2003, Mainz, Germany. (Talk)
5. RAINER ECKEL, SVEN DAVID WILKING, ALEXANDRA ROS, NORBERT SEWALD, ROBERT ROS, AND DARIO ANSELMETTI. Specific binding of a single peptide to DNA investigated by AFM force spectroscopy. *DPG-Frühjahrstagung des Arbeitskreises Festkörperphysik, Symposium "Life Sciences on the Nanometer Scale - Physics meets Biology"*, March 8 - 12, 2004, Regensburg, Germany. (Poster)
6. ANDY SISCHKA, KATJA TOENSING, ANNICA GRABBE, KAI LEFFHALM, RAINER ECKEL, SVEN DAVID WILKING, NORBERT SEWALD, JUERGEN WIENANDS, ROBERT ROS, AND DARIO ANSELMETTI. Optical tweezers: a single molecule biosensor for molecular DNA manipulation and detection of individual receptors on cells. *DPG-Frühjahrstagung des Arbeitskreises Festkörperphysik, Symposium "Life Sciences on the Nanometer Scale - Physics meets Biology"*, March 8 - 12, 2004, Regensburg, Germany. (Poster)
7. RAINER ECKEL, ROBERT ROS, BJOERN DECKER, JOCHEN MATTAY, AND DARIO ANSELMETTI. Supramolecular chemistry at the single molecule level. *Scanning Probe Microscopies and Organic Materials XIII*, September 6 - 8, 2004, Bielefeld, Germany. (Talk)
8. RAINER ECKEL, BJOERN DECKER, SVEN DAVID WILKING, KATJA TOENSING, ANKE BECKER, NORBERT SEWALD, JOCHEN MATTAY, AND DARIO ANSELMETTI. Single molecule force spectroscopy: a new approach for affinity ranking in supramolecular chemistry and synthetic biology. *40<sup>th</sup> Winter Seminar on Biophysical Chemistry, Molecular Biology and Cybernetics of Cell Functions*, January 15 - 29, 2005, Klosters, Switzerland. (Talk & Poster)
9. RAINER ECKEL, ROBERT ROS, BJOERN DECKER, JOCHEN MATTAY, AND DARIO ANSELMETTI. Supramolecular interaction at the single molecule level. *69. Jahrestagung der Deutschen Physikalischen Gesellschaft, AK Biophysik*, March 4 - 9, 2005, Berlin, Germany. (Poster)
10. VOLKER WALHORN, JOERG MARTINI, RAINER ECKEL, JEROEN STEFFEN, TOBIAS KRAMER, BJOERN DECKER, ROBERT ROS, DARIO ANSELMETTI, JUERGEN BRUGGER, AND JOCHEN MATTAY. Force spectroscopy with a novel small

- focus AFM. 69. *Jahrestagung der Deutschen Physikalischen Gesellschaft, AK Biophysik*,, March 4 - 9, 2005, Berlin, Germany. (Poster)
11. RAINER ECKEL. Single molecule force spectroscopy: a new approach for affinity ranking in supramolecular chemistry and synthetic biology. *Bio-Image Summer School “Visualization, Manipulation and Modeling of Single Biomolecules” at the École normale supérieure*, July 11 - 22, 2005, Paris, France. (Poster)
  12. Planned: RAINER ECKEL, VOLKER WALHORN, CHRISTOPH PELARGUS, JOERG MARTINI, THOMAS NANN, ROBERT ROS, AND DARIO ANSELMETTI. Controlled quenching of single quantum dots in a combined TIRF-AFM setup. *SPIE International Symposium on Biomedical Optics*, January 21 - 26, 2006, San Jose, USA. (Talk)
  13. Planned: RAINER ECKEL, VOLKER WALHORN, CHRISTOPH PELARGUS, THOMAS NANN, ROBERT ROS, AND DARIO ANSELMETTI. Optomechanical setup for single molecule biophysics. *50<sup>th</sup> Annual Meeting of the Biophysical Society*, February 18 - 22, 2006, Salt Lake City, USA. (Talk)
  14. Planned: RAINER ECKEL, VOLKER WALHORN, CHRISTOPH PELARGUS, THOMAS NANN, ROBERT ROS, AND DARIO ANSELMETTI. Control of single nanocrystal fluorescence emission in a combined TIRFM/AFM setup. *DPG-Frühjahrstagung des Arbeitskreises Festkörperphysik*, March 26 - 31, 2006, Dresden, Germany.

## **Curriculum Vitae**

### **Rainer Eckel**

Born June 16<sup>th</sup>, 1977 in Frankenberg (Eder), married, nationality: German

---

- 1983-1987    Grundschule in Frankenberg
- 1987-1996    Gymnasium Edertalschule in Frankenberg (Eder)
- 06/1996    Abitur, final result: 1.0
- 1996-2002    Studies in Chemistry and Biochemistry at the Faculty of Chemistry,  
Bielefeld University
- 09-12/2000    Internship at the Dalian Institute of Chemical Physics, Chinese  
Academy of Sciences, Dalian, P.R. China (experimental research  
on the identification of breast cancer tissue by protein FTIR spec-  
troscopy; cf. List of Publications)
- 05/2002    Diploma in Chemistry, final result: "mit Auszeichnung"  
Thesis: "*Messung und Simulation der mechanischen Elastizität  
einzelner DNA-Ligand-Komplexe*"  
at the Experimental Biophysics and Applied Nanoscience Group,  
Bielefeld University; Advisors: Prof. Dr. Dario Anselmetti and  
Prof. Dr. Norbert Sewald
- 06/2002    Started PhD at the Experimental Biophysics and Applied  
Nanoscience Group, Faculty of Physics, Bielefeld University  
Advisors: Prof. Dr. Dario Anselmetti and PD Dr. Robert Ros
-